

MEASUREMENT OF PION-CARBON
CROSS SECTIONS AT DUET
AND
MEASUREMENT OF NEUTRINO OSCILLATION
PARAMETERS AT THE T2K EXPERIMENT

ELDER SEBASTIAN PINZON GUERRA

A DISSERTATION SUBMITTED TO
THE FACULTY OF GRADUATE STUDIES
IN PARTIAL FULFILLMENT OF THE REQUIREMENTS
FOR THE DEGREE OF
DOCTOR OF PHILOSOPHY

GRADUATE PROGRAM IN
PHYSICS AND ASTRONOMY

YORK UNIVERSITY
TORONTO, ONTARIO
NOVEMBER 2017

© Elder Sebastian Pinzon Guerra, 2017

Abstract

The Tokai-to-Kamioka (T2K) experiment is a long baseline neutrino oscillation experiment. An intense ν_μ (or $\bar{\nu}_\mu$) beam is produced at the Japan Proton Accelerator Research Complex (J-PARC) by protons hitting a graphite target. The neutrinos are measured 280 m from the target, and again 295 km across Japan using the Super-Kamiokande detector. This allows for the study of the neutrino oscillations in four channels: the ν_e and $\bar{\nu}_e$ appearance and ν_μ and $\bar{\nu}_\mu$ disappearance.

In T2K, neutrinos are observed primarily via charged current quasi-elastic scattering (CCQE) interactions ($\nu_\mu + N \rightarrow \mu^- + N'$), as well as charged current single pion (CC1 π) production ($\nu_\mu + N \rightarrow \mu^- + \pi + N'$), where N and N' refer to nucleon states. The neutrino energy is obtained from the reconstructed muon kinematics, with additional pion kinematic information for the CC1 π case. If there is an unobserved pion in the event, a CC1 π event will look like CCQE and the reconstructed neutrino energy will be incorrect. The π is free to interact inside and outside the nucleus primarily via absorption and charge exchange processes. Reducing the uncertainties on these cross sections reduces the systematic uncertainties for neutrino oscillation measurements. The Dual Use Experiment at TRIUMF (DUET) was conducted to address this issue. This thesis describes the recent results from DUET: the most precise measurements of absorption and charge exchange cross sections of π^+ on carbon for the momentum range of 201.6~295.1 MeV/ c .

These DUET measurements, along with existing pion-nucleus scattering data for different atomic nuclei, are used to improve the cascade model that simulates pion-nucleus scattering in T2K, and to reduce the associated systematic uncertainties. These improvements are used in a Markov Chain Monte Carlo neutrino oscillation analysis of the T2K Run 1-8 data, corresponding to 14.7×10^{20} protons-on-target in neutrino mode and 7.6×10^{20} in antineutrino mode. As a result, the most precise measurement of θ_{13} , θ_{23} , Δm_{32}^2 , and δ_{CP} , parameters that govern the oscillation phenomenon, is obtained. The δ_{CP} parameter encodes the information about the matter-antimatter asymmetry in the neutrino sector, with $\delta_{CP} = \{0, \pm\pi\}$ indicating no such asymmetry (CP-conservation). Fitting the T2K data with a constraint on $\sin^2 \theta_{13}$ from measurements by reactor experiments, the best fit oscillation parameter values are $\sin^2 \theta_{13} = 0.0222_{-0.0009}^{+0.0016}$, $\sin^2 \theta_{23} = 0.521_{-0.021}^{+0.029}$, $\Delta m_{32}^2 = 2.46_{-0.06}^{+0.08} \times 10^{-3} \text{ eV}^2$, and $\delta_{CP} = -1.79_{-0.60}^{+0.72} \text{ rad}$. The CP-conserving values are excluded at the 95.4% (2σ) level. This constitutes the world-leading constraint for CP-violation in the leptonic sector.

To my parents.

Acknowledgements

First and foremost, I wholeheartedly thank my supervisor Sampa Bhadra for inviting me to join her group at York, and for the many -previously unimagined- opportunities that came along. I feel exceptionally lucky to have been given this chance. Knowing that she was always one Skype chat away made for a very pleasant journey as a graduate student. Her confidence in my abilities gave me the courage to explore the world of pions and neutrinos without hesitation. I enjoyed our many conversations about TV shows and movies, and the group BBQs and dinners at her home. Thanks to John Martin too for all the food!

The work presented here is built on top of an immense amount of work from many collaborators from T2K and DUET, I thank them all. I also thank the J-PARC and TRIUMF laboratories for providing the world-class facilities that allow us to perform cutting edge science.

I was fortunate to spend a lot of time with the members of the OTR/YorkU/UofT group. Mark Hartz, Slavic Galymov, and Patrick de Perio were extremely helpful in getting started in HEP, learning the details of the OTR, and losing the fear of ROOT. Fortunately for me, I was able to remain close to Mark all throughout my time as a grad student, and I was always hoping that some of his extraordinary abilities would stick on me. I thank him for hosting me at IPMU in the fall of 2016. In my opinion, Patrick represented the epitome of what a graduate student can be, so I always tried to follow in his footsteps. Mitchell Yu, Mark McCarthy, and Arturo Fiorentini became my close friends and roommates both in Tokai and Toronto. I enjoyed the countless hours we spent driving and eating in Japan. I specially thank Arturo for always being available to discuss the nitty-gritty details of my work whenever I was getting stuck. These discussions became an integral part of my thought process.

The work I developed as a member of the DUET collaboration was the most fulfilling of my graduate career. I am especially fond of DUET for giving me the opportunity to travel to fantastic places around the world to share our results with the neutrino physics community. I sincerely thank Mike Wilking, Motoyasu Ikeda, Kei Ieki, Hiro Tanaka, Patrick de Perio, Masashi Yokoyama, and Tsuyoshi Nakaya for giving me the opportunity to conclude all their hard work. Mike became my de facto supervisor during this time and I got to enjoy his brilliant and enthusiastic guidance. His passionate approach to science was a joy to watch and was powerful enough to easily convince me to march for science in the streets of New York in 2017. Ieki-san and Ikeda-san were always willing to reply to my long emails riddled with questions about $\text{PIA}\nu\text{O}$. I am deeply grateful with Yokoyama-san for supporting my JSPS Fellowship application in the

fall of 2017. I thank him for being a fantastic host when I visited UTokyo. I genuinely admire Yokoyama-san's successful career and very much enjoyed our conversations about particle detectors and physics.

My next goal was to improve the modelling of pion interactions using the DUET measurements. I thank Tom Feusels for his leadership of the FSI/SI Task Force and for staying positive at times when the end goal seemed out of reach. I also thank the NIWG conveners: Sara Bolognesi, Yoshinari Hayato, Kevin McFarland, and Callum Wilkinson for their insightful comments and suggestions, and for being so supportive of my work.

The last piece of my thesis was developed as part of the MaCh3 group. I thank the current and past members for developing such an amazing framework. I specially thank Asher Kaboth, Patrick Dunne, and Clarence Wret for their help and guidance in developing the work presented here.

The T2K-Canada group was a significant source of support and fun times. Hiro Tanaka was always around and often acted as my PhD co-adviser, which I consider an extraordinary honour. While I would describe Hiro's style (in physics and life) as elegant, he had no problem showing his graduate student abilities, whether if it was in front of a terminal or ordering the next round of drinks. Kendall Mahn is part of that select group of people who are universally admired and loved. I treasured her constant words of encouragement and support, and wish her the very best in her new role as T2K analysis coordinator. The graduate student life is made much more bearable by sharing it with other graduate students: I thank Jiae, Sophie, Shimpei, Jordan, Zoya, Xiaoyue, Yue, Minoo, Corina, Patrick, etc., for the many rounds of meat, beer, and karaoke. I specially thank Jiae for being a great travelling companion in Japan and North America. I am still surprised that we survived the road trip to Nikko. I would also like to thank other T2K-Canada members with whom I was lucky to spend time: Mark Scott, Sujeewa, Anthony, Scott, Roman, Akira, etc.

While I spent large periods of time away from York, I was fortunate to make fantastic friends there too. I will be forever grateful with Andres, Jorge-Armando, Paola, and Gabriel for making my transition to Toronto significantly more enjoyable. Andres is one of the purest, kindest, genuinely good people I have had the pleasure to meet, and I am proud to call him my friend. I thank Jorge for showing me the exciting opportunities available outside of physics. I thank Ana Maria and Susana for always being up for trying new restaurants in Toronto.

Finally and most importantly, I thank my family. Their constant support and unconditional love always kept me going. They mean everything to me and I hope I can make them proud.

Contributions

The results in this thesis are based on the work of more than two decades of the hundreds of physicists, engineers, and technicians of the T2K and DUET collaborations and the J-PARC and TRIUMF laboratories. An effort has been made to provide public references whenever possible, but unfortunately a large part of the work cited lies on internal T2K technical notes. This section will clarify my personal contributions to each experiment.

I joined the T2K and DUET collaborations in the fall of 2011. My first contribution to the T2K experiment was the operation, monitoring, and maintenance of the Optical Transition Radiation detector described in Section 3.1.2. In the winter of 2015 I had a leading role in the installation and commissioning of the current OTR system. I was an active member of the OTR and Beam groups until the fall of 2015, but I continue to provide support when necessary.

The DUET collaboration published the results of its physics runs in two articles published in the *Physical Review C*. The first paper presented a complete description of the experimental setup and the combined measurement of absorption and charge exchange cross sections of charged pions on carbon for five values of pion momentum in the 200~300 MeV/ c range [1]. I inherited this analysis from Dr. K. Ieki (Kyoto U.) when it was almost complete after he obtained his degree. I led the paper committee and fostered it to publication, being the corresponding author. In the process, I corrected bugs and re-evaluated all the systematic uncertainties. The second paper presented the separate measurement of the absorption and charge exchange cross sections for the same range of pion momenta [2]. This analysis was entirely my own work and is described in Chapter 6. I presented versions of these results at the 2013 and 2014 CAP congresses, and gave invited talks at the following major conferences on neutrino physics: NuFact 13, NuINT 15, and NuINT 17.

I took over the NEUT cascade model and its associated tools from Dr. Patrick de Perio (U. of Toronto) *et al.*. Most of my work regarding the cascade model, final state interactions (FSI), and secondary interactions (SI) was developed as part of the FSI/SI Task Force of the Neutrino Interaction Working Group (NIWG), in which I took a leading role. I developed the fitting framework (FSIFitter) used to tune the model and to set the systematic uncertainties associated with FSI and SI. The FSIFitter performed a global fit to the world π^\pm -A scattering data. This work is described in Chapter 7. I presented this result at the NuINT 17 conference. A paper describing these results is being prepared. The reduced FSI and SI uncertainties obtained as a result of this work will be used by future neutrino cross section and oscillation analyses from

T2K.

The Markov Chain Monte Carlo framework used for the oscillation analysis presented in Part III was developed by the MaCh3 group led by Dr. Asher Kaboth (Royal Holloway, U. of London). The selections of neutrino events at ND280 and SK and the parameterization and priors for the systematic uncertainties were developed by other groups, and the relevant technical notes have been referenced. The oscillation analysis presented in this thesis was built upon the MaCh3 oscillation analysis that was made public in the summer of 2017 and that is currently being prepared for publication. Dr. Patrick Dunne (Imperial College London) was the primary analyzer, while I served as a secondary co-analyzer, which allowed me to get familiarized with the framework. In particular, I evaluated the FSI and SI prior systematic uncertainties for the SK selections used by all the oscillation analysis groups, and estimated the effect of all the systematic uncertainties to the SK samples in the MaCh3 framework.

My main contribution to the oscillation analysis presented in this thesis was the improved treatment of FSI and SI systematic uncertainties at SK. As a result of this work, the constraints on FSI uncertainties obtained from the near detector can be propagated to the far detector, further reducing them. This work has been accepted by the T2K Oscillation Analysis Group and will be included in future oscillation analyses. The results and interpretations presented in Chapter 10 are all my own work.

Contents

Abstract	ii
Dedication	iii
Acknowledgments	iv
Contributions	vi
Contents	viii
List of Tables	xii
List of Figures	xv
I Introduction to Neutrinos and T2K	1
1 Overview	2
2 Neutrino Physics	7
2.1 Proposal and Discovery of Neutrinos	7
2.2 Neutrino Oscillations	9
2.2.1 Initial Evidence	9
2.2.2 Mixing Formalism	12
2.2.3 Current Knowledge and Open Questions	17
3 The T2K Experiment	21
3.1 The T2K Neutrino Beam	22
3.1.1 Beamline	22
3.1.2 The OTR Detector	24
3.1.3 Off-Axis Configuration	29
3.2 The Near Detector: ND280	30
3.2.1 INGRID	31
3.2.2 ND280	31

3.3	The Far Detector: Super-Kamiokande	33
4	Physics Simulation	36
4.1	Neutrino Flux Prediction	36
4.2	Neutrino Interaction Model	39
4.2.1	Nuclear Model	39
4.2.2	Cross Section Model	40
4.2.3	Final State Interactions Model	43
4.3	NEUT Pion Cascade Model	44
4.3.1	FSI Scaling Parameters	45
4.4	Detector Simulations	46
4.4.1	ND280 Simulation	46
4.4.2	SK Simulation	46
II	Pion Interactions on Nuclei	48
5	Dual Use Experiment at TRIUMF (DUET)	49
5.1	Introduction	49
5.2	Experimental Setup	50
5.2.1	M11 Beam Line	50
5.2.2	The PIA ν O Detector	52
5.2.3	The CEMBALOS Detector	54
5.3	Data Taking Summary	57
5.4	Physics Modelling	57
5.4.1	Elastic Scattering	58
5.4.2	Charge Exchange	58
6	Measurement of σ_{ABS} and σ_{CX} of π^+ on Carbon	60
6.1	Event Selection	60
6.1.1	PIA ν O Event Selection	60
6.1.2	CEMBALOS Event Selection	62
6.1.3	Selection Purities and Efficiencies	64
6.2	σ_{ABS} and σ_{CX} Extraction	65
6.2.1	Selection, Rejection and Mis-reconstruction Efficiencies	65
6.2.2	Selection of Nominal Model	66
6.3	Systematic Uncertainties	67
6.3.1	Beam Systematics	67
6.3.2	PIA ν O Detector Systematics	67
6.3.3	CEMBALOS Detector Systematics	68
6.3.4	Physics Modelling Systematics	69

6.4	Results	70
6.4.1	Fractional Covariance and Correlation Coefficients	70
7	Improvements to the π^\pm-A Modelling Uncertainties	72
7.1	Summary of Scattering External Data	72
7.1.1	Motivation for Using Data on Light and Heavy Nuclear Targets	72
7.1.2	Interaction Channels	73
7.1.3	Full List of Data Sets	73
7.2	Fit Strategy	73
7.2.1	Goal	73
7.2.2	Parameter Estimation	74
7.2.3	Interpolation Routines	76
7.2.4	Normalization Parameter Regimes	77
7.3	Fit Results	77
7.3.1	Fixed Normalization Parameters	77
7.3.2	Drawing Error Envelopes	77
7.3.3	Floating Normalization Parameters	79
7.3.4	Error Inflation	83
7.3.5	Final (Scaled) Uncertainties	84
7.4	Summary	85
III	Oscillation Analysis	92
8	Markov Chain Monte Carlo Oscillation Analysis Framework	93
8.1	Likelihood Definition	93
8.2	Bayesian Inference	95
8.3	Markov Chain Monte Carlo	96
8.3.1	Metropolis-Hastings Algorithm	96
8.4	Extracting Information from the Posterior	97
8.4.1	Marginalization of Nuisance Parameters	98
8.4.2	Parameter Estimation	98
9	Joint $\nu_{\mu,e} + \bar{\nu}_{\mu,e}$ Oscillation Analysis: Selections and Systematic Uncertainties	101
9.1	Event Selection	101
9.1.1	ND280 Event Selection	101
9.1.2	SK Event Selection	105
9.2	Systematic Uncertainties	107
9.2.1	Flux Prior Uncertainties	110
9.2.2	Cross Section Prior Uncertainties	110
9.2.3	ND280 Detector Model Prior Uncertainties	115

9.2.4	SK Detector Model Prior Uncertainties	117
9.3	Final State and Secondary Interaction Uncertainties	119
9.3.1	Splined Response Functions for FSI Parameters	120
9.3.2	Validations of the FSI Response Functions	122
9.3.3	Propagating the ND280 Constraints of FSI to SK	127
9.4	Effect of Prior Systematic Uncertainties	127
10	Joint $\nu_{\mu,e} + \bar{\nu}_{\mu,e}$ Oscillation Analysis: Results	129
10.1	Asimov Fits	130
10.1.1	T2K-Only Fit	130
10.1.2	T2K + Reactor Constraint Fit	133
10.2	Data Fits	135
10.2.1	Nuisance Parameters	135
10.2.2	Posterior Predictive Spectra	136
10.2.3	Effect of Propagating ND280 Constraints on FSI Uncertainties	137
10.2.4	T2K-Only Fit	141
10.2.5	T2K + Reactor Constraint Fit	144
10.2.6	Comparison to T2K Results and Other Experiments	147
10.3	Considerations for the Future	147
10.4	Summary	149
A	Glossary	151
B	OTR Post-Earthquake Alignment Studies	154
C	FSIFitter Validation Studies	156
D	Ratio of Data and NEUT Best-fit Comparisons	158
E	Comparison of π^\pm-A Scattering Models	165
E.1	Brief Description of Models	165
E.2	Comparison to NEUT	166
F	Comparison to the Official MaCh3 Run 1-8 Oscillation Analysis	174
F.1	Nuisance Parameters	174
F.2	Oscillation Parameters	176
G	Fake Data Study for the Oscillation Analysis	179
G.1	Alternative Form Factor Model	179
G.2	Fake Data Fit Results	180
	Bibliography	184

List of Tables

2.1	Summary of best-fit values and $\pm 1\sigma$ allowed ranges for the six neutrino oscillation parameters obtained from a global fit to the world neutrino data by the authors of [47]. The numbers in the 1st (2nd) column are obtained assuming NO (IO), <i>i.e.</i> , relative to the respective local minimum. Note that $\Delta m_{3l}^2 \equiv \Delta m_{31}^2 > 0$ for NO and $\Delta m_{3l}^2 \equiv \Delta m_{32}^2 < 0$ for IO. Adapted from [47].	20
4.1	NEUT FSI Parameter Descriptions	46
5.1	The number of nuclei in the fiducial volume of the fibre tracker.	52
6.1	The number of events after each stage of the cut. The numbers for MC are normalized by the numbers of good incident pion events in data.	62
6.2	Summary of number of events selected after the CEMBALOS downstream selection in Data and MC for each momentum setting, along with estimated efficiencies and purities for GEANT4	64
6.3	Predicted $N_{\text{CX}}^{\text{MC}}$, $N_{\text{BG}}^{\text{MC}}$ and extracted CX cross section σ_{CX} obtained from applying the efficiency scheme to GEANT4, FLUKA, and NEUT model predictions. See text for discussion.	67
6.4	Summary of the statistical and systematic uncertainties in percent.	68
6.5	σ_{ABS} and σ_{CX} measured by DUET.	71
7.1	Summary of π^\pm -Nucleus scattering data used for this tuning, including beam polarity, nuclear target type(s), momentum range and interaction channel(s). Note that some of this experiments might have measured data on other target nuclei. .	74
7.2	Minimum and maximum values for the NEUT FSI parameters allowed in the finite grid of precomputed NEUT predictions.	75
7.3	Post-fit FSI parameters, and the minimum χ^2 value obtained, with fixed normalization parameters using the TMultiDimFit and GNU-Octave interpolation methods	78
7.4	Post-fit NEUT FSI Parameters and the minimum $\chi^2(N_{\text{dof}})$ value obtained for fits with fixed normalization parameters and the specified external data selections. .	81

7.5	Post-fit NEUT FSI Parameters and the minimum $\chi^2(N_{dof})$ value obtained for fits with fixed normalization parameters and the 5 data sets with strongest pulls in Figure 7.6 removed.	83
7.6	Post-fit FSI parameters after error scaling.	85
9.1	Summary of number of events selected in FHC and RHC mode the in FGD1 and FGD2 in Data and MC, the efficiencies and purities of the selection, and the total POT analyzed.	104
9.2	Neutrino oscillation parameter values assumed for calculating the expected oscillated spectra in Table 9.3 and Figures 9.3 and 9.4.	107
9.3	Summary of number of events selected in SK in Data and MC, the efficiencies and purities of the selection, and the total POT analyzed.	110
9.4	Systematic parameters for cross section uncertainties. The relevant interaction mode is specified in the last column. The flat prior choices are addressed in Section 9.4.	112
9.5	Kinematic binning definition used for the SK detector and FSI+SI+PN systematic uncertainties.	117
9.6	Effect of 1σ variation of the systematic uncertainties on the predicted event rates of the SK samples used in this analysis.	128
10.1	Neutrino oscillation input values and their priors used for the Markov Chain analysis presented in this thesis and assumed for calculating the expected oscillated spectra shown in Table 9.3 and Figures 9.3 and 9.4.	130
10.2	Model comparison probabilities for normal and inverted hierarchies, as well as upper and lower octants, from the posterior of the Asimov fit to T2K data only.	132
10.3	Model comparison probabilities for normal and inverted hierarchies, as well as upper and lower octants, from the posterior of the Asimov fit to T2K + Reactor constraint.	134
10.4	Effect of 1σ variation of the FSI parameters uncertainties on the predicted event rates of the SK samples used in this analysis. The pre-fit uncertainties are calculated from random correlated throws from the prior of the FSI parameters, while the post-fit errors are calculated using the posterior predictive method.	141
10.5	Best-fit values and 68%, 90% and 95.45% 1D credible interval ranges for oscillation parameters for the data fit without reactor constraint. The 2D best-fit values are taken from the mode of the 2D marginal posterior distributions in $\sin^2 \theta_{23}$ - Δm_{32}^2 and $\sin^2 \theta_{13}$ - δ_{CP} , and the 1D 68% (95%) credible intervals correspond to the 1 (2) σ range for each parameter.	142
10.6	Model comparison probabilities for normal and inverted hierarchies, as well as upper and lower octants, from the posterior of a T2K-Only Data fit.	144

10.7	Best-fit values and 68%, 90% and 95.45% 1D credible interval ranges for oscillation parameters for the T2K + Reactor constraint Data fit. The 2D best-fit values are taken from the mode of the 2D marginal posterior distributions in $\sin^2 \theta_{23}$ – Δm_{32}^2 and $\sin^2 \theta_{13}$ – δ_{CP} , and the 1D 68% (95%) credible intervals correspond to the 1 (2) σ range for each parameter.	144
10.8	Model comparison probabilities for normal and inverted hierarchies, as well as upper and lower octants, from the posterior of a T2K + Reactor constraint Data fit.	146
10.9	Best-fit values and 68% credible interval ranges for oscillation parameters for the T2K-Only and T2K + Reactor constraint Data fits presented in Section 10.2. . .	149
B.1	Baffle centre and width measurements before and after the earthquake.	154

List of Figures

1.1	Illustration of the particle content in the Standard model of particle physics. The mass, charge, spin, and year of discovery are shown for each particle. Adapted from [6].	3
1.2	Charged current neutrino interactions with nuclei in the \sim GeV region.	5
1.3	Overview of the T2K oscillation analysis. The areas in which the author was involved are highlighted by dashed boxes.	6
2.1	Measurements of the hadron production cross section around the Z resonance. The curves indicate the predicted cross section for two, three and four neutrino species with SM couplings and negligible mass. The points represent a combination of experimental data from the ALPEH, DELPI, L3, and OPAL experiments. Reproduced from [22].	8
2.2	The ratio of the number of data events to the unoscillated MC prediction versus reconstructed L/E in Super-Kamiokande. The dashed lines show the expected shape for $\nu_\mu \rightarrow \nu_\tau$ oscillations for a model of neutrino oscillations. Reproduced from [35].	11
2.3	Ratio of the observed $\bar{\nu}_e$ spectrum to the expectation for no-oscillation versus L_0/E . The blue line shows the expectation for the best-fit model for neutrino oscillations in KamLAND. Other models are shown in red and green. Reproduced from [36].	12
2.4	Oscillation probabilities for ν_μ (blue) and $\bar{\nu}_\mu$ (red) disappearance (left), and ν_e (blue) and $\bar{\nu}_e$ (red) appearance (right) for the T2K baseline ($L=295$ km) as a function of the neutrino energy. The oscillation probabilities in vacuum (dashed lines) and matter (solid lines) are shown. An average matter density of 2.6 g/cm ³ was assumed. The following oscillation parameters were assumed for illustrative purposes: $\sin 2\theta_{12} = 0.846$, $\sin 2\theta_{13} = 0.085$, $\sin 2\theta_{23} = 1.0$, $\Delta m_{12}^2 = 7.53 \times 10^{-5}$ eV ² , $\Delta m_{32}^2 = 2.5 \times 10^{-3}$ eV ² , $\delta_{CP} = -1.0$ rad. This figure was produced using the Prob3++ software [46].	17

2.5	Results of the KamLAND experiment leading to world-best determination of the solar parameters θ_{12} and Δm_{21}^2 [49]. (a) The ratio of the observed $\bar{\nu}_e$ spectrum to the expectation for no-oscillation versus L_0/E for the full KamLAND statistics. (b) The allowed regions projected in the $(\tan^2 \theta_{12}, \Delta m_{21}^2)$ plane from a three-oscillation fit to KamLAND and global solar neutrino data. Reproduced from [49].	18
2.6	Left: Current world knowledge of the atmospheric parameters θ_{23} and Δm_{32}^2 . The 1σ and 2σ contours are plotted for the IceCube DeepCore [50], MINOS [51], NoVA [52], and T2K [53] experiments for the normal (top) and inverted (bottom) hierarchy. The coloured regions are the result of a global fit to these data sets. Right: Allowed regions in the $\sin^2 \theta_{13}$ vs. Δm_{31}^2 plane using only Daya-Bay (black lines), reactor data without Daya-Bay (violet lines), and their combination (coloured regions). In all panels solar and KamLAND data are included to constrain Δm_{21}^2 and θ_{12} . Contours are defined with respect to the global minimum of the two ordering. Reproduced from [47].	19
3.1	Schematic representation of the experimental setup of the T2K experiment. The neutrinos travel from right to left, going through the near and far detectors. Reproduced from [60].	21
3.2	Overview of the J-PARC facility.	22
3.3	Beam Power (left axis) and accumulated POT (right axis) over the years of T2K operation.	23
3.4	Primary and secondary T2K neutrino beamlines. Reproduced from [60].	24
3.5	(a) Illustration of the direction of the backward light produced by a foil oriented at 45° . Adapted from [64]. (b) The foil disk and the foils used for OTR-I. Reproduced from [64].	25
3.6	Cross section view through the shielding of the optical system used to transport the OTR light. Reproduced from [64].	27
3.7	OTR two-dimensional proton beam profiles obtained using the aluminum (left) and titanium (foils). The black circle represents the diameter of the baffle. Reproduced from [64].	27
3.8	The difference between the OTR-II x measurements of the beam centre and the extrapolation from the upstream proton beam measurements. The data points were collected from May 2014 and April 2017.	29
3.9	OTR light yield/POT vs. integrated POT for the OTR-II system. The decrease in light yield is caused by corrosion and damage of the foils.	29
3.10	(a) Neutrino energy as a function of pion momentum (Equation 3.3) for various values of the off-axis angle θ . (b) The disappearance (top) and appearance probabilities (middle) for $L = 295$ km and the oscillation parameter values listed within the figure. The bottom plot shows the ν_μ flux (in arbitrary units) at SK for various off-axis (OA) angles. Reproduced from [71].	30

3.11	Detectors in the near detector complex. Reproduced from [71, 72].	31
3.12	(a) Sample ND280 event display for a neutrino interaction in the FGD1. Reproduced from [75]. (b) Simplified cut-away schematic on one TPC. Reproduced from [60].	32
3.13	Schematic drawing of the SK detector. Reproduced from [71].	34
3.14	Sample event displays of reconstructed Cherenkov rings at SK from data. The colour scale represents the time of arrival at the PMTs, which is also represented in the vertical histogram to the right of the event display. Each square represents a PMT, and its size the amount light detected. Reproduced from [83].	35
4.1	The tuned neutrino flux predictions at ND280 (top) and SK (bottom) in FHC mode (left) and RHC mode (right). Normalized to 1×10^{21} POT. Reproduced from [89].	37
4.2	The fractional uncertainty on the ND280 (left) and SK (right) ν_μ flux prediction as a function of neutrino energy for the FHC mode. The dotted line is the uncertainty from the previous flux prediction. Reproduced from [89].	38
4.3	CC cross sections per nucleon divided by the neutrino energy and plotted as function of the energy. The QE, RES, and DIS contributions are plotted, along with their sum (Total). Data from various experiments are represented with markers, along with the predictions from the NUANCE [102] event generator. Reproduced from [103].	40
4.4	Feynman diagrams for charged current quasi-elastic interactions (left) and charged/neutral current resonance interactions (right).	41
4.5	(a) Normalized nuclear density distributions. Reproduced from [114]. (b) Graphical representation of the Intra-Nuclear cascade mechanism	44
4.6	(a) The probabilities per step at the centre of a carbon nucleus for QE scattering and absorption at low energy ($p_\pi < 500$ MeV/c) calculated from the Oset <i>et al.</i> model (dashed line). The tuned model (solid lines) corresponds to a previous tuning of the model not described in this thesis. At high energy ($p_\pi > 500$ MeV/c) the QE scattering, hadron production, and single charge exchange (SCX) are calculated from π^\pm scattering off free nucleons and deuteron targets. (b) World data for π^+ on free proton scattering cross sections. The data (grey points) was obtained from [116], while the SAID fit (solid lines) was obtained from [117]. Figures reproduced from [114].	45
5.1	Dominant π^\pm -C interactions in the sub-GeV region. “N” represents any number of nucleons leaving the nucleus.	50
5.2	Schematic overview of the experimental apparatus.	51
5.3	Cherenkov light (ADC Counts) vs. TOF (ns) for $p_\pi = 237.2$ MeV/c. The broken line corresponds to the threshold to distinguish pions from muons and electrons.	51

5.4	Front view of the PIA ν O fibre tracker detector.	52
5.5	Example of ABS candidate event in data ($p_\pi = 237.2 \text{ MeV}/c$). The filled circles (red) correspond to the large hits (> 20 p.e.), the crosses correspond to the hits identified as crosstalk hits and the thick lines (cyan, green and pink) correspond to reconstructed tracks.	54
5.6	Photo of CEMBALOS. The beam points to the right. Detailed description in the text.	55
5.7	(a) Light attenuation curves in CEMBALOS for mirrored (solid) and unmirrored (dashed) fibres. (b) Charge per CEMBALOS hit distribution (in photoelectrons) of through-going muons in the $p_\pi = 237.2 \text{ MeV}/c$ setting for data (circles) and MC (solid line), after the calibration procedure was applied. The statistical error bars are too small to be visible.	57
5.8	(a) Comparison of elastic inclusive cross section between the previous experiments (summarized in Table IV of [1]) and the default GEANT4. (b) Comparison of inelastic inclusive cross sections between the previous experiment [135] and the default GEANT4.	58
5.9	$d\sigma_{\text{CX}}/d\Omega$ as a function of the outgoing π^0 polar angle (with respect to the beam direction) for $265 \text{ MeV}/c$ π^+ interacting on ^{16}O , for FLUKA (dashed line), GEANT4 (solid line) and NEUT (dotted line), along with data from [138].	59
6.1	(a) Illustration of the <i>Good incident</i> π^+ cut requirement. A straight through-going pion track (cyan) crosses the PIA ν O detector. The broken line represents the boundary of the fiducial volume. (b) The $X - Y$ view of the incident beam position distribution. The white broken line represents the boundary of the fiducial volume.	61
6.2	dQ/dx distribution in six different angular regions for $p_\pi = 237.2 \text{ MeV}/c$ for data and MC. The dotted vertical lines represent the threshold to distinguish pions (left of the line) and protons. For multiple track events, only the smallest value of dQ/dx among the tracks is filled in the histogram. The “Others” category is mainly filled with events with pions decaying in flight and Coulomb scattering events.	62
6.3	(a) Example of a simulated CX event in the DUET detector setup. A $237.2 \text{ MeV}/c$ π^+ (red) undergoes CX in PIA ν O producing two protons (black) and a π^0 that decay into two photons (blue). The forward-going photon is identified in CEMBALOS as it produces e^+e^- pairs (purple, magenta) and hits are recorded in the scintillating material. (b) Distribution of the most upstream position of CEMBALOS hits for Data and MC (broken down into topologies and listed with their corresponding percentage composition) in the $p_\pi = 237.2 \text{ MeV}/c$ setting after applying the PIA ν O upstream selection. Each bar represents an XY module. Topologies contributing less than 1% are not plotted.	63

6.4	(a) Distribution of the number of hits in CEMBALOS for Data and MC (broken down into topologies and listed with their corresponding percentage composition) in the $p_\pi = 237.2$ MeV/ c setting after applying the veto cut. Topologies contributing less than 1% are not plotted. (b) Distribution of the number of hits in CEMBALOS vs. charge deposited for MC in the $p_\pi = 237.2$ MeV/ c setting after applying the requirement of a minimum of 5 hits. The blue entries are true CX events, whereas the black boxes correspond to neutron background events.	64
6.5	(a) Selection efficiency of true CX events as a function of the outgoing π^0 momentum and angle, for the $p_\pi = 201.6$ MeV/ c setting. (b) Rejection probability of events where an ejected proton from ABS or quasi-elastic scattering fails the veto rejection criteria, as a function of its outgoing momentum and angle, for the $p_\pi = 201.6$ MeV/ c setting.	66
6.6	(a) Charge distribution in the first layer of CEMBALOS for stopping protons in the 237.2 MeV/ c setting for data (circles) and MC (filled histogram). Only statistical uncertainties are plotted. The solid and dashed lines are Gaussian fits to data and MC respectively. (b) CEMBALOS hit inefficiency for data (circles) and MC (solid line) in the $p_\pi = 237.2$ MeV/ c setting. The statistical error bars are too small to appear.	69
6.7	(a) DUET measurements of σ_{ABS} and σ_{CX} compared with previous measurements [141, 138, 142, 137] and ABS (red) and CX (black) model predictions from GEANT4 (solid line), FLUKA (dashed line) and NEUT (dotted line). (b) Fractional covariance and correlation for the DUET measurements of σ_{ABS} and σ_{CX} . The quantities that fall on the diagonal and anything below show the fractional covariance coefficients, while the quantities above the diagonal show the correlation coefficients.	71
7.1	One-dimensional projections of the interpolated χ^2 grid for a point around the center of the grid using GNU-Octave (black) and TMultiDimFit (red). The dots are the χ^2 points in the finite grid being interpolated	76
7.2	One-dimensional projections of the interpolated χ^2 grid for a point away from the center of the grid using GNU-Octave (black) and TMultiDimFit (red). The dots are the χ^2 points in the finite grid being interpolated	76
7.3	Correlation matrices for the FSI parameters	78
7.4	Sample PDFs	79
7.5	Comparison of the available π^+ -C cross section external data with the FSIFitter best fit (solid black line) and 1σ band (red) obtained from throws of the parameter values in Table 7.3 and using the correlation matrix in Figure 7.3b.	80
7.6	Post-fit normalization parameters for each data set for carbon-only (blue), light nuclei (red) and all-nuclei (black) fits. Some points overlap each other.	81

7.7	Post-fit normalization parameters for each data set (after removing the 5 data sets with strongest pulls in Figure 7.6) for carbon-only (blue), light nuclei (red) and all-nuclei (black) fits Some points overlap each other.	82
7.8	Distribution of Ψ for various scaling factors. Fitted mean and RMS are shown in the box.	84
7.9	Fitted RMS as a function of the square root of the scaling factor.	85
7.10	Comparison of the available π^+ -C cross section external data with the FSIFitter best fit (solid black line) and 1σ band after scaling (red), and the TN-032 best fit (dashed black line) and 1σ and (blue).	86
7.11	Comparison of the available π^- -C cross section external data with the FSIFitter best fit (solid black line) and 1σ band after scaling (red), and the TN-032 best fit (dashed black line) and 1σ and (blue).	86
7.12	Comparison of the available π^+ -O cross section external data with the FSIFitter best fit (solid black line) and 1σ band after scaling (red), and the TN-032 best fit (dashed black line) and 1σ and (blue).	87
7.13	Comparison of the available π^- -O cross section external data with the FSIFitter best fit (solid black line) and 1σ band after scaling (red), and the TN-032 best fit (dashed black line) and 1σ and (blue).	87
7.14	Comparison of the available π^+ -Al cross section external data with the FSIFitter best fit (solid black line) and 1σ band after scaling (red), and the TN-032 best fit (dashed black line) and 1σ and (blue).	88
7.15	Comparison of the available π^- -Al cross section external data with the FSIFitter best fit (solid black line) and 1σ band after scaling (red), and the TN-032 best fit (dashed black line) and 1σ and (blue).	88
7.16	Comparison of the available π^+ -Fe cross section external data with the FSIFitter best fit (solid black line) and 1σ band after scaling (red), and the TN-032 best fit (dashed black line) and 1σ and (blue).	89
7.17	Comparison of the available π^- -Fe cross section external data with the FSIFitter best fit (solid black line) and 1σ band after scaling (red), and the TN-032 best fit (dashed black line) and 1σ and (blue).	89
7.18	Comparison of the available π^+ -Cu cross section external data with the FSIFitter best fit (solid black line) and 1σ band after scaling (red), and the TN-032 best fit (dashed black line) and 1σ and (blue).	90
7.19	Comparison of the available π^- -Cu cross section external data with the FSIFitter best fit (solid black line) and 1σ band after scaling (red), and the TN-032 best fit (dashed black line) and 1σ and (blue).	90
7.20	Comparison of the available π^+ -Pb cross section external data with the FSIFitter best fit (solid black line) and 1σ band after scaling (red), and the TN-032 best fit (dashed black line) and 1σ and (blue).	91

7.21	Comparison of the available π^- -Pb cross section external data with the FSIFitter best fit (solid black line) and 1σ band after scaling (red), and the TN-032 best fit (dashed black line) and 1σ and (blue).	91
8.1	Example of a one dimensional marginal posterior probability density. A Gaussian centred at 0.0, with an RMS of 2.5 and amplitude 1.0 is assumed for this example. The best fit point (star marker) is chosen as the bin with the highest posterior density. The 68%, 90%, and 95% credible intervals calculated using the highest posterior density method are presented as the yellow, blue, and red filled regions, respectively.	99
8.2	Example of a two dimensional marginal posterior probability density. A 2D Gaussian centred at 0.0, with standard deviations 2.5 and 1.5, and amplitude 1.0 is assumed for this example. The best fit point (yellow star marker) is chosen as the bin with the highest posterior density. The 68% and 90% credible intervals calculated using the highest posterior density method are shown as the overlaid dashed and solid lines, respectively.	100
9.1	ND280 pre-fit MC (broken down by interaction mode) and Data binned in p_μ (left) and $\cos\theta_\mu$ (right) for the FHC CC0 π (top), CC1 π (middle) and CC Other (bottom) samples in the FGD1. Reproduced from [175].	103
9.2	ND280 pre-fit MC (broken down by interaction mode) and Data binned in p_μ for the RHC $\bar{\nu}_\mu$ CC 1-Track (top left), RHC $\bar{\nu}_\mu$ CC N-Track (top right), RHC ν_μ CC 1-Track (bottom left), and RHC ν_μ CC N-Track (bottom right) samples in the FGD2. Reproduced from [175].	105
9.3	Pre-fit oscillated (red) and unoscillated (blue) reconstructed energy spectra for the FHC 1R $_\mu$ (top left), FHC 1R $_e$ (top right), RHC 1R $_\mu$ (middle left), RHC 1R $_e$ (middle right), and FHC 1R $_e$ 1 d.e. (bottom) samples, along with the data spectra. The FHC and RHC 1R $_\mu$ spectra are zoomed in on the 0-7 GeV range as no data are found outside that range.	108
9.4	Pre-fit reconstructed energy spectra broken down by interaction mode for the FHC 1R $_\mu$ (top left), FHC 1R $_e$ (top right), RHC 1R $_\mu$ (middle left), RHC 1R $_e$ (middle right), and FHC 1R $_e$ 1 d.e. (bottom) samples. The FHC and RHC 1R $_\mu$ spectra are zoomed in on the 0-7 GeV range as no data are found outside that range.	109
9.5	The fractional covariance matrix for the flux uncertainties. Within each group, there are further sub-divisions into sub-samples and true neutrino energy.	111
9.6	Prior covariance matrix for the cross section systematic parameters. Details are discussed in the text.	113

9.7	The Nieves relativistic RPA correction factor relative to the unmodified CCQE cross section is shown as a function of Q^2 (black solid line), along with its $\pm 1\sigma$ uncertainties (dashed black line). The BeRPA implementation best fit is also shown (black data points), along with the $\pm 1\sigma$ uncertainties (grey band) obtained from the uncertainties in the BeRPA parameters shown in Table 9.4. Reproduced from [100].	114
9.8	ND280 detector fractional covariance matrix. The bins within each sample are ordered in increasing momentum intervals, each containing all angular bins, from forward-going to backwards-going.	116
9.9	The fractional covariance matrix used for the SK detector + SI + PN uncertainties. The binning is described in Table 9.5.	118
9.10	(a) Previous prior uncertainties of the FSI parameters used in T2K analyses, obtained from [162]. (b) Prior uncertainties of the FSI parameters used for this analysis, derived from the analysis presented in Chapter 7.	119
9.11	The diagonal elements of the fractional covariance matrix for SI-only uncertainties. The binning is described in Table 9.5. The uncertainties obtained by propagating the priors from Figure 9.10a (blue line) and Figure 9.10b (red line) are shown. A reduction in the SI uncertainty is achieved from the tuning of the NEUT cascade model presented in Chapter 7.	121
9.12	Sample response function used to map the FEFABS parameter response as a function of fractional change to the parameter. The effect is evaluated for seven values of the parameters (black dots) and is interpolated using a cubic spline function (black line). This spline in particular corresponds to CC1 π events of given true and reconstructed energy in the FHC 1R $_{\mu}$ sample.	122
9.13	Effect of $+1\sigma$ variations of the FSI parameters to the FHC 1R $_{\mu}$ sample. The green line in the top left panel represents the oscillated sample and is equivalent to Figure 9.4. The weights are calculated using the full reweighting of the cascade (black line), the splined response functions in a stand-alone C++ application (dashed red line), and the splined response functions within the MaCh3 framework (dashed green line).	124
9.14	Effect of $+1\sigma$ variations of the FSI parameters to the FHC 1R $_e$ sample. The figure layout is the same as Figure 9.13.	125
9.15	Effect of $+1\sigma$ variations of the FSI parameters to the FHC 1R $_e$ 1d.e. sample. The figure layout is the same as Figure 9.13.	125
9.16	FSI Uncertainty matrices with the binning used for the SK detector uncertainties (Table 9.5) calculated from a set of simultaneous variations of the FSI parameters. The matrix to the left was calculated using the full reweighting of the NEUT cascade, while the matrix to the right was calculated using the splined response functions. The matrices agree to better than 3.5%.	126

9.17	Likelihood scan for variations of the FEFABS parameters for (a) the penalty term, (b) the Poisson term for the FHC 1R _μ sample. The likelihood was defined in Equation 8.1.	127
10.1	Posterior probability density for the appearance parameters from an Asimov fit without the reactor constraint. The 68% and 90% credible intervals are shown as the dashed and solid lines, respectively.	131
10.2	Posterior probability density for the disappearance parameters from an Asimov fit without the reactor constraint. The 68% and 90% credible intervals are shown as the dashed and solid lines, respectively. Note the break in the vertical axis. . .	131
10.3	Posterior probability density for δ_{CP} from a T2K-Only Asimov fit.	132
10.4	Posterior probability density for the disappearance parameters from a T2K + Reactor constraint Asimov fit. The 68% and 90% credible intervals are shown as the dashed and solid lines, respectively. Notice the break in the vertical axis to allow for a better visualization of the posteriors for each mass hierarchy hypothesis.	133
10.5	Posterior probability density for the appearance parameters from a T2K + Reactor constraint Asimov fit. The 68% and 90% credible intervals are shown as the dashed and solid lines, respectively. The horizontal scale is the same as Figure 10.1. . . .	134
10.6	Posterior probability density for δ_{CP} from a T2K + Reactor constraint Asimov fit.	135
10.7	Central and $\pm 1\sigma$ values of the nuisance parameters described in Section 9.2 for T2K-Only (blue) and T2K + Reactor constraint (red) Data fits. The prior uncertainty for each parameter is plotted as the grey filled band.	136
10.8	ND280 pre-fit (red) and post-fit (blue) 1σ bands for the FGD1 and FGD2 FHC mode samples, along with the data (black points). The pre-fit band is obtained by calculating the variations to the spectra for values of the nuisance parameters obtained from throws of the prior covariance matrices. The post-fit band is obtained using a posterior predictive method applied to the Markov Chain from the T2K + Reactor Constraint Data fit.	138
10.9	SK pre-fit (red) and post-fit (blue) 1σ bands for the five SK samples used in this analysis, along with the data (black points). The pre-fit band is obtained by calculating the variations to the spectra for values of the nuisance parameters obtained from throws of the prior covariance matrices. The post-fit band is obtained using a posterior predictive method applied to the Markov Chain from the T2K + Reactor Constraint Data fit.	139
10.10	Ratio of the SK data (black points), pre-fit (red), and post-fit (blue) 1σ bands to the predicted unoscillated spectra. The effect of the oscillation phenomenon to the FHC 1R _μ , RHC 1R _μ , and FHC 1R _e is clearly visible.	140
10.11	Pre-fit (red) and post-fit (blue) 1σ bands for the true momentum spectrum of charged pions in the FHC 1R _e 1 d.e. sample. The bands only contain errors from FSI uncertainties.	141

10.12	Posterior probability density for the appearance and disappearance parameters from a T2K-Only Data fit.	142
10.13	Posterior probability density for the disappearance parameters from a T2K-Only Data fit. The 68% and 90% credible intervals are shown as the dashed and solid lines, respectively. Notice the break in the vertical axis to allow for a better visualization of the posteriors for each mass hierarchy hypothesis.	143
10.14	Posterior probability density for the appearance parameters from a T2K-Only Data fit. The 68% and 90% credible intervals are shown as the dashed and solid lines, respectively.	143
10.15	Posterior probability density for the appearance and disappearance parameters from a T2K + Reactor constraint Data fit.	145
10.16	Posterior probability density for the disappearance parameters from a T2K + Reactor constraint Data fit. The 68% and 90% credible intervals are shown as the dashed and solid lines, respectively. Notice the break in the vertical axis to allow for a better visualization of the posteriors for each mass hierarchy hypothesis.	145
10.17	Posterior probability density for the appearance parameters from a T2K + Reactor Data fit. The 68%, 90%, and 95.4% credible intervals are shown as the dashed and solid lines, respectively. The horizontal scale is the same as Figure 10.14.	146
10.18	90% CL for the disappearance parameters assuming normal hierarchy from this analysis (black line) compared to the most recent T2K results [53] (blue dashed line) and other experiments [52, 51, 190, 191] (dashed lines). The constant $\Delta\chi^2$ interval was obtained from the Markov Chain for the T2K + Reactor constraint Data fit from Section 10.2.5.	148
10.19	68% and 90% CL in the $\sin^2\theta_{23} - \delta_{CP}$ parameter space for normal hierarchy from this analysis (black) compared to the NOvA experiment [52] (red). The constant $\Delta\chi^2$ interval was obtained from the Markov Chain for the T2K + Reactor constraint Data fit from Section 10.2.5.	148
B.1	OTR profiles and analysis for the baffle alignment studies. (a) Combined OTR beam profiles from horizontal and vertical beam scans. (b) Bins with large derivative of the combined profiles and fitted ellipse to find the baffle edge.	155
C.1	Distribution of starting values for the 5 FSI parameters thrown randomly inside the finite grid defined in Table 7.2.	156
C.2	Distribution of best fit values for the 5 FSI parameters thrown randomly inside the finite grid defined in Table 7.2.	157
D.1	Ratio of Data and NEUT best fit for π^+ -C cross sections. The red band represents the 1σ error band.	158
D.2	Ratio of Data and NEUT best fit for π^- -C cross sections. The red band represents the 1σ error band.	159

D.3	Ratio of Data and NEUT best fit for π^+ -O cross sections. The red band represents the 1σ error band.	159
D.4	Ratio of Data and NEUT best fit for π^- -O cross sections. The red band represents the 1σ error band.	160
D.5	Ratio of Data and NEUT best fit for π^+ -Al cross sections. The red band represents the 1σ error band.	160
D.6	Ratio of Data and NEUT best fit for π^- -Al cross sections. The red band represents the 1σ error band.	161
D.7	Ratio of Data and NEUT best fit for π^+ -Fe cross sections. The red band represents the 1σ error band.	161
D.8	Ratio of Data and NEUT best fit for π^- -Fe cross sections. The red band represents the 1σ error band.	162
D.9	Ratio of Data and NEUT best fit for π^+ -Cu cross sections. The red band represents the 1σ error band.	162
D.10	Ratio of Data and NEUT best fit for π^- -Cu cross sections. The red band represents the 1σ error band.	163
D.11	Ratio of Data and NEUT best fit for π^+ -Pb cross sections. The red band represents the 1σ error band.	163
D.12	Ratio of Data and NEUT best fit for π^- -Pb cross sections. The red band represents the 1σ error band.	164
E.1	Comparison of the available π^+ -C cross section external data with the FSIFitter best fit and its 1σ band, and other models.	167
E.2	Comparison of the available π^- -C cross section external data with the FSIFitter best fit and its 1σ band, and other models.	168
E.3	Comparison of the available π^+ -O cross section external data with the FSIFitter best fit and its 1σ band, and other models.	168
E.4	Comparison of the available π^- -O cross section external data with the FSIFitter best fit and its 1σ band, and other models.	169
E.5	Comparison of the available π^+ -Al cross section external data with the FSIFitter best fit and its 1σ band, and other models.	169
E.6	Comparison of the available π^- -Al cross section external data with the FSIFitter best fit and its 1σ band, and other models.	170
E.7	Comparison of the available π^+ -Fe cross section external data with the FSIFitter best fit and its 1σ band, and other models.	170
E.8	Comparison of the available π^- -Fe cross section external data with the FSIFitter best fit and its 1σ band, and other models.	171
E.9	Comparison of the available π^+ -Cu cross section external data with the FSIFitter best fit and its 1σ band, and other models.	171

E.10	Comparison of the available π^- -Cu cross section external data with the FSIFitter best fit and its 1σ band, and other models.	172
E.11	Comparison of the available π^+ -Pb cross section external data with the FSIFitter best fit and its 1σ band, and other models.	172
E.12	Comparison of the available π^- -Pb cross section external data with the FSIFitter best fit and its 1σ band, and other models.	173
F.1	Comparison of the Mean and RMS of the posteriors for all cross-section parameters for the official T2K Run 1-8 oscillation analysis (blue) and the analysis presented in this thesis (red).	175
F.2	Comparison of the Mean and RMS of the posteriors for all flux parameters for the official T2K Run 1-8 oscillation analysis (blue) and the analysis presented in this thesis (red).	175
F.3	Comparison of the Mean and RMS of the posteriors for all SK detector parameters for the official T2K Run 1-8 oscillation analysis (blue) and the analysis presented in this thesis (red).	176
F.4	Posterior probability densities for the appearance and disappearance parameters from T2K-Only Asimov fits for the official T2K Run 1-8 oscillation analysis (blue) and the analysis presented in this thesis (red).	177
F.5	Posterior probability densities for the appearance and disappearance parameters from T2K + Reactor Asimov fits for the official T2K Run 1-8 oscillation analysis (blue) and the analysis presented in this thesis (red).	178
G.1	2-D 68% and 90% contours in $\sin^2 \theta_{23} - \Delta m_{23}^2$ for the “Nominal” (blue) and fake data (red) Asimov fits with the reactor constraint on $\sin^2 \theta_{13}$, assuming normal hierarchy. The three fake data sets (corresponding to the nominal and $\pm 1\sigma$ alternate form factor fake data) are shown.	181
G.2	2-D 68% and 90% contours in $\sin^2 \theta_{13} - \delta_{CP}$ for fits with the reactor constraint on $\sin^2 \theta_{13}$ for the “Nominal” (blue) and fake data (red) Asimov fits with the reactor constraint on $\sin^2 \theta_{13}$, assuming normal hierarchy. The three fake data sets (corresponding to the nominal and $\pm 1\sigma$ alternate form factor fake data) are shown.	182
G.3	1-D posterior probability density plots for δ_{CP} from fits with the reactor constraint on $\sin^2 \theta_{13}$ for the “Nominal” (blue) and fake data (red) Asimov fits with the reactor constraint on $\sin^2 \theta_{13}$, assuming normal hierarchy. The three fake data sets (corresponding to the nominal and $\pm 1\sigma$ alternate form factor fake data) are shown.	183

PART I:

INTRODUCTION TO NEUTRINOS AND T2K

Chapter 1

Overview

The field of elementary particle physics has experienced stupendous growth since the discovery 120 years ago of the first elementary particle, the electron [3]. The Standard Model (SM) of particle physics provides a compact description of the properties of the known fundamental particles in the universe and of the fundamental forces describing the interactions among them, with the exception of the gravitational force. The SM constitutes one of the most successful theories ever developed by science, as it precisely accounts for an enormous body of experimental data, and has made accurate predictions that were later confirmed experimentally.

The particle content of the SM is illustrated in Figure 1.1. The mass, charge, intrinsic angular momentum (spin), and date of discovery are shown for each particle. Not shown in the diagram is the fact that each particle has a corresponding antiparticle that possesses the same mass, but carries the opposite quantum numbers¹. All the visible matter (and antimatter) seen in the universe can be described by collections of these constituent particles. The initial division among these particles occurs between *bosons* carrying integer spins, and *fermions* carrying half-integer spins. The spin-1 bosons are responsible for mediating the electroweak and the strong interactions. The model also predicts the existence of a spin-0 boson, the Higgs boson, arising from a mechanism that generates the mass of each particle. Since the discovery of a Higgs-like particle at the Large Hadron Collider (LHC) at CERN in 2012 [4, 5], all the particles contained in the SM have been observed, an extraordinary achievement!

Fermions are further divided into three flavours (or families or generations) of *quarks* and *leptons*, carrying fractional and integer electric charges, respectively. These generations are identical, except for their masses. The neutral leptons, called *neutrinos*, are the main subject of study of this thesis and will be further discussed in Chapter 2. A different flavour of neutrino is paired with each flavour of lepton, as indicated by its subscript. The weak force is mediated by the *W* and *Z* bosons, which couple to all fermions. The electromagnetic force is mediated by the photon and affects the charged leptons, along with any other particle that carries an electric charge.

¹An antiparticle will be denoted by a bar over the particle symbol or by explicitly showing the charge, for example the antimuon will be $\bar{\mu}$ or μ^+ .

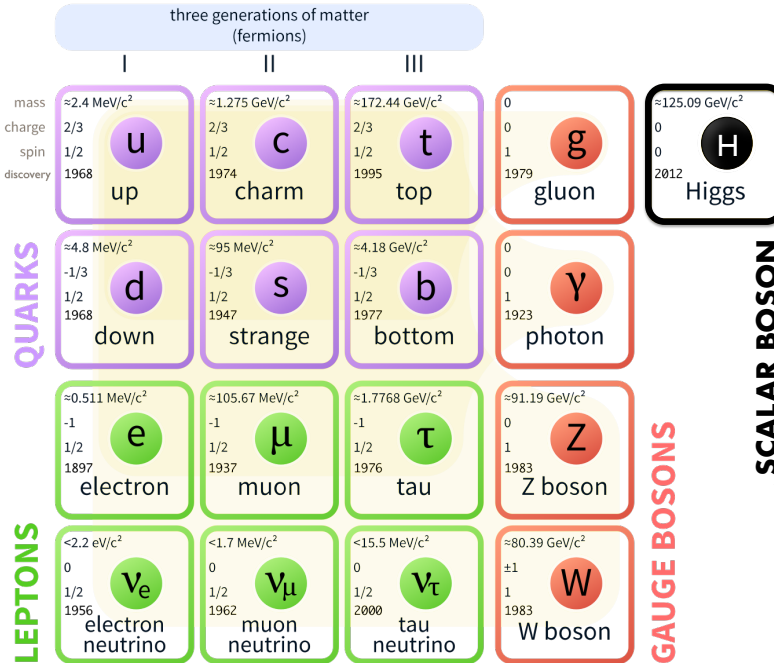


Figure 1.1: Illustration of the particle content in the Standard model of particle physics. The mass, charge, spin, and year of discovery are shown for each particle. Adapted from [6].

Unlike leptons, quarks have not been found to exist as free particles. The combinations of quarks are referred to as *hadrons*. There are two families of hadrons: *mesons* with two valence quarks, and *baryons* with three. The proton and neutron are the lightest and most common baryons, with valence quark combinations uud and ddu , respectively. The *pions* are the lightest mesons. The valence quarks for the charged pions are $u\bar{d}$ (π^+) and $d\bar{u}$ (π^-).

While the success of the SM has been unprecedented, there is compelling evidence for physics beyond the Standard Model (BSM). The quantum mechanical effect of neutrino oscillations, where neutrinos are observed to morph from one variety to another, will be discussed in Chapter 2. This oscillation phenomenon has been confirmed by multiple experiments and provides irrefutable evidence for massive neutrinos. The 2015 Nobel Prize in Physics was awarded jointly to Takaaki Kajita [7] and Arthur B. McDonald [8] for their leading roles in the discovery of solar and atmospheric neutrino oscillations by the Super-Kamiokande and SNO experiments, respectively.

The study of neutrino oscillations has additionally opened up the possibility of tackling one of the deepest questions regarding our understanding of the universe: the observed matter-antimatter asymmetry. Our present understanding is that both matter and antimatter were created in equal amounts in the Big Bang. However, current observations indicate that matter overwhelmingly dominates the observable universe. In the SM, if a particle and its corresponding antiparticle behave identically, the particle is said to respect the charge-parity (CP) symmetry.

Consequently, a violation of this CP symmetry signifies that nature draws a distinction between matter and antimatter. CP-violation has been observed indirectly [9] and directly [10, 11, 12, 13] in the quark sector through the study of the decays of K and B mesons, but the violation observed is not sufficient to explain the matter-antimatter asymmetry. The first hints of CP-violation in the leptonic sector have been recently obtained by the Tokai-to-Kamioka (T2K) experiment by comparing how neutrinos and antineutrinos oscillate. A precise measurement of the degree at which CP-violation occurs in the leptonic sector is the primary focus of current and future neutrino oscillation experiments.

The goal of the T2K experiment is to detect the signature of neutrino oscillations on an intense ν_μ beam. The neutrino beam is produced from the interactions of a 30 GeV proton beam with a graphite target. The neutrino spectra is measured by detectors in two locations: a *near* detector located 280 m from the neutrino production point to identify the properties of the neutrino at the outset in its unoscillated state, and a *far* detector located 295 km across Japan, where the properties and identity of the neutrino can be characterized after its journey. In the ν_e *appearance* channel, the experiment searches for the transformation of ν_μ s to ν_e s along their journey. In a complementary manner, in the ν_μ *disappearance* channel, the experiment measures the survival rate of ν_μ s. The neutrino event rate in the detectors can be generically expressed as,

$$R_{\nu_\beta}(\vec{\mathbf{x}}) \sim \Phi(E_{\nu_\alpha}) \times \sigma_{\nu_\beta}(E_{\nu_\beta}, \vec{\mathbf{x}}) \times \epsilon_{\nu_\beta}(\vec{\mathbf{x}}) \times P_{\nu_\alpha \rightarrow \nu_\beta}(E_{\nu_\alpha}) \quad (1.1)$$

where $R_{\nu_\beta}(\vec{\mathbf{x}})$ is the event rate for a given type of neutrino ν_β as a function of the reconstructed kinematic variables $\vec{\mathbf{x}}$, $\Phi(E_{\nu_\alpha})$ is the initial flux of ν_α , $\sigma_{\nu_\beta}(E_{\nu_\beta}, \vec{\mathbf{x}})$ is the cross section (or interaction probability) for a ν_β in the detector, $\epsilon_{\nu_\beta}(\vec{\mathbf{x}})$ is the detector efficiency for detecting that interaction, and $P_{\nu_\alpha \rightarrow \nu_\beta}(E_{\nu_\alpha})$ is the probability for oscillation. The physics governing the neutrino oscillation phenomenon, including the CP-violating phase, is contained in the P factor. It is clear from Equation 1.1 that in order to extract information about P from measurements of the neutrino spectra, the unoscillated flux must be well understood, the neutrino cross section must be known, and the detector efficiencies must be understood. The measurements of the parameters that govern neutrino oscillations will be biased or will have poor sensitivity if any of these components is not well modelled, or if there are large uncertainties associated to their modelling.

In the few GeV region, the dominant channel for neutrino interactions with the nuclear targets in the detectors is the charged current quasi-elastic (CCQE), shown in Figure 1.2a. The neutrino exchanges a charged W boson with one of the quark constituents (not shown in the figure) of a bound neutron in the target nuclei. The particles in the final state are the corresponding charged lepton and a proton. The proton generally lies below detection threshold in the detectors, so it is the signature of the lepton that is used to reconstruct the event. In particular, the energy of the neutrino (which enters into the calculation of P) is evaluated from the reconstructed kinematics of the lepton, assuming the bound nucleon is at rest.

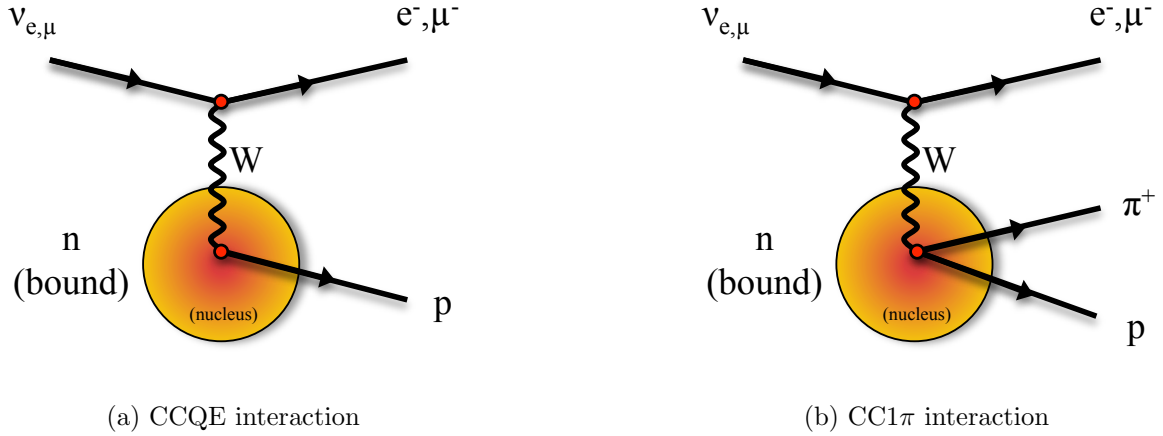


Figure 1.2: Charged current neutrino interactions with nuclei in the \sim GeV region.

In addition to CCQE, charged current interactions in which one charged pion is found in the final state (CC1 π shown in Figure 1.2b) also contribute in this energy range. These arise from a combination of resonance production, coherent scattering, and deep inelastic scattering. If the charged lepton and the pion are reconstructed in the detector, the energy of the neutrino can be similarly reconstructed from the kinematics. However, the charged pion can interact inside (*final state interactions*) or outside (*secondary interactions*) the nucleus before being detected, possibly affecting its reconstruction. These processes are leading sources of systematic uncertainty in neutrino experiments. For example, if the pion is absorbed, the CC1 π interaction will be reconstructed as CCQE, and the reconstructed neutrino energy will be biased. Therefore, the study of pion scattering on nuclei is fundamental in the context of neutrino interaction and oscillation experiments.

Figure 1.3 presents an schematic overview of the structure of an oscillation analysis at T2K. The flux, cross section, and detector models from Equation 1.1 are represented by the blue, violet, and grey boxes, respectively. The dashed boxes represent the areas of the analysis that concern the work presented in this thesis. This dissertation investigates the impact of our understanding of pion scattering on nuclei as a limiting factor for the modelling of $\sigma_{\nu\beta}(E_{\nu\beta}, \vec{x})$ and $\epsilon_{\nu\beta}(\vec{x})$, and consequently for the precision of neutrino oscillation measurements.

A good way to get a handle on the final state and secondary interaction systematic uncertainties is to improve our knowledge of pion-nucleus scattering cross sections. The Dual Use Experiment at TRIUMF (DUET) was conducted to perform such measurements. This thesis presents the recent measurements from DUET of the absorption and charge exchange cross sections of positively charged pions interacting with carbon nuclei. These measurements are then used to improve the modelling of pion-nucleus interactions and reduce the associated systematic uncertainties. As a result, the most precise measurement of the parameters that govern the neutrino oscillation phenomenon is obtained.

Chapter 2 gives a brief overview of the proposal and discovery of the neutrino, and the

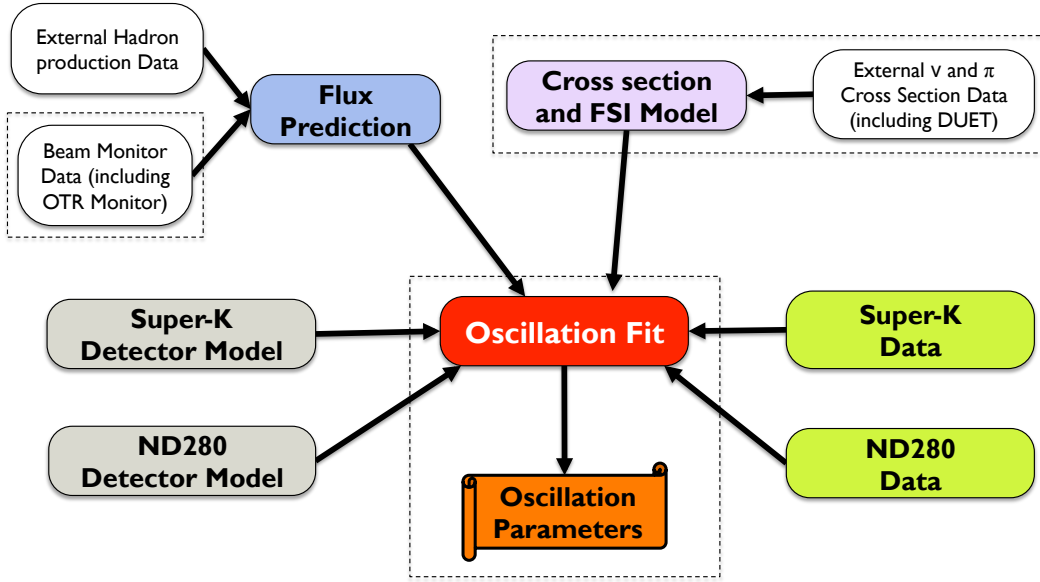


Figure 1.3: Overview of the T2K oscillation analysis. The areas in which the author was involved are highlighted by dashed boxes.

theory and discovery of neutrino oscillations. The current knowledge of the neutrino oscillation parameters is also summarized. Chapter 3 describes the T2K experiment, starting from the neutrino beam line, the Optical Transition Radiation detector, and the near detector (ND280) in Tokai, and ending with the far detector (Super-Kamiokande) in Kamioka. Chapter 4 describes the physics simulations used in T2K to obtain the flux prediction, to simulate neutrino and pion interactions, and to simulate the response of the near and far detectors.

Part II of this thesis concentrates on the study of interactions of charged pions with nuclei. Chapter 5 motivates and describes the Dual-Use Experiment at TRIUMF (DUET). Chapter 6 presents the measurement of absorption and charge exchange cross sections in the 200 to 300 MeV/ c range for positively charged pions on a carbon target. Finally, Chapter 7 describes the work to incorporate these measurements into the modelling of pion interactions.

Part III of this thesis describes a joint fit of neutrino and antineutrino data from T2K in the ν_e appearance and ν_μ disappearance channels. Chapter 8 describes the Bayesian framework used for this purpose, featuring a Markov Chain Monte Carlo fitting technique. Chapter 9 presents the event selections used for this analysis, along with their systematic uncertainties. It also describes the improvements to the framework developed to take advantage of the improved modelling of pion interactions described in Chapter 7. Finally, Chapter 10 presents the results of a fit to T2K data corresponding to 14.7341×10^{20} protons on target in neutrino mode and 7.5573×10^{20} in antineutrino mode to extract the values of the oscillation parameters.

Chapter 2

Neutrino Physics

2.1 Proposal and Discovery of Neutrinos

Following the birth of nuclear physics with the discoveries of radioactivity by H. Becquerel in 1896 [14], and of alpha (α), beta (β), and gamma (γ) rays by E. Rutherford in 1899 [15], J. Chadwick noticed that the electrons released in nuclear β decays had a continuous energy spectrum [16]. β decay is the process by which a neutron transforms into a proton, turning a heavy nucleus into a lighter one. From the law of conservation of energy, the expected amount of energy to be emitted in the form of an electron would be the difference between the neutron and the proton mass. Thus, the electrons would be mono-energetic. This led to confusion and debate, and the idea that energy conservation was violated inside the nucleus was briefly considered.

The neutrino was first postulated by W. Pauli in 1930 as a “desperate” remedy to save the law of conservation energy [17]. E. Fermi formulated in 1934 the quantitative description of β decay as follows [18]:

$$n \rightarrow p + e^{-} + \bar{\nu}_e \quad (2.1)$$

The neutrino would be a light, electrically neutral, half-integer spin particle, with a very small interaction probability (cross section), making it nearly impossible to detect. The neutrino was first detected through the inverse β decay process:

$$\bar{\nu}_e + p \rightarrow e^{+} + n \quad (2.2)$$

As it became the unavoidable norm with all neutrino experiments: an intense source of neutrinos, a large detector, the development of new technology, and a considerable amount of patience were required due to their small cross section ($\sim 10^{-44}$ barns). F. Reines and C. L. Cowan reported the observation of the electron neutrino ($\bar{\nu}_e$) in 1956 [19]. They took data for ~ 100 days from a 400 litre liquid scintillator detector (water mixed with 40 kg of dissolved CdCl_2) placed in the vicinity of a nuclear reactor at the Savannah River Plant in South Carolina. The

event signature was a signal from e^+ annihilation in coincidence with a delayed signal from n capture on cadmium. This discovery signified the beginning of the experimental neutrino physics field, and F. Reines was awarded the Nobel Prize in 1995.

The existence of a second neutrino, the muon neutrino (ν_μ), was confirmed by L. Lederman and collaborators in 1962 [20]. They pioneered the use of pion decays as a precursor for a ν_μ beam ($\pi^\pm \rightarrow \mu^\pm + (\nu_\mu/\bar{\nu}_\mu)$), a technique that is still being used by modern accelerator neutrino experiments. The confirmation of the third generation neutrino, the tau neutrino (ν_τ), came almost fifty years later from the DONUT Collaboration at Fermilab [21]. A constraint in the number of neutrinos is obtained through electroweak measurements of the Z boson decay in e^+e^- collisions [22]. The *invisible* width from Z decays to neutrinos, $\Gamma_{\text{inv}} = N_\nu \Gamma_{\nu\bar{\nu}}$, where N_ν is the number of light neutrino species, is determined from the measurements of the decay widths to all visible final states and the total width

$$\Gamma_Z = \Gamma_{ee} + \Gamma_{\mu\mu} + \Gamma_{\tau\tau} + \Gamma_{\text{had}} + \Gamma_{\text{inv}} \quad (2.3)$$

Figure 2.1 shows the strong dependence to N_ν of one of the contributors to the visible width, the hadron production process. The precision achieved in these measurements allows tight limits to be placed on the possible contribution of any invisible Z decays originating from sources other than the three known light neutrino species.

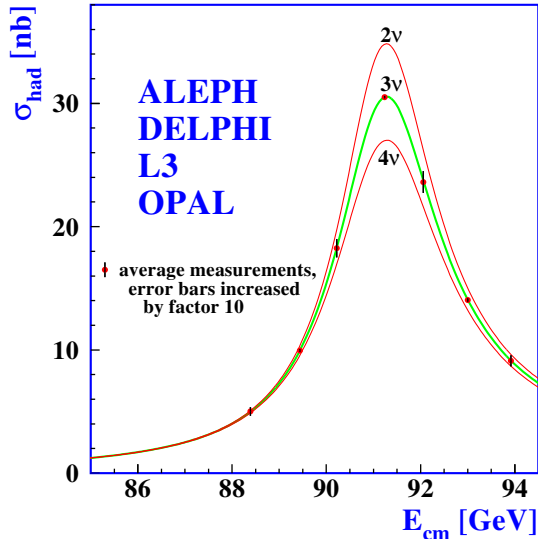


Figure 2.1: Measurements of the hadron production cross section around the Z resonance. The curves indicate the predicted cross section for two, three and four neutrino species with SM couplings and negligible mass. The points represent a combination of experimental data from the ALPEH, DELPHI, L3, and OPAL experiments. Reproduced from [22].

A fit to a combined data set consisting of 17 million Z decays accumulated by the ALEPH, DELPHI, L3 and OPAL experiments at LEP, and 600 thousand Z decays by the SLD experiment

using a polarized beam at SLC yielded $N_\nu = 2.9840 \pm 0.0822$ [22], in agreement with the three observed generations of neutrinos. This is also in agreement with recent indirect measurements obtained from observations of the temperature and polarization anisotropies of the cosmic microwave background [23]. However, this does not mean there can only be three neutrino species. The existence of *sterile* neutrinos that do not couple to the Z boson, or heavy neutrinos that are kinematically impossible to produce in Z decays has been postulated but not confirmed experimentally.

The motivation for heavy sterile neutrinos arises from another curious fact about neutrinos: only left-handed neutrinos have been experimentally confirmed [24]. The helicity (or handedness) is the term used to describe the projection of the spin of a particle onto its direction of motion. If the spin and direction of motion point in opposite directions, the particle is said to be left-handed. The non-observation of a right-handed neutrino led to the belief that the neutrino was massless, since having mass would enable the observer to move into a reference frame that overtakes the neutrino, which flips the observed helicity. This is also consistent with the fact that the weak interaction maximally violates parity, i.e., only couples to left-handed particles. As will be discussed in the following section, we now know that the neutrinos are massive. One way of dealing with this is by extending the SM with the addition of heavy sterile right-handed neutrino states [25].

2.2 Neutrino Oscillations

This thesis presents a measurement of the parameters governing the neutrino oscillation phenomenon. A historical overview of the initial evidence that led to the proposal and discovery of the oscillation phenomenon is presented in Section 2.2.1. The formalism for neutrino oscillations is described in Section 2.2.2. Finally, Section 2.2.3 contains a review of the current constraints placed on the oscillation parameters by world data, and outlines some of the open questions that remain to be answered.

2.2.1 Initial Evidence

2.2.1.1 The Solar Neutrino Problem

The first indication of neutrino oscillations came from the study of solar neutrinos. Neutrinos are profusely produced by nuclear reactions at the core of the sun. In the vicinity of the Earth, the flux of solar ν_e s is estimated to be $\sim 10^{11} \text{cm}^{-2} \text{s}^{-1}$ in the direction perpendicular to the Sun [26]. R. Davis and collaborators designed and carried out in 1968 an experiment to measure the capture of neutrinos from the ${}^8\text{B}$ decay chain (${}^8_5\text{B} \rightarrow {}^8_4\text{Be} + e^+ + \nu_e$) by an isotope of chlorine [27],



The results from Davis *et al.* were baffling. The upper bound on the solar ν_e flux was about 1/3 that of the prediction by the Standard Solar Model (SSM). This discrepancy became to be known as the “solar neutrino problem”. At the time, given the success of the electroweak theory in the SM, the general consensus was that the solution would lie in the SSM rather than the SM. Several other experiments confirmed the deficit using a variety of techniques [28, 29, 30], and the problem remained unsolved for thirty years.

The solution lay in the work of B. Pontecorvo [31], and Z. Maki, M. Nakagawa, and S. Sakata [32], who independently introduced the idea of neutrino oscillations in the 1960s. The theoretical formalism will be described in Section 2.2.2, but the general idea is as follows: neutrinos can mix in flight as they travel, oscillating from one flavour to another. The deficit could then be interpreted to be caused by a fraction of the ν_e that reach the earth having converted to ν_μ or ν_τ . Since the detection methods that had been employed so far (radio chemical capture as in Equation 2.4 or neutrino elastic scattering) were not sensitive these flavours, a deficit was to be expected. The hypothesis could be tested by an experiment that was capable to detect neutrinos of all three flavours.

The Sudbury Neutrino Observatory used a tank filled with 1000 tonnes of heavy water (D_2O) and instrumented with 9600 photo-multiplier tubes (PMTs) [33]. Taking advantage of the heavy water target, neutrinos were detected through the three following interaction channels:

$$\nu_\alpha + e^- \rightarrow \nu_\alpha + e^- \quad (\text{Elastic Scattering}) \quad (2.5)$$

$$\nu_e + d \rightarrow p + p + e^- \quad (\text{Charged Current Scattering}) \quad (2.6)$$

$$\nu_\alpha + d \rightarrow p + n + \nu_\alpha \quad (\text{Neutral Current Scattering}) \quad (2.7)$$

Unlike the charged current scattering, the elastic and neutral current scattering interactions are sensitive to all flavours, and provide a measurement of the total neutrino flux. The measured total neutrino flux was in agreement with the SSM, and the measured ratio of the ν_e flux to the total neutrino flux was 0.301 ± 0.033 [33, 34]. This gave a very strong indication that ν_e s were changing flavour into ν_μ s and ν_τ s in their travel from the sun. Arthur B. McDonald was a recipient of the 2015 Nobel Prize in Physics for his leadership of the SNO Collaboration [8].

2.2.1.2 Atmospheric Neutrino Oscillations: Super-Kamiokande

In 1998, the Super-Kamiokande Collaboration published the results of their observation of atmospheric neutrinos [35]. Super-K is a large water Cherenkov detector capable of separating electrons from muons and reconstructing the direction of the neutrino by measuring the zenith angle of the reconstructed lepton. A more complete description of the detector can be found in Section 3.3. Super-K measured ν_μ , $\bar{\nu}_\mu$, ν_e , and $\bar{\nu}_e$ produced in the decays of mesons created in collisions of high energy cosmic rays with the nuclei in the atmosphere.

A deficit in the upward-going muons relative to the downward-going muons was reported [35].

Downward-going neutrinos have a path length from the production point of $20\sim 500$ km, whereas upward-going neutrinos travel ~ 13000 km through the Earth's crust before detection. Figure 2.2 shows the ratio of the number of observed data events to the unoscillated Monte Carlo prediction in the absence of neutrino oscillations as a function of L/E , where L is the distance from the production point calculated from the reconstructed angle of the neutrino, and E is the reconstructed energy of the neutrino. At high L/E the observed ν_μ flux is $\sim 50\%$ of the prediction providing clear evidence of ν_μ disappearance due to neutrino oscillations. This result came four years before the SNO result, and thus was the first model-independent evidence for neutrino mixing. Takaaki Kajita was a recipient of the 2015 Nobel Prize in Physics for his leadership of the Super-Kamiokande Collaboration [7].

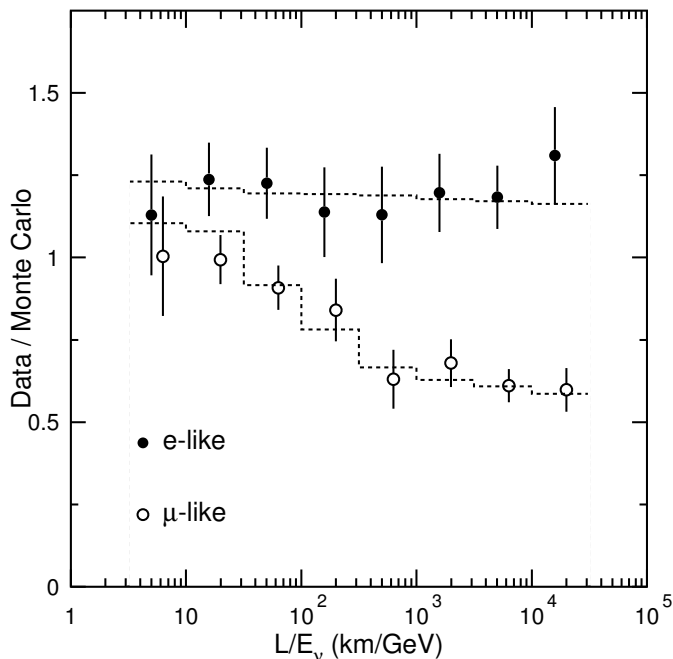


Figure 2.2: The ratio of the number of data events to the unoscillated MC prediction versus reconstructed L/E in Super-Kamiokande. The dashed lines show the expected shape for $\nu_\mu \rightarrow \nu_\tau$ oscillations for a model of neutrino oscillations. Reproduced from [35].

2.2.1.3 Reactor Neutrino Oscillations: KamLAND

The final confirmation for neutrino oscillations came in 2005 from the measurement of reactor neutrinos by the Kamioka Liquid Scintillator antineutrino Detector (KamLAND) experiment in Japan [36]. They measured antineutrinos produced in 55 Japanese nuclear power reactors, with baselines between production and detection varying between 80-800 km. The detector consisted of a 13 m diameter nylon ball filled with 1000 tonnes of liquid scintillator (mineral oil + others)

surrounded by an 18 m diameter stainless steel containment vessel lining 1325 17" PMTs and 554 20" PMTs. $\bar{\nu}_e$ events were detected via inverse β decay (Equation 2.2) and the neutrino energy was reconstructed from the positron energy.

Figure 2.3 shows the ratio of the observed $\bar{\nu}_e$ flux to that expected without neutrino oscillations as a function of L_0/E , where L_0 is the effective baseline averaged over all reactors. The shape in this ratio clearly shows both the disappearance and subsequent reappearance of $\bar{\nu}_e$ s as a function of their energy, proving beyond doubt that neutrino oscillations occur.

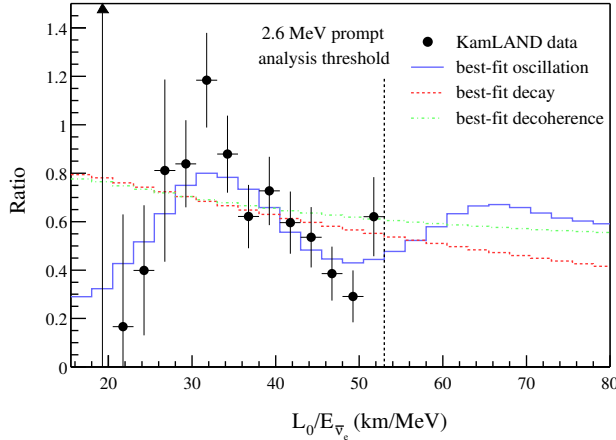


Figure 2.3: Ratio of the observed $\bar{\nu}_e$ spectrum to the expectation for no-oscillation versus L_0/E . The blue line shows the expectation for the best-fit model for neutrino oscillations in KamLAND. Other models are shown in red and green. Reproduced from [36].

In the years following these discoveries many other experiments have confirmed the existence of neutrino oscillations in nature. Experiments where accelerators are used to produce intense and pure ν_μ beams, such as T2K, have emerged. The focus in the field has moved into the precise determination of the parameters describing the phenomenon. Section 2.2.3 provides the current state of knowledge.

2.2.2 Mixing Formalism

The theory of neutrino oscillations is constructed from one underlying assumption: the neutrino flavour states that interact according to the electroweak theory of the SM are in fact a linear combination of neutrino mass eigenstates. Assuming three neutrinos, this can be expressed mathematically as

$$|\nu_\alpha\rangle = \sum_i^3 U_{\alpha i}^* |\nu_i\rangle \quad (2.8)$$

$$|\nu_i\rangle = \sum_\alpha U_{\alpha i} |\nu_\alpha\rangle \quad (2.9)$$

where $|\nu_\alpha\rangle$ represents the flavour eigenstate with $\alpha = \{e, \mu, \tau\}$, $|\nu_i\rangle$ represents the mass eigenstate i , and $U_{\alpha i}$ are elements of a unitary mixing matrix¹. The time evolution in vacuum of the state $|\nu_\alpha\rangle$ is derived from Schrödinger's equation:

$$|\nu_\alpha(x, t)\rangle = \sum_i^3 U_{\alpha i}^* e^{-i(E_i t - p_i x)} |\nu_i\rangle \quad (2.10)$$

where E_i and p_i are the energy and momentum of a neutrino in the i -th mass eigenstate. The probability of finding some flavour state $|\nu_\beta\rangle$ after the original neutrino created at $t = 0$ and at a point $x = 0$ propagates for some time t is given by

$$\begin{aligned} P_{\nu_\alpha \rightarrow \nu_\beta}(x, t) &= |\langle \nu_\beta | \nu_\alpha(x, t) \rangle|^2 = \left| \sum_i U_{\alpha i}^* U_{\beta i} e^{-i(E_i t - p_i x)} \right|^2 \\ &= \sum_{i,j} U_{\alpha i}^* U_{\beta i} U_{\alpha j} U_{\beta j}^* e^{-i(E_i t - p_i x)} e^{-i(E_j t - p_j x)} \end{aligned} \quad (2.11)$$

Given that the neutrino masses are very small, the relativistic expression for the neutrino momentum can be expanded as

$$p_i = \sqrt{E_i^2 - m_i^2} \approx E_i - \frac{m_i^2}{2E_i} \quad (2.12)$$

Assuming that the neutrino is ultra-relativistic ($v \approx c$), the time of propagation t can be written as the distance travelled L in natural units. Additionally, we assume that all the initial states have the same energy E , which allows us to average the oscillation probability over time. Putting this together, Equation 2.11 takes the form,

$$P_{\nu_\alpha \rightarrow \nu_\beta}(L, E) = \sum_{i,j} U_{\alpha i}^* U_{\beta i} U_{\alpha j} U_{\beta j}^* \exp\left(\frac{-i\Delta m_{ji}^2 L}{2E}\right) \quad (2.13)$$

where $\Delta m_{ji}^2 = m_j^2 - m_i^2$ are the mass-squared differences. The common general expression for the oscillation probability is obtained by expanding the matrix product and using the unitarity condition of the mixing matrix $U^\dagger U = \mathbb{1}$ [37, 38]

$$\begin{aligned} P_{\nu_\alpha \rightarrow \nu_\beta}(L, E) &= \delta_{\alpha\beta} - 4 \sum_{i>j} \text{Re}(U_{\alpha i}^* U_{\beta i} U_{\alpha j} U_{\beta j}^*) \sin^2\left(\frac{\Delta m_{ji}^2 L}{4E}\right) \\ &\quad + 2 \sum_{i>j} \text{Im}(U_{\alpha i}^* U_{\beta i} U_{\alpha j} U_{\beta j}^*) \sin\left(\frac{\Delta m_{ji}^2 L}{2E}\right) \end{aligned} \quad (2.14)$$

¹The star superscript indicates the complex conjugate.

From Equation 2.14 it is clear that if the mass-square differences Δm_{ji}^2 are zero then $P_{\nu_\alpha \rightarrow \nu_\beta} = \delta_{\alpha\beta}$ and no neutrino mixing occurs. Consequently, if neutrino mixing is observed, the neutrino mass eigenstates must be massive. It also implies nontrivial leptonic mixing, i.e., the matrix U must not be diagonal. The probability for neutrino mixing fluctuates with a phase given by $\frac{\Delta m_{ji}^2 L}{E}$ and an amplitude determined by U , giving rise to the term neutrino *oscillation*. Inserting the factors of \hbar and c that have been set equal to 1 so far, the argument of the \sin^2 term becomes

$$\frac{\Delta m_{ji}^2 L}{4E} = \Delta m_{ji}^2 (\text{eV}^2) \frac{1.27L((km))}{E(\text{GeV})} \quad (2.15)$$

The quantity L/E can then be conveniently used to determine the sensitivity of an experiment with a given L and E to mass-squared splittings. As will be discussed in Chapter 3, T2K has a baseline of 295 km and a peak neutrino energy of 0.6 GeV, and is therefore sensitive to mass-square splittings down to $\mathcal{O}(10^{-3}) \text{ eV}^2$.

The mixing probability for antineutrino oscillations is obtained by applying the CPT invariance ($P_{\nu_\alpha \rightarrow \nu_\beta} = P_{\bar{\nu}_\beta \rightarrow \bar{\nu}_\alpha}$) and the usage of the same parameters to describe the oscillation of neutrinos and antineutrinos [38],

$$\begin{aligned} P_{\bar{\nu}_\alpha \rightarrow \bar{\nu}_\beta}(L, E) = & \delta_{\alpha\beta} - 4 \sum_{i>j} \text{Re} (U_{\alpha i}^* U_{\beta i} U_{\alpha j} U_{\beta j}^*) \sin^2 \left(\frac{\Delta m_{ji}^2 L}{4E} \right) \\ & - 2 \sum_{i>j} \text{Im} (U_{\alpha i}^* U_{\beta i} U_{\alpha j} U_{\beta j}^*) \sin \left(\frac{\Delta m_{ji}^2 L}{2E} \right) \end{aligned} \quad (2.16)$$

Note that the only difference between Equations 2.14 and 2.16 is the sign of the third term. Therefore, a complex mixing matrix leads to $P_{\nu_\alpha \rightarrow \nu_\beta} \neq P_{\bar{\nu}_\alpha \rightarrow \bar{\nu}_\beta}$, which violates CP symmetry. The study of neutrino and antineutrino oscillations enables the study of CP-violation in the leptonic sector.

The mixing matrix U is commonly referred to as the Pontecorvo–Maki–Nakagawa–Sakata (PMNS) matrix in recognition of the pioneering contributions of these scientists to the physics of mixing and oscillation [31, 32]. It is analogous to the Cabibbo–Kobayashi–Maskawa (CKM) matrix which describes the mixing of quarks in weak interactions [39]. In general, it takes the following form:

$$U = \begin{pmatrix} U_{e1} & U_{e2} & U_{e3} \\ U_{\mu1} & U_{\mu2} & U_{\mu3} \\ U_{\tau1} & U_{\tau2} & U_{\tau3} \end{pmatrix} \quad (2.17)$$

The matrix is commonly parameterized in terms of three mixing angles θ_{12} , θ_{13} , and θ_{23} , and three CP-violating phases ξ_1 , ξ_2 , and δ_{CP} , and can be factorized in the following way [38],

$$U = \overbrace{\begin{pmatrix} 1 & 0 & 0 \\ 0 & c_{23} & s_{23} \\ 0 & -s_{23} & c_{23} \end{pmatrix}}^{\text{Atmospheric + accelerator}} \overbrace{\begin{pmatrix} c_{13} & 0 & s_{13}e^{-i\delta_{CP}} \\ 0 & 1 & 0 \\ -s_{13}e^{-i\delta_{CP}} & 0 & c_{13} \end{pmatrix}}^{\text{Reactor + accelerator}} \overbrace{\begin{pmatrix} c_{12} & s_{12} & 0 \\ -s_{12} & c_{12} & 0 \\ 0 & 0 & 1 \end{pmatrix}}^{\text{Solar}} \overbrace{\begin{pmatrix} e^{i\xi_1} & 0 & 0 \\ 0 & e^{i\xi_2} & 0 \\ 0 & 0 & 1 \end{pmatrix}}^{\text{Majorana}} \quad (2.18)$$

where $s_{ij} \equiv \sin \theta_{ij}$ and $c_{ij} \equiv \cos \theta_{ij}$. As will be discussed in Section 2.2.3, each one of the factors in Equation 2.18 is primarily constrained by experiments considering a given source of neutrinos, the exception being δ_{CP} which requires a precise measurement of all the other oscillation parameters. The phases ξ_1, ξ_2 are referred to as the *Majorana* phases, and are only physically relevant if neutrinos are identical to their own antiparticle. Furthermore, it has been shown that these phases do not affect the oscillation probabilities described above, and can be ignored when discussing neutrino oscillations [40, 41].

We are left then with six parameters describing the mixing of three generations of neutrinos: the mixing angles (θ_{12} , θ_{13} , and θ_{23}), the mass-squared differences (Δm_{21}^2 , and Δm_{32}^2)², and a CP-violating phase δ_{CP} . There is one additional degree of freedom in the sign of Δm_{32}^2 (and Δm_{31}^2) since neutrino oscillations are only concerned with the differences of the square of the neutrino masses. The convention is to call $\Delta m_{32}^2 > 0$ the *normal hierarchy* (NH) and $\Delta m_{32}^2 < 0$ the *inverted hierarchy* (IH). It is not yet known which mass hierarchy is true in nature.

The T2K experiment is able to measure neutrino oscillations in the ν_μ and $\bar{\nu}_\mu$ disappearance and ν_e and $\bar{\nu}_e$ appearance channels. To first order, the ν_μ and $\bar{\nu}_\mu$ disappearance oscillation probabilities are given by [42],

$$P_{\nu_\mu(\bar{\nu}_\mu) \rightarrow \nu_\mu(\bar{\nu}_\mu)} \simeq 1 - (\cos^2 \theta_{13} \sin^2 2\theta_{23} + \sin^4 \theta_{23} \sin^2 \theta_{13}) \sin^2 \frac{\Delta m_{32}^2 L}{4E} + \text{Solar and matter effect terms} \quad (2.19)$$

And the ν_e and $\bar{\nu}_e$ appearance probabilities are given by,

$$P_{\nu_\mu(\bar{\nu}_\mu) \rightarrow \nu_e(\bar{\nu}_e)} \simeq \sin^2 \theta_{23} \sin^2 2\theta_{13} \sin^2 \frac{\Delta m_{31}^2 L}{4E} + \sin^2 2\theta_{23} \sin^2 2\theta_{12} \sin^2 2\theta_{13} \cos \theta_{13} \sin \frac{\Delta m_{21}^2 L}{4E} \sin \frac{\Delta m_{31}^2 L}{4E} \times \left[\cos \frac{\Delta m_{32}^2 L}{4E} \cos \delta_{CP} \mp \sin \frac{\Delta m_{32}^2 L}{4E} \sin \delta_{CP} \right] + \text{Solar and matter effect terms} \quad (2.20)$$

The ν_μ and $\bar{\nu}_\mu$ disappearance probabilities are identical, as shown in Equation 2.19. On the other hand, the ν_e and $\bar{\nu}_e$ appearance probabilities have opposite signs in the term that is

²With $\Delta m_{31}^2 = \Delta m_{32}^2 - \Delta m_{21}^2$. However, we know experimentally that $\Delta m_{21}^2 \ll |\Delta m_{32}^2|$, so $\Delta m_{31}^2 \approx \Delta m_{32}^2$

proportional to $\sin \delta_{CP}$, as shown in Equation 2.20. This is term that allows for CP-violation searches in neutrino oscillation experiments. Terms dominated by Δm_{21}^2 , the so-called solar mass-squared splitting, have been omitted because T2K is not sensitive to those oscillations.

The full treatment of neutrino oscillations is more involved than that presented here. However, the derivation presented contains all the essential quantum mechanical aspects and allowed us to reach the correct expressions for the leading terms for the oscillation probabilities. One important effect not considered so far is that of the medium through which the neutrinos travel as they oscillate. For example, in long baseline neutrino experiments, neutrinos travel through the crust of the Earth. This matter effect introduces an additional source of CP violation since matter is CP asymmetric itself, being made of electrons rather than positrons. The phenomenon was first introduced by L. Wolfenstein [43] and subsequently elaborated by S.P. Mikheev and A. Y. Smirnov [44], hence it is commonly referred to as the MSW effect.

There are two possible interaction channels for neutrinos with matter, charged current (CC) of a ν_e from an electron via exchange of a W boson, or neutral current (NC) scattering of any flavour of neutrino from an electron, proton or neutron via the exchange of a Z boson. The latter does not affect the oscillation physics as it is independent of neutrino flavour. On the other hand, the CC interactions must be considered as they only affect ν_e s. The additional potential that contributes to the neutrino Hamiltonian is described by

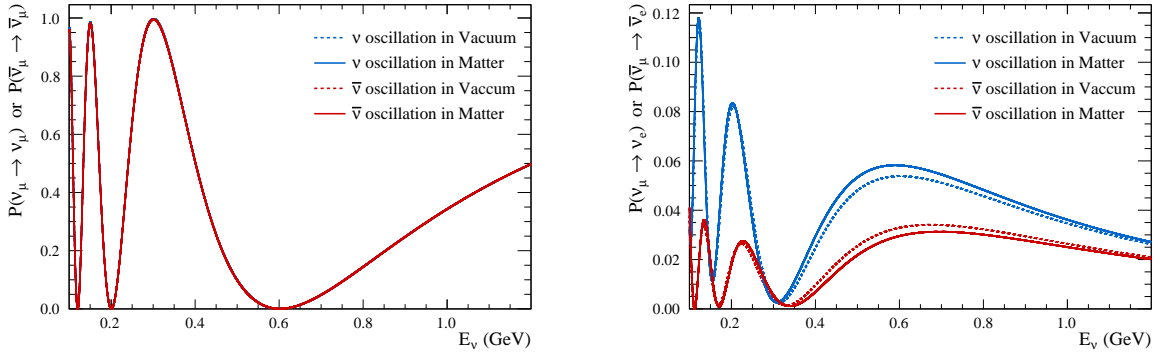
$$V_{CC} = \pm\sqrt{2}G_F N_e \quad (2.21)$$

where G_F is the Fermi coupling constant, N_e is the electron number density, and the positive and negative signs are for neutrinos and antineutrinos respectively.

The complete description of the effect of this potential to the oscillation physics is beyond the scope of this thesis. It suffices to say that there will be an additional source of CP violation that will cause a degeneracy with the intrinsic CP violation discussed earlier. It can also be shown that the neutrino oscillation probabilities in matter have a dependency on the sign of the mass splittings [45]. This means that it may be possible to determine the mass hierarchy from long-baseline neutrino experiments.

The oscillation analysis presented in this thesis calculates neutrino oscillation probabilities using the Prob3++ software [46], which includes the complete probability formulae in the case of oscillations in matter. Figure 2.4 shows the disappearance and appearance probabilities for neutrinos and antineutrinos as a function of energy for the T2K baseline (295 km). The probabilities are shown separately for oscillations in vacuum and in matter. The values assumed for the oscillation parameters are motivated by the best current knowledge, with the exception of δ_{CP} , where -1.0 was chosen for demonstrative purposes.

The disappearance probability in Figure 2.4a is the same to leading order for neutrinos and antineutrinos, as was shown in Equation 2.19. The probabilities in vacuum and matter are almost indistinguishable, indicating that the matter effect is not significant for disappearance searches at T2K. The appearance probability in Figure 2.4b is much more interesting. The effect of the



(a) $P_{\nu_\mu(\bar{\nu}_\mu) \rightarrow \nu_\mu(\bar{\nu}_\mu)}$

(b) $P_{\nu_\mu(\bar{\nu}_\mu) \rightarrow \nu_e(\bar{\nu}_e)}$

Figure 2.4: Oscillation probabilities for ν_μ (blue) and $\bar{\nu}_\mu$ (red) disappearance (left), and ν_e (blue) and $\bar{\nu}_e$ (red) appearance (right) for the T2K baseline ($L=295$ km) as a function of the neutrino energy. The oscillation probabilities in vacuum (dashed lines) and matter (solid lines) are shown. An average matter density of 2.6 g/cm^3 was assumed. The following oscillation parameters were assumed for illustrative purposes: $\sin 2\theta_{12} = 0.846$, $\sin 2\theta_{13} = 0.085$, $\sin 2\theta_{23} = 1.0$, $\Delta m_{12}^2 = 7.53 \times 10^{-5} \text{ eV}^2$, $\Delta m_{32}^2 = 2.5 \times 10^{-3} \text{ eV}^2$, $\delta_{CP} = -1.0 \text{ rad}$. This figure was produced using the Prob3++ software [46].

CP-violating term in Equation 2.20 becomes clearly visible in the comparison of the neutrino and antineutrino probabilities. The matter effect, which affects ν_e s, is now also visible and its size relative to the intrinsic CP-violation effect can be seen. Considering that a large value of the CP-violating phase was assumed for this figure, it is clear that considering matter effects is necessary for oscillation analyses at T2K.

2.2.3 Current Knowledge and Open Questions

There has been remarkable progress in the understanding of the neutrino oscillation physics in the past two decades. The field has gone from the discovery phase at the start of the 21st century, to a confirmation of the 3-neutrino model with high confidence, and is now moving to the era of precision measurements of the oscillation parameters that allow for the search of CP-violation in the leptonic sector.

The current world-best parameter values are determined from global fits to the results of several experiments. These global fits are performed by phenomenologists [47] and by the Particle Data Group [48]. The 3σ regions for each matrix element of the mixing matrix, as determined by the authors of [47], are:

$$U_{3\sigma} = \begin{pmatrix} 0.800 \sim 0.844 & 0.515 \sim 0.581 & 0.139 \sim 0.155 \\ 0.229 \sim 0.516 & 0.438 \sim 0.699 & 0.614 \sim 0.790 \\ 0.249 \sim 0.528 & 0.462 \sim 0.715 & 0.595 \sim 0.776 \end{pmatrix} \quad (2.22)$$

The PMNS matrix is found to have a significantly different structure relative to the CKM matrix [48], with large off-diagonal elements corresponding to more mixing allowed.

The best measurement of the solar parameters θ_{12} and Δm_{21}^2 comes from a three-neutrino oscillation fit to KamLAND and global solar neutrino data, using constraints on θ_{13} from reactor and accelerator experiments. Figure 2.5a shows an updated version of Figure 2.3 in which the full data statistics from the KamLAND experiment are considered [49]. The allowed regions projected in the $(\tan^2 \theta_{12}, \Delta m_{21}^2)$ plane, for solar and KamLAND data from their three-flavor oscillation analysis, where θ_{13} is a free parameter, are shown in Figure 2.5b. The side panels show the $\Delta\chi^2$ profiles projected onto the $\tan^2 \theta_{12}$ and Δm_{21}^2 axes.

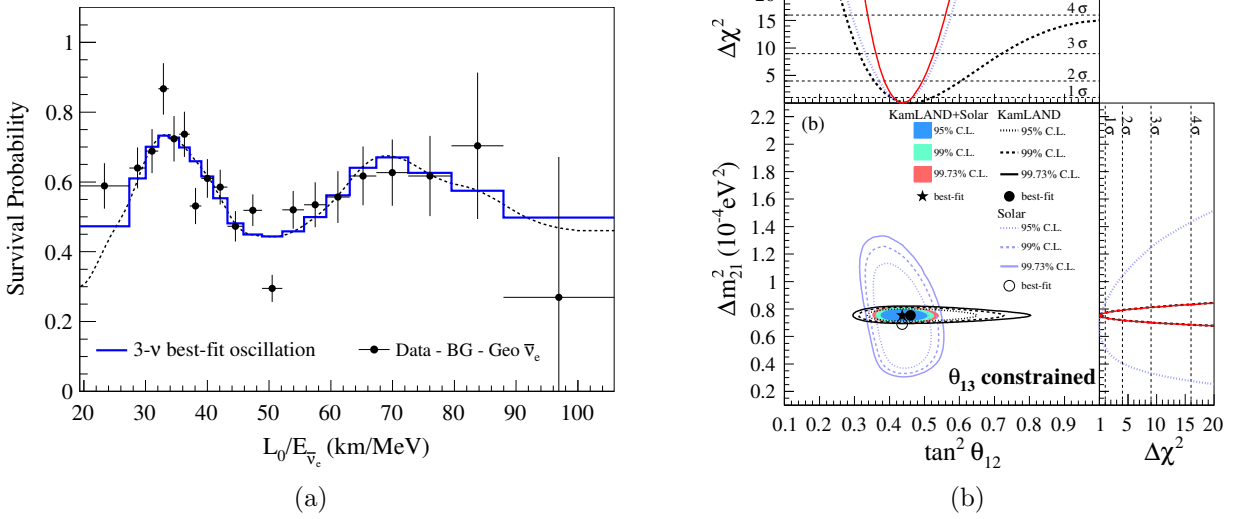


Figure 2.5: Results of the KamLAND experiment leading to world-best determination of the solar parameters θ_{12} and Δm_{21}^2 [49]. (a) The ratio of the observed $\bar{\nu}_e$ spectrum to the expectation for no-oscillation versus L_0/E for the full KamLAND statistics. (b) The allowed regions projected in the $(\tan^2 \theta_{12}, \Delta m_{21}^2)$ plane from a three-oscillation fit to KamLAND and global solar neutrino data. Reproduced from [49].

The atmospheric parameters θ_{23} and Δm_{32}^2 have been measured by atmospheric and long-baseline accelerator neutrino experiments. Similarly to the solar parameters, these parameters are highly correlated and their constraints are generally presented as two-dimensional contours in the $\sin^2 \theta_{23}$ vs. Δm_{32}^2 space. The left-panels of Figure 2.6 (reproduced from [47]) show the 68% and 90% confidence regions assuming normal and inverted hierarchy from the IceCube DeepCore [50], MINOS [51], NoVA [52], and T2K [53] experiments. Also in Figure 2.6 are the results of a global fit to these data by the authors of [47], where the reactor data was used to impose a Gaussian constraint on θ_{13} . The agreement between the different experiments is reasonable within their 68% contours, but some “tension” starts to appear in the determination of both parameters among the long-base line accelerator experiments which now have higher sensitivity than atmospheric experiments due to increased statistics. In particular, the recent results from NOvA, unlike those from T2K, favour a non-maximal ($\neq 45^\circ$) value of θ_{23} .

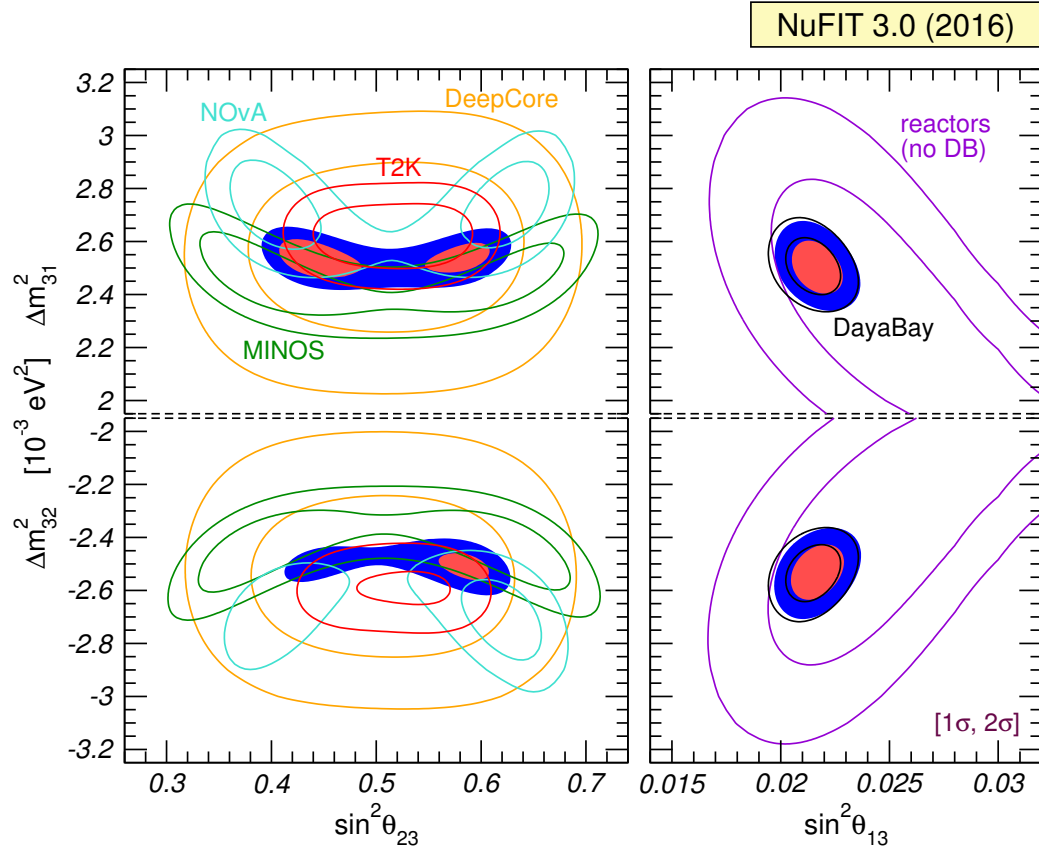


Figure 2.6: Left: Current world knowledge of the atmospheric parameters θ_{23} and Δm_{32}^2 . The 1σ and 2σ contours are plotted for the IceCube DeepCore [50], MINOS [51], NoVA [52], and T2K [53] experiments for the normal (top) and inverted (bottom) hierarchy. The coloured regions are the result of a global fit to these data sets. Right: Allowed regions in the $\sin^2 \theta_{13}$ vs. Δm_{31}^2 plane using only Daya-Bay (black lines), reactor data without Daya-Bay (violet lines), and their combination (coloured regions). In all panels solar and KamLAND data are included to constrain Δm_{21}^2 and θ_{12} . Contours are defined with respect to the global minimum of the two ordering. Reproduced from [47].

Parameter	Normal Hierarchy	Inverted Hierarchy
$\sin^2 \theta_{12}$	$0.306^{+0.012}_{-0.012}$	
$\theta_{12}(\circ)$	$33.56^{+0.77}_{-0.75}$	
Δm_{21}^2 (10^{-5} eV ²)	$7.50^{+0.19}_{-0.17}$	
$\sin^2 \theta_{23}$	$0.441^{+0.027}_{-0.021}$	$0.587^{+0.020}_{-0.024}$
$\theta_{23}(\circ)$	$41.6^{+1.5}_{-1.2}$	$50.0^{+1.1}_{-1.4}$
Δm_{3l}^2 (10^{-3} eV ²)	$+2.524^{+0.039}_{-0.040}$	$-2.514^{+0.038}_{-0.041}$
$\sin^2 \theta_{13}$	$0.02166^{+0.00075}_{-0.00075}$	$0.02179^{+0.00076}_{-0.00076}$
$\theta_{13}(\circ)$	$8.46^{+0.15}_{-0.15}$	$8.49^{+0.15}_{-0.15}$
$\delta_{CP}(\circ)$	261^{+51}_{-59}	277^{+40}_{-46}

Table 2.1: Summary of best-fit values and $\pm 1\sigma$ allowed ranges for the six neutrino oscillation parameters obtained from a global fit to the world neutrino data by the authors of [47]. The numbers in the 1st (2nd) column are obtained assuming NO (IO), *i.e.*, relative to the respective local minimum. Note that $\Delta m_{3l}^2 \equiv \Delta m_{31}^2 > 0$ for NO and $\Delta m_{3l}^2 \equiv \Delta m_{32}^2 < 0$ for IO. Adapted from [47].

The most precise measurement of θ_{13} comes from the short-baseline reactor experiments Daya-Bay in China [54], Double Chooz in France [55], and RENO in South Korea [56]. These experiments measure the disappearance of $\bar{\nu}_e$ from a nuclear reactor at ~ 1 km, which is much shorter than KamLAND. The right-panels of Figure 2.6 show the 68% and 90% allowed regions for the parameters in the $\sin^2 \theta_{13}$ vs. Δm_{31}^2 space from: i) a combination of reactor experiments not including than Daya-Bay, ii) Daya-Bay, and iii) the best-fit obtained by the authors of [47] by combining these two data sets.

There are currently no measurements of δ_{CP} , only exclusions not statistically significant of the CP-conserving values (0 and π). The result of this thesis includes one of the first hints of the existence of CP-violation at the 2σ level. T2K-II expects to achieve a 3σ sensitivity before 2026 by extending the T2K approved 7.8×10^{21} POT exposure to 20×10^{21} POT [57], but future experiments such as DUNE [58] and Hyper-K [59] are the ones that hold the key to a precise measurement of the value of δ_{CP} .

Finally, Table 2.1 lists the best-fit parameter values for the six oscillation parameters, obtained from a 3-flavour global fit to the world data by the authors of [47]. The 3σ level of precision of a parameter can be defined from its lower ($x^{-3\sigma}$) and upper ($x^{+3\sigma}$) bounds as $2(x^{+3\sigma} - x^{-3\sigma}) / (x^{+3\sigma} + x^{-3\sigma})$. The estimated relative levels of precision of the oscillation parameters are: 14% for θ_{12} , 32% for θ_{23} , 11% for θ_{13} , 14% for Δm_{21}^2 , and 9% for $|\Delta m_{3l}^2|$ [47].

Chapter 3

The T2K Experiment

The T2K (Tokai-To-Kamioka) experiment is a long-baseline neutrino oscillation experiment located in Japan [60]. A ν_μ beam is created from a 30GeV proton beam at the Japan Proton Accelerator Complex (J-PARC) in the east coast of Japan and is sent in a 295 km journey across Japan to the Super-Kamiokande detector in the west coast. The properties of the neutrino beam are first examined by the ND280 detector, located 280 m from the target. Figure 3.1 shows a schematic representation of the experimental setup.

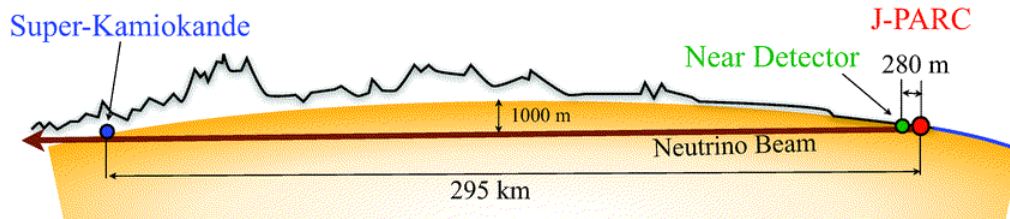


Figure 3.1: Schematic representation of the experimental setup of the T2K experiment. The neutrinos travel from right to left, going through the near and far detectors. Reproduced from [60].

The primary goal of T2K is the precision measurement of neutrino oscillation parameters. T2K has sensitivity to θ_{23} , θ_{13} , Δm_{32}^2 , and δ_{CP} through the ν_μ disappearance and ν_e appearance channels. The neutrino oscillation probability is inferred by comparing the measurements at the near and far detectors.

Section 3.1 describes how the ν_μ beam is produced and monitored. An overview of the near and far detectors is presented in Sections 3.2 and 3.3, respectively. The description of the simulations used to describe the physics of the flux prediction, the neutrino and pion interaction

models, and the detector models is reserved for Chapter 4.

3.1 The T2K Neutrino Beam

3.1.1 Beamline

The T2K ν_μ beam is produced and delivered to the near and far detectors in multiples stages. The process starts when a beam of H^- ions is accelerated to 180 MeV by a linear accelerator (LINAC). The beam of ions then passes through charge-stripping foils, turning into a proton beam. A rapid-cycling proton synchrotron (RCS) accelerates the beam up to 3 GeV, before it is finally fed to the main ring synchrotron (MR) and accelerated to 30 GeV. Figure 3.2 shows an overview of the facility.

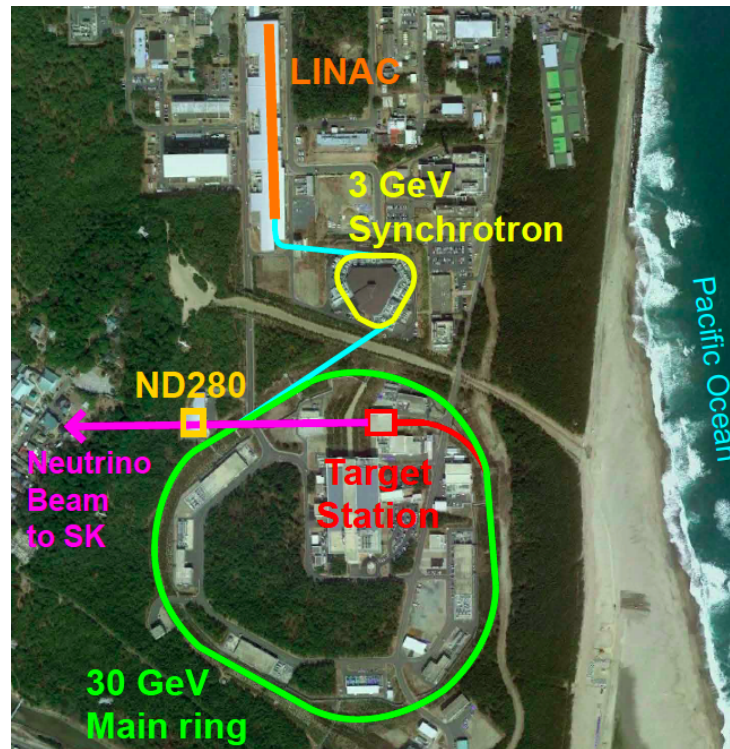


Figure 3.2: Overview of the J-PARC facility.

The beam circulates every 2 to 3 seconds, and is extracted to the T2K neutrino beamline as a “spill”. Each spill contains eight bunches in about $5\mu s$. The spill timing is used for detector synchronization, along with a GPS signal. At the current operation setting, the MR can deliver $\sim 3 \times 10^{14}$ protons per spill, corresponding to ~ 500 kW beam power. Figure 3.3 shows the history of accumulated protons on target (POT) and beam power over T2K Runs 1 to 8 (January 2010 to April 2017).

The primary beamline depicted in Figure 3.4 steers the proton beam towards the direction of ND280 and SK. The preparation and final focusing sections use normal conducting magnets,

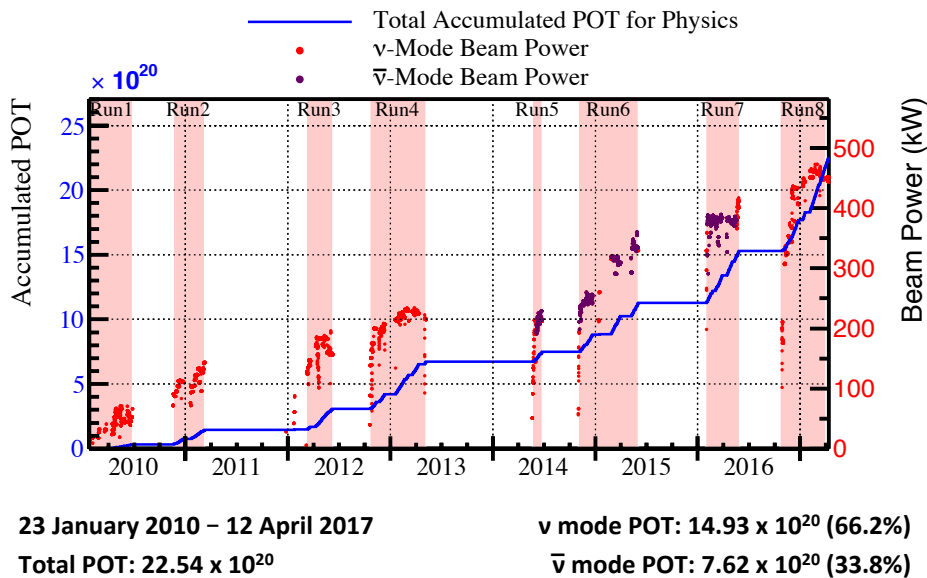


Figure 3.3: Beam Power (left axis) and accumulated POT (right axis) over the years of T2K operation.

while the arc section contains superconducting magnets to steer the beam. The measurements of the intensity, position, profile, and loss of the proton are essential to the neutrino flux prediction. The beam position and profile are measured by a collection of 21 electrostatic monitors (ESMs), 19 segmented secondary emission monitors (SSEMs), and an optical transition radiation (OTR) detector, described in Section 3.1.2. Five current transformers (CTs) measure the absolute proton beam intensity with a 2% uncertainty [61].

The secondary beamline, also depicted in Figure 3.4, consists of the target station (TS), decay volume, beam dump, and MUMON muon monitor. The target station houses the interaction carbon target, placed inside the first of three magnetic focusing horns (described below), all within a vessel filled with helium. The protons from the primary beamline impinge on the cylindrical solid graphite target of density 1.8 g/cm^3 , 90 cm long, and 2.6 cm in diameter. A $29 \times 40 \times 171.1 \text{ cm}^3$ graphite block with a 3 cm bore hole placed upstream from the target acts as a collimator (also referred to as baffle), and protects the rest of the equipment from stray protons.

The resulting charged mesons (mostly pions and kaons) from the proton on carbon interactions are focused in the original direction of the proton beam by the magnetic horns. Each magnetic horn consists of two coaxial aluminum conductors, operated with a 250 kA pulsed current producing a 1.7 T toroidal magnetic field [62]. The current can be inverted to focus either positively or negatively charged mesons. These are referred herein as “Forward Horn Current”

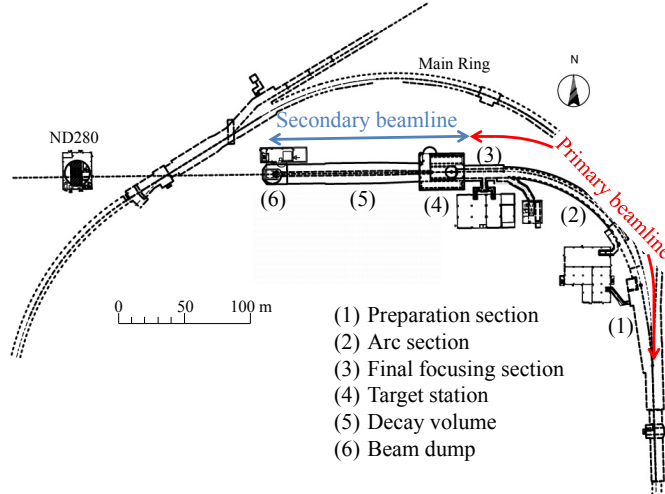


Figure 3.4: Primary and secondary T2K neutrino beamlines. Reproduced from [60].

(FHC) and “Reverse Horn Current” (RHC) modes:

$$\begin{array}{lll}
 \pi^+ \rightarrow \mu^+ + \nu_\mu & K^+ \rightarrow \mu^+ + \nu_\mu & \text{(FHC mode)} \\
 \pi^- \rightarrow \mu^- + \bar{\nu}_\mu & K^- \rightarrow \mu^- + \bar{\nu}_\mu & \text{(RHC mode)}
 \end{array}$$

These decays occur inside the decay volume, a 96 m long steel tunnel. The remnants of the decayed mesons and the long-lived mesons that make it to the end of the decay volume are stopped by a beam dump made of 75 tons of graphite and 2.4 m thick iron plates. The neutrinos pass through the beam dump and are used for the experiment. Muons above 5 GeV that also pass through the beam dump are monitored by the muon monitor (MUMON) [63] to provide additional information of the beam direction and intensity.

The simulation, tuning, and uncertainties of the flux prediction are described in Section 4.1.

3.1.2 The OTR Detector

The Optical Transition Radiation (OTR) detector measures the proton beam profile by imaging transition radiation in the visible spectrum emitted as the 30 GeV proton beam traverses a thin foil placed in its path [64]. It provides the most downstream measurement of the proton beam profile, 29 cm in front of the interaction target. Along with the rest of the beam monitors, it provides a measurement of the beam position and direction with the required accuracy of 1 mm and 0.5 mrad, respectively. The two-dimensional (2D) beam profile measured is vital during beam commissioning and for the neutrino flux prediction.

Transition radiation is produced when a charged particle traverses a boundary between materials with different dielectric constant. The moving fields of the charged particle induce a time-dependent polarization in the medium, which emits radiation. These radiated fields across

the boundary space interfere coherently to form transition radiation [65]. The formation depth for transition radiation D_{TR} can be written as [66].

$$D_{TR} = (\gamma c) \left(\frac{4\pi e^2 n_e}{m_e} \right)^{-1} = \frac{\gamma c}{\omega_p} \quad (3.1)$$

where n_e and ω_p are the electron number density and plasma frequency of the medium, respectively. For a 30 GeV proton ($\gamma \approx 32$) crossing solid titanium ($\omega_p \approx 1.34 \times 10^{16} \text{ s}^{-1}$), D_{TR} is of the order of $1 \mu\text{m}$. For the OTR system, three materials were used for foils of diameter 50 mm: five titanium alloy (Ti 15-3-3-3) foils with a thickness of $50 \mu\text{m}$ during high intensity beam ($>5 \text{ kW}$), one aluminum alloy (Al 1110) foil with the same thickness used for medium intensity beam (1-40 kW), and one ceramic wafer (AF995R) with a thickness of $100 \mu\text{m}$ used for low beam power ($<1 \text{ kW}$) typical of beam commissioning.

The number of photons N emitted by transition radiation in a frequency range $d\omega$ and solid angle $d\Omega$ for a relativistic particle ($\beta = v/c \approx 1$) leaving a medium of dielectric constant ϵ and entering vacuum is [67]

$$\frac{d^2 N}{d\omega d\Omega} = \frac{2e^2}{\pi h c \omega} \left(\frac{\sqrt{\epsilon} - 1}{\sqrt{\epsilon} + 1} \right)^2 \frac{\sin^2 \theta}{1 - \beta \cos^2 \theta} \quad (3.2)$$

where θ is the angle of emission relative to an axis pointing in the opposite direction of motion of the charged particle. In the case of the OTR, the foil is placed at 45° with respect to the proton beam axis as shown in Figure 3.5a. The backward light described by Equation 3.2 is the one imaged by the OTR detector.

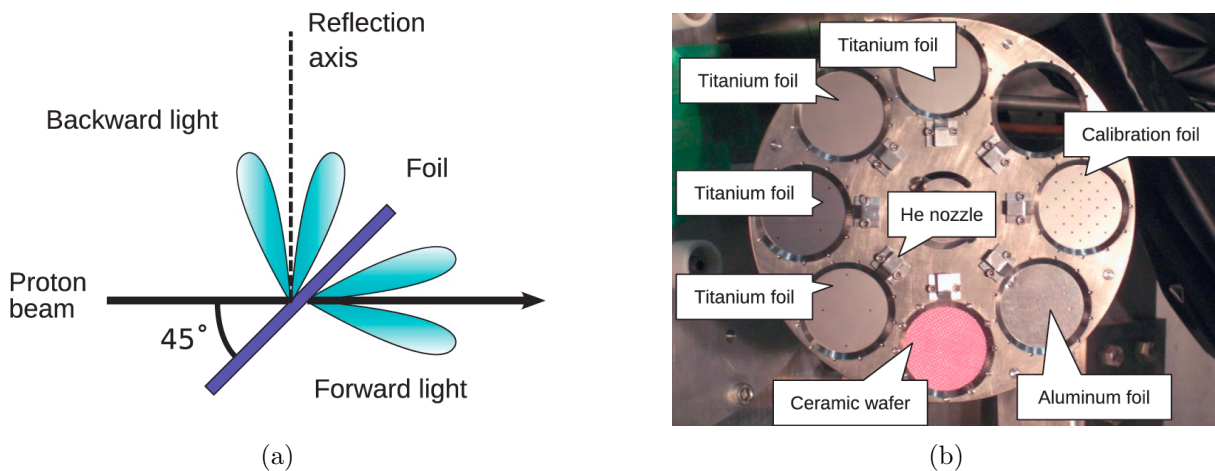


Figure 3.5: (a) Illustration of the direction of the backward light produced by a foil oriented at 45° . Adapted from [64]. (b) The foil disk and the foils used for OTR-I. Reproduced from [64].

The components of the OTR detector are:

(1) **Foil Disk System**

The OTR foils are mounted on a disk carousel which has eight foil positions as shown in Figure 3.5b. One slot is left empty for calibration purposes. Each foil is stretched by a clamping ring providing sufficient tension to keep the foil flat during the thermal shock caused by the beam. The disk is mounted on a titanium “arm” held by two “legs” to an aluminum plate of the first magnetic horn module.

The main feature of the system is the ability to rotate the disk such that the desired slot is placed in the path of the beam. This is done remotely by a stepper motor at the top of the horn module connected to a collection of rigid and flexible shafts. A spring-loaded plunger mechanism presses the disk and locks it firmly in position. A micro switch engaged by a titanium bottom on the disk prompts the motor to stop immediately prior to the activation of the plunger mechanism.

(2) **Optical System**

Due to the extreme radiation environment around the foil disk (5.4×10^8 Sv/hr at 750 kW operation), an optical system is used to transport the OTR light through the iron and concrete shielding. Four parabolic mirrors transport the light through two bends in the radiation shielding, as shown in Figure 3.6. A 25 cm diameter fused silica window in the top aluminum lid of the helium vessel allows the light to emerge for capture.

The mirrors are made of solid aluminum and are coated with a uniform 400 nm thick layer of Al_2O_3 . The focal lengths of mirrors 1, 2, and 3 is 55 cm. The image is shrunk in size to fit the optical sensor by a combination of a shorter 30 cm focal length of mirror 4 ($\sim 55\%$ reduction) and a fiber-optic taper attached to the sensor ($\sim 28\%$ reduction).

(3) **Camera**

A charge injection (CID) device (Thermo Fisher Scientific 8710D1M) placed on an optical stage secured to the top lid of the helium vessel is used to capture the transported OTR light. The camera is radiation tolerant up to 10 kGy, sufficient for the estimated radiation dose of ~ 1 kGy/year at 750 kW beam power. The sensor in the camera consists of 755×484 pixels, with pixel dimension of $12.0 \mu\text{m} \times 13.7 \mu\text{m}$.

(4) **Data Acquisition System (DAQ) and Slow Control**

The DAQ system is described in detail elsewhere [68]. Three full image frames from the CID camera are stored for each beam spill trigger. The components of the DAQ system are:

- A FastFrame 1303 frame-grabber board with an FPGA chip that controls the trigger signals from the beamline and the image acquisition, and a TriMedia TN1302 digital signal processor (DSP) chip for handling and transfer of the digitized image.
- A host DAQ computer that interfaces with the frame-grabber board via a PCI port. A MIDAS-based [69] front-end application compresses and transfers the image to a

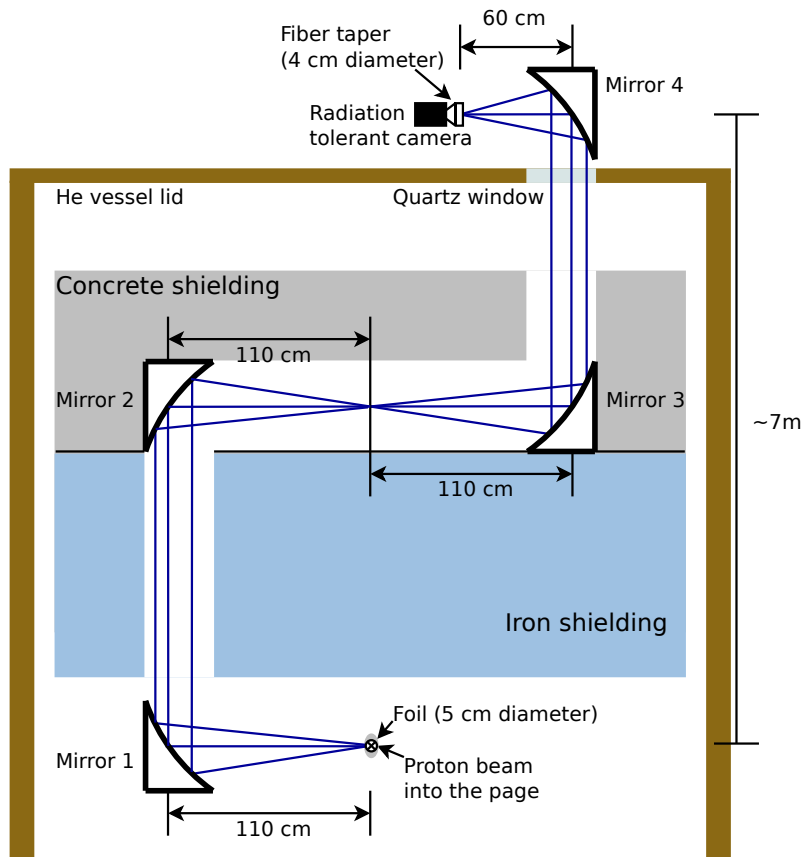


Figure 3.6: Cross section view through the shielding of the optical system used to transport the OTR light. Reproduced from [64].

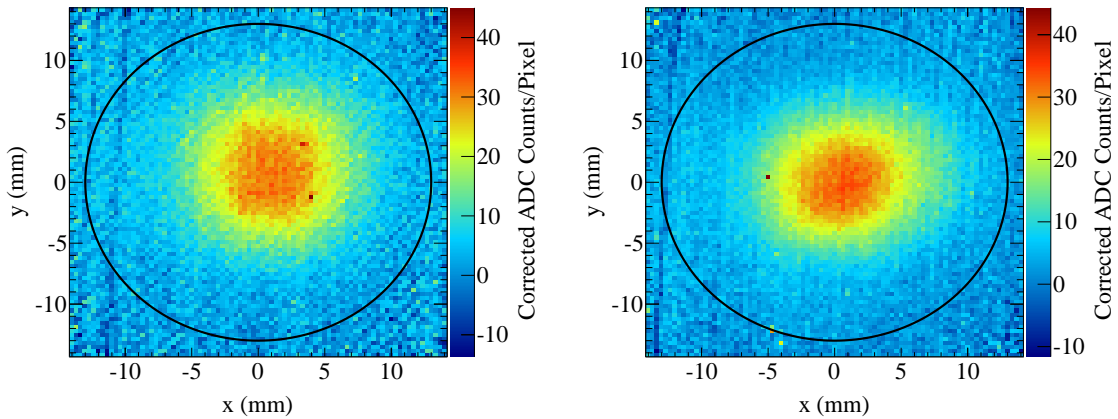


Figure 3.7: OTR two-dimensional proton beam profiles obtained using the aluminum (left) and titanium (foils). The black circle represents the diameter of the baffle. Reproduced from [64].

dedicated server for processing, and controls additional hardware in the system such as the motors and lighting systems used for calibration.

The analysis of the digitized images includes corrections for the light collection efficiency loss introduced by the optical system, as well as the image distortion introduced by the parabolic mirrors. Laser-machined holes were drilled in the fifth titanium foil to be used for calibration (see the Calibration Foil in Figure 3.5b) in conjunction with sources of back lighting. A pedestal subtraction is applied using the two additional frames stored for each spill. Figure 3.7 shows examples of the measured beam profiles obtained from the aluminum and titanium foils for proton beams at 40 kW and 140 kW, respectively. The beam centre and width are obtained by fitting a two-dimensional Gaussian function for the signal, plus a linear function for the background.

Several sources of systematic uncertainties were considered [68]. The largest contribution arises from the 0.3 mm alignment uncertainty of the calibration foil, obtained from a survey carried out during the commissioning of the detector. Other sources are: the alignment of the calibration light sources, the choice of the model for the signal and background, and biases from the fitter and the image distortion corrections.

3.1.2.1 Detector Stability

The OTR detector has operated stably over the seven years of beam data taking of T2K. Three versions of the system have been built. OTR-I operated from 2009 to 2013, receiving a total of 6.6×10^{20} POT. In 2014 the first magnetic horn was replaced and the current system, OTR-II, was installed. OTR-III was assembled, calibrated, and tested during this period and is now the spare system.

J-PARC experienced a high seismic activity during the Great East Japan Earthquake of March 2011. An alignment and surveying campaign was carried out as part of the efforts to return to beam operation. Given that the OTR foil disk is rigidly attached to the front plate of the first horn, the OTR system is ideal for a beam based check of the relative alignment between the primary and secondary beamlines. This was achieved by performing horizontal and vertical beam scans, and comparing the OTR measurements with extrapolations of the SSEMs and ESMs measurements at the OTR foil position. The measurements were found to be consistent within alignment uncertainties. Additionally, Appendix B describes a beam-based study to determine the relative alignment of the baffle.

Figure 3.8 shows the stability of the OTR-II horizontal beam centre measurement relative to the extrapolation from the upstream beam monitors. The measurements are consistent to better than 1 mm and the consistency is stable with a standard deviation of less than 0.3 mm. Similar results have been reported for previous running periods [64].

Figure 3.9 shows the normalized OTR light yield vs. the integrated POT for the OTR-II system. The peak around 4×10^{20} POT corresponds to a new titanium foil coming in place. The light yield is found to decrease and the exposure increases due to deposition and browning of the

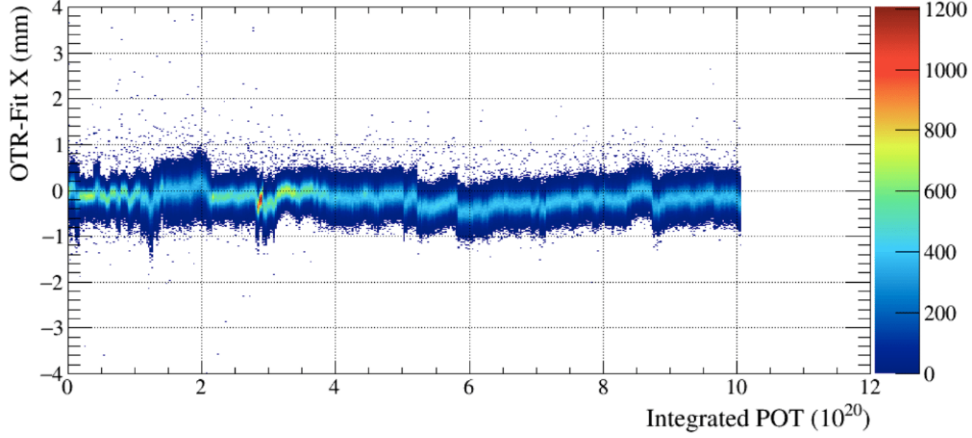


Figure 3.8: The difference between the OTR-II x measurements of the beam centre and the extrapolation from the upstream proton beam measurements. The data points were collected from May 2014 and April 2017.

foil. The additional titanium foils in the system will be sufficient to receive the exposure until the OTR-III system is installed in the summer of 2018.

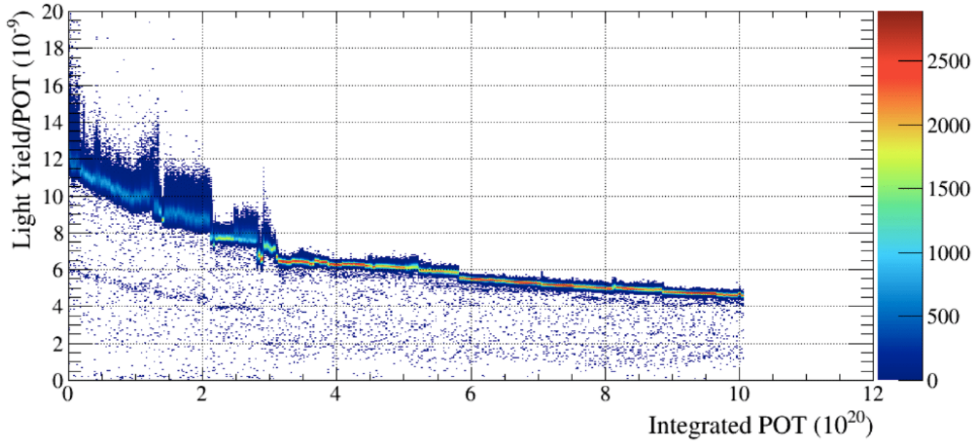


Figure 3.9: OTR light yield/POT vs. integrated POT for the OTR-II system. The decrease in light yield is caused by corrosion and damage of the foils.

3.1.3 Off-Axis Configuration

Unlike previous long-baseline experiments, the near and far detectors of T2K are placed 2.5° off-axis from the beam line. This off-axis method allows for the creation of a neutrino beam with a small energy spread, also referred to as a narrow-band beam, by utilizing the fact that the energy of a neutrino emitted at a large angle relative to its parent meson in a two-body decay ($\pi^+ \rightarrow \mu^+ \nu_\mu$ or $\pi^- \rightarrow \mu^- \bar{\nu}_\mu$) depends weakly on the parent meson momentum [70]. From the two body decay kinematics, the neutrino energy E_ν can be written in the lab frame as,

$$E_\nu = \frac{m_\pi^2 - m_\mu^2}{2(E_\pi - p_\pi \cos \theta)} = \frac{m_\pi^2 - m_\mu^2}{2\left(\sqrt{m_\pi^2 + p_\pi^2} - p_\pi \cos \theta\right)} \quad (3.3)$$

where θ is the angle between the direction of the pion and the neutrino, p_π is the momentum of the pion, m_π and m_μ are the masses of the pion and muon, respectively, and the mass of the neutrino has been neglected. Figure 3.10a illustrates the E_ν vs. p_π dependence for various values of θ , as given by Equation 3.3. For $\theta = 0$, the energy of the neutrino is proportional to the pion momentum. This is not the case for values of θ different than zero (off-axis). For instance, for 2.5° degrees the neutrino energy is nearly independent of the pion momentum (for $p_\pi > 2$ GeV/c), allowing the production of a narrow-band neutrino beam.

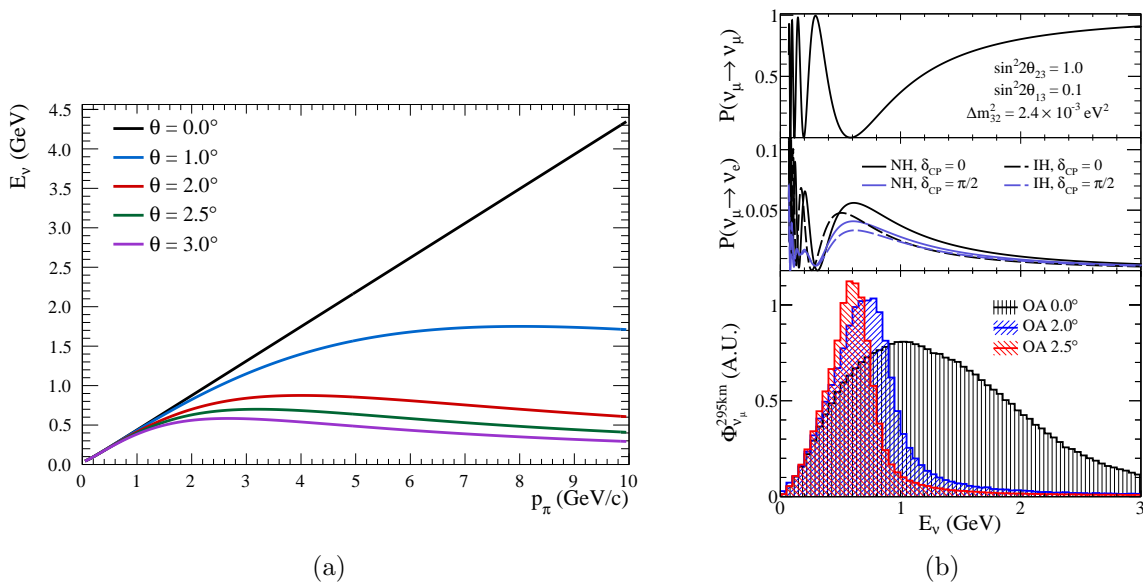


Figure 3.10: (a) Neutrino energy as a function of pion momentum (Equation 3.3) for various values of the off-axis angle θ . (b) The disappearance (top) and appearance probabilities (middle) for $L = 295$ km and the oscillation parameter values listed within the figure. The bottom plot shows the ν_μ flux (in arbitrary units) at SK for various off-axis (OA) angles. Reproduced from [71].

The 2.5° off-axis angle used for T2K was chosen such that the peak of the neutrino energy distribution (~ 0.7 GeV) matches the maximum ν_μ disappearance probability values representative of T2K, as can be seen in Figure 3.10b. Additionally, the narrow band beam minimizes possible sources of background from neutrinos in the high energy tail of the distribution.

3.2 The Near Detector: ND280

The near detector complex is located 280 m downstream of the neutrino production target. The near detector provides measurements of the following properties of the unoscillated ν_μ beam:

- (1) The ν_μ energy spectrum before oscillation.

- (2) The flavour contents of the neutrino beam before oscillation, i.e., the ν_e component of the beam from decays of muons and kaons, which produces an irreducible background for the ν_e appearance channel.
- (3) Neutrino cross sections (or event rates) for relevant interaction processes. In particular, the separation of exclusive CC and NC channels with π^0 and π^\pm , which are backgrounds for the ν_e appearance and ν_μ disappearance channels, respectively.

The near detector is comprised of the on-axis detector INGRID, and the ND280 off-axis detector (herein called ND280).

3.2.1 INGRID

The Interactive Neutrino GRID (INGRID) [72] monitors the neutrino beam intensity and profile, and contributes in the determination of the beam direction, and consequently the off-axis angle. It consists of 16 identical modules arranged in horizontal and vertical arrays around the beam axis, as shown in Figure 3.11a. Each 7.1 ton module has a sandwich structure of iron plates and scintillating trackers. The neutrino beam centre and direction is monitored on a daily basis with a 10 cm and 0.4 mrad precision, respectively.

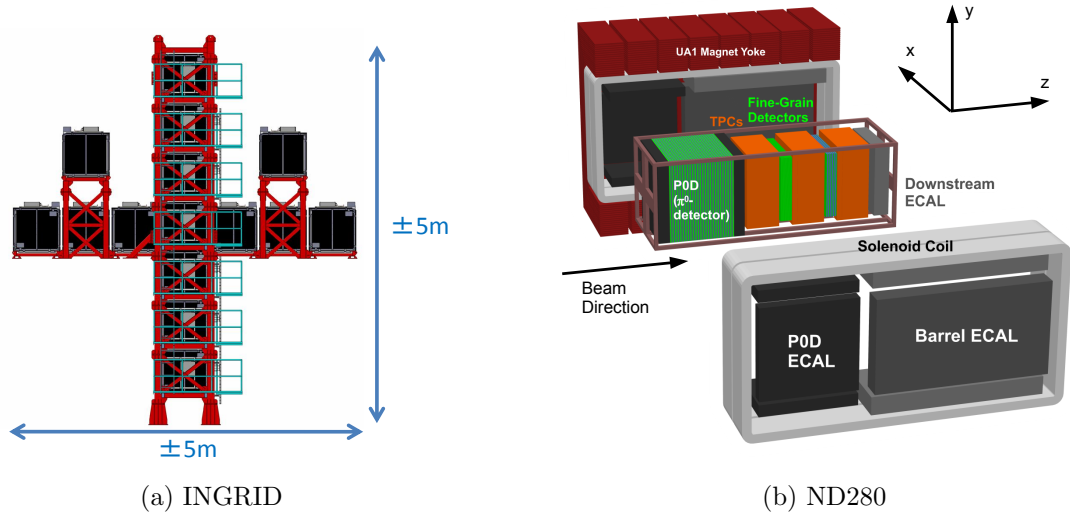


Figure 3.11: Detectors in the near detector complex. Reproduced from [71, 72].

3.2.2 ND280

The ND280 detector is used directly in the oscillation analysis presented in Part III to reduce uncertainties to the neutrino event rate predictions coming from the flux and cross section models. It is located 2.5° off-axis the beam centre, and is composed of several sub-detectors, as shown in Figure 3.11b. The *basket* contains the π^0 detector (PØD) [73] and the *tracker* made up of three time projection chambers (TPCs) and two fine grained detectors (FGDs). Several

electromagnetic calorimeters (ECals) [74] surround the basket. The UA1 magnet encloses all detectors. The magnet is instrumented with scintillator panels that act as side muon range detectors (SMRDs) [60].

Only the tracker is used in the event selection presented in Section 9.1.1, therefore only the UA1 magnet, and the FGD and TPC sub-detectors will be described in more detail below. Figure 3.12a shows a sample event display from the tracker portion of ND280. Two FGDs are interspersed in between three TPCs.

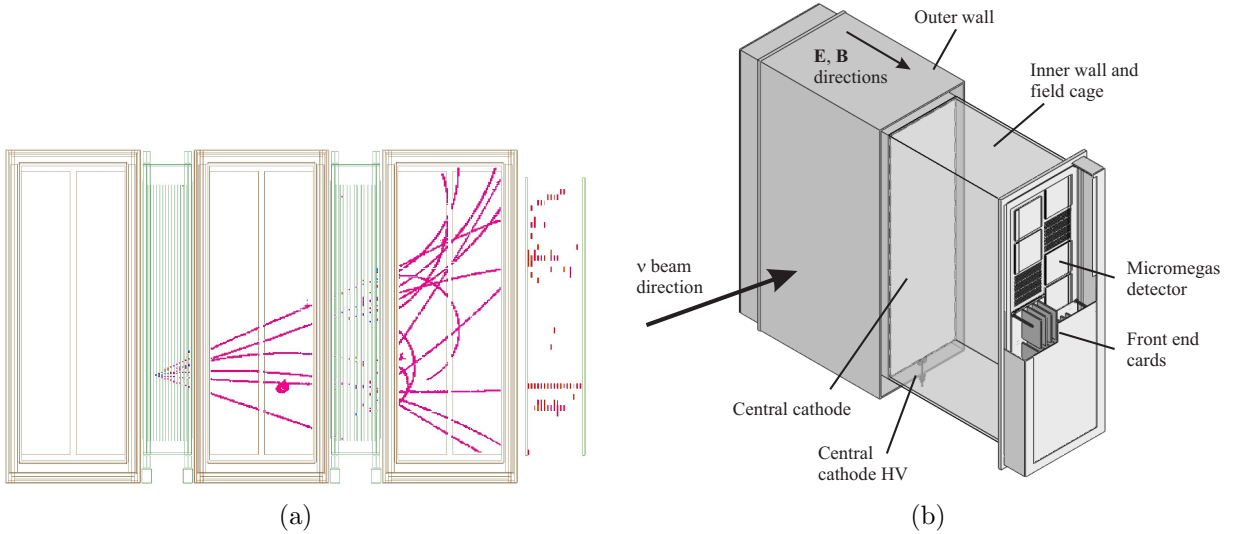


Figure 3.12: (a) Sample ND280 event display for a neutrino interaction in the FGD1. Reproduced from [75]. (b) Simplified cut-away schematic on one TPC. Reproduced from [60].

3.2.2.1 UA1 Magnet

The magnet used in ND280 was originally used by the UA1 experiment at CERN [76]. It provides a dipole magnetic field of 0.2 T, perpendicular to the neutrino beam direction, which allows the TPCs to determine the sign of the charged particles and to measure their momentum with resolution better than 10%. The magnet consists of aluminum coils, and a flux return yoke. The coils are cooled by water flowing through a central bore.

The outer dimensions of the magnet are $7.6 \text{ m} \times 5.6 \text{ m} \times 6.1 \text{ m}$, and the basket dimensions are $6.5 \text{ m} \times 2.6 \text{ m} \times 2.4 \text{ m}$. The magnetic field is produced by a current of $\sim 3 \text{ kA}$ in the coils. The spatial components of the field were mapped in-situ using Hall probes.

3.2.2.2 Time Projection Chambers

The time projection chambers (TPCs) [77] provide high resolution tracking of charged particles. The magnetic field provided by the UA1 magnet allows the TPC information to measure

the momenta of charged particles. The three TPCs all have identical designs and alternate with the two FGDs in the ND280 tracker.

Each TPC consists of an inner and outer box, as shown in Figure 3.12b with the outer box measuring $2.3 \text{ m} \times 2.4 \text{ m} \times 1.0 \text{ m}$. The inner box is filled with an argon-based drift gas, Ar:CF₄:C₄H₁₀ (95:3:2), while the outer box is filled with CO₂ as an insulator. The inner box is subdivided by a central cathode at its midpoint, and the walls parallel to the cathode are covered with a precisely machined copper strip pattern. This produces a uniform 280 V/cm electric drift field inside the module, precisely aligned with the magnetic field.

The charged particles entering the TPC ionize the gas, creating electrons that drift away from the cathode towards the TPC readout planes. These readout planes are instrumented with micromegas detectors [77], segmented in horizontal and vertical pads. 3D track reconstruction is achieved by combining information from the micromegas pads, timing information, and the known ionization drift velocity. In addition, the ionization per unit length is used for particle identification.

3.2.2.3 Fine Grained Detectors

The fine grained detectors (FGDs) act as the active target for the interaction of neutrinos to be used in this analysis. The FGDs are constructed from $9.6 \text{ mm} \times 9.6 \text{ mm} \times 1864.3 \text{ mm}$ bars of extruded polystyrene scintillator, which are oriented perpendicular to the beam direction [75]. Each FGD has outer dimensions of $2300 \text{ mm} \times 2400 \text{ mm} \times 365 \text{ mm}$, and contains 1.1 tons of target material. The scintillating bars are read out by Multi-Pixel Photon Counters (MPPCs).

There are two FGD modules in the tracker: “FGD1” constructed only from scintillator bars, and “FGD2” consisting of scintillating bars and 2.5 cm thick layers of water that act as a passive target. This configuration allows measurements of neutrino interactions on carbon and water. Most particles from neutrino interactions inside the FGD will reach the TPCs, however, it is possible to have fully-contained tracks from recoil protons or interacting pions. Only events where the neutrino interaction vertex is reconstructed inside the FGD1 are used in this analysis.

3.3 The Far Detector: Super-Kamiokande

The Super Kamiokande (SK) detector [78] acts as the far detector for T2K to measure the oscillated neutrino beam. It is a 50 kton pure water Cherenkov detector, situated about 1 km deep within Mt. Ikenoyama in Kamioka, Gifu prefecture. It is located 295 km downstream of the neutrino interaction target. Like ND280, it sits 2.5° off-axis relative to the neutrino beam centre. It has been in operation since 1996 with a broad physics program in addition to neutrino oscillation physics, including proton decay [79], dark matter searches [80], supernova relic neutrinos [81], and magnetic monopoles [82].

SK consists of a cylindrical tank, 39.3 m in diameter and 41.4 m tall. A cylindrical stainless-steel framework inside the tank divides it into two optically separated volumes, the inner and

outer detector. This structure support is placed approximately 2 m from the walls, and supports ~ 13000 50 cm-diameter Hamamatsu R3600 photo-multiplier tubes (PMTs). The outer detector is used primarily as an effective veto of cosmic rays and other backgrounds. 85 % of the PMTs are inward-facing, providing ~ 40 % photo-coverage. Figure 3.13 shows a schematic drawing of the detector.

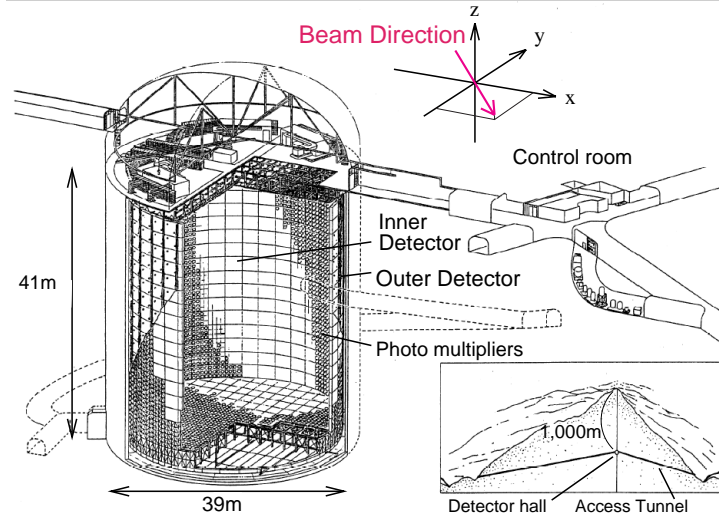


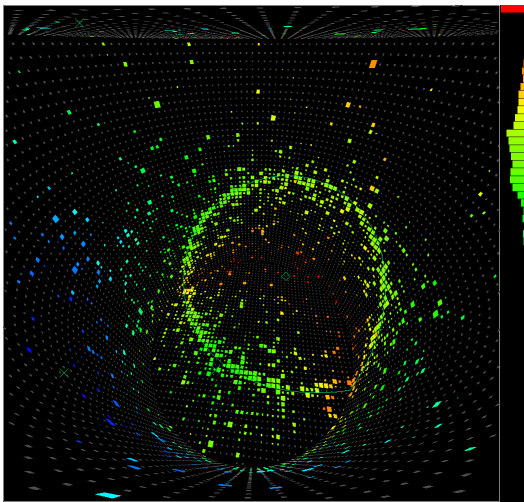
Figure 3.13: Schematic drawing of the SK detector. Reproduced from [71].

The detection of particles at SK is achieved via the imaging of Cherenkov cone of radiation produced when the speed v of a charged particle exceeds the phase velocity of light in the medium c/n . The half-opening angle θ_c of the Cherenkov cone relative to the particle direction is given by,

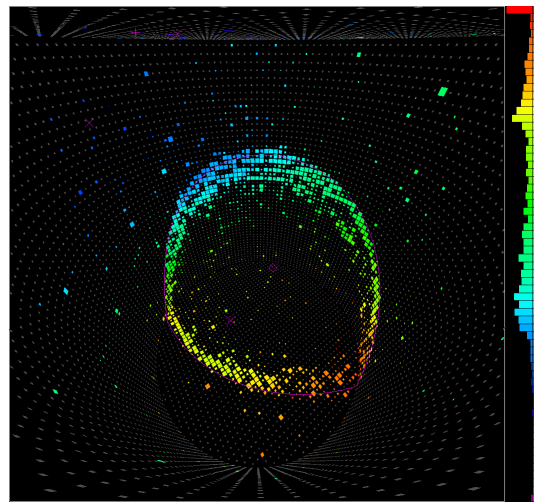
$$\cos \theta_c = \frac{1}{\beta n} \quad (3.4)$$

where $\beta = v/c$ and n is the refractive index. The cone of light around the particle trajectory is projected as a ring on the detector walls. When the particle slows down and falls below threshold, the cone collapses. The energy loss is proportional to $\sin^2 \theta_c$ and is determined by counting the number of Cherenkov photons produced [66]. The hit pattern produced by the Cherenkov photons as measured by the PMTs, along with timing information, makes it possible to extract information about the vertex position, particle momentum, and the flavour of the charged lepton.

As was explained in Section 4.2, the signal for T2K analyses comes from CCQE interactions. At SK, only the lepton will be detected: a muon from a ν_μ interaction, or an electron from a ν_e interaction. Electrons scatter off water molecules and also induce electromagnetic showers as they travel. These effects result in a “fuzzy” Cherenkov ring. Muons are less likely to scatter, hence they will produce a sharper Cherenkov ring. The reconstruction algorithm is outlined in Section 4.4.2.1. Figure 3.14 shows an example of reconstructed electron and muon Cherenkov rings at SK.



(a) Ring reconstructed as a 492 MeV electron.



(b) Ring reconstructed as a 603 MeV muon.

Figure 3.14: Sample event displays of reconstructed Cherenkov rings at SK from data. The colour scale represents the time of arrival at the PMTs, which is also represented in the vertical histogram to the right of the event display. Each square represents a PMT, and its size the amount light detected. Reproduced from [83].

Chapter 4

Physics Simulation

Oscillation analyses rely on the prediction of the neutrino energy spectra to extract the values of the oscillation parameters. The spectra can be expressed as a convolution of the neutrino flux, the neutrino-nucleus cross section, and detector efficiencies and smearing, as was shown in Equation 1.1. Each one of those components are calculated from separate simulations that use Monte Carlo (MC) methods.

The neutrino flux simulation is described in Section 4.1. The predicted neutrino fluxes are propagated to the neutrino interaction simulation described in Section 4.2 to obtain the final state particles for each event. The interaction of final state particles are simulated using the cascade model described in Section 4.3. These final state particles are propagated through the geometries of the ND280 and SK detectors by the simulations described in Section 4.4. The oscillation probabilities are calculated at the oscillation analysis stage using the Prob3++ software [46].

4.1 Neutrino Flux Prediction

The neutrino flux is modelled by a data-driven Monte Carlo (MC) simulation of a 30 GeV proton beam starting upstream of the baffle that collides with the graphite target to produce hadrons, which are then tracked as they decay to produce neutrinos. The simulation is tuned to the proton beam parameters measured by the proton beam line monitors, the measured magnetic horn currents, the measured alignment and off-axis of the neutrino beam, and external hadron production measurements [61, 68].

The hadronic interactions are simulated using the FLUKA 2011 package [84, 85]. The resulting particles emitted from these interactions are propagated using JNUBEAM, GEANT3 [86], including the magnetic field produced by the horns. The hadronic interactions in JNUBEAM are simulated using the GCALOR package [87]. The particles are tracked until they decay according to the current best knowledge of branching ratios [48], or until their kinetic energy drops below 10 MeV. All the neutrinos that are produced are recorded and used to calculate the neutrino flux at the ND280 and SK positions.

The FLUKA model is reweighted according to external data measurements, most significantly to the π^\pm and K^\pm production rates measured by the NA61/SPS Heavy Ion and Neutrino Experiment (NA61/SHINE) at CERN [88]. NA61/SHINE operated in two target configurations: a thin target (2 cm) and a T2K replica target, and data from both configurations is used for tuning. The tuned neutrino flux at ND280 and SK are shown in Figure 4.1 in the FHC mode and RHC mode, broken down by neutrino species.

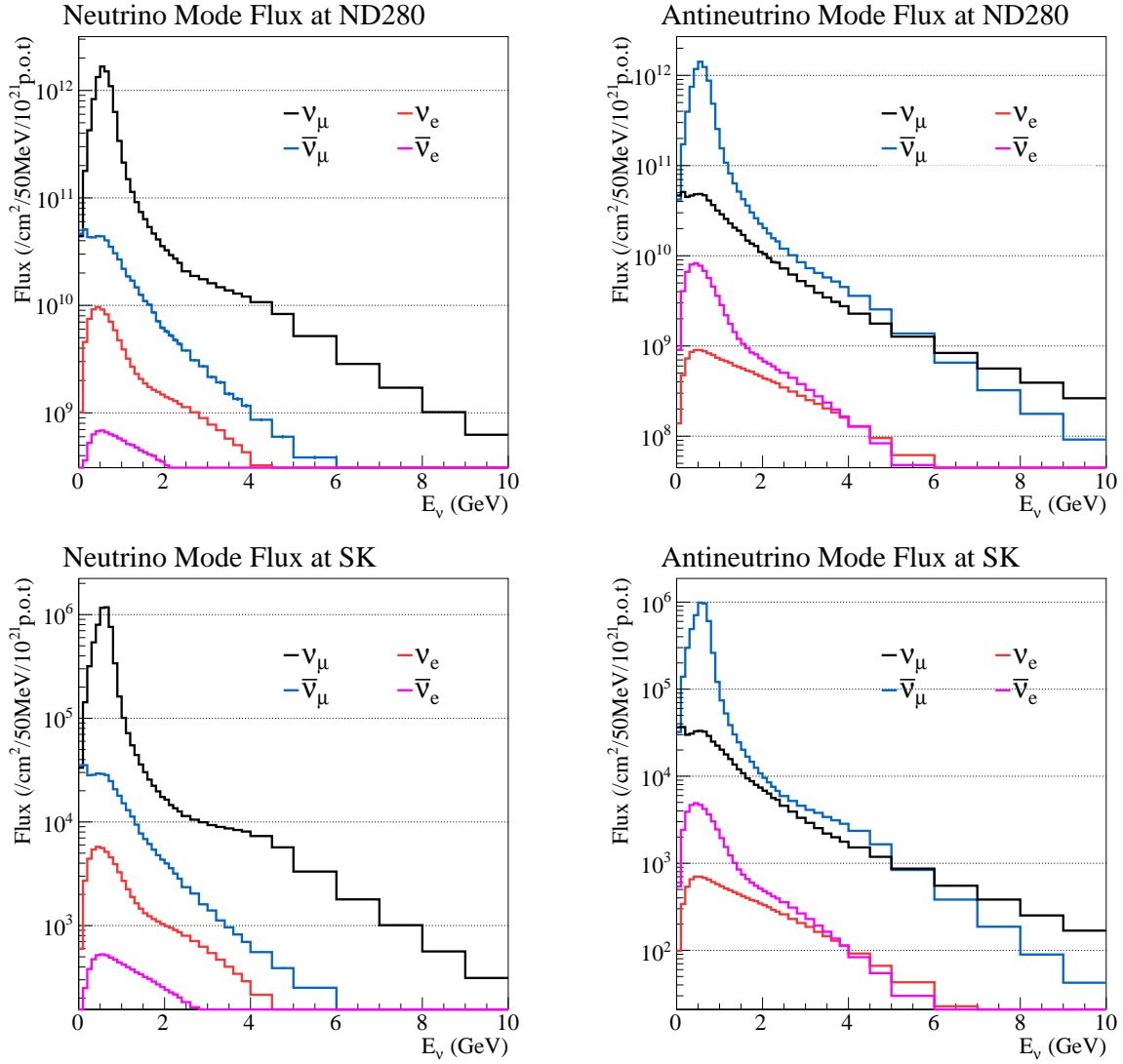


Figure 4.1: The tuned neutrino flux predictions at ND280 (top) and SK (bottom) in FHC mode (left) and RHC mode (right). Normalized to 1×10^{21} POT. Reproduced from [89].

Figure 4.2 shows the fractional uncertainty for the ν_μ component of the FHC mode flux at ND280 and SK. Several sources of uncertainties in the neutrino flux prediction are considered [61, 89]:

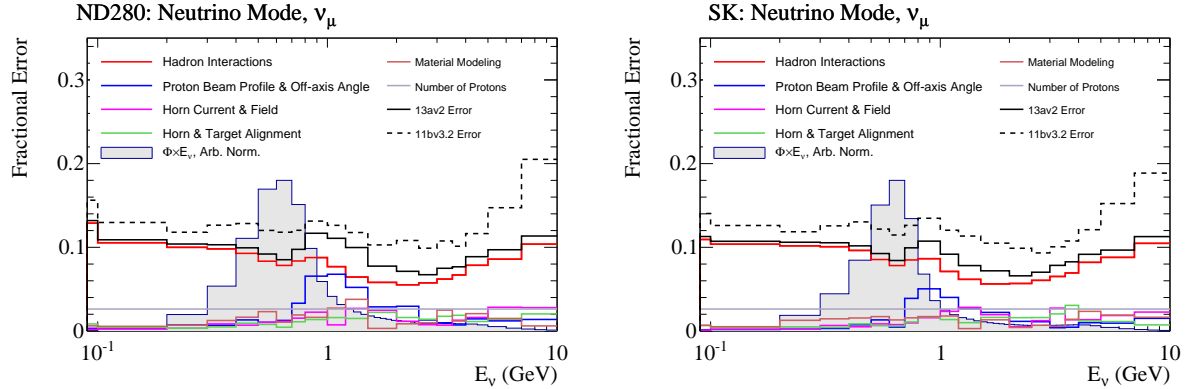


Figure 4.2: The fractional uncertainty on the ND280 (left) and SK (right) ν_μ flux prediction as a function of neutrino energy for the FHC mode. The dotted line is the uncertainty from the previous flux prediction. Reproduced from [89].

- (1) *Hadron interactions*: The systematic uncertainties associated with the hadronic interactions that currently dominate the neutrino flux error budget come from a variety of sources. One of them is the experimental uncertainties in the data used for tuning. Another arises from the scaling of the differential production yields to different incident particle momenta and target materials. Finally, the systematic uncertainties associated with the total interaction rate (production cross section) are also included.
- (2) *Proton beam profile and off-axis angle*: The dominant sources of uncertainty for the proton beam are the y -alignment uncertainty from the OTR detector (4.13 mm) and the relative alignment uncertainty in the y direction between the primary and secondary beamlines (0.539 mrad). The uncertainty in the off-axis angle is calculated to be 0.39 mrad from INGRID data.
- (3) *Horn current*: The horn current is estimated to be 250 ± 5 kA. The effect of this uncertainty is estimated by changing the horn current by $\pm 1\sigma$ relative to the nominal value in the JNUBEAM simulation.
- (4) *Horn and target alignment*: The uncertainties on the alignment of the horns and target are estimated to be ± 1 mm in all directions. The effect of this uncertainty is estimated by shifting the horn and target positions by $\pm 1\sigma$ relative to the nominal value in the JNUBEAM simulation.
- (5) *Material modelling*: Some components of the beamline are not included in the JNUBEAM simulation. One example is the cooling water inside the horns. These effects are estimated by taking the ratio of the flux with additional materials included to the nominal flux that does not include these materials.
- (6) *Number of protons*: An absolute normalization error on the flux is calculated based on the uncertainty on the POT measurement obtained from the most downstream current

transformer (CT) beam current.

While the contribution from each source of systematic uncertainty is calculated independently and assumed to be uncorrelated, a correlation between different energy bins is expected. A covariance matrix is calculated as shown in Section 9.2.1.

4.2 Neutrino Interaction Model

The interactions of neutrinos inside the detectors of T2K are simulated using the NEUT neutrino event generator [90], developed by the Super-K and T2K collaborations. The analysis presented in this thesis uses NEUT version 5.3.2.

Unlike early neutrino experiments where hydrogen or deuterium targets were used, modern experiments like T2K have turned to heavier targets like carbon and oxygen to increase the neutrino event statistics. The importance of an accurate understanding of neutrino-nucleus interactions for the study of the neutrino oscillation phenomenon can not be overstated, and constitutes an active and continually growing field [91, 92, 93, 94, 95]. However, this falls outside the scope of this thesis, and only an overview is provided below.

A complete model of neutrino-nucleus interactions can be factorized into the three following components: a nuclear model (Section 4.2.1), a cross section model (Section 4.2.2), and a final state interaction model (Section 4.2.3). The uncertainties in the modelling of neutrino interactions and their implementation are described in Section 9.2.2.

4.2.1 Nuclear Model

The nucleus is a complicated environment. A model describing the initial state of the nucleons within the nucleus is necessary. The *Impulse Approximation* (IA), in which the neutrino interacts with a single “free” nucleon, has been commonly used. In the Relativistic Fermi Gas (RFG) model, nucleons are treated as non-interacting fermions and all possible momentum states are filled up to the Fermi momentum, p_F [96]. The probability density of finding a nucleon with three momentum \vec{p} and energy E is described by

$$P_{RFG}(|\vec{p}|, E) = \frac{6\pi^2 A}{p_F^2} \Theta(p_F - |\vec{p}|) \delta(E_p - E_b + E) \quad (4.1)$$

where A is the number of nucleons within the nucleus, E_p is the energy of the proton, and E_b is the binding energy of the nucleus. The values for p_F and E_b are obtained from fits to electron scattering data [97].

While the RFG model is the reference model for T2K, more complex models exist in the literature and some are available in Monte Carlo event generators. The Local Fermi Gas (LFG) model includes a dependence of the proton or neutron density of the nucleus to the Fermi momentum [92]. The Benhar Spectral Function (SF) model adds short range correlations which describe particles in quasi-deuteron states within the nucleus [98].

4.2.2 Cross Section Model

In T2K, neutrinos are detected indirectly from the products of their weak interactions with the nuclear target material in the detectors. Weak interactions can proceed via charged current (CC) or neutral current (NC) channels. In CC interactions, the interaction is mediated by a W^\pm boson and the neutrino converts into its charged lepton partner. These interactions are the most useful for T2K, since they allow us to determine the flavour of the neutrino. In NC interactions the interaction is mediated by the exchange of a Z^0 boson that leaves the neutrino flavour unchanged.

Furthermore, in the few-GeV energy range of interest for T2K, the neutrino-nucleus interaction processes can be divided into the following three categories: quasi-elastic scattering (QE or CCQE), resonance scattering (RES), and deep inelastic scattering (DIS). Figure 4.3 summarizes the existing CC neutrino and antineutrino cross section measurements. In the neutrino energy range of T2K (see Figure 3.10b), the dominant interaction channel is CCQE.

The base model for CCQE interactions used in NEUT was selected from a fit to previous experiments on deuterium and nuclear targets [99]. Similarly, the model for CC1 π interactions was selected and tuned to data [100], notably including a recent re-analysis of ANL and BNL bubble chamber data [101].

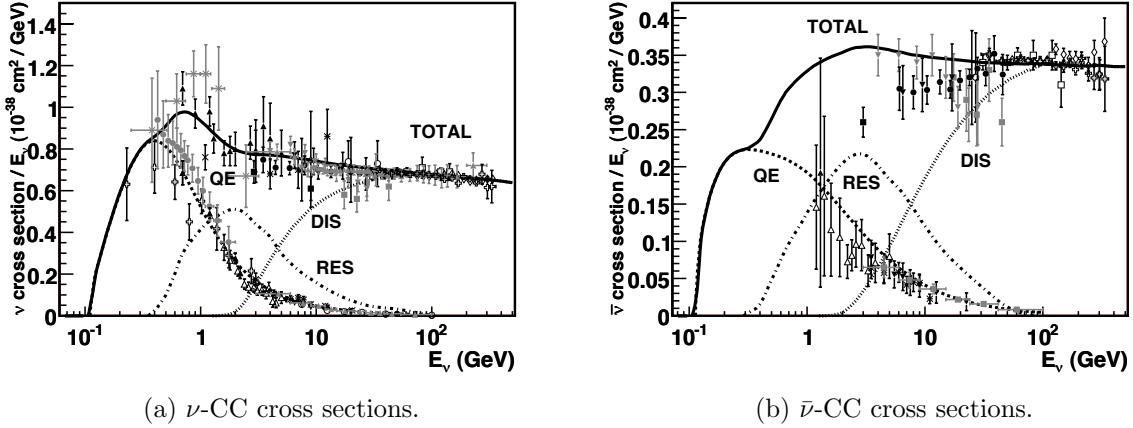


Figure 4.3: CC cross sections per nucleon divided by the neutrino energy and plotted as function of the energy. The QE, RES, and DIS contributions are plotted, along with their sum (Total). Data from various experiments are represented with markers, along with the predictions from the NUANCE [102] event generator. Reproduced from [103].

- **Quasi-elastic Scattering**

The Feynman diagram for a neutrino CCQE interaction is shown in Figure 4.4a. Assuming the interaction occurs with a bound neutron at rest, it is possible to reconstruct the energy of the neutrino from the energy and direction of the lepton

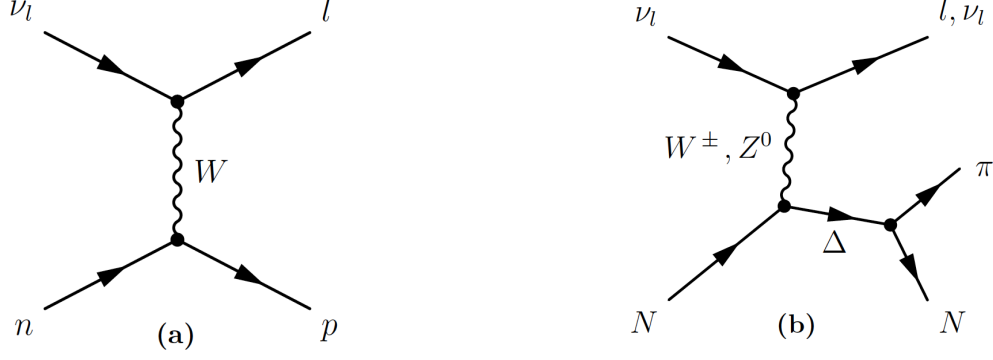


Figure 4.4: Feynman diagrams for charged current quasi-elastic interactions (left) and charged/neutral current resonance interactions (right).

$$E_{rec} = \frac{m_p^2 - (m_n - E_b)^2 - m_\mu^2 + 2(m_n - E_b)E_\mu}{2(m_n - E_b - E_\mu + p_\mu \cos \theta_\mu)} \quad (4.2)$$

The CCQE neutrino-nucleon differential cross section as a function of the squared four momentum transfer Q^2 can be expressed using the Llewellyn-Smith formalism [104],

$$\frac{d\sigma}{dQ^2} = \frac{G_F^2 M^2 \cos \theta_C}{8\pi E_\nu^2} \left(A(Q^2) \pm B(Q^2) \frac{(s-u)}{M^2} + C(Q^2) \frac{(s-u)^2}{M^4} \right) \quad (4.3)$$

where the sign $(-)+$ refers to (anti)neutrino scattering, G_F is the Fermi coupling constant, M is the nucleon mass, m is the lepton mass, E_ν is the energy of the incoming neutrino, θ_C is the Cabibbo angle, and s and u are the Mandelstam variables. The terms $A(Q^2)$, $B(Q^2)$, and $C(Q^2)$ are functions of the vector (F_V^1 and F_V^2), axial-vector (F_A), and pseudoscalar (F_P) form factors of the nucleon:

$$\begin{aligned} A(Q^2) = & \frac{m^2 + Q^2}{M^2} \left((1 + \tau)F_A^2 - (1 - \tau)(F_V^1)^2 \right. \\ & + \tau(1 - \tau)(\xi(F_V^1))^2 + 4\tau\xi(F_V^1 F_V^2) \\ & \left. - \frac{m^2}{4M^2} ((F_V^2 + \xi F_V^2)^2 + (F_A + 2F_P)^2 - 4(1 + \tau)F_P^2) \right) \end{aligned} \quad (4.4)$$

$$B(Q^2) = \frac{Q^2}{M^2} F_A (F_V^1 + \xi F_V^2) \quad (4.5)$$

$$C(Q^2) = \frac{1}{4} (F_A^2 + (F_V^1)^2 + \tau(\xi F_V^2)^2) \quad (4.6)$$

where $\tau = Q^2/4M^2$, $\xi = (\mu_p - \mu_n) - 1$, μ_p μ_n are the magnetic moments of the proton and neutron, respectively, and m is the mass of the outgoing lepton. Using the conserved vector current hypothesis (CVC), the vector form factors can be related to the electromagnetic

form factors measured in electron-nucleon elastic scattering experiments. The BBA07 form factors [105] are widely used in the neutrino community for this purpose. The full CCQE cross section calculation in the Llewellyn-Smith formalism assuming the RFG model for the initial state of the nucleons can be found elsewhere [106].

It is customary to assume the following dipole form for the axial form factor:

$$F_A(Q^2) = \frac{g_A}{\left(1 + \frac{Q^2}{M_A^2}\right)} \quad (4.7)$$

where g_A is the axial coupling constant, measured to be $g_A = -1.271 \pm 0.002$ from β decay measurements [48], and M_A is the axial mass. The value of M_A has recently been subject of discussion in the neutrino cross section community due to discrepancies found between the value extracted from bubble chamber measurements of H₂ and D₂ targets, and heavier nuclear targets [107]. It is widely believed that nuclear effects beyond the impulse approximation approach are responsible. In particular, the effects arising from nucleon-nucleon correlations and two-body exchange currents are considered necessary for an accurate description of QE scattering.

The Nieves [108] and Martini [109] models include possible W boson self-energy diagrams in nuclear matter and consider diagrams where the interaction is with more than one nucleon, but produces a CCQE-like cross section. The first order (tree level) diagram corresponding to “true CCQE” interactions is alternatively called *one-particle one hole* (1p-1h), while higher order diagrams are referred to as *two-particle two-hole* (2p-2h). These models are alternatively referred to as meson-exchange currents (MEC).

Additionally, the Random Phase Approximation (RPA) is a nuclear screening effect that modifies the propagator for interactions in nuclear matter [108], and needs to be included in the Martini and Nieves model calculations to obtain good agreement with data. RPA calculations consider effective interaction terms between particle hole excitations within the nucleus which change the electroweak coupling in nuclear matter due to strongly interacting nucleons [110]. While the RPA screening has a small effect on the overall cross section as a function of neutrino energy, it is found to have a significant effect on the differential cross section as a function of Q^2 (see Figure 9.7).

- **Resonance Production**

In resonance production, inelastic neutrino interactions with the nucleon as a whole produce a baryon resonance, which then decays to produce mesons and hadrons. Figure 4.4b shows the Feynman diagram for charged and neutral current resonance production interactions, and assuming the Δ resonance decays to a pion. Analogous to the CCQE interactions, it is possible to reconstruct the energy of the neutrino from the kinematics of the lepton and assuming the mass of the Δ resonance.

$$E_{rec} = \frac{2m_p E_\mu + m_\Delta^2 - m_p^2 - m_l^2}{2(m_p - E_\mu + p_\mu \cos \theta_\mu)} \quad (4.8)$$

The Rein-Sehgal model considers 18 resonances with invariant mass $W \leq 2$ GeV, including interference terms, and also considers multi-pion production [111]. A free parameter M_A^{RES} , analogous to M_A in CCQE, appears for the axial-vector form factor.

The RES interaction channel gives rise to the important CC1 π mode ($\nu_l + N \rightarrow l + N' + \pi$) shown in Figure 1.2b. If the pion is not detected due to detector efficiencies (for example if the pion is emitted beyond Cherenkov threshold), or because of final state interactions (discussed in Section 4.2.3), the event will mimic the CCQE interaction and the reconstruction of the neutrino energy will be biased.

In addition to resonance production, neutrinos can also scatter off the entire nucleus transferring negligible energy to the target via a process called *coherent scattering*. A distinctly forward-scattered pion, compared to their resonance mediated counterparts, is produced. Both NC and CC coherent pion production processes are possible. The predicted and measured cross section for this process is comparatively low (10^{-42} for CC-Coherent vs. 10^{-38} for CCQE).

- **Deep Inelastic Scattering**

In deep inelastic scattering, the energetic neutrino scatters off a constituent quark via the exchange of a W or Z boson producing a lepton and a hadronic jet. As shown in Figure 4.3a, there exists a wealth of data at the high energies where DIS is dominant. In spite of that, the modelling of these events is difficult for neutrino experiments, particularly at the transition between RES and DIS, where the limits of the theoretical descriptions for both process lay and overlaps are a concern.

4.2.3 Final State Interactions Model

After the particles are produced by neutrino interactions, they must leave the nuclear medium before they can be detected. The probability of interacting with the nuclear medium or with other particles produced is nonzero. These *final state interactions* are sizable, not well known, and significantly complicate the description of neutrino-nucleus interactions. Any attempts to relate the final states observed in the detector to the underlying cross section physics is necessarily model dependent. For this reason, FSI are possibly the most challenging aspect of neutrino interaction modelling.

For example, a pion produced in a CC1 π interaction can scatter, be absorbed, or charge exchange along its nuclear journey. This process can be described using *cascade models*, in which each particle is stepped through the nucleus in discrete steps. A detailed description of the cascade model used for T2K is provided in Section 4.3. Brief descriptions of the models on the market that are used to simulate pion-nucleus scattering can be found in Appendix E, along

with comparisons among these models. These models are tested and tuned using hadron-nucleus scattering measurements. Part II of this thesis describes this effort in detail.

4.3 NEUT Pion Cascade Model

The interactions of pions produced from neutrino events are simulated in NEUT using a semi-classical intra-nuclear cascade model [112]. Following its creation from a neutrino interaction, the starting position of the pion is chosen randomly from a nuclear density profile in the form of a three-parameter Fermi model (Woods-Saxon potential) described in Eqn. 4.9 and shown in Figure 4.5a:

$$\frac{\rho(r)}{\rho_0} = \frac{1 + w \frac{r^2}{c^2}}{1 + \exp\left(\frac{r-c}{\alpha}\right)} \quad (4.9)$$

where r is the distance from the centre of the nucleus, c is the nuclear radius, α is the surface thickness, and w is the “wine-bottle” parameter. These parameters were determined from an analysis of electron scattering measurements [113]. This is the only way in which an A-dependence is introduced in the cascade model. In the case of oxygen, the two-parameter Fermi model is used ($w = 0$). The initial kinematic information of the pion is taken directly from the neutrino interaction model.

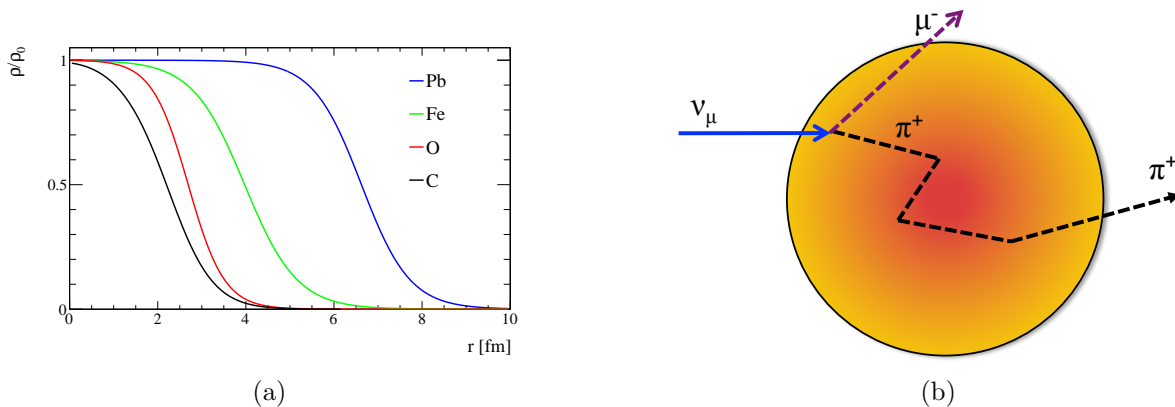


Figure 4.5: (a) Normalized nuclear density distributions. Reproduced from [114]. (b) Graphical representation of the Intra-Nuclear cascade mechanism

The pion is then propagated “classically” in finite steps within the nuclear medium. The steps are only in space and were chosen as $dx = R_N/100$, where R_N is the size of the nucleus and is defined as 2.5 times the nuclear radius from [113]. The probabilities for various interactions are calculated at each step and a Monte-Carlo random number generator is used to determine which, if any, interaction takes place. The cascade continues until the pion is absorbed or its position exceeds R_N . The product of the interaction probabilities at each step is defined as the escape probability. Figure 4.5b shows a pictorial description of this mechanism.

For low momentum pions ($p_\pi < 500$ MeV/c), tables computed from the Oset *et al.* model [115] are used to determine quasi-elastic, single charge exchange and absorption interaction probabilities. This model involves a computational many-body calculation in infinite nuclear matter, with a local density approximation added. The π nucleus scattering is represented as a wave in a complex optical potential. The individual channel contributions are obtained from separating the real and complex parts of the potential and calculating the corresponding Feynman diagrams. Figure 4.6a shows the interaction probabilities calculated for a carbon target from the Oset *et al.* model. For high momentum pions ($p_\pi > 500$ MeV/c) the interaction probabilities are calculated from π^\pm scattering off free proton and deuteron cross section data compiled by the PDG [116]. Figure 4.6b shows the world data for π^+ on free proton scattering used in the model. To avoid discontinuities, the two models are blended in the 400 MeV/c $< p_\pi < 500$ MeV/c region.

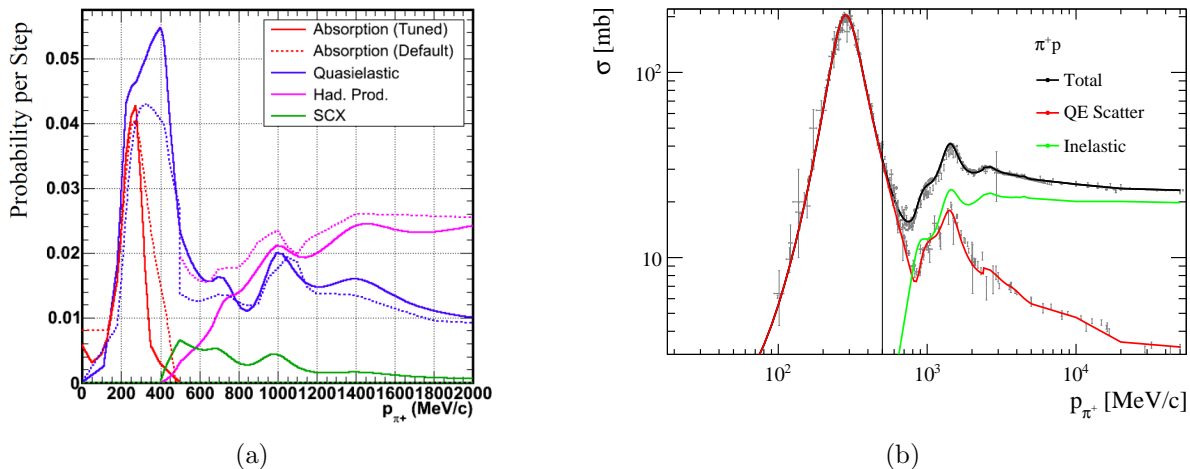


Figure 4.6: (a) The probabilities per step at the centre of a carbon nucleus for QE scattering and absorption at low energy ($p_\pi < 500$ MeV/c) calculated from the Oset *et al.* model (dashed line). The tuned model (solid lines) corresponds to a previous tuning of the model not described in this thesis. At high energy ($p_\pi > 500$ MeV/c) the QE scattering, hadron production, and single charge exchange (SCX) are calculated from π^\pm scattering off free nucleons and deuteron targets. (b) World data for π^+ on free proton scattering cross sections. The data (grey points) was obtained from [116], while the SAID fit (solid lines) was obtained from [117]. Figures reproduced from [114].

Other generators and simulation toolkits such as GENIE, NUWRO, FLUKA, and GEANT4 have similar models implemented. The exception is GiBUU, where the Boltzmann-Uehling-Uhlenbeck transport equation is solved for a more complete description of the nuclear medium [118].

4.3.1 FSI Scaling Parameters

The model is parameterized by the scaling factors summarized in Table 4.1, henceforth referred to simply as “FSI parameters” or f_{FSI} . Each parameter scales the corresponding microscopic probability of π interaction at each step, except for FEFCX, which scales the charge exchange fraction of low momentum QE scattering.

A reweighting scheme [114] allows the propagation of variations of these parameters to ND280 and SK predictions. It essentially uses the information of the cascade that is stored for each event and re-runs the cascade algorithm with varied parameters to obtain a new value for the escape probability. The FSI weight is then defined as the ratio between the varied and nominal escape probabilities.

f_{FSI} parameter	Description	Momentum Region (MeV/c)
FEFABS	Absorption	< 500
FEFQE	Quasi-elastic scatter	< 500
FEFCX	Single charge exchange	< 500
FEFQEH	Quasi-elastic scatter	> 400
FEFCXH	Single charge exchange	> 400
FEFINEL	Hadron (N+n π) production	> 400

Table 4.1: Description of the NEUT FSI probability scaling parameters (f_{FSI}) used to propagate in the pion scattering fit. The overlap in the momentum regions is due to blending of the high and low energy models in NEUT [114].

4.4 Detector Simulations

4.4.1 ND280 Simulation

Neutrino interactions in ND280 are simulated using NEUT, as was described in Section 4.2. The particles in the final state are propagated through the detectors using a detailed simulation based in the GEANT4 simulation toolkit [119]. The hadronic interactions are currently simulated by the Bertini cascade model [120], rather than the NEUT cascade model. However, the `NeutG4CascadeInterface` package [121, 122] that allows the usage of the NEUT cascade model within GEANT4 has been developed and will be used in upcoming ND280 MC productions.

The `elecSim` package simulates the response of the detectors, including the light production in the scintillator bars and the response of the MPPCs. The calibration of data is handled by the `oaCalib` package. Custom reconstruction routines are built for each detector (`tpcRecon`, `fgdRecon`), and a global reconstruction merges their output by combining individual reconstructed tracks [60].

4.4.2 SK Simulation

Neutrino interactions in SK are also simulated using NEUT, as described in Section 4.2. The detector simulation at SK is carried out by the SKDETSIM package, which is based in GEANT3. The GCALOR package [87] is used to simulate hadronic interactions, except for pions below 500 MeV/c which are simulated by an implementation of the NEUT cascade model described in Section 4.3 [112]. The propagation of Cerenkov photons in water is simulated including the effects of scattering and absorption. The charge and timing response of the PMTs are based

on calibration data [123]. The overall detector response such as energy scale is tuned to control samples built from cosmic ray muons and atmospheric neutrinos.

4.4.2.1 fitQun Event Reconstruction

A new event reconstruction algorithm, fitQun, has been developed for SK [124]. fitQun is able to reconstruct the detailed kinematics of the neutrino interaction from the charge and timing information of each PMT. It uses a maximum-likelihood approach that takes advantage of the known Cherenkov emission profiles and the detector response to evaluate the likelihood of a given reconstruction hypothesis. This approach provides a unifying framework for all aspects of the event reconstruction, including kinematics, ring counting, and particle identification.

The event selection (described in Section 9.1.2) has been considerably improved by the reduction of charged and neutral pion backgrounds, the improvement in the separation of electrons and muons, and an increase precision in the reconstructing the neutrino energy.

PART II:
PION INTERACTIONS ON NUCLEI

The work described in Chapters 5 and 6 has been published in [1, 2].

Chapter 5

Dual Use Experiment at TRIUMF (DUET)

5.1 Introduction

The scattering of pions off of atomic nuclei has been the subject of extensive study due to its ability to serve as a probe of nuclear structure through the understanding of the interactions among mesons and nucleons. The $\Delta(1232)$ pion-nucleon resonance dominates in the sub-GeV energy region, and thus the range of the momentum of the pion (p_π) between 200 to 300 MeV/ c is of special interest.

As explained in Section 4.2.3, the understanding of pion inelastic interactions is deeply connected to that of neutrino interactions through the modelling of final state interactions (FSI) and secondary interactions (SI). FSI and SI are leading contributors to systematic uncertainties in neutrino oscillation and cross section experiments. Their impact is typically evaluated using predictions based on models implemented in Monte Carlo neutrino event generators such as NEUT [90], NUWRO [125], and GENIE [126] for FSI, or detector simulation toolkits such as GEANT4 [120] and FLUKA [84, 85] for SI. Other important scenarios in which pion-nucleus interactions are relevant for neutrino physics are: i) the enhancement of the neutral-current π^0 background in neutrino oscillation appearance experiments, and, ii) pion reconstruction capabilities in water Cherenkov detectors via the explicit identification of their hadronic interactions.

The dominant pion interactions on carbon (π^\pm -C) in the sub-GeV region are represented diagrammatically in Fig. 5.1. Comprehensive reviews of data and theory including π^\pm -C interactions for total, elastic and quasi-elastic, absorption (ABS), single charge exchange (CX), double charge exchange, and the sum of two processes (ABS + CX) can be found in [127, 128]. The total, elastic and quasi-elastic processes have been measured with $< 10\%$ precision by various experiments [129, 130, 131, 132, 133, 134, 135, 136, 137], while the individual absorption (ABS) and single charge exchange (CX) processes have been measured with less ($> 10\%$) precision [137, 138, 139, 140, 141, 142]. Subsequent measurements of ABS were performed with the goal of understanding multi-nucleon correlations and thus concentrated on

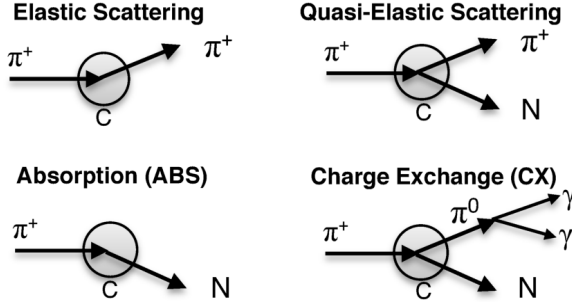


Figure 5.1: Dominant π^\pm -C interactions in the sub-GeV region. “N” represents any number of nucleons leaving the nucleus.

final states with multiple protons [143, 137, 144]. There exist combined measurements of (ABS+CX) [136, 135, 145, 146, 147], but these relied on other experimental results or on theoretical calculations of the CX component to separate the ABS contribution, and possible correlations and systematic uncertainties were not accounted. The importance of correlations when performing global fits of a large number of datasets has been well documented in the literature [148, 149, 99].

The Dual-Use Experiment at TRIUMF (DUET) is intended to improve the precision of pion absorption and charge exchange interactions on carbon for pions in the 200 to 300 MeV/ c range. A compact scintillator tracker PIA ν O (Pion detector for Analysis of ν Oscillations) was placed in the path of a mono-energetic pion beam provided by the M11 beam line at TRIUMF. It served as the target and provided information for tracking and the energy loss per unit length (dE/dx) of charged particles. An additional downstream detector was used for tagging of reaction products. I was the corresponding author for the two published articles presenting the results of this effort. In the first one [1], a measurement of the combined ABS and CX cross section $\sigma_{\text{ABS+CX}}$ was presented. In the second one [2], separate measurements of σ_{CX} and σ_{ABS} were presented. I was the first author and sole analyzer.

5.2 Experimental Setup

5.2.1 M11 Beam Line

The experiment took place at the M11 secondary beam line at TRIUMF. A 500 MeV proton beam extracted from the TRIUMF main cyclotron was directed onto a 1 cm carbon target, producing pions, muons and electrons. The secondary beam was focused by six quadrupole magnets and its momentum was controlled by two dipole magnets. Six momentum settings were used for this experiment: 201.6, 216.6, 237.2, 265.5, and 295.1 MeV/ c . Figure 5.2 shows a schematic overview of the experimental apparatus.

The pions were selected using time-of-flight (TOF) measurements and a Cherenkov detector. The TOF was measured between the current transformer (CT) located near the production target

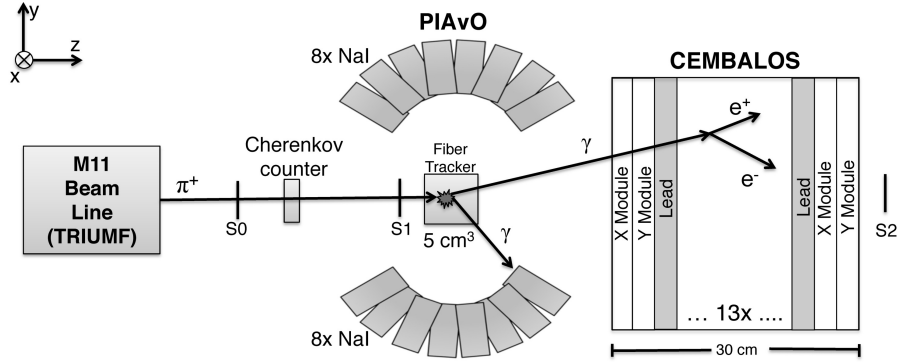


Figure 5.2: Schematic overview of the experimental apparatus.

and a scintillation counter (S1) placed ~ 15 m downstream from the CT. The Cherenkov counter was placed ~ 11 cm downstream of the scintillator counter (S0) and consisted of a $3.5 \times 3.5 \times 20$ cm³ bar of Bicorn UV-transparent acrylic plastic read out at each end by photo multiplier tubes. The refractive index of the bar was 1.49, so muons with momentum larger than ~ 250 MeV/ c produced Cherenkov light at an angle that was largely transmitted. Figure 5.3 shows an example of a Cherenkov light vs. TOF distribution for $p_\pi = 237.2$ MeV/ c . The electron, muon, and pion signals are clustered around the upper-left, middle, and bottom-right of the plot, respectively. The purity of pions is estimated to be larger than 99% for all momentum settings used.

The S0 and S1 scintillation counters were used in coincidence to select low-angle charged particles entering the PIA ν O detector.

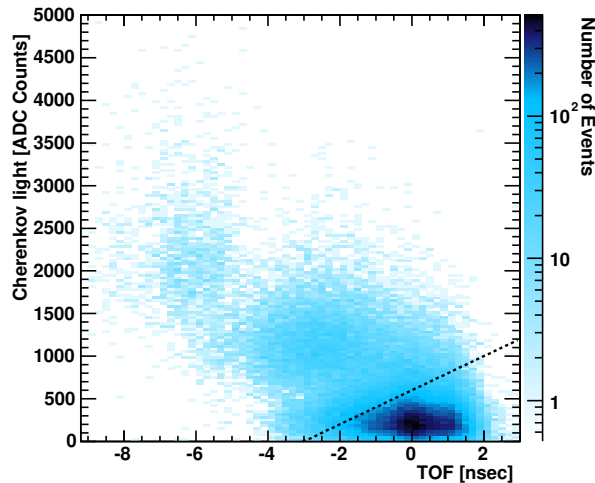


Figure 5.3: Cherenkov light (ADC Counts) vs. TOF (ns) for $p_\pi = 237.2$ MeV/ c . The broken line corresponds to the threshold to distinguish pions from muons and electrons.

5.2.2 The PIA ν O Detector

The PIA ν O fibre tracker consists of 1.5 mm scintillation fibres and is read out by multi-anode photo multiplier tubes (Hamamatsu H8804 MAPMTs). Figure 5.4 shows a picture of the setup and a diagram of the front view of the fibres. There were 16 horizontal and 16 vertical layers crossing each other perpendicularly, each with 32 fibres. The dimension of the region where the fibres cross each other is $\sim 5 \times 5 \times 5 \text{ cm}^3$.

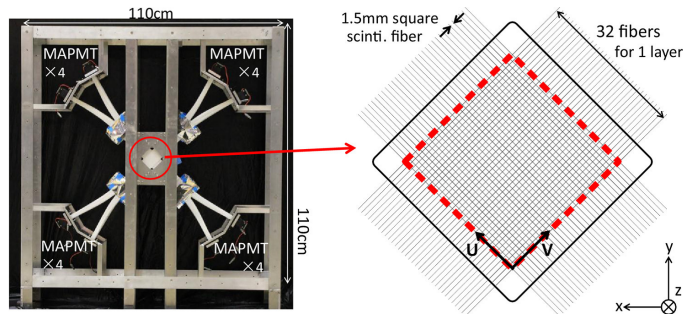


Figure 5.4: Front view of the PIA ν O fibre tracker detector.

The scintillation fibres (Kuraray SCSF-78SJ) were coated with a reflective coating (EJ-51) which contains TiO_2 to increase the light yield and to optically separate the fibres from each other. One end of the fibre is mirrored by vacuum deposition to further increase the light yield by 70%. The measured light yield is ~ 11 photoelectrons (p.e.) per fibre for a minimum ionizing particle. The number of nuclei in the fiducial volume of the fibre tracker is estimated from the material and dimensions of the fibre and are shown in Table 5.1.

Nuclei	Number of nuclei [$\times 10^{24}$]
C	1.518 ± 0.007
H	1.594 ± 0.008
O	0.066 ± 0.004
Ti	0.006 ± 0.0002

Table 5.1: The number of nuclei in the fiducial volume of the fibre tracker.

5.2.2.1 Detector Simulation

The fibre core, cladding, and coating structure are included in a GEANT4 version 9.4 patch 04 [119] simulation of the detector. Details such as the misalignment of the fibre layers, the thickness of the coating, and crosstalk hits are implemented in the simulation. The energy deposit for each fibre in the simulation is converted to p.e. by the following procedure:

- (1) *Conversion of energy deposit to photons (p.e.):* The expected number of photons (N_{ex}) is obtained by multiplying the value of the energy deposit (E_{dep}) by a conversion factor C_{conv}

of 57 p.e./MeV determined from the light yield observed in through-going data is applied.

$$N_{\text{ex}} = C_{\text{conv}} E_{\text{dep}} \quad (5.1)$$

The saturation of scintillation light is also taken into account using Birk's formula.

- (2) *Photon statistics and MAPMT gain:* The number of observed photoelectrons is obtained from a Poisson and Gaussian smearing of N_{ex} representing the photon statistics and the statistical fluctuation in the multiplication of electrons in the PMT:

$$N_{\text{p.e.}} = \text{Poisson}(N_{\text{ex}}) \quad (5.2)$$

$$N_{\text{obs}} = N_{\text{p.e.}} + \sqrt{N_{\text{p.e.}}} C_{\text{gain}} \text{Gauss}(1) \quad (5.3)$$

The second term in Equation 5.3 corresponds to the statistical fluctuation in the multiplication of electrons in the PMT. Gauss(1) is a random value which follows a Gaussian distribution with mean = 0 and sigma = 1. C_{gain} is defined for each channel from the charge distribution of 1 p.e. light measured in an LED test bench.

- (3) *Electronics:* The number of photoelectrons is converted to ADC counts (ADC_{raw}) by multiplying another conversion factor (C_{conv2}) with N_{obs} . C_{conv2} is measured from the 1 p.e. distribution obtained by LED light, and it is typically ~ 60 ADC counts/p.e. The non-linearity of electronics is simulated with an empirical function:

$$ADC_{\text{obs}} = ADC_{\text{raw}} / (1 + C_{\text{nonlin}} ADC_{\text{raw}}) \quad (5.4)$$

where C_{nonlin} is 0.000135/ADC counts and is obtained from the charge distributions of through-going pions. In case the ADC count is greater than 4095, it is set to 4095 to account for saturation in the electronics.

5.2.2.2 Event Reconstruction

The measured ADC count is converted to the number of photoelectrons, followed by an electronics nonlinearity correction. Only hits above 2.5 p.e. are used in the track reconstruction routine. The tracks are reconstructed in horizontal (U) and vertical (V) layers individually before being combined to make three-dimensional (3D) tracks according to the following procedure:

- (1) *Incident track candidates* are identified by searching for hits on nearly-horizontal (0 ± 4 degrees) trajectories. At least three hits are required to define a track. A maximum of 20 p.e. is allowed so that hits from a secondary proton track are not included. In the event of multiple incident track candidates, the longest track is selected
- (2) *The vertex* is initially defined from the end position of the incident track. A search is then conducted around this vertex in ± 3 layers and ± 1 fibre region, where the best vertex

position is defined as the position where the largest number of hits can be traced to. The tracks traced from the best vertex position to the subsequent layers are selected as final-state tracks.

- (3) *3D tracks* are obtained by combining two-dimensional (2D) tracks if the track ends in the U and V projections agree within ± 2 layers.

The position resolution of the interaction vertex is estimated to be ~ 1 mm in U and V, and ~ 2 mm in Z. The angular resolution is estimated to be ~ 3 degrees. For each track, the deposited charge per track length, dQ/dx is obtained by dividing the total charge deposit by the total length of the track. dQ/dx is used for identifying particles in the event selection.

As an illustration of the reconstruction, an ABS candidate event in the data is shown in Figure 5.5 in the UZ projection, where Z is the direction of the beam. The upstream horizontal (cyan) track is identified as a pion (“pion-like” track). The two final state particles (green and pink) are identified as protons (“proton-like”) produced by a nuclei interacting with the incident pion.

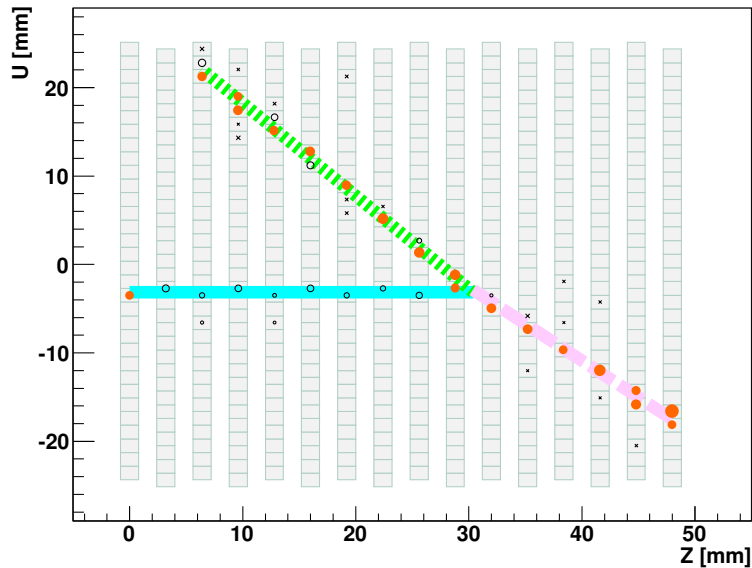


Figure 5.5: Example of ABS candidate event in data ($p_\pi = 237.2 \text{ MeV}/c$). The filled circles (red) correspond to the large hits (> 20 p.e.), the crosses correspond to the hits identified as crosstalk hits and the thick lines (cyan, green and pink) correspond to reconstructed tracks.

5.2.3 The CEMBALOS Detector

The CEMBALOS detector was a scaled down (1/6) version of the Fine-Grained Detectors (FGDs) [75] of T2K. It was located 25 cm downstream of PIA ν O. The active portion of the detector was composed of scintillator bars made of polystyrene co-extruded with a 0.25 mm thick reflective coating of polystyrene mixed with TiO_2 . The light yield from the far end of a bar

was measured to be up to 18 photoelectrons (p.e.) for a minimum ionizing particle. The optical crosstalk through the TiO_2 coating between bars was measured to be $0.5 \pm 0.02\%$.

The scintillator bars were arranged into 15 XY modules oriented perpendicular to the beam. Each XY module contained 32 bars in the x direction glued to 32 bars in the y direction. Layers of 0.25 mm thick fibreglass (G10) were glued to both the upstream and downstream surfaces to provide support, and no adhesive was applied between the bars. Each module had dimensions of $32 \times 32 \times 2.02 \text{ cm}^3$. Unlike the FGDs, 0.8~1 mm thick lead layers were interspersed in between each module to enhance photon conversion. Figure 5.6 shows a picture of CEMBALOS.



Figure 5.6: Photo of CEMBALOS. The beam points to the right. Detailed description in the text.

The scintillation light from each bar was collected by a $1 \pm 0.02 \text{ mm}$ diameter wavelength shifting (WLS) double-clad Kuraray Y11 (200) S-35 J-type fibre inserted through an axial hole. The absorption and subsequent emission wavelengths for these fibres were 430 nm and 476 nm, respectively. Unlike the FGDs, due to limited availability only fibres in the last 3 XY modules had one of their ends mirrored to enhance light collection by aluminizing.

Multi-Pixel Photon Counters (MPPCs) manufactured by Hamamatsu Photonics (S10362-13-050C) were used as photo sensors to measure the scintillation light. These provided excellent photon counting capability with higher quantum efficiency than photo multipliers for the spectra of light produced by the WLS fibres. The outer dimensions of the MPPC were $5 \times 6 \text{ mm}^2$, while the sensitive area containing 667 avalanche photo-diode pixels was $1.3 \times 1.3 \text{ mm}^2$. The small size allowed for using one MPPC per bar, eliminating the possibility of crosstalk at the sensor. A custom connector was developed to achieve good optical coupling. The XY modules were held rigidly in place inside an aluminum light-tight box. The readout electronics were mounted on the outer sides of the box to separate elements generating heat and to prevent temperature induced effects on the MPPCs.

5.2.3.1 Detector simulation and calibration

The simulation of the CEMBALOS detector was based on that developed for the FGDs used by T2K. It made use of the GEANT4 version 9.4 patch 04 [119] simulation toolkit. Details of the geometry of the detector were simulated, including, but not limited to, the fibre structure (core, double cladding and coating), the G10 layers and the glue used to hold them to the fibres, and the measured thickness of the interspersed lead layers.

The energy deposit from charged particles traversing the scintillating bars was calculated from the pulse height (PH) of the digitized MPPC waveforms by the following procedure:

- (1) *Conversion from PH to photoelectrons ($p.e.$):* The PH measured in ADC units was translated into the number of photoelectrons N_{pe} by normalizing to the average pulse height $\langle PH \rangle$ corresponding to a single-pixel avalanche.

$$N_{pe} = PH / \langle PH \rangle \quad (5.5)$$

The distribution of dark noise pulse heights was used to measure $\langle PH \rangle$ and it was found to be 48.65 ADC units.

- (2) *Corrections for variations in overvoltage:* Temperature variations can change the overvoltage, the difference between the operating and breakdown voltages in the MPPCs, affecting the photon detection efficiency and the crosstalk and after-pulsing probabilities. Empirical corrections were applied to compensate for these effects.
- (3) *Correction for saturation of the MPPCs:* Since each MPPC has a finite number of pixels, the pulse height can get saturated. A correction based on an empirical exponential expression was applied.
- (4) *Correction for bar-to-bar variations:* The differences in light yield from each CEMBALOS scintillator bar due to minor variations in the fibre-MPPC coupling, scintillation material, fibre mirroring, etc. were accounted for in a manner similar to [75] by an additional correction factor (C_{bar}).
- (5) *Correction for light loss along the bar:* The light attenuation in each fibre was measured for both mirrored and unmirrored bars using cosmic rays. Figure 5.7a shows the resulting fitted distributions for the measured yield (N_{DPE}) of detectable photoelectrons as a function of the distance of the hit to the MPPC. The fit function is an empirical descriptor of the attenuation process.
- (6) The final conversion from number of scintillation photons to energy deposition measured in p.e. involved an empirical normalization constant and Birk's formula was used to account for the nonlinearity in the scintillator response. We adopted $0.0208 \pm 0.0003(\text{stat}) \pm 0.0023(\text{sys})$ cm/MeV for the value of Birk's constant as measured by the K2K SciBar group [150]. A minimum of 5 p.e. was required to label an energy deposit as a hit.

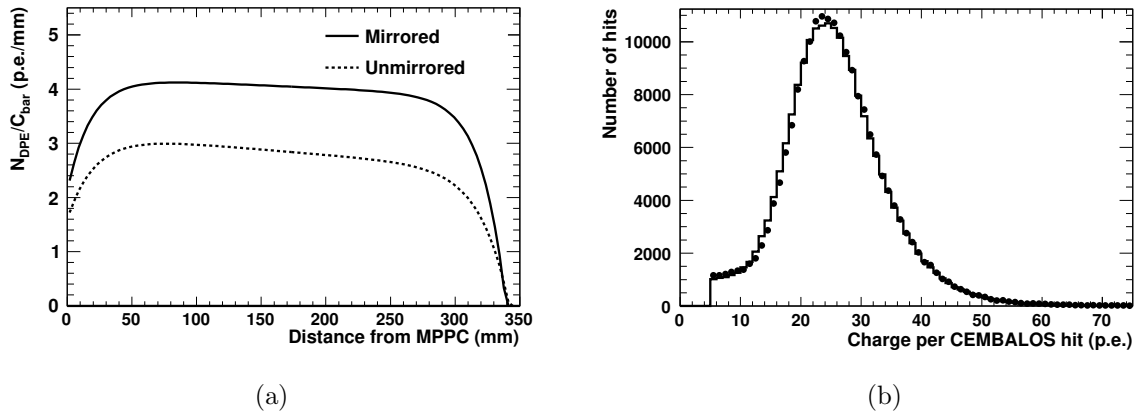


Figure 5.7: (a) Light attenuation curves in CEMBALOS for mirrored (solid) and unmirrored (dashed) fibres. (b) Charge per CEMBALOS hit distribution (in photoelectrons) of through-going muons in the $p_\pi=237.2$ MeV/ c setting for data (circles) and MC (solid line), after the calibration procedure was applied. The statistical error bars are too small to be visible.

A control sample of beam muons in the $p_\pi=237.2$ MeV/ c setting traversing CEMBALOS was used to calibrate the charge simulation. Figure 5.7b shows the deposited charge distribution of through-going muons for data and MC after the calibration procedure.

5.3 Data Taking Summary

The project started in May 2010. Data taking took place in TRIUMF during October and December of 2010, August and September of 2011, and August and September of 2012. Data were recorded on an additional water target to measure the cross section on Oxygen, but this data has not been analyzed. Calibration data were recorded during all run periods.

Data were recorded from a π^+ beam on the PIA ν O scintillator (carbon) target for five incident momenta (201.6, 216.6, 237.2, 265.5, 295.1 MeV/ c). There were ~ 1.5 million beam triggered events recorded for each momentum setting, except for the 216.6 MeV/ c setting where only 30% was recorded due to limited beam time.

5.4 Physics Modelling

The hadronic interactions of the pions with a nuclei are simulated in GEANT4 using the list of physics models called “QGSP-BERT”. For the elastic scattering, it uses a model called “hElasticLHEP” based on a simple parameterization of the cross section. The inelastic scattering (INEL), ABS and CX are included in the inelastic process, which are simulated using the Bertini Cascade model [120]. There are also other processes, namely double charge exchange and hadron production, but the cross sections for those interactions are negligibly small in the

pion momentum range in this experiment.

5.4.1 Elastic Scattering

Figure 5.8a and 5.8b show the comparison of the cross sections between the previous experiments and the default GEANT4 MC data, for elastic and inelastic processes. There are disagreements between GEANT4 cross section (ver9.4, QGSP-BERT) and the measurements from the previous experiments, especially for π -H elastic scattering process. The π^+ -C and π^+ -H elastic cross sections and differential cross sections ($d\sigma/d\theta$) were tuned by interpolating the data points from previous measurements. The inclusive π^+ -C inelastic scattering, ABS and CX cross sections were also tuned.

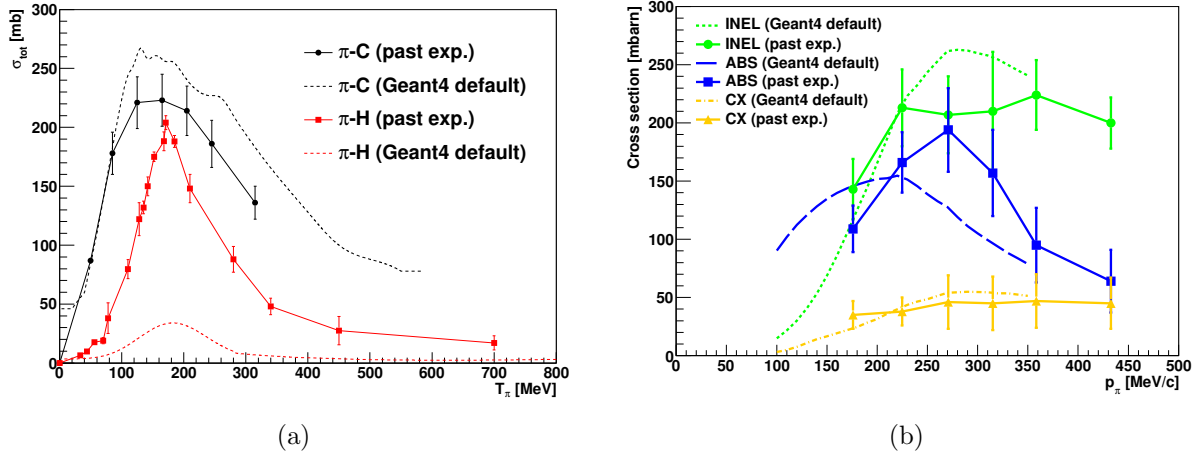


Figure 5.8: (a) Comparison of elastic inclusive cross section between the previous experiments (summarized in Table IV of [1]) and the default GEANT4. (b) Comparison of inelastic inclusive cross sections between the previous experiment [135] and the default GEANT4.

5.4.2 Charge Exchange

The kinematics of the outgoing π^0 from CX interactions in the momentum region of interest have large variance for different models. This can be seen in Figure 5.9 where predictions from the NEUT (v5.3.5) cascade model [90], the GEANT4 (v9.04.04) Bertini cascade model [120], and the FLUKA cascade model [84, 85] are confronted with the differential cross section measurement from Ashery *et al.* [138] of 265 MeV/c π^+ on oxygen in the angular phase space of DUET (as discussed in Section 6.2.1). The discrepancy among models is largest in the forward ($< 40^\circ$) region, where CEMBALOS is most sensitive. The GEANT4 Bertini Cascade model used by our simulation shows the largest disagreement with data [138].

The modelling of the multiplicity and kinematics for nucleons ejected following an ABS or CX interaction show even larger discrepancies among models. The mechanisms for these processes are further complicated by the possibility of FSI of the nucleons before they exit the nucleus.

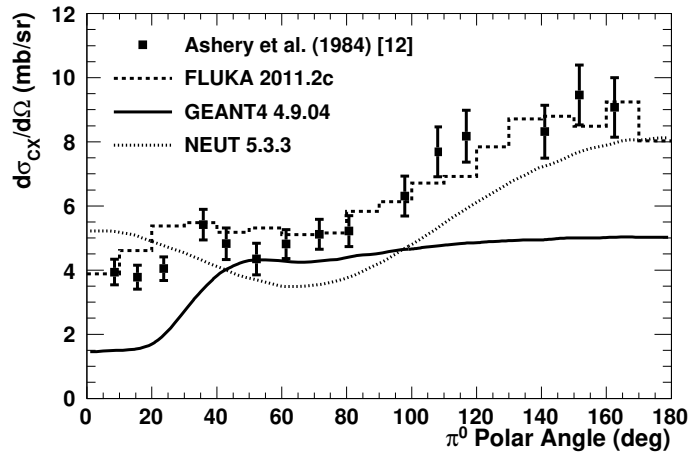


Figure 5.9: $d\sigma_{CX}/d\Omega$ as a function of the outgoing π^0 polar angle (with respect to the beam direction) for 265 MeV/c π^+ interacting on ^{16}O , for FLUKA (dashed line), GEANT4 (solid line) and NEUT (dotted line), along with data from [138].

NEUT uses nucleon multiplicities published by [151] of σ_{ABS} on N and Ar targets, but it is unclear what other models use.

Chapter 6

Measurement of σ_{ABS} and σ_{CX} of π^+ on Carbon

The measurement of σ_{ABS} and σ_{CX} of π^+ on Carbon using the PIA ν O and CEMBALOS detectors is presented in this chapter. These results were published in [2].

6.1 Event Selection

The event selection of ABS and CX events is performed in two steps. The PIA ν O detector is used to identify events with no π^+ in the final state which are consistent with ABS+CX final states. This selection is then extended by using the downstream detector CEMBALOS to tag the forward-going photons from the decay of a π^0 produced in a CX interaction.

6.1.1 PIA ν O Event Selection

The main goal is to separate elastic and quasi-elastic scattering events with charged pions in the final state, from ABS+CX events where no charged pions are found the final state. The ABS+CX event selection criteria is described as follows:

- (1) *Good incident π^+* : This criteria is threefold. First, the incident particle is required to be a charged pion. A cut is applied in the Cherenkov light vs. TOF space as described in Section 5.2.1.

Second, a straight track is obtained by requiring hits in the same fibre position (i.e., same U and V position) for the first, third, and fifth layers. The background muons originating from pion decay in the beam pipe are rejected by this cut because in most cases the angle of these muons are shifted with respect to the beam axis.

Third, the incident track is required to enter the fiducial volume (FV). The FV is shown as the broken lines in Figure 6.1a and 6.1b. Figure 6.1b shows the X, Y position distribution of the incident beam. The hexagonal shape corresponds to the region where the S1 trigger

overlaps with the fibre crossing region. Because the reconstruction algorithm requires at least 3 hits to reconstruct a track, the fiducial volume is defined to be ≥ 3 fibres (3 layers) from the upstream edge of the fibre crossing region. The X, Y position of the incident track is required to be inside the $X - Y$ plane of the FV.

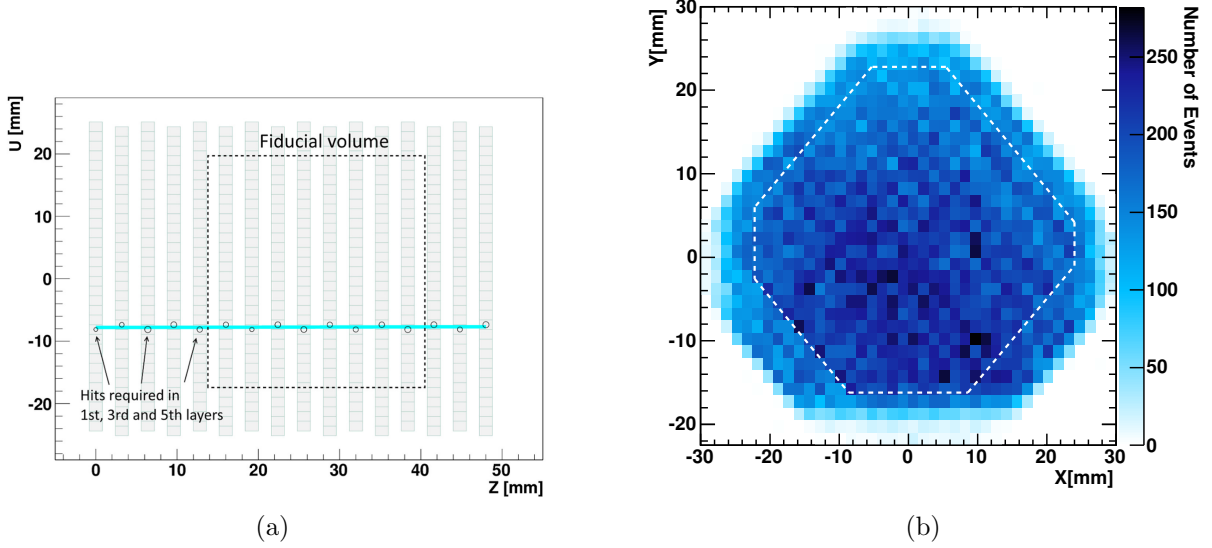


Figure 6.1: (a) Illustration of the *Good incident π^+* cut requirement. A straight through-going pion track (cyan) crosses the PIA ν O detector. The broken line represents the boundary of the fiducial volume. (b) The $X - Y$ view of the incident beam position distribution. The white broken line represents the boundary of the fiducial volume.

- (2) *Vertex in the FV*: At this stage in the selection, $\sim 90\%$ of the events are through-going pion events as the one shown in Figure 6.1a. The events with pion interactions are selected by requiring a reconstructed vertex inside the FV. Additional cuts in the events in the vicinity of the vertex are applied to reject small angle scattering events.
- (3) *No π^+ in the final state*: The pion tracks are distinguished from proton tracks by applying an angle-dependent dQ/dx cut. Figure 6.2 shows an example of dQ/dx distributions for $p_\pi = 237.2$ MeV/c for data and MC for six different angular regions ($0^\circ < \theta < 30^\circ$, $30^\circ < \theta < 60^\circ$, ..., $150^\circ < \theta < 180^\circ$), where θ is the angle of the reconstructed track with respect to the beam direction. The histograms for MC are normalized by the number of incident pions. The colour of the histograms represents the interaction types. The vertical broken line represents the threshold to distinguish pions and protons. If any of the reconstructed tracks except the incident track is found to have dQ/dx below the threshold, then that track is identified as a charged pion, and the event is not selected.

The number of selected events after each stage of the PIA ν O selection is summarized in Table 6.1. There are ~ 7000 events in data after the event selection, except for the 216.6 MeV/c data

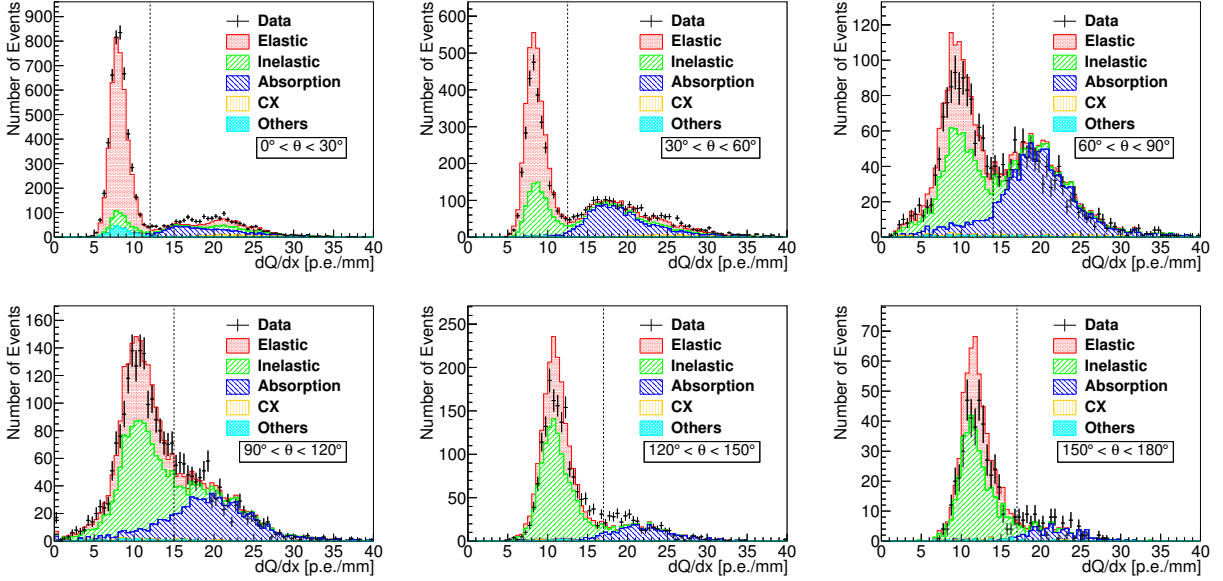


Figure 6.2: dQ/dx distribution in six different angular regions for $p_\pi = 237.2$ MeV/c for data and MC. The dotted vertical lines represent the threshold to distinguish pions (left of the line) and protons. For multiple track events, only the smallest value of dQ/dx among the tracks is filled in the histogram. The “Others” category is mainly filled with events with pions decaying in flight and Coulomb scattering events.

set in which the number of incident pions is smaller due to the limited data taking time. The efficiency to select ABS+CX events which occurs inside the fiducial volume is estimated to be $\sim 79\%$, and the purity of ABS + CX events in the selected sample is estimated to be $\sim 73\%$.

Cut	201.6 MeV/c		216.6 MeV/c		237.2 MeV/c		265.5 MeV/c		295.1 MeV/c	
	Data	MC	Data	MC	Data	MC	Data	MC	Data	MC
<i>Good incident π^+</i>	273625		67164		276671		238534		282611	
<i>Vertex in FV</i>	17522	18895.9	4833	5118.8	21861	22932.1	20567	20895.1	24327	24136.7
<i>No final π^+</i>	6797	6331.2	1814	1695.9	7671	7619.0	6772	7005.1	7289	7491.1
Efficiency [%]	79.0		79.6		79.9		79.2		77.1	
Purity [%]	73.0		73.3		73.1		73.5		73.1	

Table 6.1: The number of events after each stage of the cut. The numbers for MC are normalized by the numbers of good incident pion events in data.

The selection described in this section was used to extract $\sigma_{\text{ABS+CX}}$ and the results were published in [1].

6.1.2 CEMBALOS Event Selection

A simulated CX event is shown in Figure 6.3a. The upstream horizontal (red) track represents a π^+ interacting in the PIA ν O detector. As it undergoes a CX interaction, two protons (black) and a π^0 are produced. The π^0 subsequently decays into two photons (blue). The forward-going

photon travels to CEMBALOS where it converts into e^+e^- pairs and deposits charge in the scintillating material.

DUET Reconstruction - XZ projection

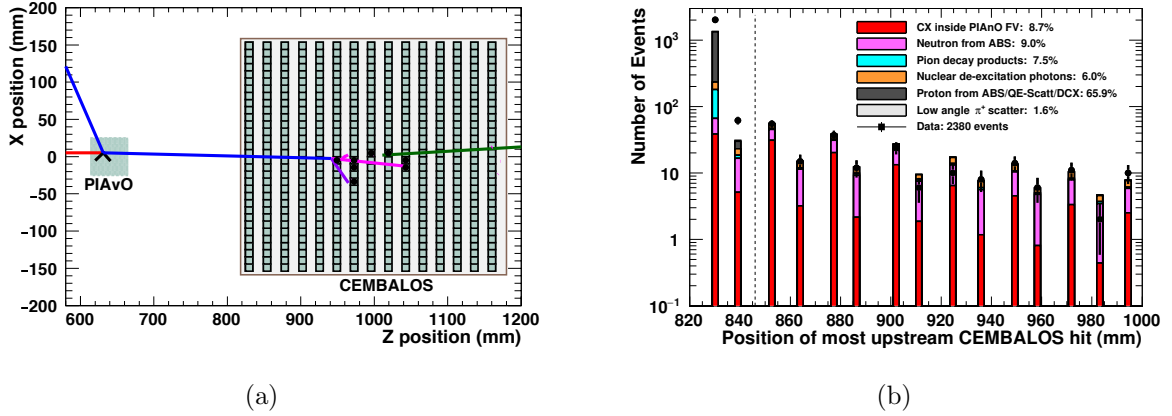


Figure 6.3: (a) Example of a simulated CX event in the DUET detector setup. A $237.2 \text{ MeV}/c \pi^+$ (red) undergoes CX in $\text{PIA}\nu\text{O}$ producing two protons (black) and a π^0 that decay into two photons (blue). The forward-going photon is identified in CEMBALOS as it produces e^+e^- pairs (purple, magenta) and hits are recorded in the scintillating material. (b) Distribution of the most upstream position of CEMBALOS hits for Data and MC (broken down into topologies and listed with their corresponding percentage composition) in the $p_\pi = 237.2 \text{ MeV}/c$ setting after applying the $\text{PIA}\nu\text{O}$ upstream selection. Each bar represents an XY module. Topologies contributing less than 1% are not plotted.

Charge deposition information from CEMBALOS was used to identify CX interactions occurring in $\text{PIA}\nu\text{O}$. The main goal was to tag one of the photons from the decay of a π^0 by identifying the corresponding electromagnetic shower in CEMBALOS. The limited angular coverage ($\sim 0.53sr$) of CEMBALOS imposed the largest efficiency loss. The selection criteria were as follows:

(1) **Veto cut**

Charged particles in CEMBALOS left a signal in the scintillator material. Figure 6.3b shows the distribution of the position of the most upstream hit in CEMBALOS for each event. Each bar represents a scintillation plane. A veto cut on the first XY modules was applied to remove most of the charged particle backgrounds, such as low-angle π^+ scatters and protons from ABS events.

(2) **Hit Charge vs. Multiplicity**

The remaining backgrounds after the veto cut are produced by neutrons from ABS events and nuclear de-excitation γ -rays. Figure 6.4a shows the distribution of the number of hits (multiplicity) in CEMBALOS. A minimum of five hits was required to reduce background from these sources. Figure 6.4b shows the CEMBALOS hit charge vs. multiplicity distribution after applying the veto cut. A diagonal cut in this plane was applied to further

reduce the remaining background of neutrons from ABS.

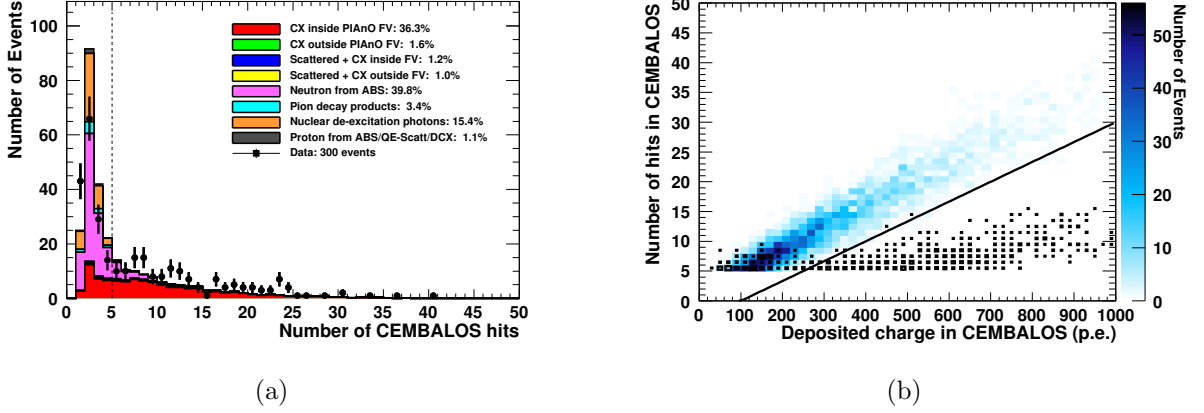


Figure 6.4: (a) Distribution of the number of hits in CEMBALOS for Data and MC (broken down into topologies and listed with their corresponding percentage composition) in the $p_\pi = 237.2$ MeV/c setting after applying the veto cut. Topologies contributing less than 1% are not plotted. (b) Distribution of the number of hits in CEMBALOS vs. charge deposited for MC in the $p_\pi = 237.2$ MeV/c setting after applying the requirement of a minimum of 5 hits. The blue entries are true CX events, whereas the black boxes correspond to neutron background events.

6.1.3 Selection Purities and Efficiencies

The numbers of selected events for each momentum setting after the PIA ν O and CEMBALOS selections were applied are summarized in Table 6.2 for data (N_{Data}) and GEANT4 MC (split into signal $N_{\text{CX}}^{\text{G4}}$ and background $N_{\text{BG}}^{\text{G4}}$). There are ~ 100 events in data after the event selection, except for the 216.6 MeV/c setting. The efficiencies and purities to select CX events which occurred inside the FV were around $\sim 6\%$ and $\sim 90\%$ respectively. The efficiencies to select events which occurred inside the FV and had at least one of the CX photons in the direction of CEMBALOS were estimated to be $\sim 30\%$.

p_π [MeV/c]	N_{Data}	$N_{\text{CX}}^{\text{G4}}$	$N_{\text{BG}}^{\text{G4}}$	Efficiency [%]	Purity [%]
201.6	104	60.4	8.6	5.1	87.5
216.6	20	15.8	2.4	5.3	86.6
237.2	141	75.9	11.1	5.9	87.2
265.6	152	87.1	10.4	7.0	89.3
295.1	163	119.4	12.8	8.1	90.3

Table 6.2: Summary of number of events selected after the CEMBALOS downstream selection in Data and MC for each momentum setting, along with estimated efficiencies and purities for GEANT4

6.2 σ_{ABS} and σ_{CX} Extraction

As was mentioned in Section 5.4, our simulation is based on the GEANT4 package which uses the Bertini cascade model for modelling pion inelastic interactions but also handles other complex aspects of the analysis such as the geometrical description of the detectors. In order to estimate the number of signal ($N_{\text{CX}}^{\text{MC}}$) and background ($N_{\text{BG}}^{\text{MC}}$) events predicted by the different models shown in Section 5.4.2 without having to rewrite the simulation using each toolkit, a scheme was developed to replace the detector simulation with a set of 2D selection, rejection, and mis-reconstruction efficiencies in momentum and angle bins of the outgoing particles and is presented in Section 6.2.1. These were then applied to the predictions from NEUT and FLUKA obtained using ~ 1 mm thick target simulations and a nominal model was selected in Sec 6.2.2.

The measured σ_{CX} was obtained for each model from $N_{\text{CX}}^{\text{MC}}$, $N_{\text{BG}}^{\text{MC}}$, and the corresponding predicted CX cross section $\sigma_{\text{CX}}^{\text{MC}}$ following Eq. (6.1). Corrections for the fraction of muons in the beam (f_{μ}) and the fraction of interactions on the TiO_2 coating of the $\text{PIA}\nu\text{O}$ fibres ($R_{\text{TiO}_2}^{\text{Data}}$ and $R_{\text{TiO}_2}^{\text{MC}}$) were also applied as in [1].

$$\begin{aligned} \sigma_{\text{CX}} &= \sigma_{\text{CX}}^{\text{MC}} \times \frac{N_{\text{Data}} - N_{\text{BG}}^{\text{MC}}}{N_{\text{CX}}^{\text{MC}}} \\ &\times \frac{1 - R_{\text{TiO}_2}^{\text{Data}}}{1 - R_{\text{TiO}_2}^{\text{MC}}} \times \frac{1}{1 - f_{\mu}}, \end{aligned} \quad (6.1)$$

σ_{ABS} was obtained by subtracting σ_{CX} from the measured valued of $\sigma_{\text{ABS}+\text{CX}}$ obtained in [1].

6.2.1 Selection, Rejection and Mis-reconstruction Efficiencies

- (1) **π^0 selection efficiency:** the probability of a true CX event passing the selection criteria as a function of the outgoing π^0 momentum and angle is defined as the ratio of the distributions before and after the selection is applied. This selection efficiency is shown in Figure 6.5a for the $p_{\pi} = 201.6$ MeV/ c setting as an example.
- (2) **Proton/neutron veto rejection:** the probability that an ejected proton or neutron will produce hits in the first two XY modules of CEMBALOS. Figure 6.5b shows the rejection efficiency for protons in the 201.6 MeV/ c setting. The CEMBALOS forward acceptance ($< 45^\circ$) can be clearly seen.
- (3) **Proton mis-reconstruction:** the probability of a proton being mis-reconstructed as a “pion-like” track in $\text{PIA}\nu\text{O}$ thus causing the event to be rejected.
- (4) **π^+ mis-reconstruction and veto:** the probability of an outgoing π^+ following a quasi-elastic scatter to be mis-reconstructed in $\text{PIA}\nu\text{O}$ as a “proton-like” track and then producing hits in the first two XY modules of CEMBALOS.

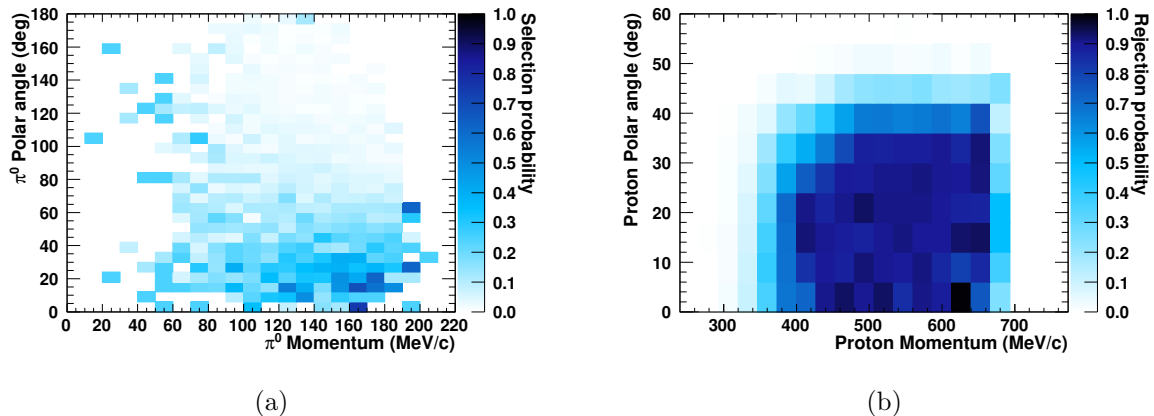


Figure 6.5: (a) Selection efficiency of true CX events as a function of the outgoing π^0 momentum and angle, for the $p_\pi = 201.6$ MeV/ c setting. (b) Rejection probability of events where an ejected proton from ABS or quasi-elastic scattering fails the veto rejection criteria, as a function of its outgoing momentum and angle, for the $p_\pi = 201.6$ MeV/ c setting.

- (5) **Neutron selection efficiency:** the probability of a neutron from an ABS event passing the selection criteria.

In this scheme a true CX event would be categorized as a signal event if: the π^0 is selected, the ejected proton(s) is not mis-reconstructed as a “pion-like” track in PIA ν O, and the ejected nucleons do not trigger the veto rejection. On the other hand, an ABS or quasi-elastic scattering event would be categorized as a background event if: a neutron is selected, any outgoing π^+ is mis-reconstructed as “proton-like”, ejected protons are not mis-reconstructed in PIA ν O as “pion-like”, and the ejected nucleons do not trigger the CEMBALOS veto rejection.

6.2.2 Selection of Nominal Model

The results of applying this scheme to predictions from various models are summarized in Table 6.3 for each momentum setting. In addition to NEUT and FLUKA, the scheme was applied to the GEANT4 model prediction calculated from a thin target simulation (independent of the DUET simulation) as a means of validation of the procedure. The predictions of $N_{\text{CX}}^{\text{MC}}$ for GEANT4 agree with $N_{\text{CX}}^{\text{G4}}$ from Table 6.2 within $\sim 3\%$, while $N_{\text{BG}}^{\text{MC}}$ were underestimated as not all sources of background were included in the scheme. These are discussed in Sec. 6.3.4.2.

The differences in the extracted cross section among models range from 21.9% at $p_\pi = 201.6$ MeV/ c to 5.7% at $p_\pi = 295.1$ MeV/ c , with FLUKA and GEANT4 being the extreme case scenarios. This is consistent with the model comparison from Figure 5.9. Considering the good agreement between FLUKA and the external data in Figure 5.9, the results from applying the efficiency scheme to FLUKA, with the $N_{\text{BG}}^{\text{MC}}$ prediction scaled up to increase the additional backgrounds not included in the scheme, were chosen as our nominal result.

p_π [MeV/c]	Model	σ_{CX}^{MC} [mb]	N_{CX}^{MC}	N_{BG}^{MC}	σ_{CX} [mb]
201.6	GEANT4	36.7	63.3	6.1	58.0
	FLUKA	55.5	122.2	6.3	45.3
	NEUT	50.5	83.0	4.5	61.8
216.6	GEANT4	37.5	16.5	2.0	41.6
	FLUKA	59.5	32.5	1.5	34.4
	NEUT	55.7	24.2	1.5	43.5
237.2	GEANT4	39.6	80.0	9.7	65.4
	FLUKA	61.7	149.4	5.8	56.1
	NEUT	57.5	111.7	6.1	69.8
265.5	GEANT4	44.7	88.8	9.6	71.4
	FLUKA	62.4	143.5	5.0	63.7
	NEUT	57.9	129.4	6.9	64.8
295.1	GEANT4	45.1	122.5	12.7	55.1
	FLUKA	58.5	176.2	5.6	52.0
	NEUT	58.3	170.3	8.4	52.7

Table 6.3: Predicted N_{CX}^{MC} , N_{BG}^{MC} and extracted CX cross section σ_{CX} obtained from applying the efficiency scheme to GEANT4, FLUKA, and NEUT model predictions. See text for discussion.

6.3 Systematic Uncertainties

Multiple sources of systematic errors were investigated. Estimation procedures for beam and PIA ν O detector systematics are unchanged from [1] and are briefly outlined in Sec. 6.3.1 and 6.3.2. CEMBALOS detector systematics are summarized in Sec. 6.3.3. Uncertainties related to the physics modelling are discussed in Sec. 6.3.4. Table 6.4 shows a summary of all the systematic uncertainties estimated for this analysis.

6.3.1 Beam Systematics

The pion beam profile and momentum were measured using PIA ν O through-going pion data. The uncertainties were less than ~ 1 mm and ~ 1 MeV/c, respectively. The systematic error was evaluated by changing the momentum, the centre position, and the beam spread in the MC within their uncertainty and re-calculating the cross sections.

6.3.2 PIA ν O Detector Systematics

Various sources of systematic uncertainty were estimated for PIA ν O following the procedures described in [1]. These account for uncertainties on the scintillator fibre composition, the size of the fiducial volume, the alignment of the fibres, and the simulation of the charge deposition, hit detection efficiency, and crosstalk. For this analysis the same procedures were used.

	CX					ABS				
π^+ Momentum [MeV/c]	201.6	216.6	237.2	265.5	295.1	201.6	216.6	237.2	265.5	295.1
Beam systematics										
Beam profile	3.5	4.9	6.2	4.2	2.0	2.2	2.7	3.8	2.9	2.5
Beam momentum	4.1	1.6	3.5	4.1	2.8	1.5	2.3	1.9	2.5	3.0
Muon Contamination	0.5	0.8	0.9	0.3	0.2	0.5	0.8	0.9	0.3	0.2
PIAνO systematics										
Fiducial volume	3.6	2.3	4.3	3.9	4.5	1.1	5.4	4.1	3.8	3.4
Charge distribution	3.3	4.1	3.3	2.4	3.0	4.3	3.2	4.1	4.1	4.4
Crosstalk probability	3.9	4.9	4.4	2.5	2.2	1.9	2.0	2.7	1.7	1.3
Layer alignment	1.3	3.6	2.9	0.9	1.1	1.0	2.3	2.8	1.7	2.4
Hit inefficiency	1.0	2.1	2.1	2.5	2.6	1.1	1.3	1.5	2.0	1.0
Target material	2.0	2.0	2.9	2.9	2.9	1.2	1.2	1.2	1.2	1.3
CEMBALOS systematics										
Charge calibration	1.7	1.6	3.7	3.1	6.7	1.3	1.1	2.0	1.7	2.5
Hit inefficiency	1.6	2.1	1.1	1.3	2.0	1.2	1.1	1.1	1.0	0.9
Position and alignment	7.7	7.9	8.3	5.7	4.6	0.7	1.0	0.7	0.7	1.0
Physics modelling systematics										
π^0 kinematics	6.1	6.9	7.9	9.4	10.6	2.1	1.6	3.2	4.3	4.1
Nuclear de-excitation γ background	0.9	0.8	0.7	0.6	0.6	0.4	0.2	0.7	0.3	0.2
Multiple interactions	1.1	1.9	1.7	1.5	1.8	0.5	0.5	0.8	0.7	0.7
Pion decay background	1.9	2.8	1.2	0.6	0.9	0.8	0.7	0.5	0.3	0.3
Statistical error	11.0	26.0	9.4	8.9	8.8	3.9	6.2	3.9	4.2	3.6
Total error	17.9	30.3	19.4	17.0	18.0	7.8	10.5	10.4	9.7	9.6

Table 6.4: Summary of the statistical and systematic uncertainties in percent.

6.3.3 CEMBALOS Detector Systematics

6.3.3.1 Position and Alignment

The overall uncertainty in the position of CEMBALOS relative to PIA ν O, and of the position of the scintillator and lead modules relative to the dark box as well as each other is estimated to be ± 5 mm. This corresponds to a change of $\sim 3.4\%$ in the subtended solid angle. The effect on the calculated cross section is estimated by shifting the position of CEMBALOS in the simulation ± 5 mm in the x , y , and z directions. The relatively large size of this systematic uncertainty (4.5 \sim 8.3%) is due to the sensitivity of this measurement to the π^0 kinematics and will be discussed in further detail in Sec. 6.3.4.

6.3.3.2 Charge Simulation

The calibration procedure presented in Sec. 5.2.3.1 and Figure 5.7b shows that for single hits from minimum ionizing particles (< 50 p.e.) the charge simulation agrees with data at the $\sim 5\%$ level. However, as can be seen from Figure 6.4b, for most of the background events the charge deposited per hit is above this region. A control sample of protons stopping within the first two XY modules of CEMBALOS was used to estimate the accuracy of the charge simulation for higher energy depositions. It was obtained by using dQ/dx information from PIA ν O to select “proton-like” tracks and requiring all CEMBALOS hits to be in the first two XY modules. Figure 6.6a shows the charge deposition distribution in the first layer of CEMBALOS for this sample in data and MC.

Based on the the distributions in Figure 6.6a, a random Gaussian smearing with a 20% width

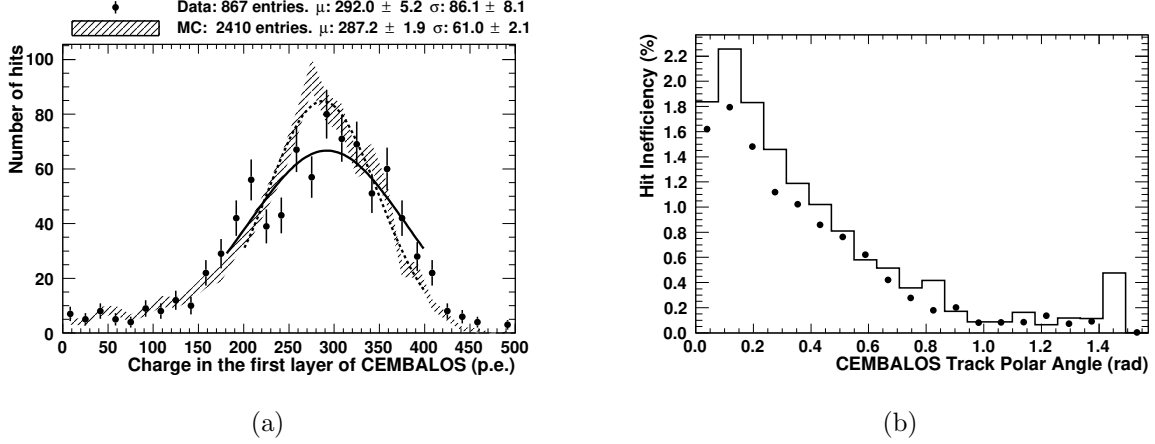


Figure 6.6: (a) Charge distribution in the first layer of CEMBALOS for stopping protons in the 237.2 MeV/c setting for data (circles) and MC (filled histogram). Only statistical uncertainties are plotted. The solid and dashed lines are Gaussian fits to data and MC respectively. (b) CEMBALOS hit inefficiency for data (circles) and MC (solid line) in the $p_\pi = 237.2$ MeV/c setting. The statistical error bars are too small to appear.

was applied to the charge deposited by each hit in every event for 1000 toy MC experiments to determine what fraction of the time signal events were mis-reconstructed as background and vice versa. The cross section was calculated for each toy experiment and the spread was taken as the uncertainty.

6.3.3.3 Hit Inefficiency

The hit reconstruction inefficiency in CEMBALOS was measured by counting how often a hit was missing in a reconstructed track. The tracks were required to have at least two hits in both the first and last two layers. Figure 6.6b shows the hit inefficiency, defined as the ratio of missing hits over the total number of hits expected, for data and MC in the 237.2 MeV/c setting as a function of the CEMBALOS reconstructed polar angle. The hit inefficiency integrated over all angles is 1.16% and 1.33% for data and MC, respectively.

The effect on the measured cross section is estimated by randomly deleting CEMBALOS hits in 1000 MC toy experiments with a probability given by the difference of the integrated hit inefficiencies for data and MC, affecting both the hit multiplicity and total charge deposited.

6.3.4 Physics Modelling Systematics

6.3.4.1 Uncertainty from π^0 kinematics

True CX events were reweighted following the discrepancy between [138] and the FLUKA model prediction as a function of the π^0 angle. The weights ranged from 0.7 to 1.3, while the average weight applied was 0.9. The effect on σ_{CX} ranged from 6.1% to 10.6%, representing the

largest systematic uncertainty for this analysis.

6.3.4.2 Other Backgrounds

The uncertainties from additional contributions to the number of predicted background events were estimated in three different categories, as described in the following text.

Nuclear de-excitation γ -rays: inelastic interactions can leave the nucleus in an excited state. Low-energy (< 25 MeV/ c) γ -rays can be emitted as the nucleus returns to its ground state. If these photons interact in CEMBALOS they can fake a signal event. While these nuclear processes are believed to be well modelled by our simulation, we assign a conservative 100% error on the number of background events from this process.

Multiple interactions: it is possible for the initial π^+ to be scattered (both elastically or quasi-elastically) before it undergoes a CX interaction. The CX interaction can take place inside the PIA ν O FV ($\sim 58\%$), outside the FV but still in a scintillator fibre ($\sim 37\%$), or somewhere in the aluminum support structure and/or dark boxes of PIA ν O or CEMBALOS ($\sim 5\%$). The uncertainty of the number of events of this type of background event is estimated from the uncertainty on elastic and CX interactions on carbon and aluminum from previous experiments.

π^+ decay products: a π^+ that scatters in PIA ν O and produces a fake “proton-like” track can then stop and decay around or inside CEMBALOS, possibly circumventing the veto rejection. The decay products can then deposit enough energy in CEMBALOS to produce a fake signal event. A conservative 100% uncertainty is assigned to these events, which amount to $\sim 1\%$ of the selected events.

6.4 Results

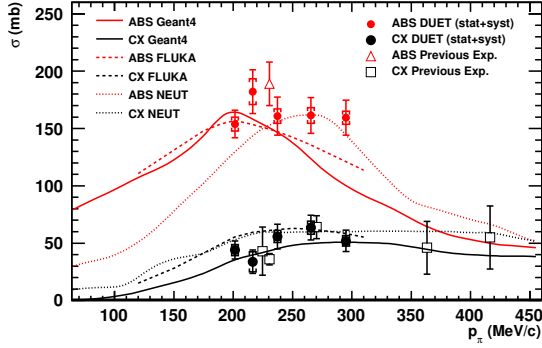
The measured σ_{ABS} and σ_{CX} are presented in Table 6.5 and shown in Fig. 6.7a with statistical and systematic error as a function of pion momentum, compared with the results from previous experiments [141, 138, 142, 137] where the absorption and charge exchange cross sections were explicitly measured. Our results are in agreement with previous experiments, but we have extended the momentum region over which the data is presented. As summarized in Table 6.4, the total error is $\sim 9.5\%$ for σ_{ABS} and $\sim 18\%$ for σ_{CX} , except for the $p_\pi = 216.6$ MeV/ c data set.

6.4.1 Fractional Covariance and Correlation Coefficients

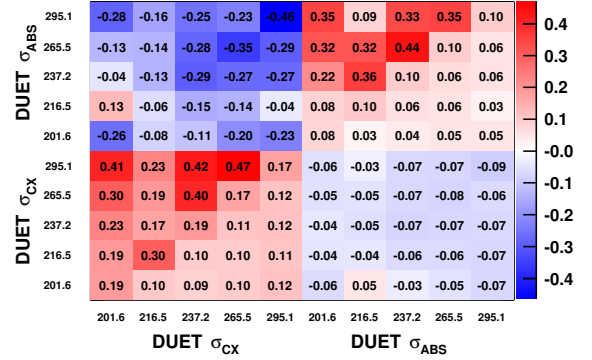
We provide the fractional covariance and correlation coefficients for the 5 σ_{ABS} and 5 σ_{CX} measured data points in the matrix in Fig. 6.7b. The quantities that fall on the diagonal of the matrix and anything below show the fractional covariance ($\text{Sign}(V_{ij}) * \sqrt{V_{ij}}$), where $V_{ij} = (\Delta\sigma_i\Delta\sigma_j)/(\sigma_i\sigma_j)$, and σ_k and $\Delta\sigma_k$ are the nominal cross sections and their systematic

p_π [MeV/c]	σ_{ABS} [mb]	σ_{CX} [mb]
201.6	153.8 ± 12.0	44.0 ± 7.9
216.6	182.1 ± 19.2	33.8 ± 10.2
237.2	160.8 ± 16.6	55.8 ± 10.8
265.6	161.4 ± 15.7	63.5 ± 10.8
295.1	159.4 ± 15.3	52.0 ± 9.3

Table 6.5: σ_{ABS} and σ_{CX} measured by DUET.



(a)



(b)

Figure 6.7: (a) DUET measurements of σ_{ABS} and σ_{CX} compared with previous measurements [141, 138, 142, 137] and ABS (red) and CX (black) model predictions from GEANT4 (solid line), FLUKA (dashed line) and NEUT (dotted line). (b) Fractional covariance and correlation for the DUET measurements of σ_{ABS} and σ_{CX} . The quantities that fall on the diagonal and anything below show the fractional covariance coefficients, while the quantities above the diagonal show the correlation coefficients.

shift, respectively. The quantities above the diagonal of the matrix show the correlation coefficients, where the correlation matrix is calculated as $(\text{diag}(V))^{-1/2}V(\text{diag}(V))^{-1/2}$. The statistical uncertainties were included as an uncorrelated diagonal matrix. There are positive correlations within the σ_{ABS} and σ_{CX} measurements, and negative correlations across them, as is expected from the subtraction method used. This is the first time that a correlation matrix is published for a pion inelastic cross section measurement.

Chapter 7

Improvements to the π^\pm -A Modelling Uncertainties

This chapter describes the tuning of the NEUT cascade model described in Section 4.3 to π^\pm -A scattering external data. It has been adapted from [152]. Section 7.1 provides a summary of all the external scattering data sets that were used for this tuning. Section 7.2 describes the fit strategy followed for this tuning. Section 7.3 presents the best fit values for the FSI parameters as well as their correlation matrix.

7.1 Summary of Scattering External Data

7.1.1 Motivation for Using Data on Light and Heavy Nuclear Targets

As was described in Chapter 3, the Fine-Grained-Detector serves as the main tracker for the near detector suite (ND280) of T2K, and uses scintillator material (C_8H_8) as the target for neutrino interactions. In Super-Kamiokande, the target material is water (H_2O). In principle, the goal is to develop and understand a nuclear FSI model that applies to light nuclei such as carbon and oxygen.

However, in the near detector there are also heavier materials where neutrino interactions and final state interactions occur. For example, the P0D and ECAL detectors have lead tracker planes. These heavier targets are now being used for neutrino cross section measurements, and there are plans to include neutrino interaction samples from these detectors to the ND fits used to constrain uncertainties for the Oscillation Analyses. It is then important to develop a model that is also valid for these heavier nuclei, and to determine uncertainties that span external data on these nuclei.

The strategy for this tuning was to include external data on light nuclei: **carbon** (${}^{12}_6\text{C}$), **oxygen** (${}^{16}_8\text{O}$), and **aluminum** (${}^{27}_{13}\text{Al}$), as well as heavier nuclei: **iron** (${}^{56}_{26}\text{Fe}$), **copper** (${}^{63}_{29}\text{Cu}$), and **lead** (${}^{207}_{82}\text{Pb}$).

7.1.2 Interaction Channels

Data from both positive and negative polarity beams (π^+ and π^-) were used, over a momentum range from 60 to 2000 MeV/ c . The interaction channels are defined exclusively from the number of pions in the final state, with any number of nucleons. This allows direct comparisons of the external measurements of cross sections and NEUT predicted cross sections. The following interaction channels were used for this tuning:

- **Absorption (ABS):** No pions in the final state
- **Quasi-elastic Scattering (QE):** Only one pion in the final state of the same charge as the incident beam. Also referred to as *Inelastic* scattering on some occasions.
- **Single Charge Exchange (CX):** Only one π^0 in the final state
- **Absorption + Single Charge Exchange (ABS+CX):** Sum of ABS and CX.
- **Reactive (REAC):** Sum of ABS, CX, QE, Double Charge Exchange, and Hadron Production. Double Charge Exchange is defined as final states with one pion in the final state having opposite charge as the incident beam. Hadron production is defined as final states with more than one pion in the final state.

Elastic and Total (Reactive + Elastic) cross sections are not used for this tuning since NEUT does not simulate elastic scatterings.

7.1.3 Full List of Data Sets

Table 7.1 lists the external data sets used, specifying the channels and range measured by each experiment, and providing a reference to the corresponding publication. This selection of external data is based on the collection presented in [114]. The DUET measurement of ABS and CX [2] described in Chapter 6 is the most significant addition relative to that list. Other data sets added are [132, 139].

Some measurements of ABS [137, 143, 144] were not used since those were performed with the goal of understanding multi-nucleon correlations and thus concentrated on final states with multiple protons. Other measurements such as [155, 156] were of the total (elastic + reactive) cross section. They also reported values for the reactive cross sections, but these were not *true* measurements as theoretical models were used to separate the reactive and the elastic components.

7.2 Fit Strategy

7.2.1 Goal

The goal of the fit is two-fold:

Reference	Polarity	Targets	p_π [MeV/c]	Channel(s)
B. W. Allardyce <i>et al.</i> [129]	π^\pm	C, Al, Pb	710-2000	REAC
A. Saunders <i>et al.</i> [136]	π^\pm	C, Al	116-149	REAC
C. J. Gelderloos <i>et al.</i> [131]	π^-	C, Al, Cu, Pb	531-615	REAC
F. Binon <i>et al.</i> [130]	π^-	C	219-395	REAC
O. Meirav <i>et al.</i> [132]	π^+	C, O	128-169	REAC
C. H. Q. Ingram [153]	π^+	O	211-353	QE
S. M. Levenson <i>et al.</i> [134]	π^+	C	194-416	QE
M. K. Jones <i>et al.</i> [137]	π^+	C, Pb	363-624	QE, CX
D. Ashery <i>et al.</i> [135]	π^\pm	C, Al, Fe	175-432	QE, ABS+CX
H. Hilscher <i>et al.</i> [139]	π^-	C	156	CX
T. J. Bowles [140]	π^\pm	O	128-194	CX
D. Ashery <i>et al.</i> [138]	π^\pm	C, O, Pb	265	CX
K. Nakai <i>et al.</i> [154]	π^\pm	Al, Cu	83-395	ABS
E. Bellotti <i>et al.</i> [141]	π^+	C	230	ABS
E. Bellotti <i>et al.</i> [142]	π^+	C	230	ABS
I. Navon <i>et al.</i> [146]	π^+	C, Fe	128	ABS+CX
R. H. Miller <i>et al.</i> [145]	π^-	C, Pb	254	ABS+CX
E. S. Pinzon Guerra <i>et al.</i> [2]	π^+	C	206-295	ABS, CX

Table 7.1: Summary of π^\pm -Nucleus scattering data used for this tuning, including beam polarity, nuclear target type(s), momentum range and interaction channel(s). Note that some of this experiments might have measured data on other target nuclei.

- (1) Find the set of f_{FSI} parameters (described in Table 4.1) that provides the best fit to the external scattering data listed in Section 7.1.
- (2) Set uncertainties for f_{FSI} parameters that span the errors from the external data, and extract their correlation information directly from the fit.

7.2.2 Parameter Estimation

The NEUT cascade and its reweighting routine are very CPU-intensive and make an iterative fit in the style of the NIWG CCQE fits [99] difficult. In lieu of this, predictions for the π^\pm -A cross sections, $\sigma_j^{\text{NEUT}}(f_{FSI})$, were pre-computed for a finite grid of FSI parameters. The minimum and maximum values allowed for the FSI parameters and the step sizes are summarized in Table 7.2. To reduce the computational load, the predictions were calculated only for values of p_π for which data was available. The predictions were calculated from a simulation of a mono-energetic pion beam incident at the boundary of a target nucleus of radius R_N , and that is propagated through the nucleus by the cascade model as described in Section 4.3. The cross section is calculated as

$$\sigma_j^{\text{NEUT}} = \pi R_N^2 \frac{N_j}{N_T} \quad (7.1)$$

where N_j is the numbers of events selected in a given interaction channel j , and N_T is the number of incident pions. This task was carried out using ~ 15 core-years on the SciNet GPC cluster.

Parameter	Grid min	Grid max	Step size
FEFQE	0.1	1.7	0.1
FEFABS	0.35	1.95	0.1
FEFCX	0.1	1.6	0.1
FEFINEL	0.2	2.6	0.2
FEFQEH	0.8	2.8	0.2
FEFCXH	1.8	1.8	0.2

Table 7.2: Minimum and maximum values for the NEUT FSI parameters allowed in the finite grid of precomputed NEUT predictions.

The best fit is found by minimizing the χ^2 defined in Equation 7.2. The summation in the first term runs over all the data sets listed in Table 7.1, except for the DUET measurements. Each channel measured by each data set is treated as an uncorrelated point in the fit. The second term runs over the 5 σ_{ABS} and 5 σ_{CX} cross section measurements from DUET and takes advantage of the correlation information available.

$$\chi^2(f_{FSI}) = \sum_i^{\text{Datasets}} \left(\sum_j^{n_i} \frac{1}{n_i} \left(\frac{\sigma_j^{\text{Data}} - \lambda_i^{-1} \sigma_j^{\text{NEUT}}(f_{FSI})}{\Delta\sigma_j^{\text{Data}}} \right)^2 + \left(\frac{\lambda_i - 1}{\epsilon} \right)^2 \right) + \sum_{i,j}^{10} (\sigma_i^{\text{DUET}} - \sigma_i^{\text{NEUT}}(f_{FSI})) (V_{ij}^{-1})^{\text{DUET}} (\sigma_j^{\text{DUET}} - \sigma_j^{\text{NEUT}}(f_{FSI})) \quad (7.2)$$

In Equation 7.2, n_i represents the number of data points on each data set, σ_j^{Data} and $\Delta\sigma_j^{\text{Data}}$ are the external data set cross sections and their respective uncertainties, σ_i^{DUET} are the cross sections measured by DUET, and $(V_{ij})^{\text{DUET}}$ is the DUET covariance matrix shown in Figure 6.7b. The normalization parameters λ_i scale the model prediction, and are additionally included as penalty terms for each data set. The uncertainty for the normalization parameters (ϵ) was assigned to be 40% following the representative correlations in the DUET data sets as seen in Figure 6.7b, and was an ad-hoc simple choice made for this analysis.

The minimization was performed using the MIGRAD algorithm of the MINUIT package [157]. The main advantage of using this algorithm is that in addition to the best fit parameters, the correlation information is also obtained. The difficulty is that the algorithm requires a χ^2 surface with smooth first and second order derivatives. The interpolation methods used to smooth out the finite precomputed grid are summarized in Section 7.2.3.

The FSIFitter package [158] was developed for this analysis and is described in [152]. Appendix C shows a series of validation studies carried out before obtaining the fit results presented in Section 7.3.

7.2.3 Interpolation Routines

Two interpolation routines were investigated for this analysis. The main goal of using two methods was to determine if biases were being introduced by either method.

- (1) **TMultiDimFit** The TMultiDimFit class of ROOT was used to obtain a polynomial expression for the χ^2 grid in terms of the FSI parameters. A full description of this routine can be found in [159].

The best-fit polynomial function obtained contained up to fourth-degree polynomials, with 53 terms in total, including cross-terms. A comparison of the best-fit polynomial function to the finite grid reported a reduced χ^2 of 0.29.

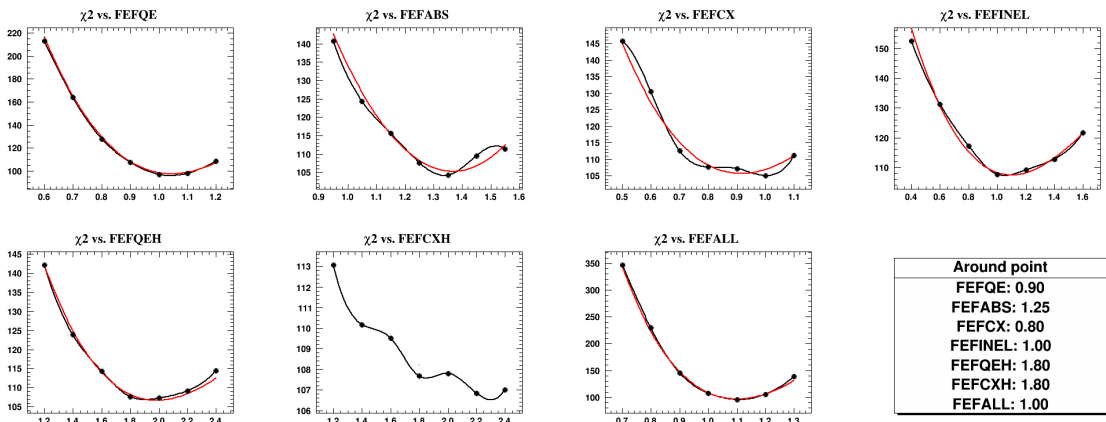


Figure 7.1: One-dimensional projections of the interpolated χ^2 grid for a point around the center of the grid using GNU-Octave (black) and TMultiDimFit (red). The dots are the χ^2 points in the finite grid being interpolated

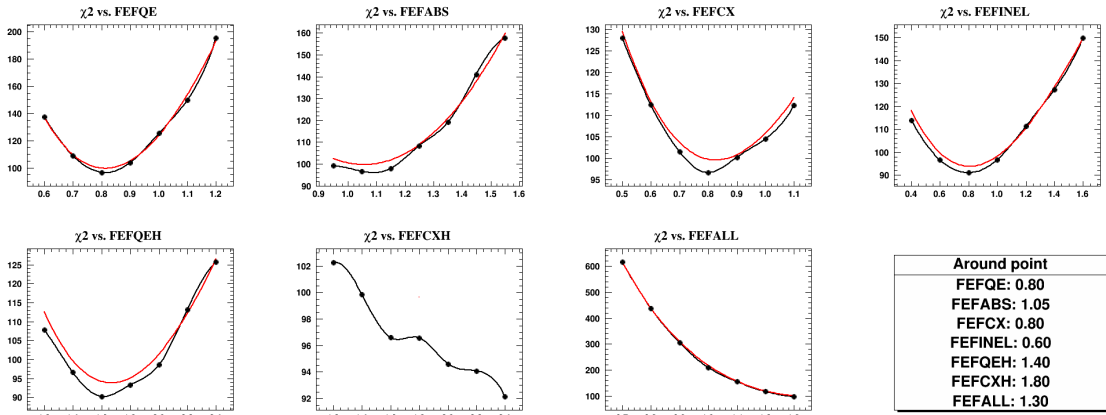


Figure 7.2: One-dimensional projections of the interpolated χ^2 grid for a point away from the center of the grid using GNU-Octave (black) and TMultiDimFit (red). The dots are the χ^2 points in the finite grid being interpolated

- (2) **GNU-Octave n-dim splines** The interpfn function of GNU-Octave [160] was used to

obtain a multi-dimensional spline interpolation of the χ^2 grid. Cubic splines are evaluated around the requested point. The GNU-Octave C++ API allowed a seamless incorporation into the FSIFitter code.

In general, it is difficult to compare multi-dimensional distributions. The two interpolation methods are compared for illustrative purposes in Figure 7.1 and 7.2 by drawing one-dimensional projections centred around points near and away from the centre of the pre-computed finite grid. The FEFCXH parameter caused problems with the convergence of the TMultiDimFit parameterization due to its low constraining power, and thus was dropped for this comparison. The interpolation methods are found to be consistent and no significant biases are expected.

7.2.4 Normalization Parameter Regimes

The fit was carried out under two regimes:

- (1) Fixed normalization parameters λ_i to their nominal value of 1.0. These results are presented in Section 7.3.1.
- (2) Floating normalization parameters λ_i . These results are presented in Section 7.3.3.

7.3 Fit Results

7.3.1 Fixed Normalization Parameters

The best fit FSI parameters, while keeping the normalization parameters fixed, are presented in Table 7.3 for both interpolation methods. The spread in the results from the methods was found to be covered by the uncertainties of the fitted parameters. The minimum χ^2 values obtained from each method are in agreement and are shown in the last row of Table 7.3, along with the number of degrees of freedom in the fit (N_{dof}). This confirms that the interpolation methods are not introducing biases, and indicates that the χ^2 didn't have a local minimum that would affect the minimization process. Thus, no additional uncertainties due to the interpolation method choice were deemed necessary.

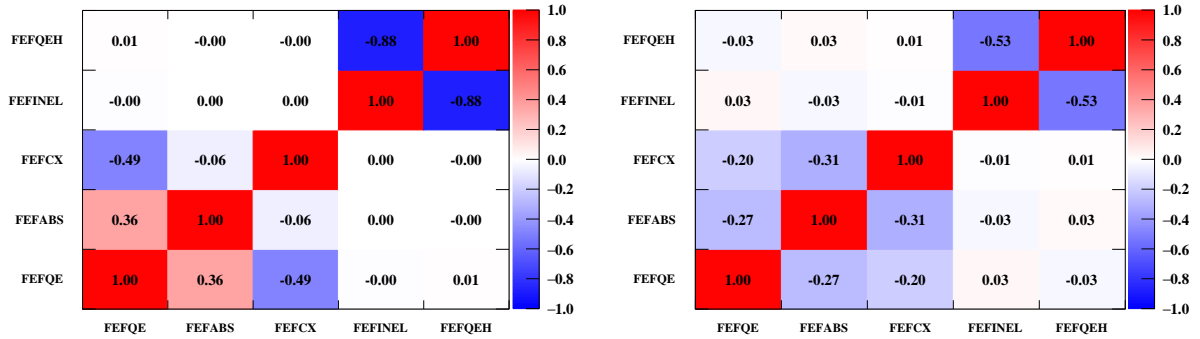
Figures 7.3a and 7.3b show the covariance matrices obtained from Minuit using each interpolation method. Stronger correlations across the FSI parameters are observed when using the TMultiDimFit interpolation. This can be understood as the effect of the polynomial parameterization, which inherently carries strong correlations from the large number of cross-terms. For this reason, it was decided to use the GNU-Octave interpolation for the final results.

7.3.2 Drawing Error Envelopes

In order to convert the constraints of the FSI parameters from this covariance into allowed variations of the macroscopic scattering cross sections to allow for comparisons with external data, the following procedure was followed:

Parameter	Best fit $\pm 1\sigma$	
	TMultiDimFit	GNU-Octave
FEFQE	1.07 ± 0.06	1.07 ± 0.04
FEFABS	1.50 ± 0.08	1.40 ± 0.06
FEFCX	0.69 ± 0.05	0.70 ± 0.04
FEFINEL	0.89 ± 0.20	1.00 ± 0.14
FEFQEH	1.90 ± 0.25	1.82 ± 0.11
FEFCXH	1.8 (Fixed)	1.8 (Fixed)
$\chi^2(N_{dof})$	150.74(59)	149.03(59)

Table 7.3: Post-fit FSI parameters, and the minimum χ^2 value obtained, with fixed normalization parameters using the TMultiDimFit and GNU-Octave interpolation methods

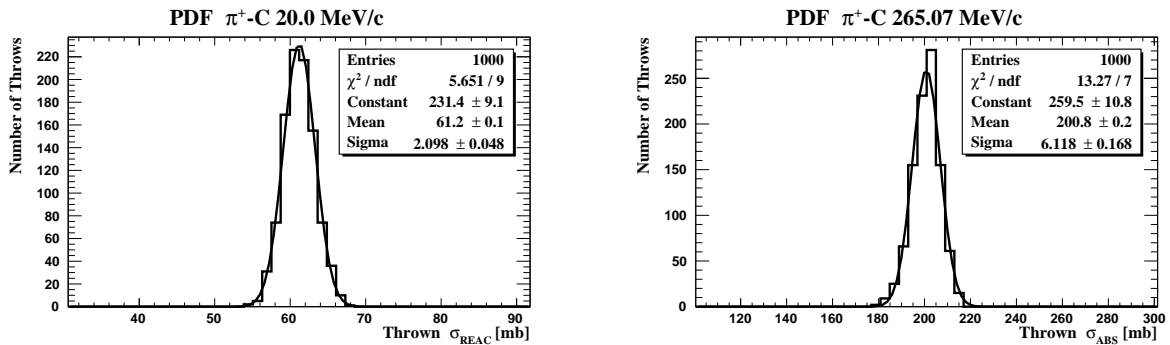


(a) Using the TMultiDimFit interpolation

(b) Using the GNU-Octave interpolation

Figure 7.3: Correlation matrices for the FSI parameters

- (1) Generate a random correlated throw from the covariance matrix in Figure 7.3b using the Cholesky decomposition method [161]. Throws outside the finite grid defined in Table 7.2 are discarded since the interpolation does not apply in that region.
- (2) Build a probability density function (PDF) for each momentum value for which $\sigma^{NEUT}(f_{FSI})$ has been calculated using the GNU-Octave spline interpolation. Figure 7.4 shows examples of these distributions for two combinations of interaction channel and momentum. Fit a Gaussian function to each one of these PDFs.
- (3) Use the obtained means and variances for each value of momentum to draw the 1σ error envelopes.



(a) PDF for π^+ -C σ_{REAC} for 20.0 MeV/c

(b) PDF for π^+ -C σ_{ABS} for 265.07 MeV/c

Figure 7.4: Sample PDFs

Figure 7.5 shows the resulting error bands for the π^+ -C macroscopic cross sections, obtained using the constraints from the correlation matrix in Figure 7.3b and the procedure described above. It is clear that when using the constraints from Table 7.3 the error envelope does not cover the uncertainties in the data. The error envelopes for cross sections on other nuclei showed similar insufficient coverage of the external data.

7.3.3 Floating Normalization Parameters

So far, the fits presented have kept the normalization parameters fixed. To investigate the effect of each data set on the χ^2 and fit results, the normalization parameters (λ_i) in Equation 7.2 are allowed to float in the fit for the results presented in this section. Each normalization parameter contributes 1 degree of freedom (dof) and 1 parameter so the N_{dof} remains the same. These parameters should give an estimation of the effect of each data set. For instance, a data set with a large pull on the fitted FSI parameters in Section 7.3.1 would instead get a normalization parameter largely deviating from its nominal value of 1.0. As will be discussed in this section, the results obtained using this approach are compatible with those found in Section 7.3.1, and thus this approach is not used in further sections.

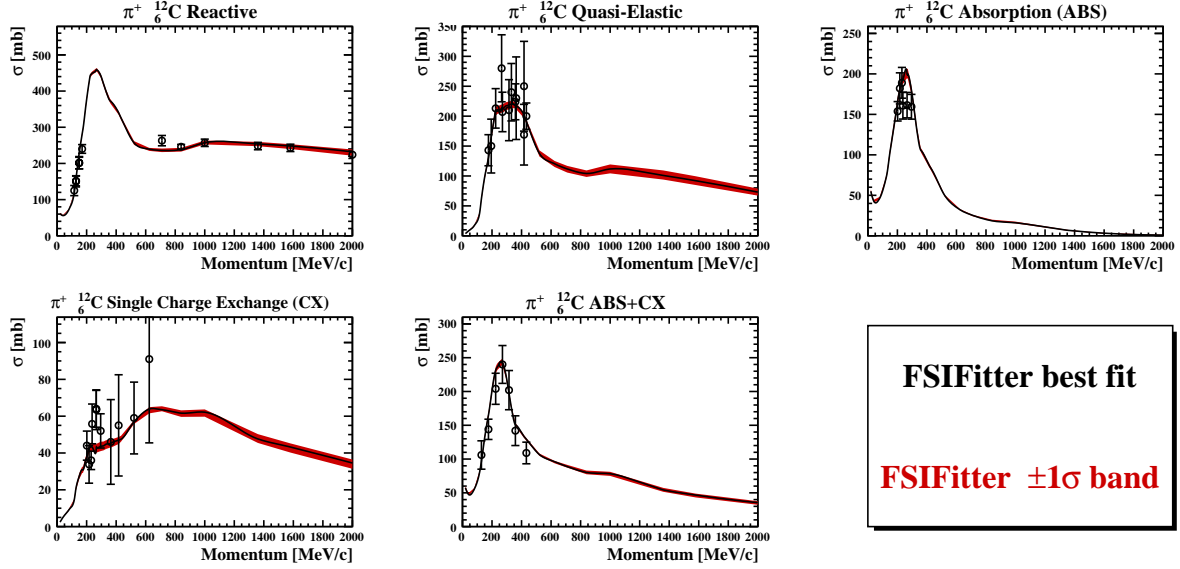


Figure 7.5: Comparison of the available π^+ -C cross section external data with the FSIFitter best fit (solid black line) and 1σ band (red) obtained from throws of the parameter values in Table 7.3 and using the correlation matrix in Figure 7.3b.

To investigate how the cascade model scales with increasing nuclear size and the effect on the FSI parameters, the fit was performed for three selections of external data sets: 1) data on carbon nuclei only, 2) data on light nuclei (carbon, oxygen, aluminum), and 3) data on light and heavy nuclei (carbon, oxygen, aluminum, iron, copper, and lead). Table 7.4 shows the best fit FSI parameters for each case. The agreement across the three cases indicates that the model is able to consistently describe all the data and that the fit is well behaved.

For the fits presented in this section the GNU-Octave interpolation routine was applied directly to the pre-calculated cross section values ($\sigma_j^{NEUT}(f_{FSI})$ in Equation 7.2) rather than to the χ^2 surface since these are scaled by the normalization parameters λ_i . This explains the difference between the “GNU-Octave” result in Table 7.3 and the “All nuclei” result from Table 7.4. This approach was not used for fit results presented in previous sections for economy of CPU-time.

Figure 7.6 shows the fitted normalization parameters for the three selections of external data. The normalization parameters roughly follow a Gaussian distribution, and the results from each of the three cases essentially overlap each other. The varying sizes of the post-fit errors is understood to be a consequence of the assigning the same 40% pre-fit error to all the parameters, as different channels have been experimentally measured with different levels of precision. For instance, inelastic and reactive processes tend to have much smaller uncertainties and the model is more successful in reproducing these channels.

Normalization Parameters

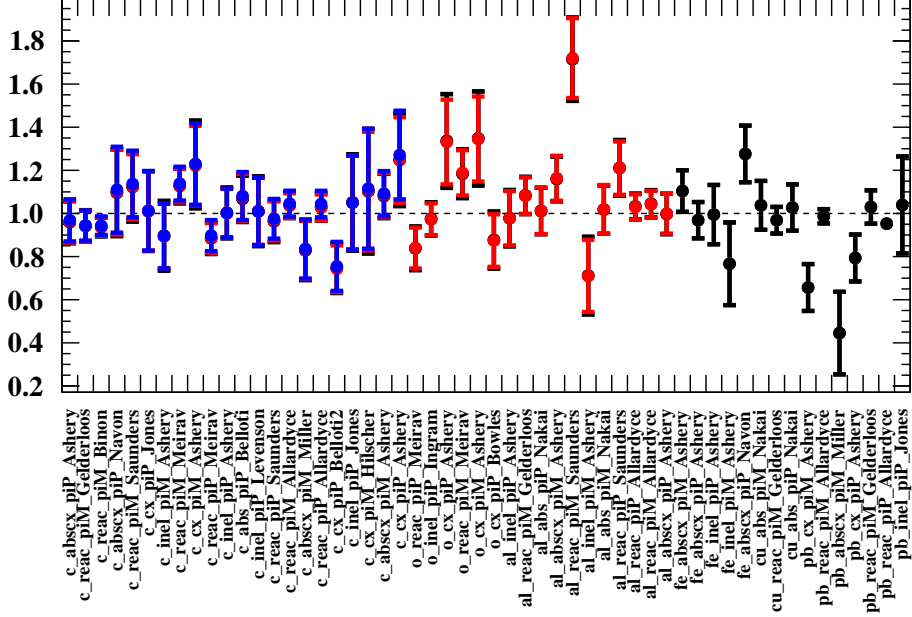


Figure 7.6: Post-fit normalization parameters for each data set for carbon-only (blue), light nuclei (red) and all-nuclei (black) fits. Some points overlap each other.

Parameter	Best fit $\pm 1\sigma$		
	Carbon-only	Light nuclei	All nuclei
FEFQE	1.07 ± 0.07	1.08 ± 0.07	1.08 ± 0.07
FEFABS	1.24 ± 0.05	1.25 ± 0.05	1.26 ± 0.05
FEFCX	0.79 ± 0.05	0.80 ± 0.04	0.80 ± 0.04
FEFINEL	0.63 ± 0.27	0.71 ± 0.21	0.70 ± 0.20
FEFQEH	2.16 ± 0.34	2.14 ± 0.24	2.13 ± 0.22
$\chi^2(N_{dof})$	18.36(23)	40.14(40)	53.48(55)

Table 7.4: Post-fit NEUT FSI Parameters and the minimum $\chi^2(N_{dof})$ value obtained for fits with fixed normalization parameters and the specified external data selections.

Normalization Parameters

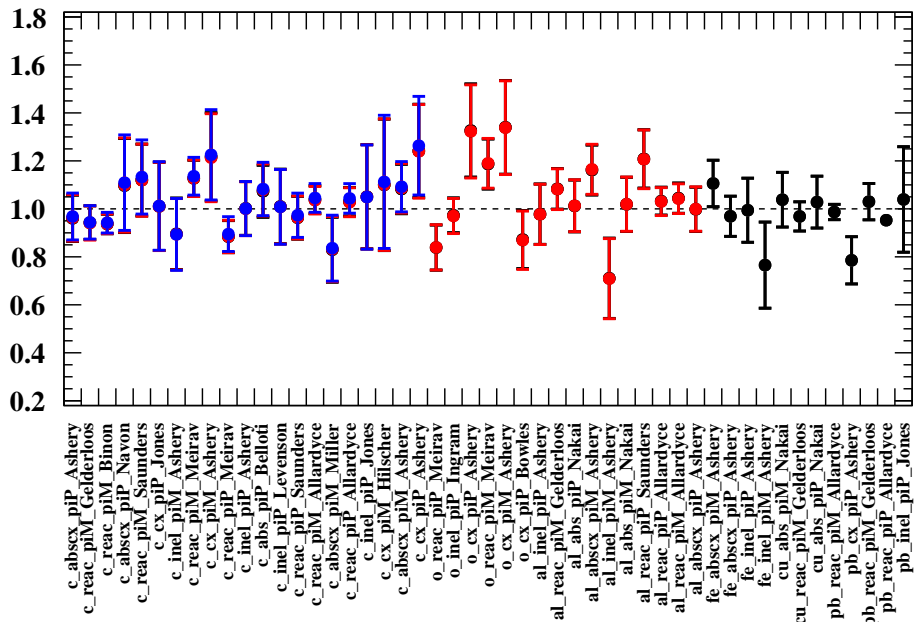


Figure 7.7: Post-fit normalization parameters for each data set (after removing the 5 data sets with strongest pulls in Figure 7.6) for carbon-only (blue), light nuclei (red) and all-nuclei (black) fits. Some points overlap each other.

7.3.3.1 Removing Data Sets with Strong Pulls

The fit was repeated after removing the five data sets whose post-fit normalization parameters are more than 1σ away from the nominal value of 1.0. Table 7.5 shows the post-fit FSI parameters. The post-fit normalization parameters for the remaining data sets are shown in Figure 7.7. The effect to both the post-fit FSI parameters and normalization parameters was found to be negligible. As mentioned earlier, this approach will not be used in further sections.

Parameter	Best fit $\pm 1\sigma$		
	Carbon-only	Light nuclei	All nuclei
FEFQE	1.07 ± 0.08	1.09 ± 0.06	1.09 ± 0.06
FEFABS	1.23 ± 0.05	1.25 ± 0.04	1.26 ± 0.04
FEFCX	0.79 ± 0.05	0.81 ± 0.04	0.80 ± 0.04
FEFINEL	0.63 ± 0.27	0.71 ± 0.21	0.71 ± 0.19
FEFQEH	2.15 ± 0.34	2.14 ± 0.24	2.13 ± 0.21
$\chi^2(N_{dof})$	17.95(22)	35.55(38)	45.13(50)

Table 7.5: Post-fit NEUT FSI Parameters and the minimum $\chi^2(N_{dof})$ value obtained for fits with fixed normalization parameters and the 5 data sets with strongest pulls in Figure 7.6 removed.

7.3.4 Error Inflation

As was mentioned before, it was clear that the 1σ error band plotted in Figure 7.5 does not properly cover the external data. This is believed to be caused by the lack of correlation information in the external data sets used. A simple way to inflate the error, while keeping the post-fit central values and correlations of the FSI parameters is to scale the χ^2 from Equation 7.2 as follows:

$$\chi_{\text{Scaled}}^2(f_{FSI}) = \frac{\chi^2(f_{FSI})}{\text{Scale factor}} \quad (7.3)$$

The figure of merit Ψ defined in Equation 7.4 was calculated for each data point of each data set in the fit and used to determine the ideal scaling factor. It compares the cross sections from external measurements (σ_j^{Data}) with the ones obtained using the best fit values of the FSI parameters ($\sigma_j^{\text{Bestfit}}(f_{FSI})$), and their 1σ error envelope ($\Delta\sigma_j^{\text{Bestfit}}(f_{FSI})$), as described in Section 7.3.2. $\Delta\sigma_j^{\text{Bestfit}}(f_{FSI})$ already have incorporated in them the uncertainties in the data.

$$\Psi = \frac{\sigma_j^{\text{Bestfit}}(f_{FSI}) - \sigma_j^{\text{Data}}}{\Delta\sigma_j^{\text{Bestfit}}(f_{FSI})} \quad (7.4)$$

Figure 7.8 shows the distribution of Ψ for various scaling factors. The ideal scaling factor is defined to be the one for which the RMS of this distribution is 1.0. This ensures a 1σ coverage of the external data sets. Figure 7.9 shows the fitted RMS for the various scaling factors. Following a linear fit, the scaling factor was chosen to be 57.0, which allows for a conservative coverage of

the data as touched upon in the next section.

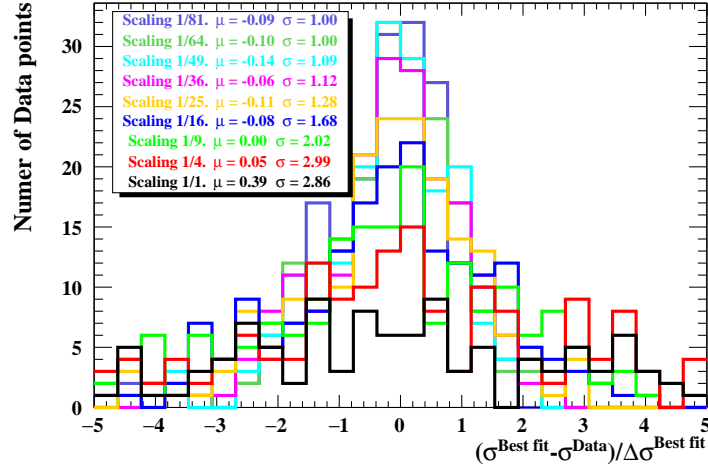


Figure 7.8: Distribution of Ψ for various scaling factors. Fitted mean and RMS are shown in the box.

7.3.5 Final (Scaled) Uncertainties

The final post-fit values of the FSI parameters after applying scaling the χ^2 surface are shown in Table 7.6. The correlation among parameters is not affected by the scaling procedure, and thus the correlation matrix presented in Figure 7.3b is final.

The resulting error bands for the macroscopic cross sections are shown in Figures 7.10 and 7.11 for π^\pm -C, Figures 7.12 and 7.13 for π^\pm -O, Figures 7.14 and 7.15 π^\pm -Al, Figures 7.16 and 7.17 for π^\pm -Fe, Figures 7.18 and 7.19 for π^\pm -Cu, and Figures 7.20 and 7.21 for π^\pm -Pb.

The error bands are significantly reduced relative to the previous iteration of this tuning work, described in the T2K technical note 032 [162], while still properly covering the uncertainties from the external data. The main improvements relative to the work in [162] the are:

- (1) The fit in [162] is fitted to π^\pm -C data only. The work presented here fitted to data on both light and heavy nuclei.
- (2) The correlations among the FSI parameters were extracted directly from the fit. In [162] the correlations are determined by manually choosing 16 sets of parameters in the corners of the parameter space.
- (3) The method used in [162] for error scaling was too conservative. The scaling factor was chosen to be the total number of data points in the fit. The ad-hoc error scaling method presented here allows for a more realistic and controlled way of setting the uncertainties.

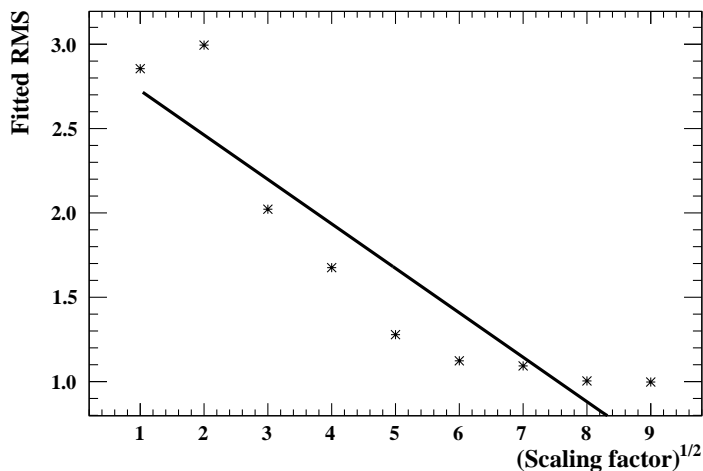


Figure 7.9: Fitted RMS as a function of the square root of the scaling factor.

Parameter	Best fit $\pm 1\sigma$
FEFQE	1.07 ± 0.31
FEFABS	1.40 ± 0.43
FEFCX	0.70 ± 0.30
FEFINEL	1.00 ± 1.10
FEFQEH	1.82 ± 0.86
FEFCX	1.8 (Fixed)

Table 7.6: Post-fit FSI parameters after error scaling.

To aid the interpretation of the error bands, the ratio of the external data and the NEUT best fit is plotted in Appendix D. The error bands are found to cover the external data points as designed.

7.4 Summary

The cascade model used to simulate pion interactions in NEUT has been tuned to scattering data on carbon, oxygen, aluminum, iron, and lead. A set of five in-built parameters that scale the microscopic probabilities of the possible interaction channels were used for this purpose. The post-fit values for these parameters are presented in Table 7.6, and their correlation matrix can be found in Figure 7.3b. These new constraints are compared to the ones described in [162] in Figures 7.10 through 7.21. The corresponding error envelopes are significantly smaller.

The effect of these reduced constraints of the FSI parameters to the FSI and SI uncertainties in the Oscillation Analysis of T2K will be described in Chapter 9.3.

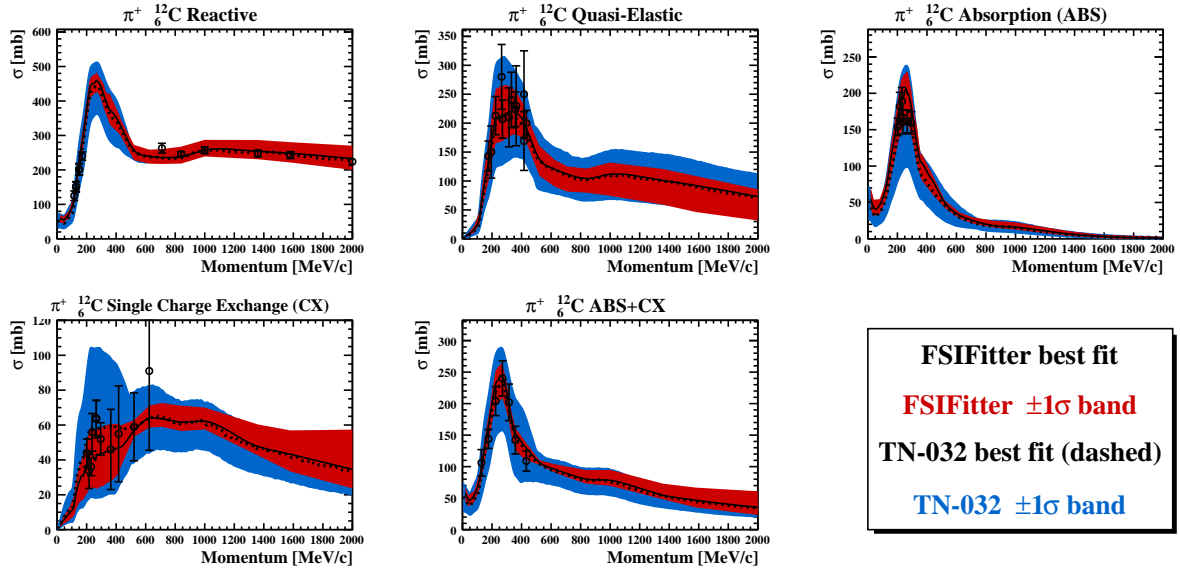


Figure 7.10: Comparison of the available π^+ -C cross section external data with the FSIFitter best fit (solid black line) and 1σ band after scaling (red), and the TN-032 best fit (dashed black line) and 1σ and (blue).

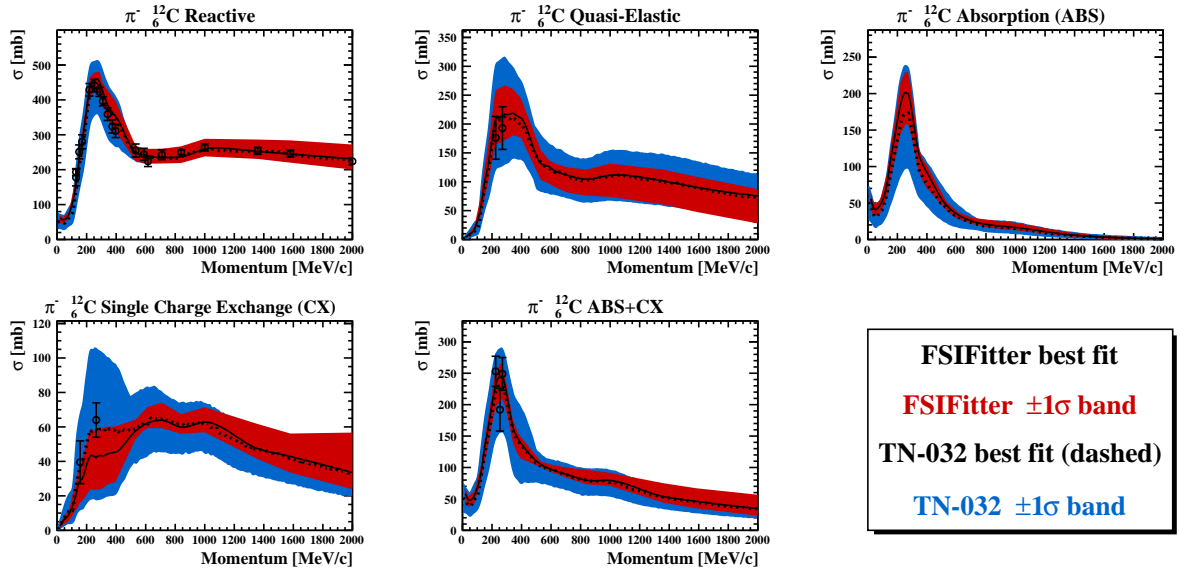


Figure 7.11: Comparison of the available π^- -C cross section external data with the FSIFitter best fit (solid black line) and 1σ band after scaling (red), and the TN-032 best fit (dashed black line) and 1σ and (blue).

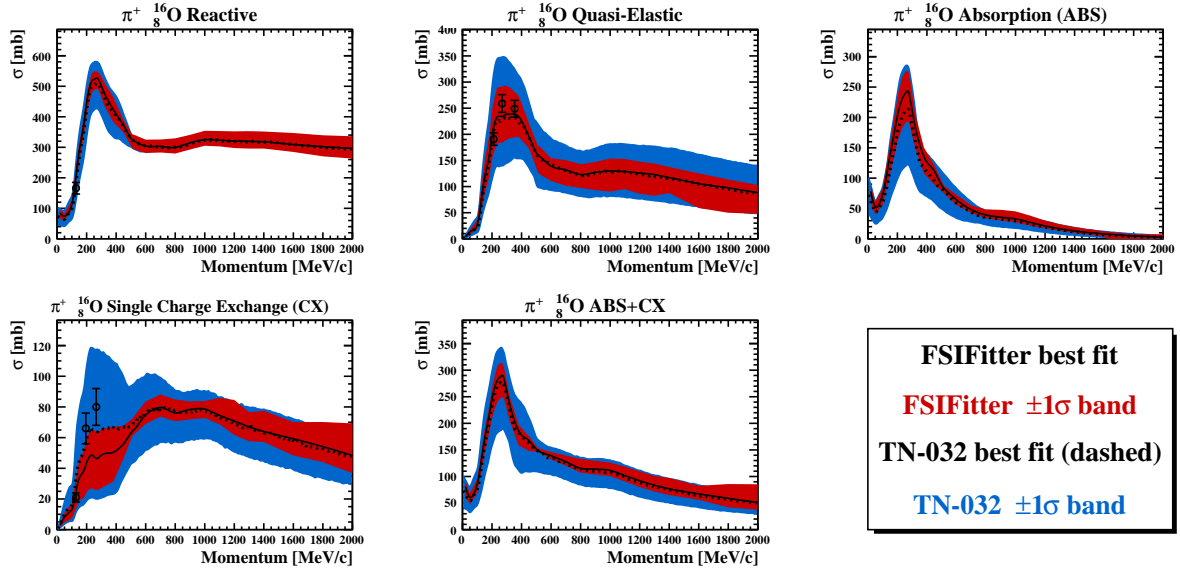


Figure 7.12: Comparison of the available π^+ -O cross section external data with the FSIFitter best fit (solid black line) and 1σ band after scaling (red), and the TN-032 best fit (dashed black line) and 1σ and (blue).

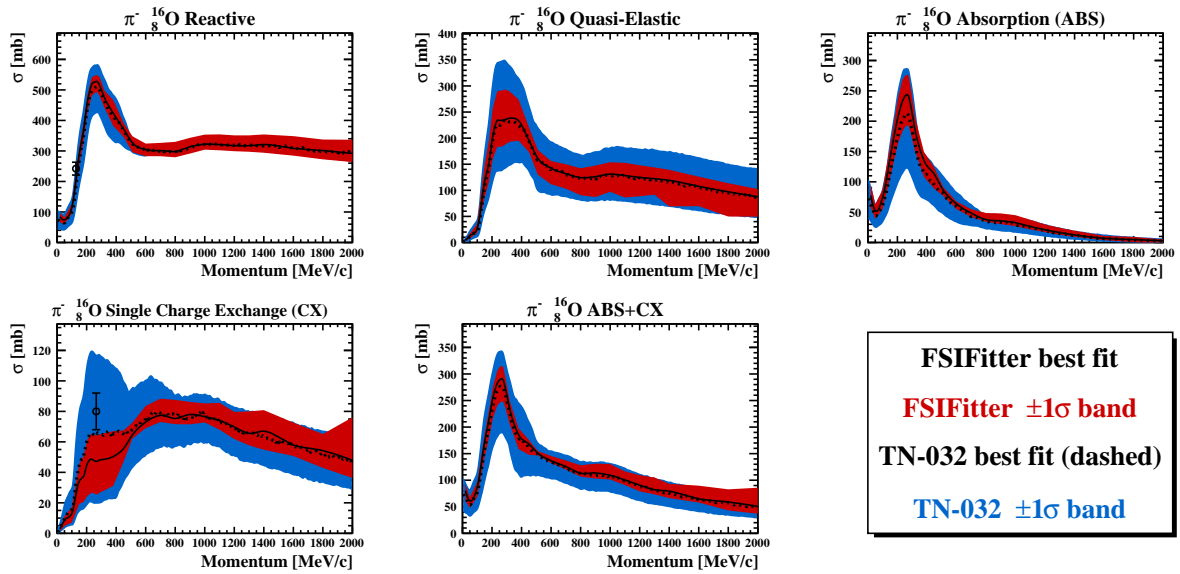


Figure 7.13: Comparison of the available π^- -O cross section external data with the FSIFitter best fit (solid black line) and 1σ band after scaling (red), and the TN-032 best fit (dashed black line) and 1σ and (blue).

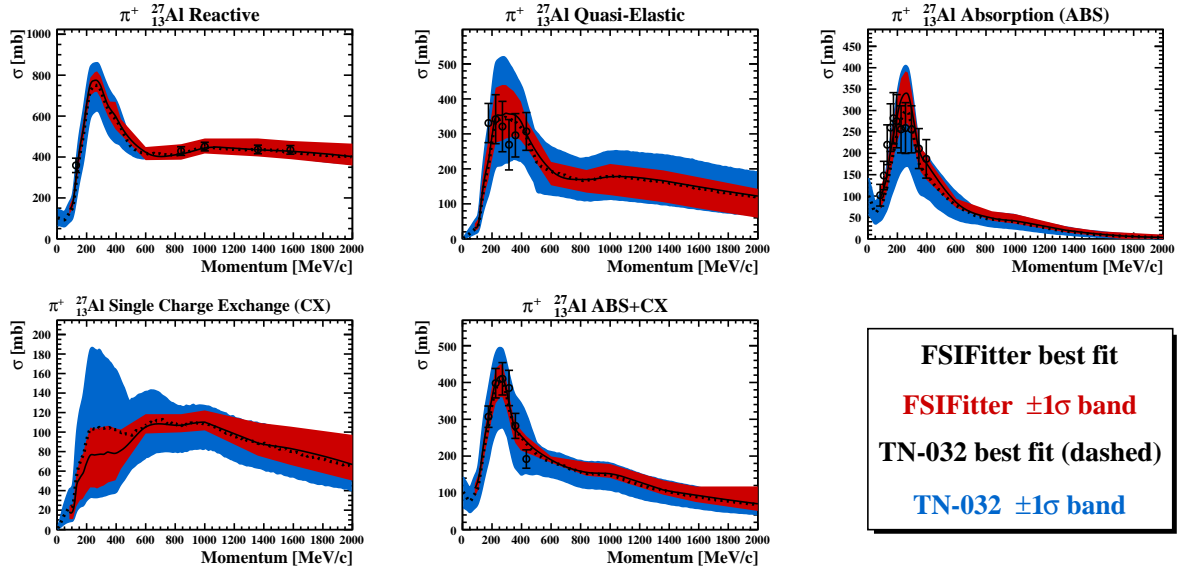


Figure 7.14: Comparison of the available π^+ -Al cross section external data with the FSIFitter best fit (solid black line) and 1σ band after scaling (red), and the TN-032 best fit (dashed black line) and 1σ and (blue).

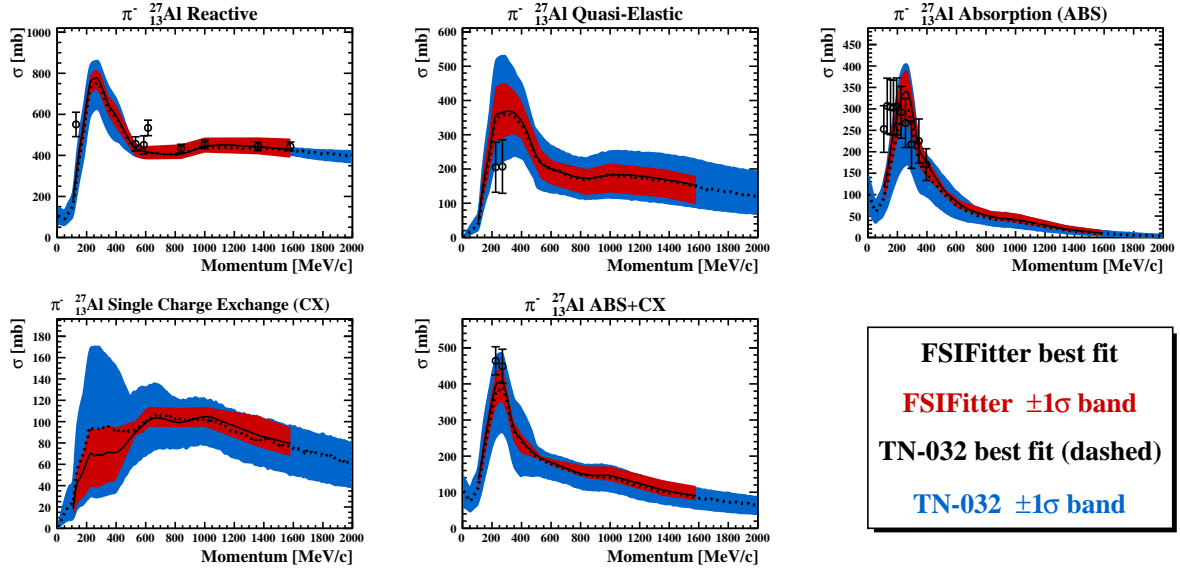


Figure 7.15: Comparison of the available π^- -Al cross section external data with the FSIFitter best fit (solid black line) and 1σ band after scaling (red), and the TN-032 best fit (dashed black line) and 1σ and (blue).

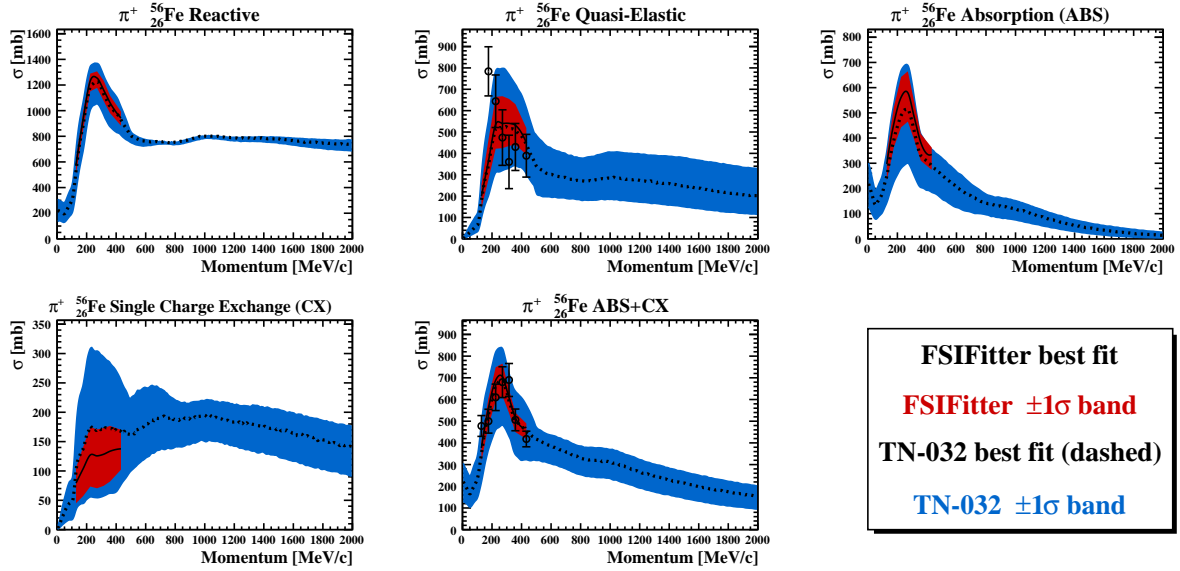


Figure 7.16: Comparison of the available π^+ -Fe cross section external data with the FSIFitter best fit (solid black line) and 1σ band after scaling (red), and the TN-032 best fit (dashed black line) and 1σ and (blue).

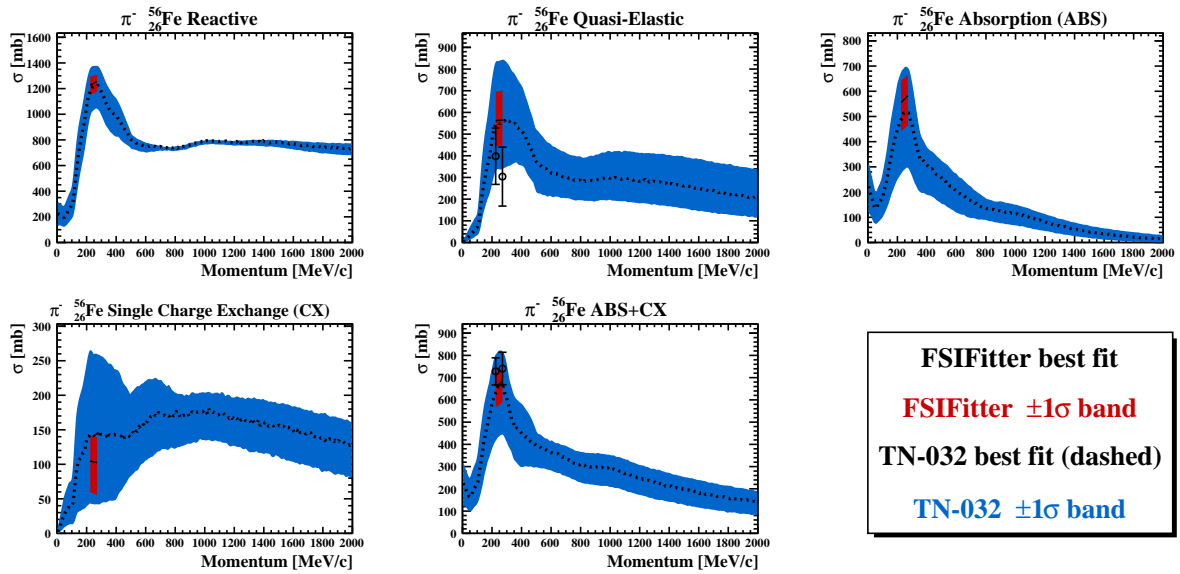


Figure 7.17: Comparison of the available π^- -Fe cross section external data with the FSIFitter best fit (solid black line) and 1σ band after scaling (red), and the TN-032 best fit (dashed black line) and 1σ and (blue).

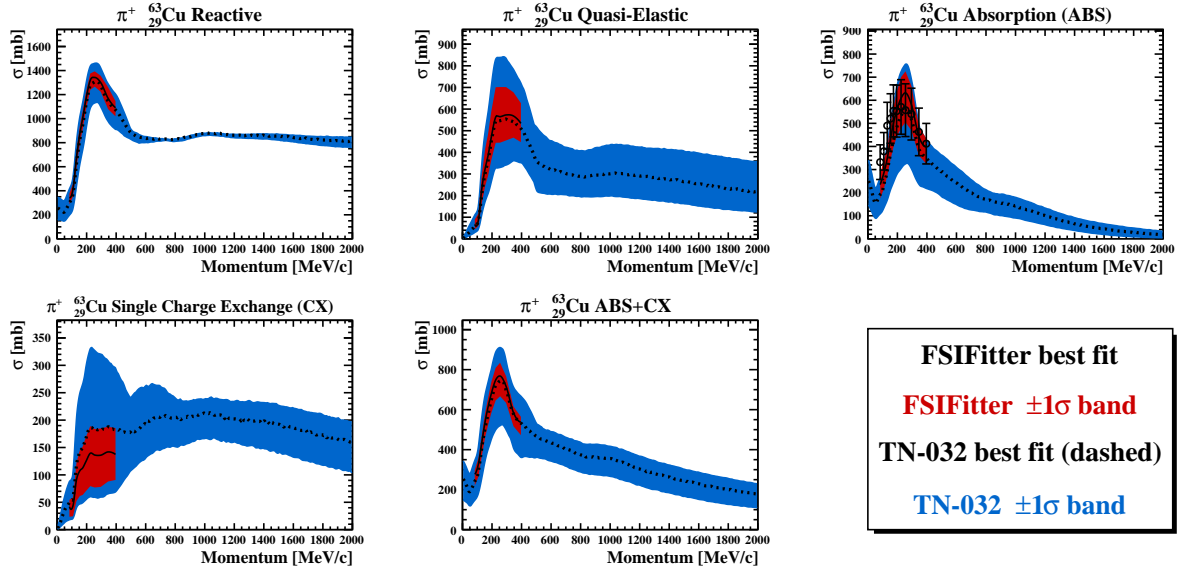


Figure 7.18: Comparison of the available π^+ -Cu cross section external data with the FSIFitter best fit (solid black line) and 1σ band after scaling (red), and the TN-032 best fit (dashed black line) and 1σ and (blue).

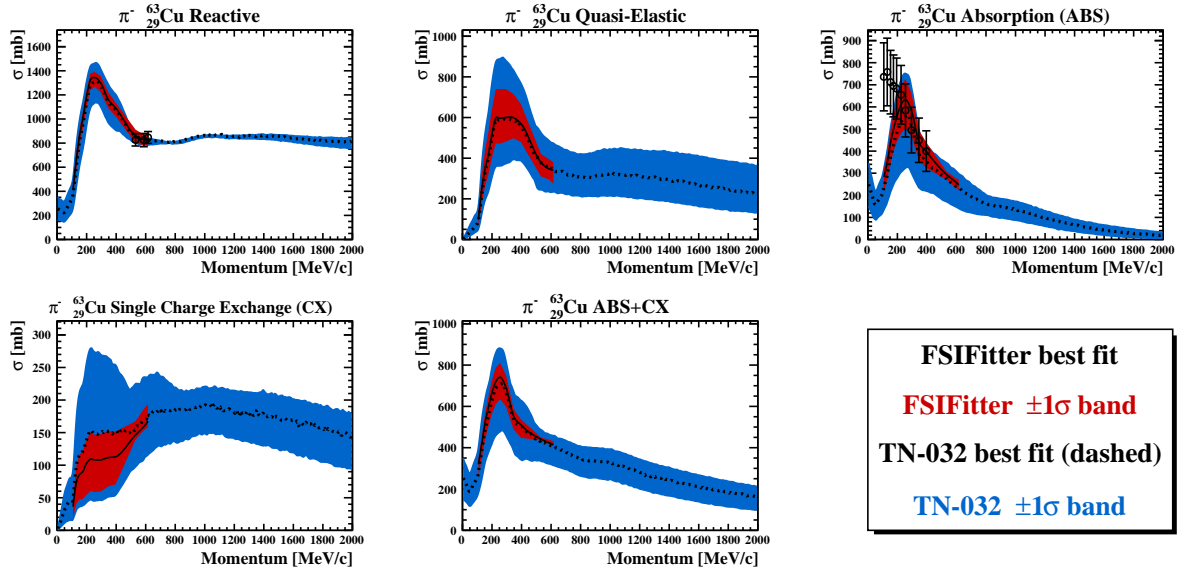


Figure 7.19: Comparison of the available π^- -Cu cross section external data with the FSIFitter best fit (solid black line) and 1σ band after scaling (red), and the TN-032 best fit (dashed black line) and 1σ and (blue).

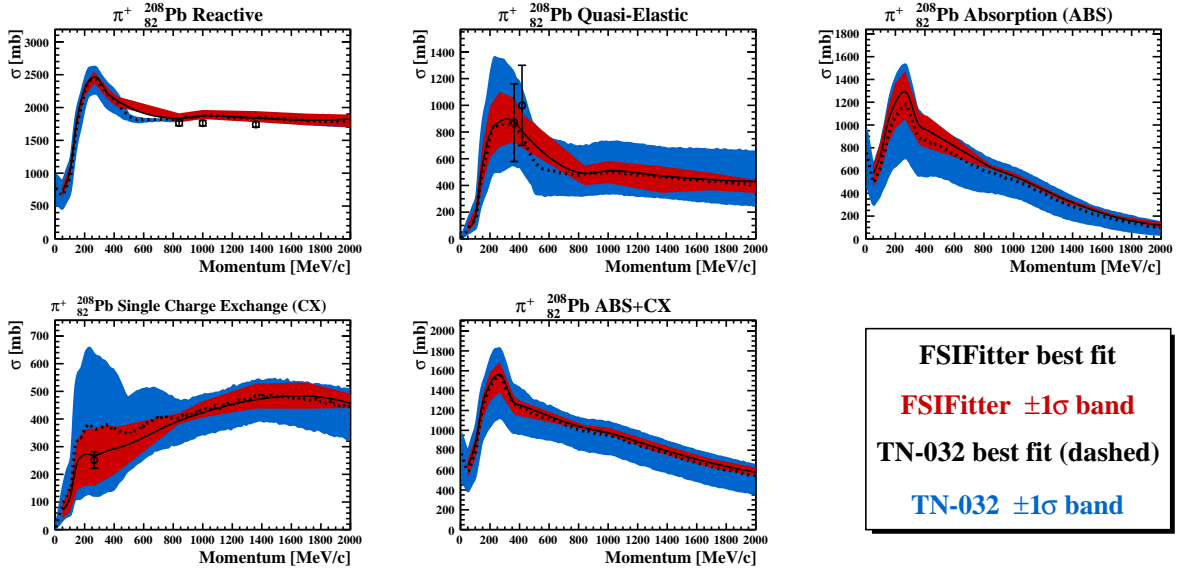


Figure 7.20: Comparison of the available π^+ -Pb cross section external data with the FSIFitter best fit (solid black line) and 1σ band after scaling (red), and the TN-032 best fit (dashed black line) and 1σ and (blue).

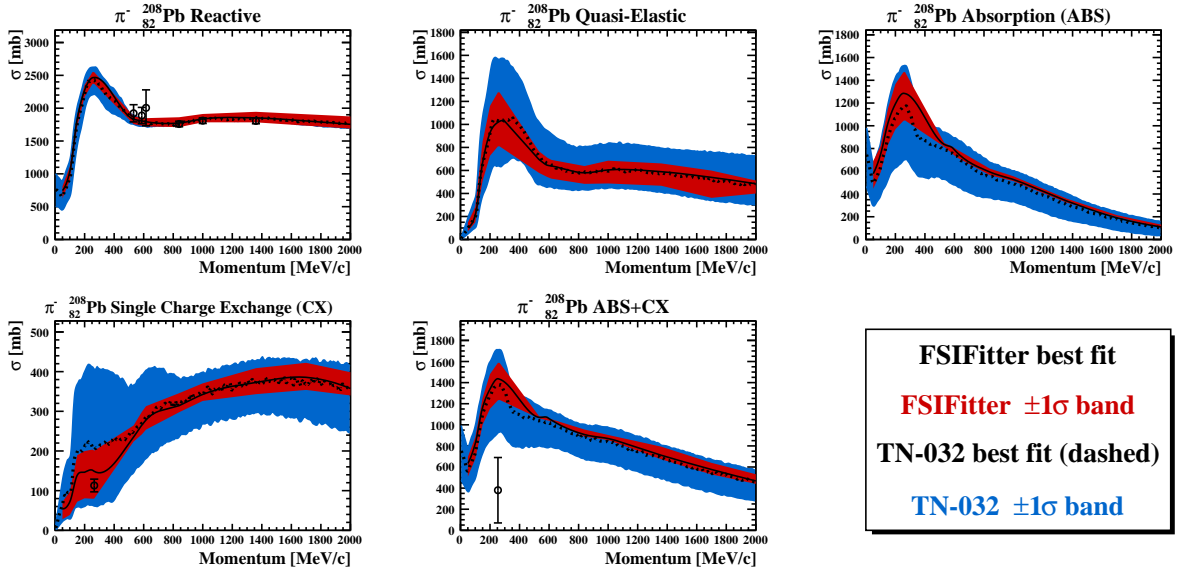


Figure 7.21: Comparison of the available π^- -Pb cross section external data with the FSIFitter best fit (solid black line) and 1σ band after scaling (red), and the TN-032 best fit (dashed black line) and 1σ and (blue).

PART III:
OSCILLATION ANALYSIS

Chapter 8

Markov Chain Monte Carlo Oscillation Analysis Framework

The third part of this thesis describes a Bayesian analysis of T2K neutrino and antineutrino data from ND280 and SK to extract estimates of the neutrino oscillation parameters. The “**Markov Chain Monte Carlo for a 3 flavour oscillation analysis**” (MaCh3) framework has been used for this purpose. This highly modular framework has been developed and validated through three generations of T2K oscillation analyses, and has been described in detail by its primary contributors [163, 164, 165, 166].

This chapter describes the likelihood definition employed in this oscillation analysis, and the theory behind the framework: Bayesian inference, the Markov Chain Monte Carlo method and the Metropolis-Hastings algorithm, and how estimates of the parameters of interest are inferred from their posterior probability distributions.

8.1 Likelihood Definition

The analysis presented here uses a likelihood-ratio function (\mathcal{L}) to perform a simultaneous fit of the ND280 and SK data using a Bayesian technique. \mathcal{L} is defined as the product of the likelihood function for each binned data sample (D_{ND} and D_{SK}) and the prior probability functions (π) for the systematic and oscillation parameters

$$\begin{aligned} \mathcal{L}(\vec{f}, \vec{x}, \vec{d}_{ND}, \vec{d}_{SK}, \vec{\theta} | D_{ND}, D_{SK}) &= P(D_{ND} | \vec{f}, \vec{x}, \vec{d}_{ND}) \\ &\times P(D_{SK} | \vec{f}, \vec{x}, \vec{d}_{SK}, \vec{\theta}) \\ &\times \pi(\vec{f}) \times \pi(\vec{x}) \times \pi(\vec{d}_{ND}) \times \pi(\vec{d}_{SK}) \times \pi(\vec{\theta}) \end{aligned} \quad (8.1)$$

where the systematic parameters are labelled \vec{f} for flux uncertainties, \vec{x} for cross section modelling uncertainties, \vec{d}_{ND} for ND280 detector uncertainties, \vec{d}_{SK} for SK detector uncertainties, and $\vec{\theta}$ for the oscillation parameters.

The probability density function (p.d.f.) for N^d events observed in the data has a Poisson distribution given by [167]:

$$f_{\text{Poisson}} = \frac{\left(N^p(\vec{\theta})\right)^{N^d} e^{-N^p(\vec{\theta})}}{(N^d)!} \quad (8.2)$$

where $N^p(\vec{\theta})$ is the expected event rate for some subset of parameters $\vec{\theta}$. The data is binned in terms of reconstructed variables in the analysis. Since there are n possible outcomes for placing an event in a bin, the p.d.f. of those outcomes is multinomial [167]:

$$f_{\text{Multinomial}} = (N^d)! \prod_i^n \left(\frac{1}{(N_i^d)!} P_i^{N_i^d} \right) \quad (8.3)$$

where $N_i^p(\vec{\theta})$ and N_i^d are the expected and observed event rates in the i -th bin, such that the probability of an event being placed in the i -th bin $P_i^{N_i^d}$ is given by:

$$P_i^{N_i^d} = \frac{N_i^p(\vec{\theta})^{N_i^d}}{N^p(\vec{\theta})^{N_i^d}}. \quad (8.4)$$

The conditional probability $P(D|\vec{\theta})$ for a binned data set D and some subset of parameters $\vec{\theta}$ is derived as the joint product in the large-sample limit of the Poisson and Multinomial probability density functions described in Equations 8.2 and 8.3, respectively

$$P(D|\vec{\theta}) = e^{(N^d - N^p(\vec{\theta}))} \prod_i \left(\frac{N_i^p(\vec{\theta})}{N_i^d} \right)^{N_i^d} \quad (8.5)$$

$$-\ln \left(P(D|\vec{\theta}) \right) = \sum_i \left[N_i^p(\vec{\theta}) - N_i^d + N_i^d \ln \left(\frac{N_i^d}{N_i^p(\vec{\theta})} \right) \right]. \quad (8.6)$$

The binning can be multi-dimensional, and will be described in Section 9.1. The likelihood in Equation 8.1 can then be written in its full form for variations ($\Delta\vec{\theta}$) of the systematic and oscillation parameters

$$\begin{aligned}
-\ln(\mathcal{L}) = & \sum_i^{\text{ND280 bins}} \left[N_i^{\text{ND280},p}(\vec{f}, \vec{x}, \vec{d}_{\text{ND}}) - N_i^{\text{ND280},d} + N_i^{\text{ND280},d} \ln \left(\frac{N_i^{\text{ND280},d}}{N_i^{\text{ND280},p}(\vec{f}, \vec{x}, \vec{d}_{\text{ND}})} \right) \right] \\
& + \sum_i^{\text{SK bins}} \left[N_i^{\text{SK},p}(\vec{f}, \vec{x}, \vec{d}_{\text{SK}}, \vec{o}) - N_i^{\text{SK},d} + N_i^{\text{SK},d} \ln \left(\frac{N_i^{\text{SK},d}}{N_i^{\text{SK},p}(\vec{f}, \vec{x}, \vec{d}_{\text{SK}}, \vec{o})} \right) \right] \\
& + \frac{1}{2} \sum_{i,j}^{\text{osc}} \Delta o_i (V_o^{-1})_{i,j} \Delta o_j \\
& + \frac{1}{2} \sum_{i,j}^{\text{flux}} \Delta f_i (V_f^{-1})_{i,j} \Delta f_j \\
& + \frac{1}{2} \sum_{i,j}^{\text{xsec}} \Delta x_i (V_x^{-1})_{i,j} \Delta x_j \\
& + \frac{1}{2} \sum_{i,j}^{\text{ND280 det}} \Delta d_{\text{ND}i} (V_{d_{\text{ND}}}^{-1})_{i,j} \Delta d_{\text{ND}j} \\
& + \frac{1}{2} \sum_{i,j}^{\text{SK det}} \Delta d_{\text{SK}i} (V_{d_{\text{SK}}}^{-1})_{i,j} \Delta d_{\text{SK}j}
\end{aligned} \tag{8.7}$$

where $N_i^{\text{ND280},p}(\vec{f}, \vec{x}, \vec{d}_{\text{ND}})$ and $N_i^{\text{SK},p}(\vec{f}, \vec{x}, \vec{d}_{\text{SK}}, \vec{o})$ represent the number of predicted events in a particular bin for ND280 or SK respectively, given the values of the systematic parameters, and $N_i^{\text{ND},d}$ and $N_i^{\text{SK},d}$ represent the number of data events observed in that bin. The fractional covariance matrices V_{ij} encode the Gaussian prior constraints for each group of systematic parameters. The parameterization of systematics and the choice of priors are described in Section 9.2. The priors for the oscillation parameters of interest $\sin^2 \theta_{13}$, $\sin^2 \theta_{23}$, Δm_{23}^2 , and δ_{CP} are flat, while Gaussian priors from the PDG are used for the solar parameters.

8.2 Bayesian Inference

The goal of a Bayesian analysis is to construct the posterior probability distribution $P(\vec{\theta}|D)$ (herein called the posterior) of a model hypothesis defined by a set of parameters $\vec{\theta}$, given some prior knowledge $P(\vec{\theta})$ and an observed data set D . This can be derived using Bayes Theorem:

$$P(\vec{\theta}|D) = \frac{P(D|\vec{\theta})P(\vec{\theta})}{\int P(D|\vec{\theta}')P(\vec{\theta}')d\vec{\theta}'}. \tag{8.8}$$

The numerator of Equation 8.8 is equivalent to the likelihood \mathcal{L} defined in Equation 8.1 and expanded in 8.7. The denominator can not be easily evaluated, as it involves the integral of the likelihood over all the possible model parameter hypothesis. The posterior gives us information about parameters, but is a high dimensional function, so visualizing it may not be possible, nor

solving analytically. Instead, we choose to build a distribution of samples from the posteriors, as will be described in the following section.

8.3 Markov Chain Monte Carlo

The Markov Chain Monte Carlo (MCMC) technique is in general useful for computing high dimension integrals. It employs a semi-random walk through the high dimensional parameter space sampling the likelihood function. This collection of discrete steps, or *Markov chain*, is by construction distributed according to that of the posterior distribution. This ensures an efficient sampling, because the MCMC naturally tends towards the high probability regions.

One defining characteristic of Markov chains is their stochastic behaviour. The position at the end of each step in the chain $\vec{\theta}_i$ depends exclusively on the previous position $\vec{\theta}_{i-1}$. The lack of memory of the chain ensures its ability to converge to a stationary sampled distribution, given the following conditions of *ergodicity* [168]:

- The chain is *irreducible*, meaning that each state of the chain can be visited starting from any other.
- The chain is *aperiodic*, meaning that each state can be visited at any iteration n larger than some fixed number.
- The chain is *recurrent*, meaning that once the stationary distribution has been reached, then all the following steps must be samples from the same stationary distribution

It is worth noting that while the MCMC technique increases the sampling efficiency of the Monte Carlo method, this does not mean that the process is not computationally costly. The analysis presented in this thesis made use of roughly 25 CPU-years and 3.2 GPU-years and was run using OpenMP [169] and CUDA [170] parallel computing techniques.

8.3.1 Metropolis-Hastings Algorithm

The Metropolis-Hastings algorithm [171, 172] provides a method to construct a Markov chain that fulfills the ergodicity conditions and that properly samples from the target stationary posterior. There are two ingredients:

- A distribution to be sampled: in our case the posterior $P(\vec{\theta}|D)$.
- A proposal function $Q(\vec{\theta}_a, \vec{\theta}_b)$, where $\vec{\theta}_a$ is the current step and $\vec{\theta}_b$ is the proposed step. In our case, $Q(\vec{\theta}_a, \vec{\theta}_b)$ is defined to be a multivariate Gaussian with the dimension of the number of parameters. The prior knowledge for each parameter (encoded in V_{ij}) are used for the mean and standard deviation. This increases the efficiency of the algorithm.

The starting point of the chain $\vec{\theta}_0$ is chosen to be a random fluctuation of all the parameters $\vec{\theta}$ according to their prior uncertainties about their nominal values. The algorithm follows the following scheme:

- (1) Propose a new step $\vec{\theta}_{i+1}$ from the proposal function $Q(\vec{\theta}_a, \vec{\theta}_b)$ and calculate the posterior $P(\vec{\theta}_{i+1}|D)$
- (2) Calculate the acceptance ratio $\alpha(\theta_{i+1}, \theta_i)$

$$\alpha(\vec{\theta}_{i+1}, \vec{\theta}_i) = \min \left(1, \frac{P(\vec{\theta}_{i+1}|D)Q(\vec{\theta}_i, \vec{\theta}_{i+1})}{P(\vec{\theta}_i|D)Q(\vec{\theta}_{i+1}, \vec{\theta}_i)} \right) \quad (8.9)$$

Notice how the ratio of the posteriors cancels out the contribution from the denominator of the posterior in Equation 8.8.

- (3) Generate a uniformly distributed random number ϵ between 0 and 1. This accounts for the *Monte Carlo* in MCMC.
- (4) If $\epsilon \leq \alpha(\vec{\theta}_{i+1}, \vec{\theta}_i)$, then accept the step, otherwise reject the step and keep the current step $\vec{\theta}_i$.
- (5) Return to (1) until a sufficient number of steps have been included into the chain and the sampled posteriors are sufficiently smooth.

The MCMC will always accept steps proposed with a larger posterior probability than the current step. However, it is the non-zero probability to accept steps with lower posterior probability that allows the MCMC method to escape possible local minima and give a correct coverage of the full target distribution. This poses a major advantage relative to traditional minimization routines such as the gradient descent algorithm implemented in MINUIT [157].

The modification of the model ($N_i^{\text{ND}280,p}(\vec{\theta})$ and $N_i^{\text{SK},p}(\vec{\theta})$) given a proposed set of parameters $\vec{\theta}$ in step (2) cannot require to run a new full simulation as this is prohibitively onerous. In lieu of this, each Monte Carlo event is reweighted using response functions for the parameters. The oscillation weights are obtained using a version of the Prob3++ library [46] ported to GPU [173]. While this technique reduces the computational load by orders of magnitude, this remains the most computationally costly item in the stepping algorithm.

Additional important properties of the MCMC such as the step size tuning, the burn-in period, and auto-correlations have been described in the literature [165].

8.4 Extracting Information from the Posterior

The MCMC method allows for an efficient sampling of the posterior distribution. Ideally, the full posterior distribution would be the “result” to be made public. However, as will be discussed in Section 9.2, the parameterization of the systematic uncertainties in Equation 8.7 utilizes 731 parameters, for a total of 737 parameters including the oscillation parameters. This very high-dimensional distribution is difficult to visualize and interpret. This section explains how the information regarding the physical parameters of interest is extracted.

8.4.1 Marginalization of Nuisance Parameters

While the posterior is a function of many parameters, our interest rests solely in a few oscillation parameters $\vec{\phi}$ (namely $\sin^2 \theta_{13}$, $\sin^2 \theta_{23}$, Δm_{32}^2 , and δ_{CP}), without regard for the values of other model parameters. These additional parameters are commonly labelled *nuisance* parameters ($\vec{\eta}$) and their impact must be properly accounted for. Fortunately, the Bayesian approach deals straight-forwardly with nuisance parameters by integrating over them, yielding a *marginal* posterior:

$$P(\vec{\phi}|D) = \frac{\int P(D|\vec{\phi}, \vec{\eta})P(\vec{\phi}, \vec{\eta})\overline{d\vec{\eta}}}{\int P(D|\vec{\theta})P(\vec{\theta})\overline{d\vec{\theta}}} \quad (8.10)$$

This is equivalent to projecting the full posterior distribution onto a smaller number of dimensions. In practice it simply entails projecting all steps of the MCMC chain onto the desired $\vec{\phi}$ parameter axes. In this analysis the posterior is marginalized onto either one dimension (1D) or two dimensions (2D), resulting in 1D and 2D histograms.

While marginalization is the correct way to deal with nuisance parameters in a Bayesian framework, it can produce non-intuitive results if the nuisance parameters which are being marginalized have non-Gaussian distributions, or if they are correlated with the parameters of interest. This effect is visible in the Asimov fits shown in Section 10.1 as shifts in the regions of high probability in marginal posterior probability distributions.

8.4.2 Parameter Estimation

In the MCMC method, the best-fit value of a parameter is chosen as the most probable point from its marginal posterior probability distribution. The uncertainty on that best-fit value estimate is obtained by constructing Bayesian *credible intervals* from the marginal posterior distribution. A credible interval is defined as the interval in the marginal posterior that contains a certain fraction of the total posterior density. This analysis uses highest posterior density (HPD) credible intervals, which are defined such that any point inside the credible interval has a larger posterior density than any point outside the interval.

For this analysis, best-fit values are obtained from 2D marginal posteriors, while uncertainties are obtained from both 1D and 2D marginal posteriors. Both cases are explained with examples below.

Figure 8.1 shows an example of a 1D marginal posterior distribution for some parameter α . The posterior in this example is assumed to be a Gaussian centred at 0.0, with an RMS of 2.5, and amplitude 1.0. The bin containing the most points is then the region of highest density, and consequently is the best fit value. The credible intervals are constructed by adding from the histogram in order of highest to lowest population until the bins counted so far contain the required percentage of the total posterior density. For example, to report a 90% credible interval bins are added until the counted bins contain 90% of the integral of the posterior.

The results of this thesis are typically presented as 68%, 90%, and 95% credible intervals, in

keeping with the precedent set by frequentist analyses (a 68.3% frequentist confidence level is equivalent to $\Delta\chi^2 = 1\sigma$, while a 95.4% frequentist confidence level is equivalent to $\Delta\chi^2 = 2\sigma$). These 1D credible intervals are shown as colour bands in Figure 8.1. Consequently, the best fit value would be reported as $\alpha = -0.05 \pm 2.45$.

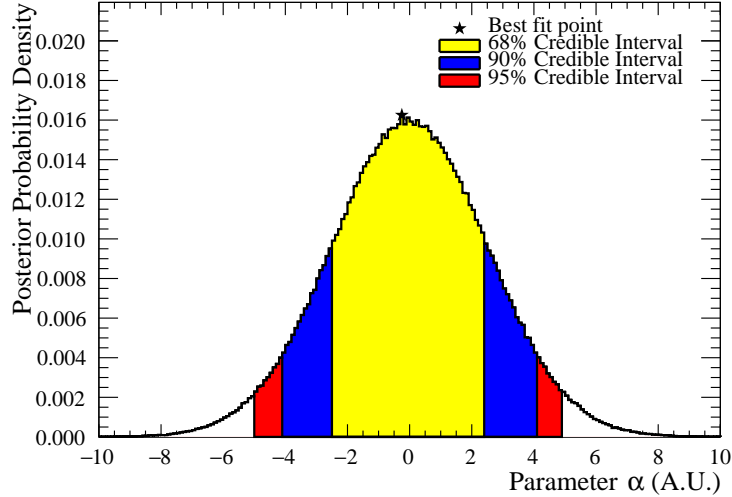


Figure 8.1: Example of a one dimensional marginal posterior probability density. A Gaussian centred at 0.0, with an RMS of 2.5 and amplitude 1.0 is assumed for this example. The best fit point (star marker) is chosen as the bin with the highest posterior density. The 68%, 90%, and 95% credible intervals calculated using the highest posterior density method are presented as the yellow, blue, and red filled regions, respectively.

Figure 8.2 shows an example of a 2D marginal posterior distribution for some correlated parameters α and β . A two-dimensional Gaussian centred at 0.0, with standard deviations 2.5 and 1.5, and amplitude 1.0 is assumed for this example. Similar to the 1D case, the best fit point is chosen as the bin with the highest posterior probability density. The 68% and 90% confidence intervals are also calculated using the highest posterior density method. Extending from the 1D case, the region containing the desired percentage of the posterior is determined by adding bins in order of highest to lowest probability density. The resulting region is determined by a collection of bins, which are then connected by a smooth line¹that forms the contours shown in Figure 8.2.

Note that if the posterior distribution has multiple maxima the HPD credible interval construction can lead to a single credible interval being composed of multiple non-contiguous areas. For example, in the case of Δm_{23}^2 , the credible intervals for normal and inverted hierarchy regions will be separated.

¹The `TH2D::SetContour` function of ROOT [174] is useful for this task.

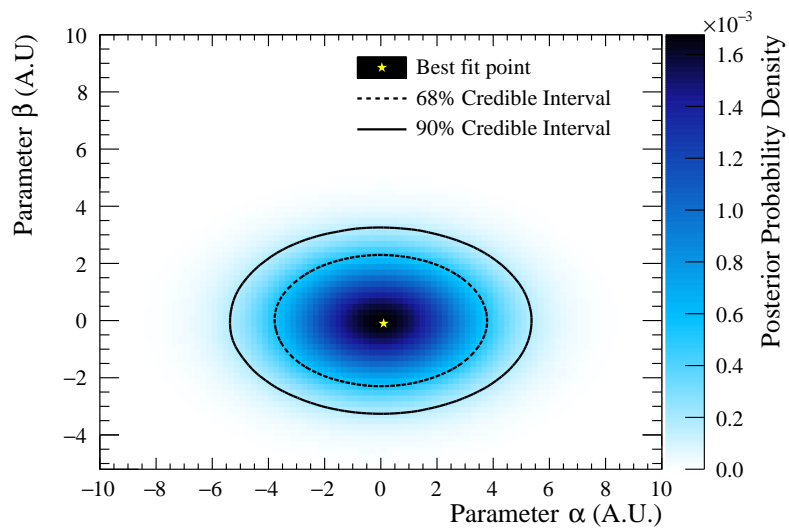


Figure 8.2: Example of a two dimensional marginal posterior probability density. A 2D Gaussian centred at 0.0, with standard deviations 2.5 and 1.5, and amplitude 1.0 is assumed for this example. The best fit point (yellow star marker) is chosen as the bin with the highest posterior density. The 68% and 90% credible intervals calculated using the highest posterior density method are shown as the overlaid dashed and solid lines, respectively.

Chapter 9

Joint $\nu_{\mu,e} + \bar{\nu}_{\mu,e}$ Oscillation Analysis: Selections and Systematic Uncertainties

Data from ND280 and SK are fitted simultaneously in the analysis presented in this thesis. The event selection criteria for each detector are summarized in Section 9.1. The systematic uncertainties coming from the flux prediction, the cross section model, and from each detector, are summarized in Section 9.2. A particular emphasis is placed in Section 9.3 on the treatment of Final State Interactions and Secondary Interactions at SK for this fit, since this has been improved relative to previous T2K oscillation analyses. The results of the fit are presented in Chapter 10.

9.1 Event Selection

9.1.1 ND280 Event Selection

The goal is to select ν_{μ} and $\bar{\nu}_{\mu}$ charged current inclusive interactions within the FGD, and that contain one charged track traversing a downstream TPC and identified as a muon. The FHC mode data was collected between November 2010 and February 2015 (T2K runs 2 to 6) and amounts to 5.8×10^{20} POT, while the RHC mode was collected between June 2014 and April 2015 (T2K Runs 5 and 6) and amounts to 2.8×10^{20} POT.

The selected samples are used to constrain the flux and cross section uncertainties that are correlated between the near and far detectors. The samples are topologically subdivided by: the number of reconstructed pion tracks in FHC mode, and the number of tracks of any kind in RHC mode. This allows the fit to constrain specific cross section model parameters. The following event selection criteria are common for FHC and RHC mode selections:

- (1) *Data quality*: The global ND280 data quality flag must be good to ensure detector stability.

- (2) *Time bunching*: The reconstructed tracks must be within 60 nanoseconds of the mean proton beam bunch time.
- (3) *Fiducial Volume and TPC Measurement*: There must be one charged track beginning inside the Fiducial Volume (FV) of an FGD. The FV is defined as the FGD volume subtracting the two first layers and 5.7 cm from the x and y edges. It is defined with the goal of rejecting background events originating outside the FGDs.
The same track must enter a downstream TPC. At least 18 hits are required to ensure a proper momentum and PID reconstruction.
- (4) *Upstream Veto*: All the events generated upstream of FGD1 are rejected by excluding events with a track in the first TPC.
- (5) *Broken tracks*: Any FGD-only tracks present must not start in the last two layers of the FGD. This avoids possible mis-reconstruction issues due to broken FGD-TPC tracks.
- (6) *TPC PID*: The highest momentum track must be identified as a negatively (positively) charged μ for ν_μ ($\bar{\nu}_\mu$) interactions.

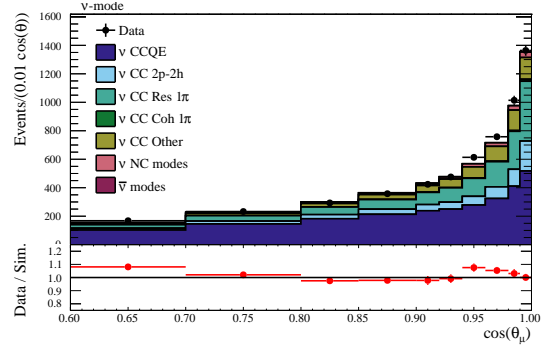
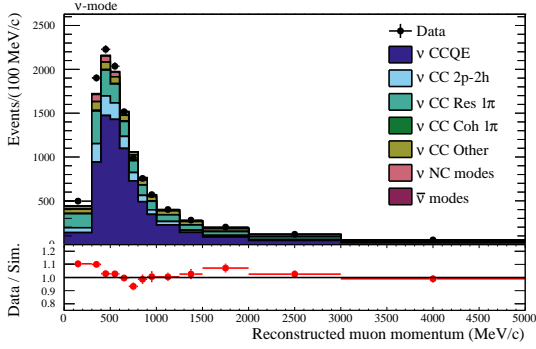
The last criterion, summarized below, is specific for the FHC and RHC selections and subdivides the selections by their topologies.

9.1.1.1 FHC mode

In the FHC mode the CC-inclusive sample is divided into three sub-samples as follows:

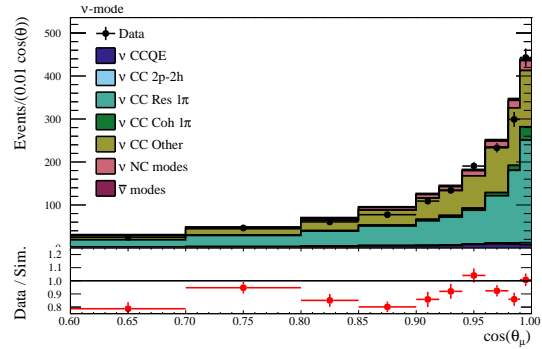
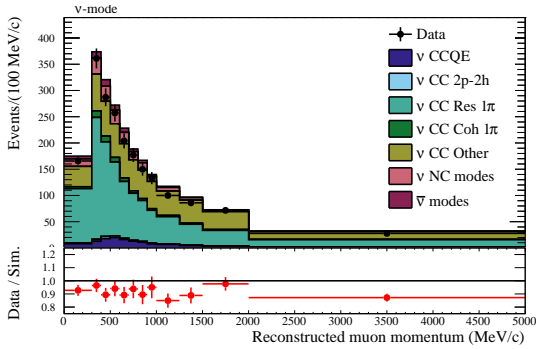
- **CC0 π sample**: No events with a π^\pm or e^\pm reconstructed in a TPC, nor a delayed “Michel” electron produced by a pion decay electron or a π^\pm in the FGDs.
- **CC1 π sample**: No events with a π^- or e^\pm in a TPC, and one π^+ or one “Michel” electron reconstructed in an FGD.
- **CC Other sample**: The remaining events that passed the cuts (1) to (6) and are not CC0 π or CC1 π events.

Table 9.1 shows the number of events selected in Data and MC for the FHC mode, the efficiencies and purities of the selection, and the total integrated POT analyzed. The samples are binned in $(p_\mu, \cos\theta_\mu)$, where p_μ is the reconstructed momentum of the muon candidate track, and θ_μ is the reconstructed angle relative to the neutrino beam direction. The asymmetrical binning is chosen such that there are at least 25 events in each bin. Figure 9.1 shows the p_μ and $\cos\theta_\mu$ projections of the selected MC (broken down by interaction mode) and the Data for the FGD1.



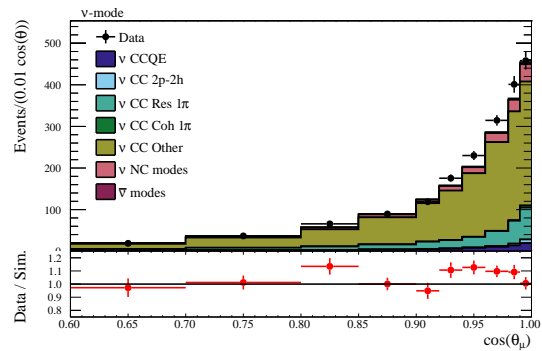
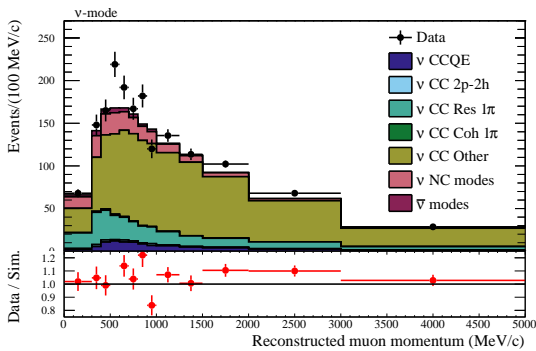
PRELIMINARY

PRELIMINARY



PRELIMINARY

PRELIMINARY



PRELIMINARY

PRELIMINARY

Figure 9.1: ND280 pre-fit MC (broken down by interaction mode) and Data binned in p_μ (left) and $\cos\theta_\mu$ (right) for the FHC CC0 π (top), CC1 π (middle) and CC Other (bottom) samples in the FGD1. Reproduced from [175].

Sample	Sub-Detector	MC	Efficiency (%)	Purity (%)	Data	POT	
FHC CC0 π	FGD1	16950.81	47.6	70.4	17354	5.8×10^{20}	
	FGD2	17211.71	48.4	67.4	17650		
FHC CC1 π	FGD1	4460.15	27.5	54.1	3984		
	FGD2	3616.62	23.7	53.5	3383		
FHC CC Other	FGD1	4009.78	27.6	72.9	4220		
	FGD2	3626.56	28.2	72.8	4118		
RHC $\bar{\nu}_\mu$ CC 1-Track	FGD1	2708.65	66	74.4	2663		2.8×10^{20}
	FGD2	2729.88	68	74.5	2762		
RHC $\bar{\nu}_\mu$ CC N-Track	FGD1	797.73	29	46.4	775		
	FGD2	804.45	31	45.6	737		
RHC ν_μ CC 1-Track	FGD1	938.13	46.3	50.5	989		
	FGD2	943.90	46.4	46.2	980		
RHC ν_μ CC N-Track	FGD1	995.33	36.5	66.1	1001		
	FGD2	916.61	46.7	67.4	936		

Table 9.1: Summary of number of events selected in FHC and RHC mode the in FGD1 and FGD2 in Data and MC, the efficiencies and purities of the selection, and the total POT analyzed.

9.1.1.2 RHC mode

In the case of the CC-inclusive in RHC mode, the wrong-sign contamination is significant, as can be seen in Figure 4.1. For this reason the selection is divided into four sub-samples as follows:

- **$\bar{\nu}_\mu$ CC 1-Track sample:** The highest momentum track is a positively charged muon. No events with a π^\pm or e^\pm reconstructed in a TPC. May contain events with short FGD-only tracks or with “Michel” electrons. This is considered a CCQE enhanced sample.
- **$\bar{\nu}_\mu$ CC N-Track sample:** The highest momentum track is a positively charged muon. Any number of secondary tracks are accepted. This is considered a CC-nonQE enhanced sample.
- **ν_μ CC 1-Track sample:** The highest momentum track is a negatively charged muon. No events with a π^\pm or e^\pm reconstructed in a TPC. May contain events with short FGD-only tracks or with “Michel” electrons. This is considered a CCQE enhanced sample.
- **ν_μ CC N-Track sample:** The highest momentum track is a negatively charged muon. Any number of secondary tracks are accepted. This is considered a CC-nonQE enhanced sample.

Table 9.1 shows the number of events selected in RHC mode in Data and MC, the efficiencies and purities of the selection, and the total integrated POT analyzed. Similarly to the FHC mode selection, the distributions are binned in $(p_\mu, \cos\theta_\mu)$, although the bin edges are different

to account for the reduced statistics. Figure 9.2 shows the p_μ and $\cos\theta_\mu$ projections of the selected MC broken down by interaction mode and the Data for the FGD2 in RHC mode.

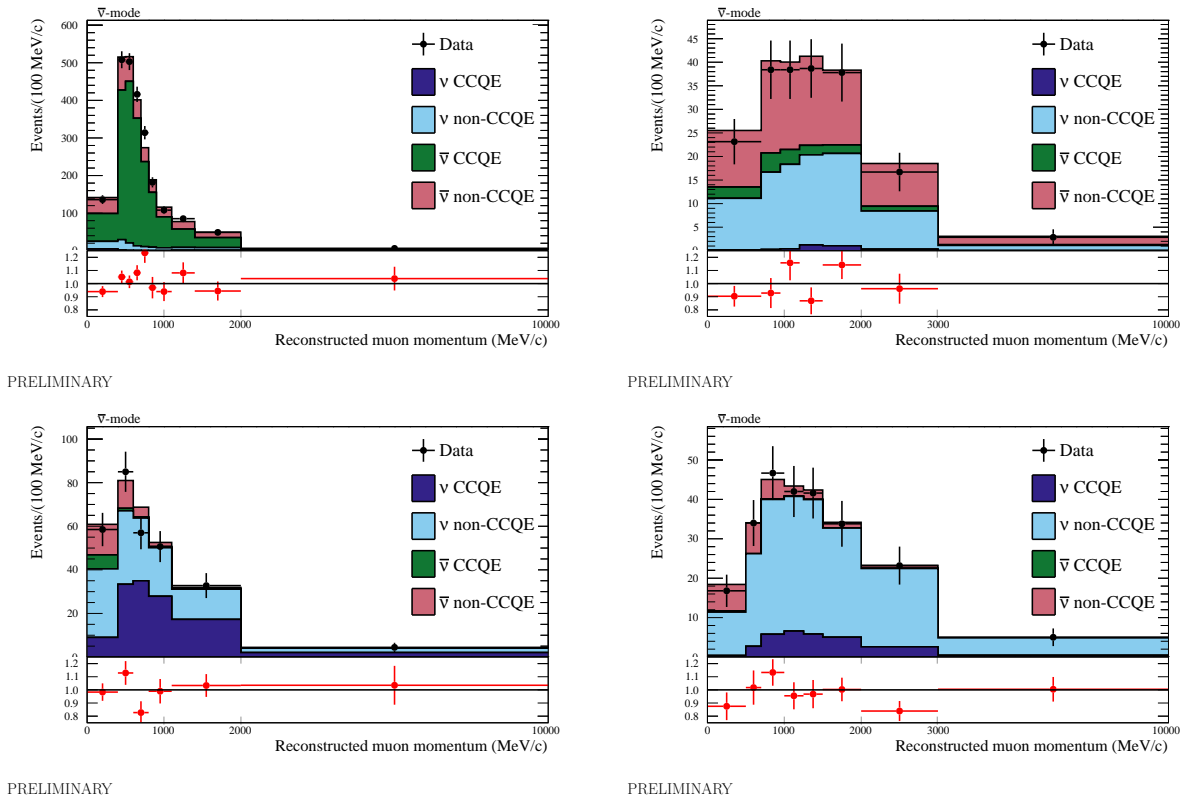


Figure 9.2: ND280 pre-fit MC (broken down by interaction mode) and Data binned in p_μ for the RHC $\bar{\nu}_\mu$ CC 1-Track (top left), RHC $\bar{\nu}_\mu$ CC N-Track (top right), RHC ν_μ CC 1-Track (bottom left), and RHC ν_μ CC N-Track (bottom right) samples in the FGD2. Reproduced from [175].

9.1.2 SK Event Selection

As was mentioned in Section 4.4.2.1, the likelihood-based fitQun reconstruction algorithm was recently adopted by T2K-SK and the fiducial volume was recently expanded [176], providing an increase of $\sim 20\%$ in the event rate. In addition, the π^0 and π^+ cuts were optimized for appearance and disappearance signal and backgrounds in T2K oscillation analyses [177]. The complete details of the selection can be found in [178].

The five samples used in this analysis share the characteristic of having one reconstructed ring and being fully contained (FC) in the fiducial volume (FV) of SK. This is achieved by the applying the following criteria:

- (1) *Data quality*: The SK and beam flag must be “good”. The recorded PMT hits must be within $(-2, +10)$ μsec from the arrival time of the leading edge of the spill.

- (2) *Fully contained*: The visible energy must be greater than 30 MeV and a maximum of 16 hits in the Outer Detector (OD) may be recorded.
- (3) *Fiducial volume*: The FV is defined as the inner volume more than 2 m from the Inner Detector (ID) wall. The reconstructed vertex is required to be inside the FV.
- (4) *Cherenkov ring count*: Only events for which a single ring is found by the ring counting algorithm are accepted.

The FC+FV 1-ring sample is further divided into five sub-samples: single-ring muon-like in FHC mode (FHC 1R_μ), single-ring muon-like in RHC mode (RHC 1R_μ), single-ring e-like in FHC mode (FHC 1R_e), single-ring e-like in RHC mode (RHC 1R_e), and single-ring e-like with a decay electron in FHC mode (FHC 1R_e 1d.e.). Since the Cherenkov technique for particle identification used does not provide information about the electric charge, this information simply comes from the beam mode configuration and the selection criteria is the same for both modes.

FHC and RHC 1R_μ Samples

The additional selection criteria for the FHC and RHC 1R_μ samples is the following:

- (5) *Ring PID*: The ring is identified as muon-like by the single-ring reconstruction algorithm.
- (6) *Reconstructed momentum*: The reconstructed muon momentum must be larger than 200 MeV/c.
- (7) *Decay electrons*: There must be 0 or 1 decay-e.
- (8) *π⁺ rejection*: The π⁺ ring hypothesis must be rejected to remove NC1π⁺ background events.

FHC and RHC 1R_e samples

The additional selection criteria for the FHC and RHC 1R_e samples is the following:

- (5) *Ring PID*: The ring is reconstructed as electron-like by the single-ring reconstruction algorithm.
- (6) *Minimum visible energy*: The reconstructed electron momentum must be larger than 100 MeV/c.
- (7) *Decay electron*: There must be no decay-e.
- (8) *Reconstructed neutrino energy (E_{rec})*: $E_{rec} < 1.25$ GeV.
- (9) *π⁰ rejection*: The hypothesis that the ring was created by a π⁰ must be rejected to remove NC1π⁰ background events.

1R_e 1d.e. sample

The additional selection criteria for the FHC 1R_e 1d.e sample is the following:

- (5) *e-like*: The ring is reconstructed as electron-like.
- (6) *Minimum visible energy* E_{vis} : $E_{vis} > 100$ MeV.
- (7) *Decay electron*: There must be one decay-e.
- (8) *Reconstructed neutrino energy* E_{rec} : $E_{rec} < 1.25$ GeV.
- (9) π^0 *rejection*: The hypothesis that the ring was created by a π^0 must be rejected.

Table 9.3 shows the selected number of events in the data for each sample, along with the number of events predicted in the absence of oscillations (unoscillated) and when assuming the oscillation parameter values in Table 9.2. The values in Table 9.2 for $\sin^2 \theta_{12}$, Δm_{21}^2 , and $\sin^2 \theta_{13}$ are taken the 2017 PDG [48], while the values for $\sin^2 \theta_{23}$, Δm_{32}^2 , and δ_{CP} are taken from the result of a previous T2K $\nu_e + \nu_\mu$ joint fit [179].

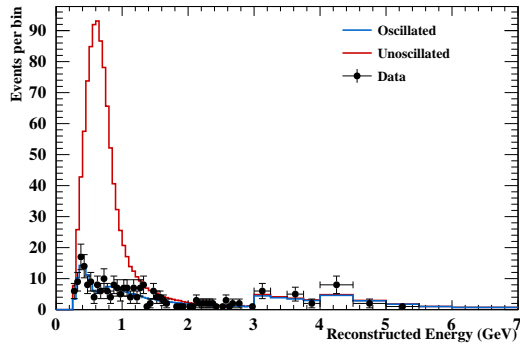
Figure 9.3 shows the pre-fit predicted energy spectra of the five samples for the un-oscillated and oscillated case, assuming the values in Table 9.2, along with the data. In the fit the 1R_e and 1R_e 1d.e samples are additionally binned in the momentum of the reconstructed electron θ_e . The predictions for the oscillated spectra are broken down by interaction mode in Figure 9.4. The additional decay electron requirement of the 1R_e 1 d.e. sample allows the tagging of the pion under Cherenkov threshold via the decay electron emitted by the decay of the muon from the pion decay. This is reflected in the dominant composition of CC1 π events in this sample.

Parameter	Value
$\sin^2 \theta_{12}$	0.304
$\sin^2 \theta_{23}$	0.528
$\sin^2 \theta_{13}$	0.0219
Δm_{21}^2 (eV ²)	7.53×10^{-5}
Δm_{32}^2 (eV ²)	2.509×10^{-3}
δ_{CP}	-1.601

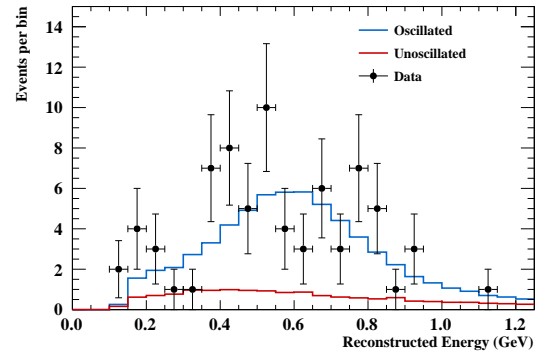
Table 9.2: Neutrino oscillation parameter values assumed for calculating the expected oscillated spectra in Table 9.3 and Figures 9.3 and 9.4.

9.2 Systematic Uncertainties

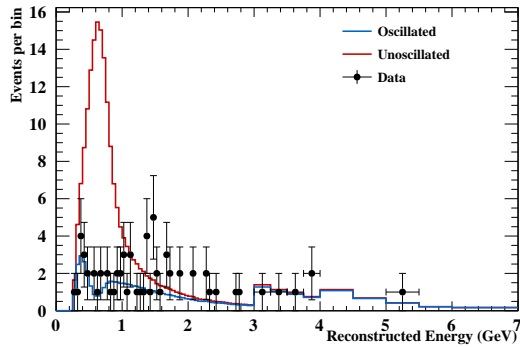
The implementation and priors for the systematic uncertainty considered for this analysis are described in this section. These are represented by the penalty terms in Equation 8.7.



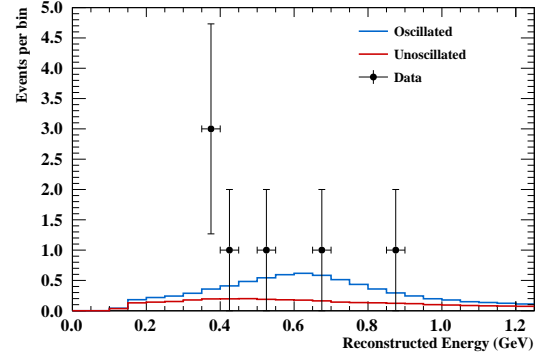
(a) FHC $1R_\mu$



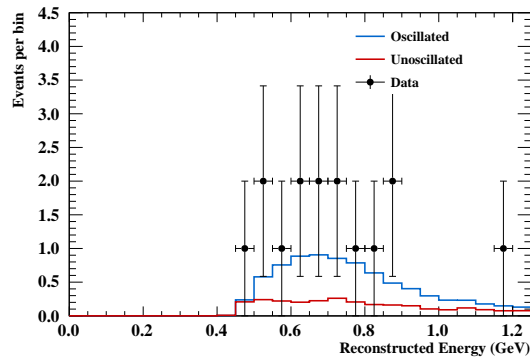
(b) FHC $1R_e$



(c) RHC $1R_\mu$

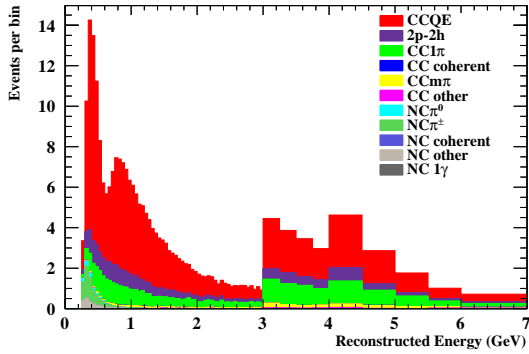


(d) RHC $1R_e$

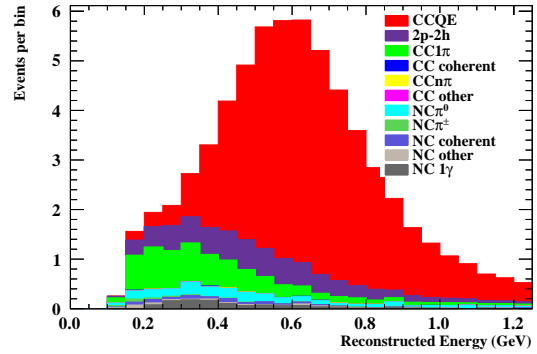


(e) FHC $1R_e$ 1d.e

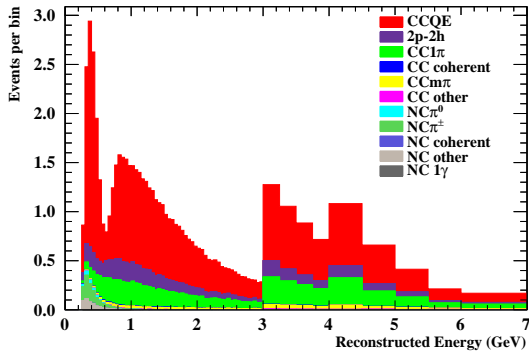
Figure 9.3: Pre-fit oscillated (red) and unoscillated (blue) reconstructed energy spectra for the FHC $1R_\mu$ (top left), FHC $1R_e$ (top right), RHC $1R_\mu$ (middle left), RHC $1R_e$ (middle right), and FHC $1R_e$ 1 d.e. (bottom) samples, along with the data spectra. The FHC and RHC $1R_\mu$ spectra are zoomed in on the 0-7 GeV range as no data are found outside that range.



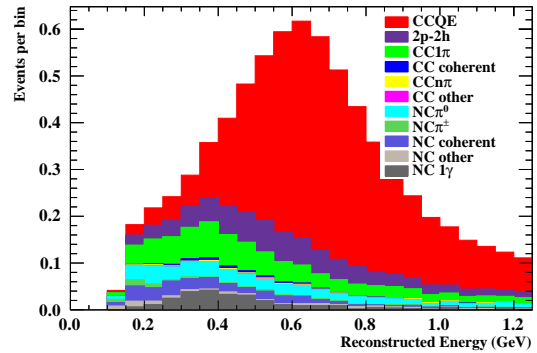
(a) FHC $1R_\mu$



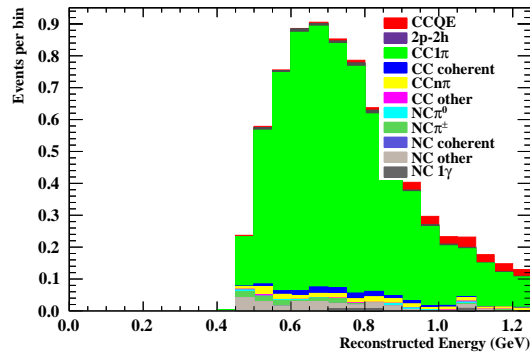
(b) FHC $1R_e$



(c) RHC $1R_\mu$



(d) RHC $1R_e$



(e) FHC $1R_e$ 1 d.e

Figure 9.4: Pre-fit reconstructed energy spectra broken down by interaction mode for the FHC $1R_\mu$ (top left), FHC $1R_e$ (top right), RHC $1R_\mu$ (middle left), RHC $1R_e$ (middle right), and FHC $1R_e$ 1 d.e. (bottom) samples. The FHC and RHC $1R_\mu$ spectra are zoomed in on the 0-7 GeV range as no data are found outside that range.

Sample	MC (unoscillated)	MC (oscillated)	Efficiency (%)	Purity (%)	Data	POT
FHC 1R $_{\mu}$	1062.7	242.3	83.7	82.9	240	
FHC 1R $_e$	14.2	63.3	67.2	81.2	74	14.7×10^{20}
FHC 1R $_e$ 1d.e	2.6	7.7	6.5	78.7	15	
RHC 1R $_{\mu}$	194.1	59.4	88.9	79.2	32	
RHC 1R $_e$	3.1	7.3	71.6	62.0	7	7.6×10^{20}

Table 9.3: Summary of number of events selected in SK in Data and MC, the efficiencies and purities of the selection, and the total POT analyzed.

9.2.1 Flux Prior Uncertainties

The T2K neutrino flux production was described in Section 3.1, and its prediction and uncertainties were described in Section 4.1. Several sources of systematic error are considered for the flux prediction, the hadron production modelling uncertainties being dominant at the peak neutrino energy. The uncertainty for the flux prediction at ND280 and SK is provided by the Beam group on T2K as a covariance matrix binned in eight categories of true neutrino energy and flavour as follows [89]:

- ND280 FHC (25 bins in total):
 - 11 bins for ν_{μ} : 0.0, 0.4, 0.5, 0.6, 0.7, 1.0, 1.5, 2.5, 3.5, 5.0, 7.0, 30.0
 - 5 bins $\bar{\nu}_{\mu}$: 0.0, 0.7, 1.0, 1.5, 2.5, 30.0
 - 7 bins for ν_e : 0.0, 0.5, 0.7, 0.8, 1.5, 2.5, 4.0, 30.0
 - 2 bins $\bar{\nu}_e$: 0.0, 2.5, 30.0
- ND280 RHC (25 bins in total). Same binning as for ND280 FHC.
- SK RHC (25 bins in total). Same binning as for ND280 FHC.
- SK RHC (25 bins in total). Same binning as for ND280 FHC.

The binning scheme was chosen to have finer binning around the oscillation maximum (~ 0.6 GeV). The uncertainties on each bin are highly correlated as shown in Figure 9.5. The uncertainties from each bin are implemented in the fit as normalization parameters. A Gaussian prior with mean 1.0 and width determined from the covariance matrix is set for each parameter. Each parameter affects the normalization of the events falling on the categories described above.

These normalization parameters and their covariance matrix (Figure 9.5) correspond to \vec{f} and V_f in Equation 8.7, respectively.

9.2.2 Cross Section Prior Uncertainties

The T2K cross section model was described in Section 4.2.2. The parameterization and uncertainties for the model are provided by the *Neutrino Interaction Working Group* (NIWG) of

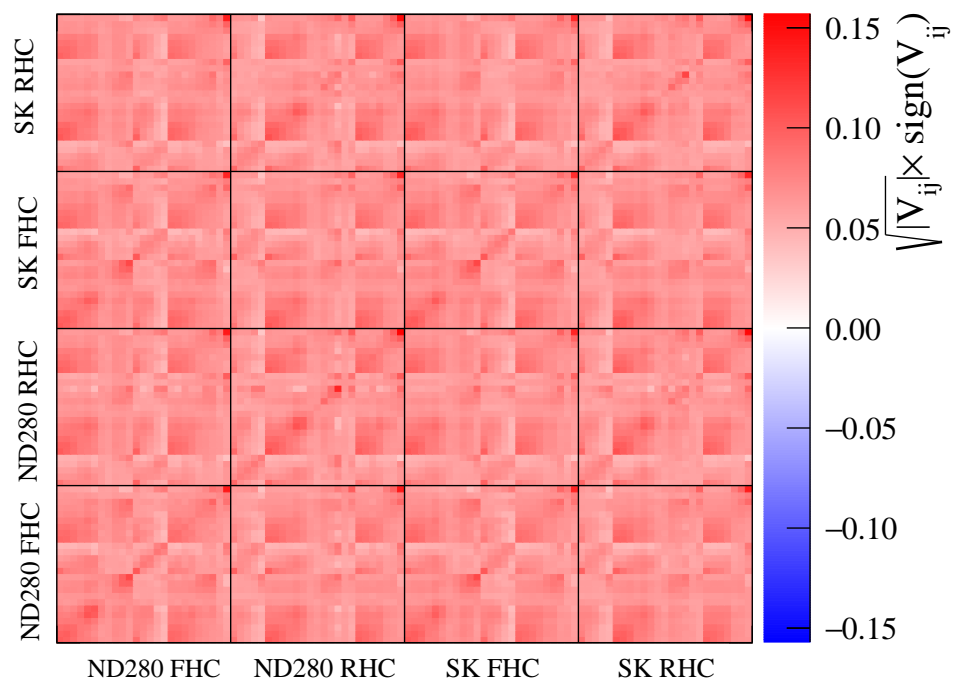


Figure 9.5: The fractional covariance matrix for the flux uncertainties. Within each group, there are further sub-divisions into sub-samples and true neutrino energy.

T2K [100] and are implemented into the MaCh3 framework through the systematic parameters listed in Table 9.4. The parameters for FSI uncertainties are discussed in Section 9.3. The prior correlation among the parameters is shown in Figure 9.6.

These parameters and their covariance matrix (Figure 9.6) correspond to \vec{x} and V_x in Equation 8.7, respectively.

Parameter	Type	Prior value	Prior uncertainty	Mode
M_A^{QE} (GeV/ c^2)	Shape	1.20	Flat	
$p_F^{12\text{C}}$ (MeV/ c)	Shape	217.00	Flat	CCQE
$p_F^{16\text{O}}$ (MeV/ c)	Shape	225.00	Flat	
2p2h norm ν	Normalization	1.00	Flat	
2p2h norm $\bar{\nu}$	Normalization	1.00	Flat	
2p2h norm ^{12}C to ^{16}O	Normalization	1.00	0.20	2p2h
2p2h shape ^{16}O ν	Shape	1.00	3.00	
2p2h shape ^{12}C ν	Shape	1.00	3.00	
BeRPA A	Functional	0.59	0.12	
BeRPA B	Functional	1.05	0.21	
BeRPA D	Functional	1.13	0.17	CCQE
BeRPA E	Functional	0.88	0.35	
BeRPA U	Functional	1.20	Fixed	
C_5^A	Shape	0.96	0.15	
M_A^{RES} (GeV/ c^2)	Shape	1.207	0.15	RES
ISO background	Shape	0.96	0.40	
ν_e/ν_μ	Normalization	1.0	0.03	ν CC
$\bar{\nu}_e/\bar{\nu}_\mu$	Normalization	1.0	0.03	$\bar{\nu}$ CC
CC DIS	Shape	0.00	0.40	CC DIS
CC Coh ^{12}C	Normalization	1.00	0.30	CC Coh
CC Coh ^{16}O	Normalization	1.00	0.30	CC Coh
NC Coh	Normalization	1.00	0.30	NC Coh
NC1 γ	Normalization	1.00	1.00	NC1 γ
NC Other (near)	Normalization	1.00	0.30	NC Other
NC Other (far)	Normalization	1.00	0.30	NC Other

Table 9.4: Systematic parameters for cross section uncertainties. The relevant interaction mode is specified in the last column. The flat prior choices are addressed in Section 9.4.

There are three types of cross section systematic parameters:

- (1) *Normalization* parameters, which simply weight a given event, regardless of its energy.
- (2) *Functional* parameters, whose effect is parameterized by a functional form in terms of a kinematic variable (in this case Q^2).
- (3) *Shape* parameters which introduce an energy dependence to the effect. This dependence is implemented through splined response functions, built by evaluating the weight for a particular MC event at evenly spaced points in the parameter value (between 2 and 13

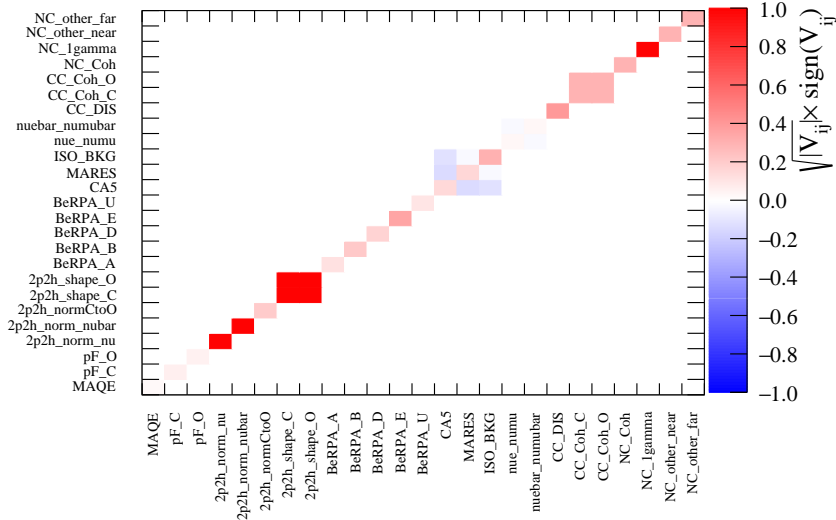


Figure 9.6: Prior covariance matrix for the cross section systematic parameters. Details are discussed in the text.

points, depending on the parameter) and creating a cubic spline to interpolate between the points. This spline is then evaluated at the desired value of the parameter, and the result applied to the event as a weight. For the ND280 MC, the splines are calculated event-by-event. For the SK MC, the events are binned in reconstructed and true neutrino energy, and splines created from the averaged weight calculated for a particular kinematic bin. This was done to reduce the computational load on the analysis. Some examples of splined response functions are presented in Section 9.3.1.

The last row of Table 9.4 specifies the interaction mode for which each parameter is valid. The M_A^{QE} and p_F parameters are modelled following the dipole form factor and RFG implementations described in Equations 4.7 and 4.1. An attempt to fit the model to CCQE external data [99] to determine the prior uncertainties for these parameters was unsuccessful, and a flat prior is used instead. The RPA effect is implemented as an *effective* Q^2 -dependent weighting of the nominal CCQE model. The broad features of the RPA correction relative to the free nucleon cross section are a suppression at low Q^2 , an enhancement at intermediate Q^2 , and equivalence at high Q^2 , as shown in Figure 9.7. The effect is parameterized in terms of Bernstein polynomials [180] to avoid strong correlations across the five free parameters (BeRPA A , B , C , D , and U).

$$f(x) = \begin{cases} A(1-x')^3 + 3B(1-x')^2x' + 3p_1(1-x')x'^2 + Cx'^3, & x < U \\ 1 + p_2 \exp(-D(x-U)), & x > U \end{cases} \quad (9.1)$$

where $x = Q^2$, $x' = x/U$. Note that the parameters A , B , C and p_1 are simply normalization

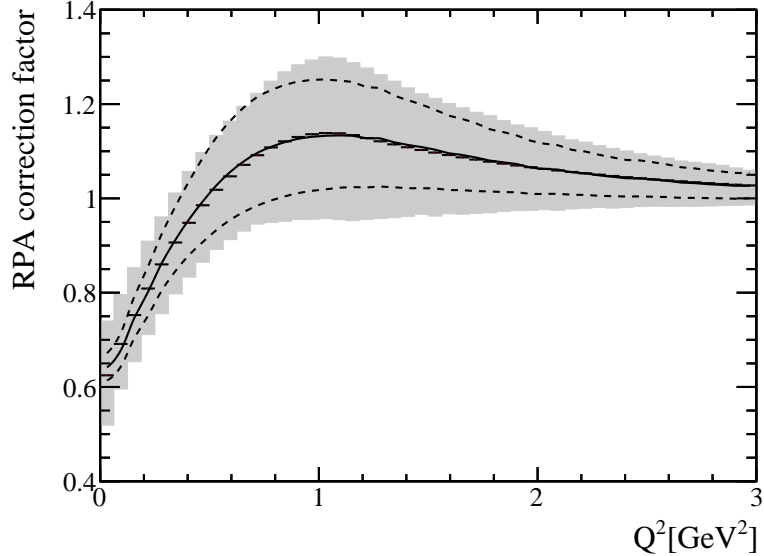


Figure 9.7: The Nieves relativistic RPA correction factor relative to the unmodified CCQE cross section is shown as a function of Q^2 (black solid line), along with its $\pm 1\sigma$ uncertainties (dashed black line). The BeRPA implementation best fit is also shown (black data points), along with the $\pm 1\sigma$ uncertainties (grey band) obtained from the uncertainties in the BeRPA parameters shown in Table 9.4. Reproduced from [100].

factors for the 4 basis functions, and p_1 and p_2 absorb the continuity condition at U .

$$p_1 = C + \frac{UD(C-1)}{3}$$

$$p_2 = C - 1$$

The nominal value for the BeRPA parameters is obtained from a fit to the Q^2 function provided by the authors of the Nieves model [110]. The prior uncertainties are set to cover the theoretical uncertainties also provided by the authors of the model. These effective parameters are then tuned using ND280 data.

While the existence of 2p2h interactions has been established from electron scattering data, the various models for neutrino interactions available differ by up to a factor of two [108, 109]. In addition, these interactions can not be discriminated from CCQE interactions by the data from the near detector, which is binned in muon kinematics. A flat prior is assumed for the overall normalization of neutrino and antineutrino 2p2h events, while an additional parameter which scales the effect from carbon to oxygen is applied with a 20% uncertainty.

A 2p2h shape parameter allows the model to control the relative contribution from the two sources of 2p2h interactions: Meson Exchange Currents (MEC) which are dominated by Δ pionless decay, or nucleon-nucleon correlations. Separate uncorrelated parameters are implemented for carbon and oxygen interactions, and flat priors are assumed.

Uncertainties in CC and NC RES interactions are modelled by the M_A^{RES} , C_A^5 , from the Rein-

Seghal model in NEUT. The resonant production is a pure isospin $I = 3/2$ process, therefore processes with $I = 1/2$ constitute a background. Their best fit values and priors are obtained from a fit to neutrino scattering data from the ANL and BNL bubble chamber experiments [101], as well as more recent experiments on nuclear targets [181].

Only data from ν_μ interactions in the near detector is considered. Two parameters that account for the differences between ν_e and ν_μ cross sections in neutrino and antineutrinos are implemented. The different phase-space reachable by the lepton, radiative corrections at tree level, and effects of second class currents on the interaction form factors are among the possible sources of discrepancy [182].

Normalization parameters with large priors for CC and NC coherent interactions are included, as well as for other rare NC processes such as pion resonant interactions where a photon is produced (NC1 γ).

9.2.3 ND280 Detector Model Prior Uncertainties

The ND280 detector and its simulation were described in Sections 3.2 and 4.4.1. Multiple sources of systematic uncertainty are evaluated for the FGD and TPC detectors by the *NuMu* physics group of T2K from the comparison of simulated and real data in control samples [183]. Some of the uncertainties evaluated are: FGD tracking efficiency, FGD PID, FGD fiducial volume mass, TPC clustering efficiency, TPC tracking efficiency, TPC track charge identification, TPC momentum scale and resolution, and the matching of tracks from the FGD and TPC.

The uncertainty for the ND280 detector model is provided by the *Beam And ND280 Flux extrapolation task Force* (BANFF) group on T2K as a covariance matrix binned in 580 ($p_\mu, \cos \theta_\mu$) bins. Separate bins for each sample from each FGD are used, but the binning is coarser than that one used for the selections themselves (used in Figures 9.1 and 9.2).

The covariance is obtained from the variations induced by 2000 throws of the input detector systematics to the number of events in each bin for each sample. This allows for event weights and observables to vary, and for events to migrate across samples. The fractional covariance matrix is shown in Figure 9.8.

The uncertainty from secondary interactions (SI) is included in this matrix and is treated effectively as a detector effect. As was mentioned in Section 4.4.1, hadronic interactions in the ND280 detector are currently simulated using the Bertini cascade model of GEANT4 [120]. This model has been found to be in significant disagreement with external pion scattering data (see Appendix E). For this reason, a large uncertainty is currently assigned to these processes, and it dominates the ND280 detector error budget. In future analyses, the hadronic interactions will be simulated by the NEUT cascade model using the `NeutG4CascadeInterface` package [121, 122]. It will then be possible to use similar methods as those discussed in Section 9.3 to uniformly propagate this uncertainty, while taking advantage of the tuning of the NEUT cascade model described in Chapter 7.

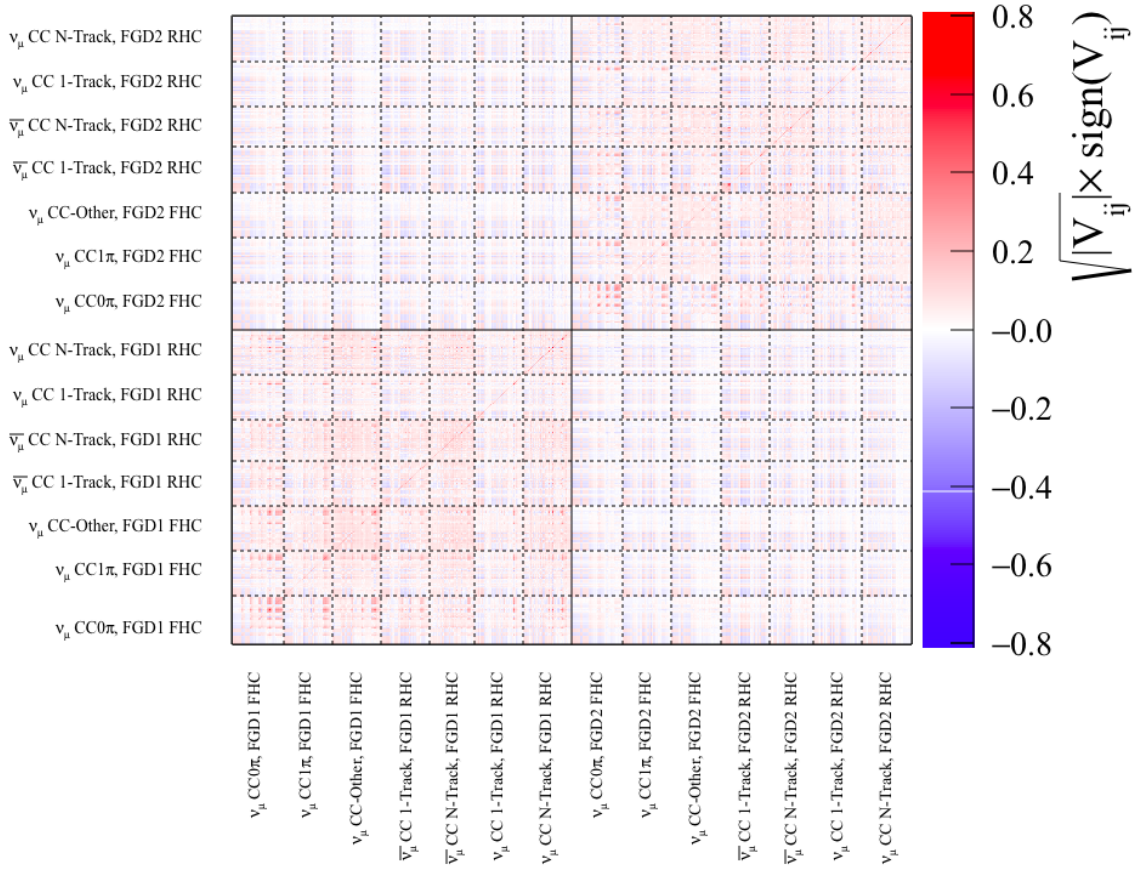


Figure 9.8: ND280 detector fractional covariance matrix. The bins within each sample are ordered in increasing momentum intervals, each containing all angular bins, from forward-going to backwards-going.

9.2.4 SK Detector Model Prior Uncertainties

The SK detector and its simulation were described in Sections 3.3 and 4.4.2. The uncertainties in the modelling of the detector response to CC interactions are obtained from Data and Monte Carlo comparisons of samples of atmospheric neutrino interactions in the detector, and cosmic muons stopping in the detector. The response to NC interactions is studied using *hybrid* π^0 samples. A *hybrid* π^0 is constructed by combining a reconstructed electron ring from a data event with a simulated electron ring, such that their invariant mass is that of a π^0 . Uncertainties arising from the vertex location, ring identification, ring counting, background caused by flasher events, and π^0 tagging are included.

An MCMC fit of the MC to the Data is used to parameterize the discrepancies in the detector efficiency MC simulation, relative to the Data. These discrepancies are then propagated as an uncertainty in the number of T2K selected events, shown in Table 9.3. A fractional covariance matrix consisting of 45 bin-normalization parameters is provided by the T2K-SK group [176, 184]. Each bin represents a reconstructed energy bin, as summarized in Table 9.5.

Sample Type	Bin Index	Interaction Type	E_{rec} Bins (GeV)
FHC $1R_e$	1-3	Oscillated $\nu_e + \bar{\nu}_e$ CC	[0.0, 0.35, 0.8, 1.25]
	4-6	Beam $\nu_\mu + \bar{\nu}_\mu$ CC	[0.0, 0.35, 0.8, 1.25]
	7-9	Beam $\nu_e + \bar{\nu}_e$ CC	[0.0, 0.35, 0.8, 1.25]
	10-12	All NC	[0.0, 0.35, 0.8, 1.25]
FHC $1R_\mu$	13-15	$\nu_\mu + \bar{\nu}_\mu$ CCQE	[0.0, 0.4, 1.1, 30.0]
	16	$\nu_\mu + \bar{\nu}_\mu$ CC-nonQE	Single bin
	17	$\nu_e + \bar{\nu}_e$ CC	Single bin
	18	All NC	Single bin
RHC $1R_e$	19-21	Oscillated $\nu_e + \bar{\nu}_e$ CC	[0.0, 0.35, 0.8, 1.25]
	22-24	$\nu_\mu + \bar{\nu}_\mu$ CC	[0.0, 0.35, 0.8, 1.25]
	25-27	$\nu_e + \bar{\nu}_e$ CC	[0.0, 0.35, 0.8, 1.25]
	28-30	All NC	[0.0, 0.35, 0.8, 1.25]
RHC $1R_\mu$	31-33	$\nu_\mu + \bar{\nu}_\mu$ CCQE	[0.0, 0.4, 1.1, 30.0]
	34	$\nu_\mu + \bar{\nu}_\mu$ CC-nonQE	Single bin
	35	$\nu_e + \bar{\nu}_e$ CC	Single bin
	36	All NC	Single bin
FHC $1R_e$ 1d.e.	37-38	Oscillated $\nu_e + \bar{\nu}_e$ CC	[0.0, 0.8, 1.25]
	39-40	$\nu_\mu + \bar{\nu}_\mu$ CC	[0.0, 0.8, 1.25]
	41-42	$\nu_e + \bar{\nu}_e$ CC	[0.0, 0.8, 1.25]
	43-44	All NC	[0.0, 0.8, 1.25]
All	45	Energy Scale	Single bin

Table 9.5: Kinematic binning definition used for the SK detector and FSI+SI+PN systematic uncertainties.

The final parameter in the covariance matrix corresponds to the energy scale uncertainty. This is the only systematic uncertainty which is not applied as a weight to an MC event; instead, the reconstructed energy itself of every event is adjusted according to the value of the parameter, before the MC is binned. The energy scale uncertainty used for this analysis is 2.4% regardless of the energy of the neutrino [185].

In addition to the detector modelling uncertainties, the SK covariance matrix used in the oscillation analysis contains additional systematic uncertainties. The uncertainties from Final State and Secondary Interactions (SI), as well as those from Photo-Nuclear (PN) effects have been traditionally assumed uncorrelated, parameterized using the same binning as Table 9.5, and added in quadrature. Improvements in the treatment of FSI and SI uncertainties will be discussed in Section 9.3. Most importantly the FSI effects are no longer added to the detector matrix. Additionally, the SI uncertainties have been reduced by using the results of the analysis presented in Chapter 7.

Photo-Nuclear effects refer to the process by which one of the photons from a π^0 decay is absorbed inside the nucleus where the neutrino interaction occur. This might cause a NC π^0 event to be identified as a CC ν_e interaction, affecting the FHC and RHC 1 R_e samples. A conservative 100% uncertainty is assumed for these events due to the lack of external measurements for this process.

The fractional covariance matrix containing SK detector, SI, and PN uncertainties is shown in Figure 9.9.

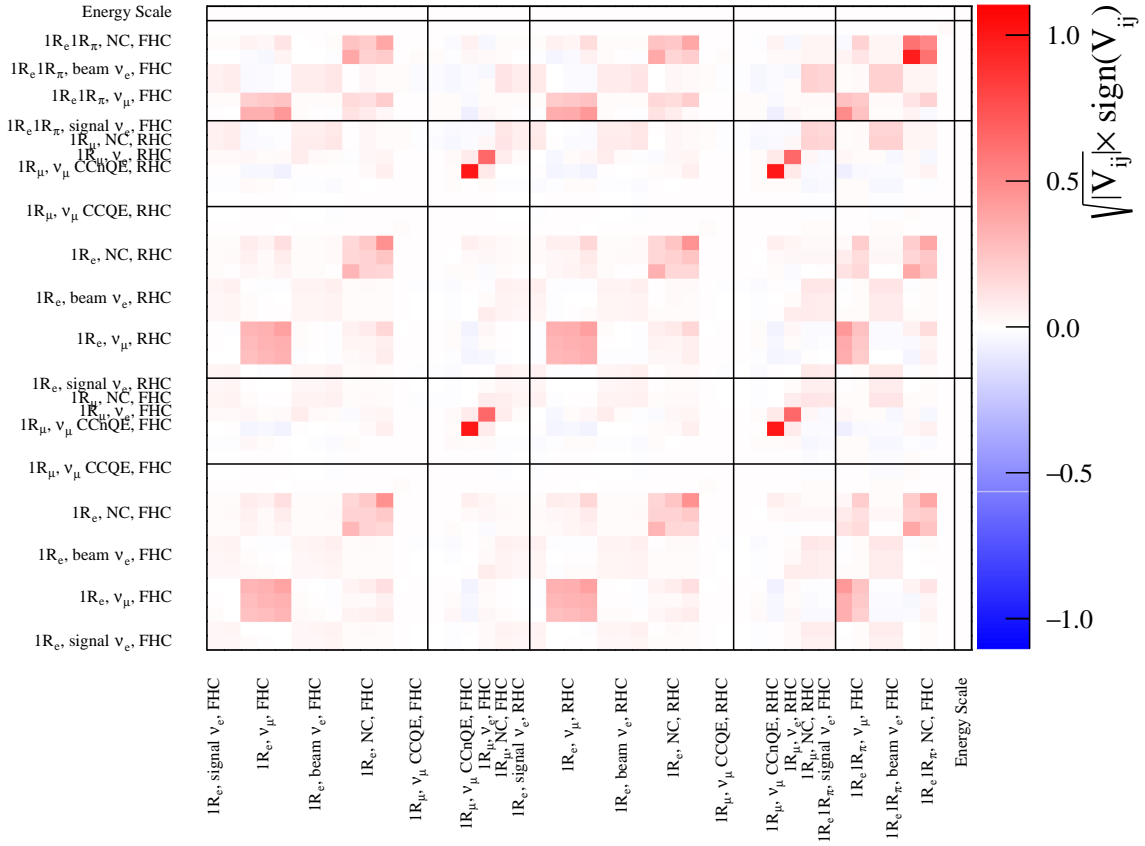


Figure 9.9: The fractional covariance matrix used for the SK detector + SI + PN uncertainties. The binning is described in Table 9.5.

9.3 Final State and Secondary Interaction Uncertainties

The uncertainties from final state and secondary interactions are propagated to the observables in ND280 and SK by propagating the uncertainties assigned to the FSI parameters of the NEUT cascade model (described in Sections 4.3.1 and 4.3). The constraints for the FSI parameters obtained in Chapter 7 will be used in an T2K oscillation analysis for the first time in the analysis presented in this thesis.

Figure 9.10 shows a comparison of the previous FSI prior uncertainties used in T2K analyses (obtained from T2K-TN-032 [162]), and the covariance matrix derived in Chapter 7. Following what was shown in Figures 7.10 and 7.12, the improved tuning of the NEUT cascade will result in reduced FSI and SI uncertainties.

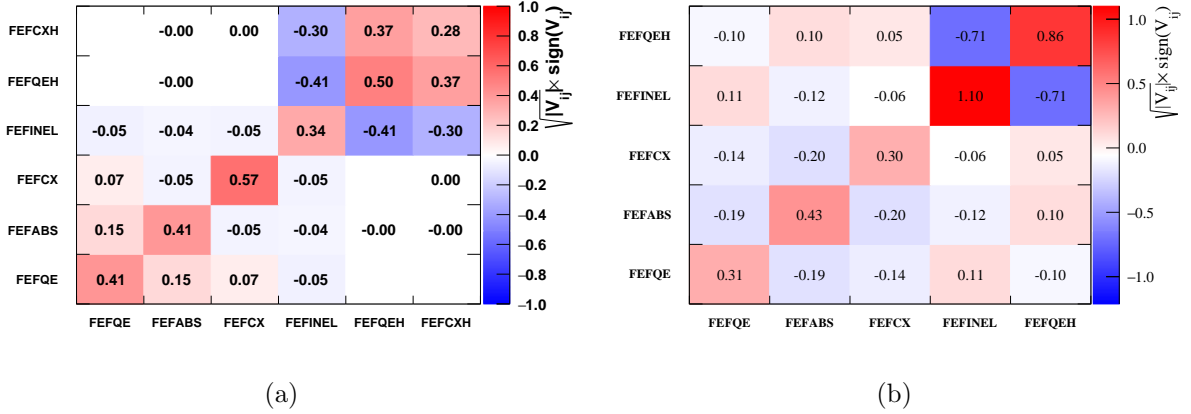


Figure 9.10: (a) Previous prior uncertainties of the FSI parameters used in T2K analyses, obtained from [162]. (b) Prior uncertainties of the FSI parameters used for this analysis, derived from the analysis presented in Chapter 7.

Ideally, the effect of the FSI uncertainties would be propagated to ND280 and SK event samples by running the NEUT cascade algorithm for variations of the FSI parameters at each step of the Markov Chain and re-applying the event selections. Unfortunately, this process is computationally prohibitive and alternatives must be considered. Previous T2K oscillation analyses propagated the constraints from Figure 9.10a by following an approach similar to that followed for the flux and detector uncertainties. The variations to the selected samples induced by a set of randomly correlated throws from the FSI covariance matrix would be encoded into a covariance matrix V_{ij} with the same binning as that used for the detector uncertainties (i.e. Table 9.5 for SK).

$$V_{ij} = \frac{1}{n} \sum \frac{(N_i^k - N_i^{nom})(N_j^k - N_j^{nom})}{N_i^{nom} N_j^{nom}} \quad (9.2)$$

where n is the number of throws, i and j are the kinematic bins used for the detector uncertainties, N_i^{nom} is the nominal event rate for a given bin i , and N_i^k is the event rate for a given bin i for the

k -th throw. The covariance matrix produced would then be added to the corresponding detector covariance. While this method is mathematically correct, it has disadvantages. The binning used for detector uncertainties was optimized only for that purpose. In the case of ND280 the reconstructed muon kinematic information is insensitive to FSI effects, while in the case of SK the E_{rec} kinematic binning (see Table 9.5) is too coarse to properly represent the effect of FSI variations to the neutrino energy spectra (See Figures 9.13, 9.14, and 9.15).

In addition, as was explained in Section 4.2, the final state interactions are a nuclear effect, and as such, its uncertainties are expected to be correlated to that of the cross section model parameters described in Section 9.2.2. It is then necessary to have the ability to vary the FSI parameters within the Markov Chain. This is achieved using response functions, as discussed in Section 9.3.1.

Secondary interactions at SK are also modelled using the NEUT cascade model, which means that the constraints from the FSI parameters are also used to evaluate the uncertainty. Analogous to the propagation of FSI uncertainties, it is computationally prohibitive to run the cascade algorithm for each secondary interaction in the detector at every step of the Markov Chain. Additionally, because pions can interact on multiple occasions, using the framework of response functions may not be adequate. This will be further investigated for future analysis. For this analysis, the effect of variations of the pion re-interaction probability to the SK spectra is evaluated using the method prescribed by Equation 9.2. The weight for each event is calculated as:

$$w_{\text{SI}}(f_{\text{FSI}}) = \prod_i \frac{\sigma_i^{\text{Throw}}(p_i, f_{\text{FSI}})}{\sigma_i^{\text{Nominal}}(p_i)} \quad (9.3)$$

where $w_{\text{SI}}(f_{\text{FSI}})$ is the SI event weight for a given throw (f_{FSI}) of the FSI parameters, the index i runs over all the pion secondary interactions in the event, p_i is the pion incident momentum at each secondary interaction vertex, and $\sigma_i^{\text{Nominal}}(p_i)$ is the nominal macroscopic cross section for the interaction process at vertex i . The macroscopic cross section at the vertex i for a given throw of the FSI parameters, $\sigma_i^{\text{Throw}}(p_i, f_{\text{FSI}})$, is obtained by using a GNU-Octave interpolation similar to that used in Section 7.3.2.

Figure 9.11 shows the diagonal elements of the resulting fractional error matrices ($\sqrt{V_{ij}}$) for the SI uncertainties obtained from using the constraints from Figure 9.10a and 9.10b. A reduction of $\sim 25\%$ in the size of the uncertainty is achieved by applying the results of the improved tuning of the NEUT cascade model presented in Chapter 7. This reduction of the SI uncertainties was already included in the matrix shown in Figure 9.9.

9.3.1 Splined Response Functions for FSI Parameters

Response functions for non-linear parameters in the cross section model and FSI model are built by computing the effect of the parameter (the weight) for a set of values around the parameter nominal value. These *knots* are then connected using a cubic spline that allows

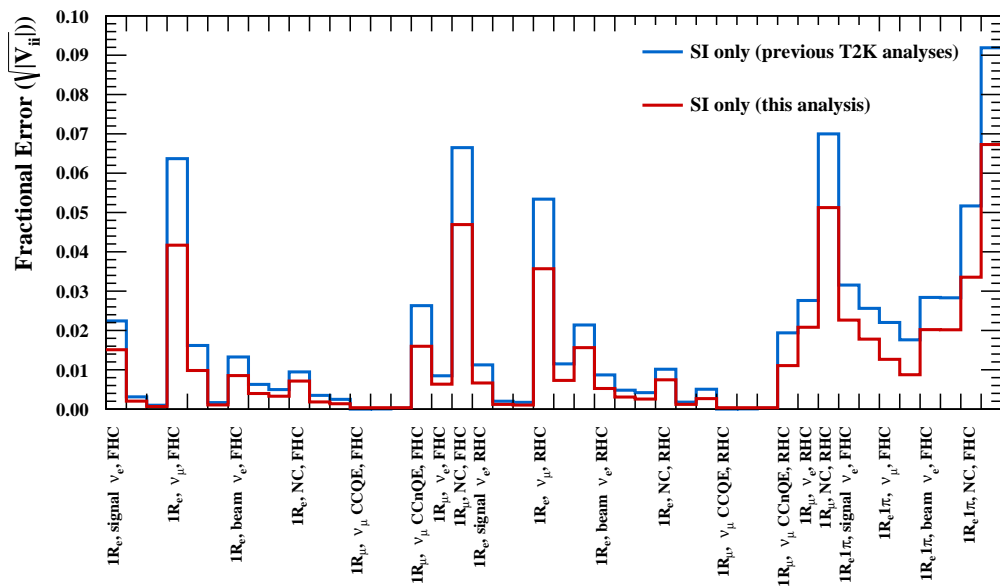


Figure 9.11: The diagonal elements of the fractional covariance matrix for SI-only uncertainties. The binning is described in Table 9.5. The uncertainties obtained by propagating the priors from Figure 9.10a (blue line) and Figure 9.10b (red line) are shown. A reduction in the SI uncertainty is achieved from the tuning of the NEUT cascade model presented in Chapter 7.

interpolation to any value of the parameter. These objects are built using the `TSpline3` class from ROOT [174].

For ND280, the response functions are calculated for each event in the MC. This is currently not possible for SK due to the number of events in the MC and RAM constraints at the computing facilities used for this analysis. Rather than calculating the response functions for each event, the samples are binned in a multidimensional space (NEUT mode, E_{rec} , E_{true} (and θ_e for $1R_e$ samples)) and the response functions are computed for each bin. Figure 9.12 shows an example of a splined response function for $CC1\pi$ events in the FHC $1R_\mu$ sample for a given bin. This binning was chosen to match that used by the response functions for cross section parameters.

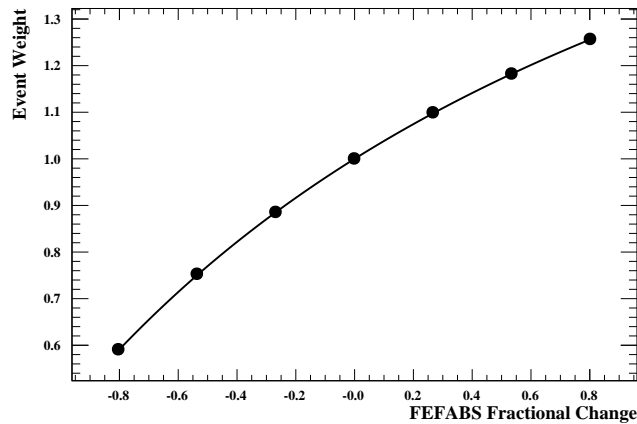


Figure 9.12: Sample response function used to map the FEFABS parameter response as a function of fractional change to the parameter. The effect is evaluated for seven values of the parameters (black dots) and is interpolated using a cubic spline function (black line). This spline in particular corresponds to $CC1\pi$ events of given true and reconstructed energy in the FHC $1R_\mu$ sample.

9.3.2 Validations of the FSI Response Functions

There are multiple reasons to validate the use of splined response functions in the analysis. The simplest one arises from the large number of splines (~ 10000) and the inherent complexity of correctly constructing, loading, and evaluating them. It is also important to confirm that the binning selected for the splines does not have a large effect on the calculated weights. Finally, the validity of the assumption that the effect of each individual parameter can be factorized when doing simultaneous variations of the parameters must be checked.

9.3.2.1 Independent Variations of the FSI Parameters

In order to test the soundness and validity of the response functions, the variations to the SK spectra induced from $\pm 1\sigma$ individual shifts of each FSI parameter were calculated under three

regimes:

- (1) Running the NEUT cascade with varied FSI parameters for each event. This is the “ideal” case to be used as a benchmark.
- (2) Weights calculated from the splined response functions binned in a multidimensional space (NEUT mode, E_{rec} , E_{true} (and θ_e for $1R_e$ samples)) using a stand-alone C++ application. This was an intermediate validation step before implementing the response functions in the MaCh3 framework.
- (3) Weights calculated from splined response function directly in the MaCh3 OA framework.

Figure 9.13 shows the effect of $+1\sigma$ variations of each FSI parameter to the SK spectra for the FHC $1R_\mu$ sample as a ratio to the nominal spectra. The correspondence between the variations under the three regimes outlined above signals the success of the validation check. It should be noted that the energy scale uncertainty was not applied when loading the sample in the second validation regime, resulting in a small difference in the samples (black line vs. green line in the top left panel of Figure 9.13).

Figures 9.14 and 9.15 show the same validation for the FHC $1R_e$ and the FHC $1R_e$ 1d.e. samples. The finer binning (additional θ_e bins) allows for an even more accurate mapping of the FSI induced variations of the spectra. The validations for -1σ variations of the spectra yield similar conclusions.

The peaked shape around 0.6 GeV in the FEFABS $+1\sigma$ variation of the FHC $1R_\mu$ spectra shown in Figure 9.13 is of particular importance. As was discussed in Chapters 2 and 3, the T2K neutrino flux was designed to peak at 0.6 GeV since this is the location of the first oscillation maximum for ν_μ disappearance (see Figure 3.10b). The depth of the oscillation dip is closely related to $\sin^2 \theta_{23}$, while the location as a function of E_ν is dictated by Δm_{23}^2 . The coarse binning used for the SK detector uncertainties (Table 9.5) completely washes out this E_ν dependent FSI effect, and induces a bias. As will be shown in Chapter 10, the primary effect of using splined response functions for FSI parameters in the T2K oscillation analysis is visible in the $\sin^2 \theta_{23}$ and Δm_{23}^2 posterior probabilities.

9.3.2.2 Simultaneous Variations of the FSI Parameters

The assumption that the effect of a simultaneous variation of the FSI parameters can be factorized into independent variations must be tested, that is:

$$w_{\text{FSI}}(\text{FEFQE}, \text{FEFABS}, \text{FEFCX}, \text{FEFINEL}, \text{FEFQEH}) = w(\text{FEFQE}) \times w(\text{FEFABS}) \times w(\text{FEFCX}) \times w(\text{FEFINEL}) \times w(\text{FEFQEH}) \quad (9.4)$$

where w_{FSI} represents the FSI event weight. This was achieved by selecting a set of simultaneous variations representative of the 1σ FSI uncertainty band from T2K-TN-032 [162] and calculating

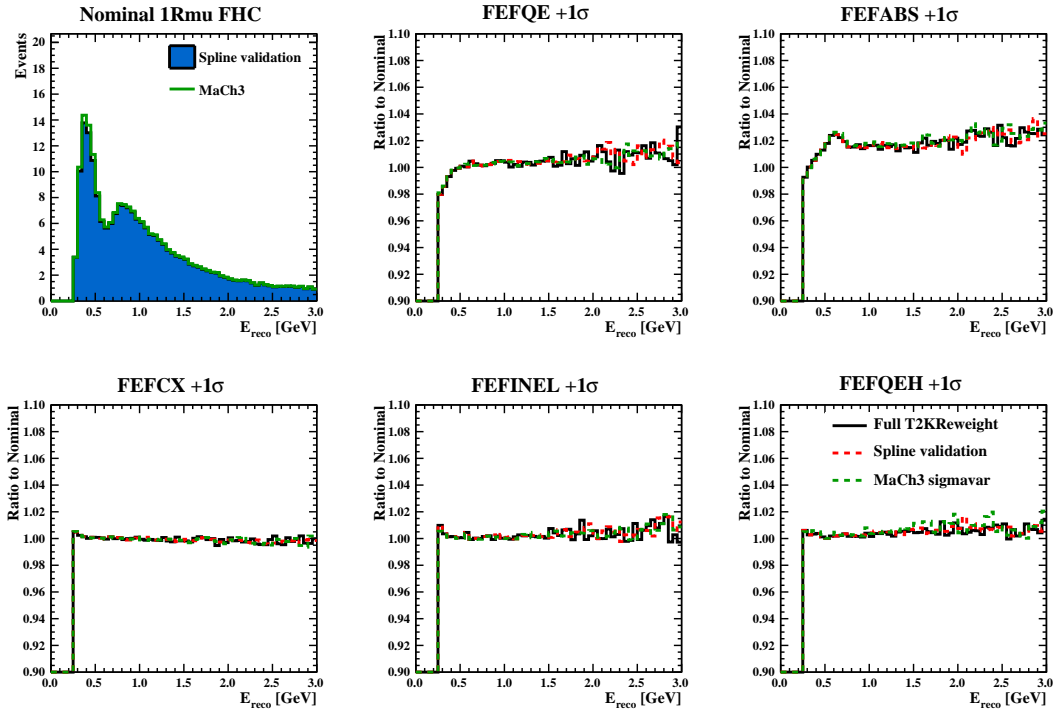


Figure 9.13: Effect of $+1\sigma$ variations of the FSI parameters to the FHC $1R_\mu$ sample. The green line in the top left panel represents the oscillated sample and is equivalent to Figure 9.4. The weights are calculated using the full reweighting of the cascade (black line), the splined response functions in a stand-alone C++ application (dashed red line), and the splined response functions within the MaCh3 framework (dashed green line).

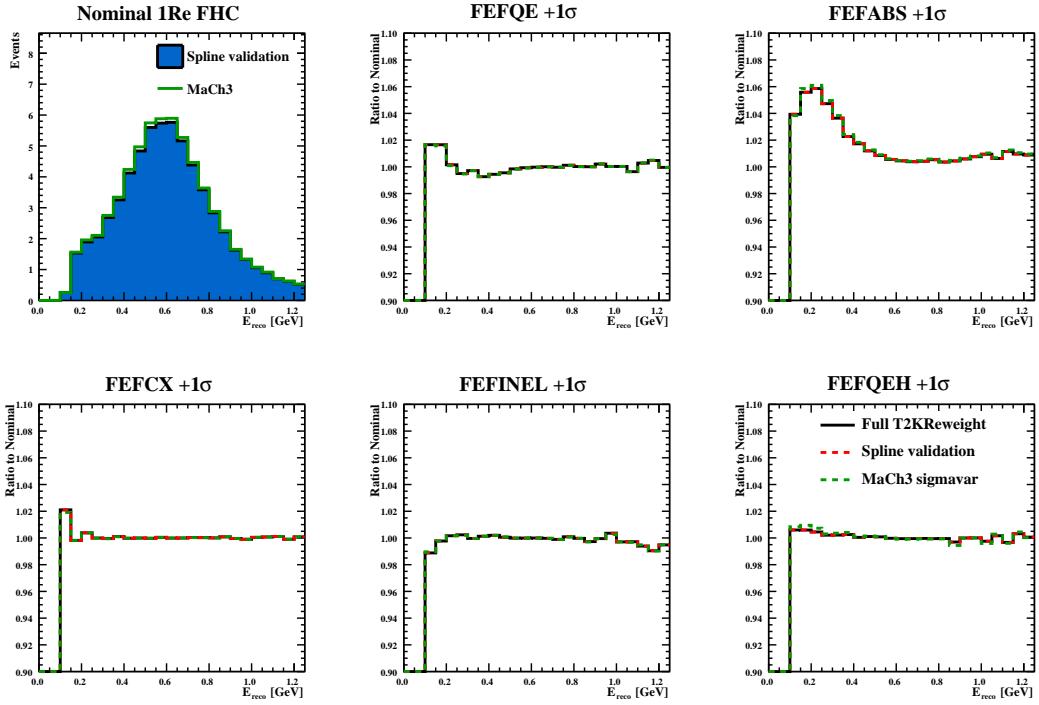


Figure 9.14: Effect of $+1\sigma$ variations of the FSI parameters to the FHC $1R_e$ sample. The figure layout is the same as Figure 9.13.

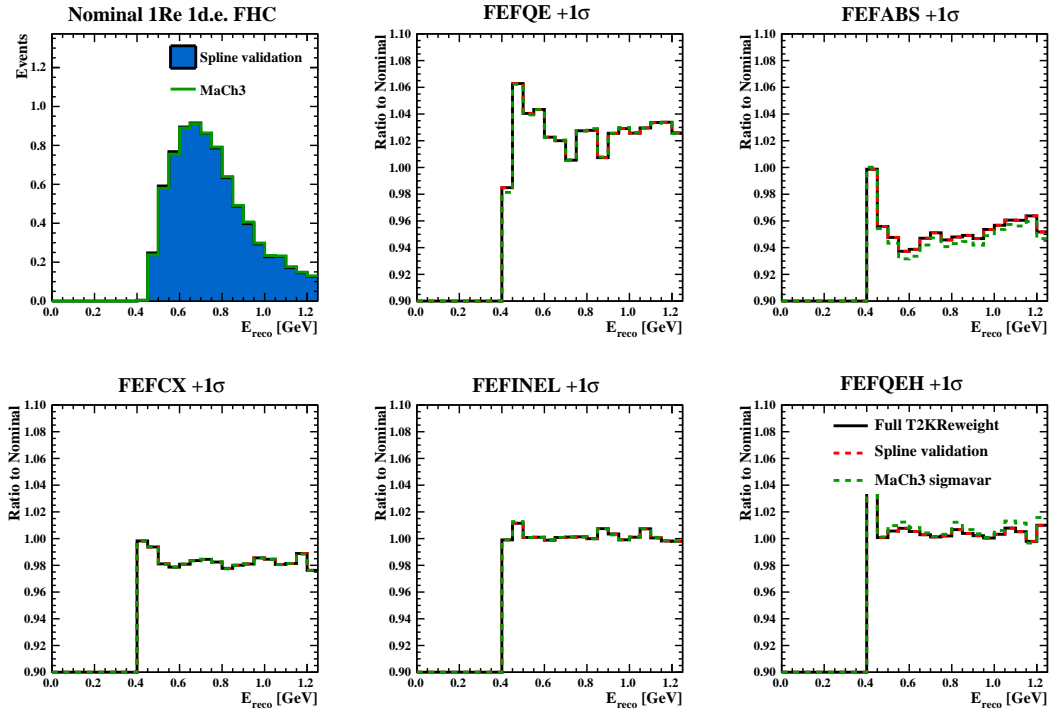


Figure 9.15: Effect of $+1\sigma$ variations of the FSI parameters to the FHC $1R_e$ 1d.e. sample. The figure layout is the same as Figure 9.13.

an FSI uncertainty matrix for the SK samples using the same binning as the SK detector matrix (Table 9.5). Similarly to Section 9.3.2.1, this was done under two regimes:

- (1) Running the NEUT cascade with varied FSI parameters for each event. This is the “ideal” case to be used as a benchmark.
- (2) Weights calculated from the splined response functions binned in NEUT mode vs. E_ν vs. E_{rec} (vs. θ_e for $1R_e$ samples).

Figure 9.16 show the matrices in both regimes. The entries in the histograms agree to better than 3.5%. From Figures 9.13, 9.14, and 9.15, the characteristic size of the effect of 1σ variations of FSI parameters to the SK spectra is below 10%, so this approximation is reasonable at the 1% level.

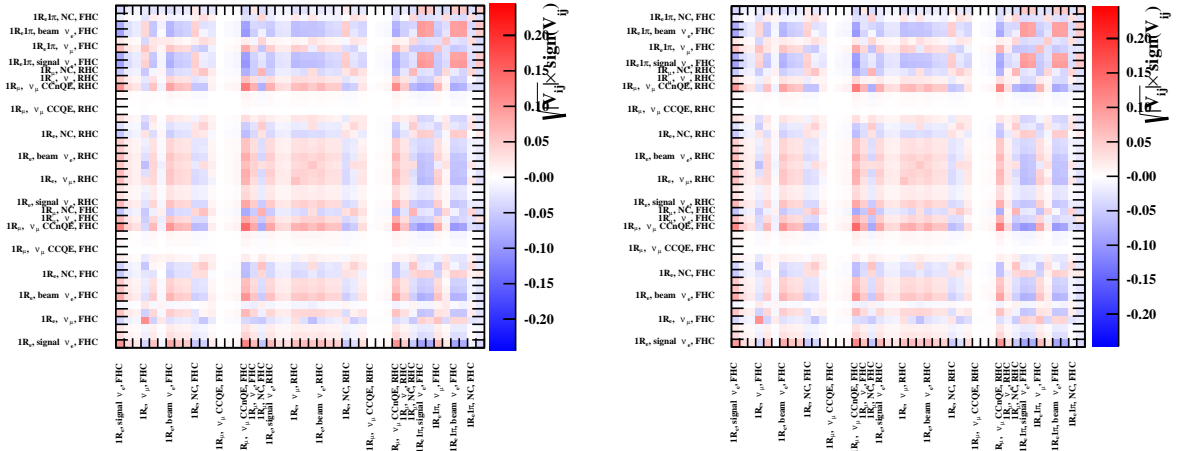


Figure 9.16: FSI Uncertainty matrices with the binning used for the SK detector uncertainties (Table 9.5) calculated from a set of simultaneous variations of the FSI parameters. The matrix to the left was calculated using the full reweighting of the NEUT cascade, while the matrix to the right was calculated using the splined response functions. The matrices agree to better than 3.5%.

9.3.2.3 Likelihood Scans

The constraints from the systematic uncertainties are introduced as penalty terms to the likelihood, as was discussed in Section 8.1. The correct implementation of this term is checked by scanning the likelihood for different values of the FSI parameters. Figure 9.17a shows the expected Gaussian shape of the penalty term for the FEABS parameter. Similar Gaussian functions with widths determined by the prior uncertainties in Figure 9.10b are obtained for the other FSI parameters.

The variation of the FSI parameter also affects the observed number of events, as was shown previously. That means that variations of the FSI parameters also have an impact on the Poisson

terms of Equation 8.1. Figure 9.17b shows the effect of such variations to the Poisson term for the FHC $1R_\mu$ sample. The continuous dependence to variations of the parameter is sufficient for this check. Similar shapes are obtained for other iterations of SK samples and FSI parameters.

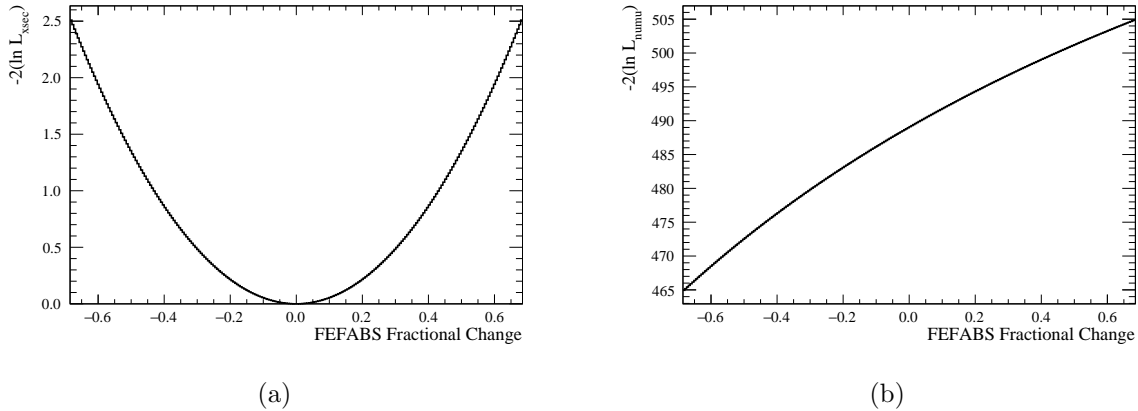


Figure 9.17: Likelihood scan for variations of the FEFABS parameters for (a) the penalty term, (b) the Poisson term for the FHC $1R_\mu$ sample. The likelihood was defined in Equation 8.1.

9.3.3 Propagating the ND280 Constraints of FSI to SK

One additional significant advantage of this updated framework is that it introduces the ability to propagate the FSI parameters constraints from ND280 data to the SK MC prediction. As will be shown in Section 10.2.1, migrations among the ND280 samples (i.e., $CC1\pi$ to $CC0\pi$ from pion absorption) are able to further constrain the FSI parameters in the oscillation fit. These constraints can then be naturally propagated to the SK samples within the fit, leading to smaller post-fit FSI uncertainties.

9.4 Effect of Prior Systematic Uncertainties

Table 9.6 shows the impact of the systematic parameters to the SK samples described in Section 9.1.2, as an uncertainty on the total number of events in each sample. The uncertainty is calculated by throwing 5,000 times each set of parameters from Gaussian distributions according to the prior covariance matrices introduced in the previous sections, accounting for their correlations. The errors are presented as $\Delta N_{SK}/N_{SK} \times 100$, where N_{SK} is the mean and ΔN_{SK} is the RMS of the distribution of the number of predicted events obtained from the throws, and is calculated separately for each sample.

The prior of some parameters in the cross section model is assumed flat (see Table 9.4). Instead of throwing from Gaussian distributions, these parameters are thrown uniformly within the ranges specified below. These ranges were provided by the NIWG group and allow for maximum freedom of the components of the model controlled by these parameters.

Error Source	FHC 1R _μ	RHC 1R _μ	FHC 1R _e	RHC 1R _e	FHC 1R _e 1d.e
Flux	7.6	6.8	8.5	7.5	8.5
Cross section	12.5	10.0	13.4	10.0	8.3
FSI (previous T2K analyses)	2.5	2.0	2.1	1.5	9.1
FSI (this analysis)	2.0	1.7	1.6	0.9	7.5
SI+PN (only)	0.4	0.3	1.2	2.2	2.3
SK Detector (only)	2.3	1.8	3.1	4.4	16.9
SK Detector+SI+PN	2.4	1.8	3.4	4.9	17.4
All	14.3	12.1	16.2	14.0	22.8

Table 9.6: Effect of 1σ variation of the systematic uncertainties on the predicted event rates of the SK samples used in this analysis.

- M_{AQE} : [0.8 - 1.2]
- p_F ^{12}C : [0.92 - 1.27]
- p_F ^{16}O [0.89 - 1.22]
- 2p2h norm ν : [0.0 - 2.5]
- 2p2h norm $\bar{\nu}$: [0.0 - 2.5]

Two rows are highlighted (in red) in Table 9.6 due to their particular importance for this analysis. They showcase the effect of the reduced uncertainties assigned to the FSI model as a result of the NEUT pion cascade tuning presented in Chapter 7. The reduction in the size of the prior is convoluted with the new method of propagating the uncertainties using the response functions described above.

Chapter 10

Joint $\nu_{\mu,e} + \bar{\nu}_{\mu,e}$ Oscillation Analysis: Results

The goal of this analysis is to constrain the oscillation parameters $\sin^2 \theta_{23}$, Δm_{23}^2 , $\sin^2 \theta_{13}$, and δ_{CP} by analyzing neutrino data collected by the near and far detectors of T2K to search for the signature of the ν_e appearance and ν_μ disappearance channels. The Markov Chain Monte Carlo framework used for this purpose was described in Chapter 8. The selected samples of neutrino and antineutrino events at the near and far detectors, along with the systematic uncertainties considered in the analysis, were described in Chapter 9.

The sensitivity to the disappearance parameters ($\sin^2 \theta_{23}$, and Δm_{23}^2) comes from the muon ring samples. The electron ring samples enable the analysis to be sensitive to $\sin^2 \theta_{13}$ and the mass ordering, i.e., the sign of Δm_{23}^2 . The inclusion of neutrino and antineutrino events introduces the sensitivity to δ_{CP} .

This analysis is not sensitive to the neutrino oscillation solar parameters ($\sin^2 \theta_{12}$ and Δm_{12}^2). Gaussian priors with mean and RMS from [48] are assumed for these parameters, as specified in Table 10.1. A conservative uniform prior is assumed for the oscillation parameters of interest. The exception is $\sin^2 \theta_{13}$, for which two types of fits are performed. In the *T2K-only* fits presented in Sections 10.1.1 and 10.2.4, a uniform prior is assumed. For the *T2K + Reactor Constraint* fits presented in Sections 10.1.2 and 10.2.5 a Gaussian prior using the PDG data fit constrained by the reactor experiments data is assumed [48].

Asimov fits are presented in Section 10.1 as a validation of the fitting framework, and as a representation of the expected experimental sensitivity to the oscillation parameters. The results to fitting the T2K data are presented in Section 10.2. The analysis presented in this thesis is not an official T2K analysis. The improvement in sensitivity achieved in this analysis are compared to previous T2K and NOvA results in Section 10.2.6. Finally, a summary of the results from this analysis and some considerations for future improvements of the work presented are outlined in Sections 10.4 and 10.3.

Parameter	Input value	Prior
$\sin^2 \theta_{12}$	0.304	0.05
Δm_{21}^2 (eV ²)	7.53×10^{-5}	0.18×10^{-5}
Δm_{32}^2 (eV ²)	2.509×10^{-3}	Uniform
$\sin^2 \theta_{23}$	0.528	Uniform
$\sin^2 \theta_{13}$	0.0219	Uniform or 0.0013
δ_{CP} (rad)	-1.601	Uniform

Table 10.1: Neutrino oscillation input values and their priors used for the Markov Chain analysis presented in this thesis and assumed for calculating the expected oscillated spectra shown in Table 9.3 and Figures 9.3 and 9.4.

10.1 Asimov Fits

In an Asimov fit the MC prediction is considered as the “data” to be fitted. This “fake data” prediction is achieved by reweighting the MC to chosen values of protons on target, and to nominal values of the oscillation and systematics parameters. The primary advantage of this method is that no statistical fluctuations exist, given enough MC statistics. This allows for a useful validation of the fitting framework: if the fitter is working properly, the best-fit values extracted should match the known input values. It also provides an estimate of the sensitivity of the analysis, i.e., the maximum precision with which we expect to be able to measure the parameters of interest.

In T2K we don’t perform *true* Asimov fake data fits. Instead, they are fits to ND280 data and SK Asimov fake data. This allows for internal cross-validations among oscillation fitting groups. Nevertheless, the validations described above can be performed. The *input* oscillation parameter values used are listed in Table 10.1. As was described before, two fits are performed: a T2K-Only fit presented in Section 10.1.1, and a T2K + Reactor Constraint fit presented in Section 10.1.2.

An additional validation study was performed by comparing the results of the Asimov fits presented in this thesis with those of the most recent T2K analysis presented in the summer of 2017 and currently being readied for publication [186]. A summary of these comparisons can be found in Appendix F.

10.1.1 T2K-Only Fit

Figure 10.1 shows the two-dimensional posterior probability and credible intervals for the appearance parameters obtained from an Asimov fit without the reactor constraint. Similarly, the posterior probability density for the disappearance parameters is shown Figure 10.2. The best fit point estimation and credible interval construction methods were discussed in Section 8.4.2.

The best-fit values in the appearance contour are found to be close to the input value, as discussed. In the disappearance contour, the best fit values are found within 1σ of the input values. This difference arises as an effect from marginalizing over non-Gaussian nuisance and

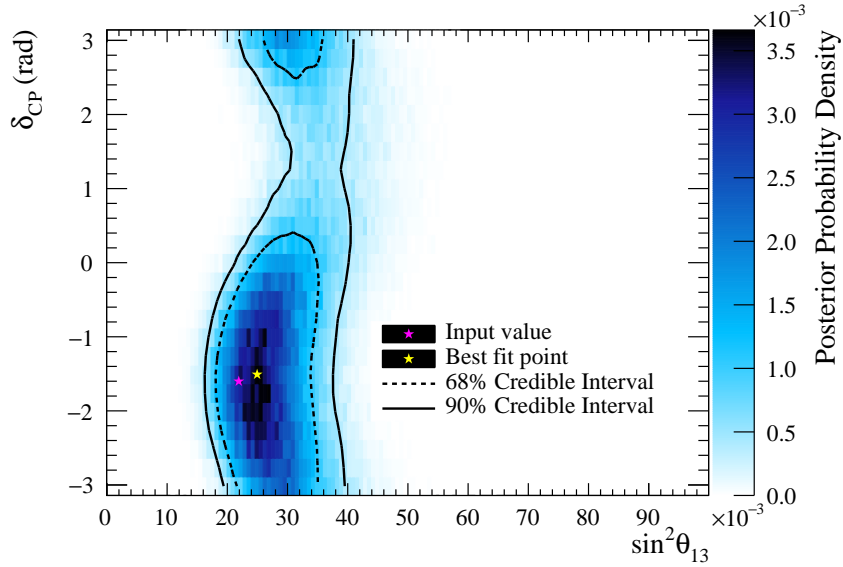


Figure 10.1: Posterior probability density for the appearance parameters from an Asimov fit without the reactor constraint. The 68% and 90% credible intervals are shown as the dashed and solid lines, respectively.

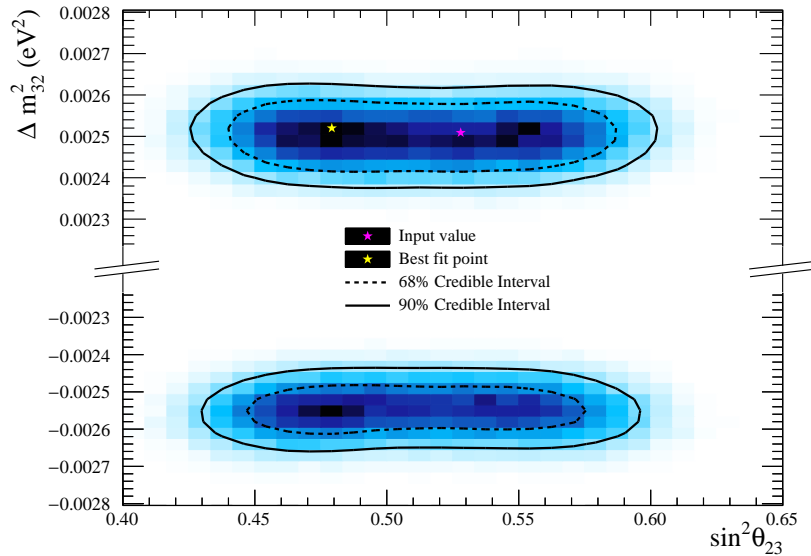


Figure 10.2: Posterior probability density for the disappearance parameters from an Asimov fit without the reactor constraint. The 68% and 90% credible intervals are shown as the dashed and solid lines, respectively. Note the break in the vertical axis.

oscillation parameters, as was discussed in Section 8.4.1. In fact, many parameters show non-Gaussian posteriors, see for example the posterior for δ_{CP} shown in Figure 10.3. Being able to fully marginalize over the nuisance parameters with complex correlations without having to assume a Gaussian for the posterior is one of the distinct features of a Bayesian analysis such as this analysis, as opposed to the more common frequentist analysis by χ^2 minimization.

More importantly, Figures 10.1 and 10.3 show that the T2K data by itself is able to provide a closed 68% contour on δ_{CP} , as has been previously confirmed [53].

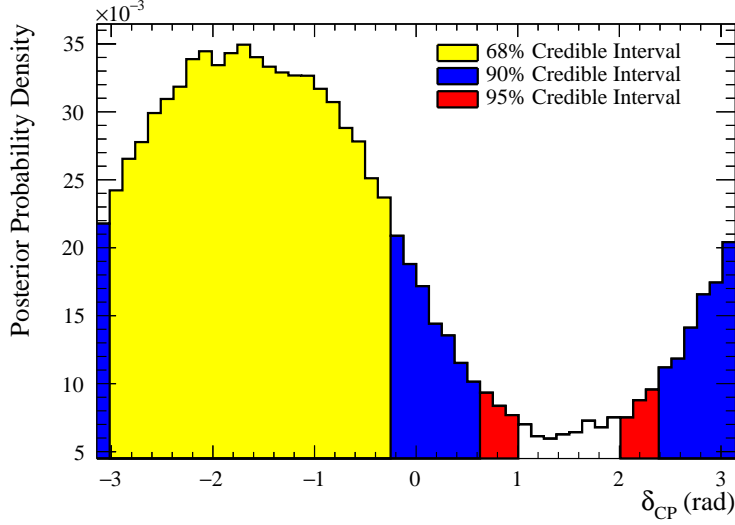


Figure 10.3: Posterior probability density for δ_{CP} from a T2K-Only Asimov fit.

The Markov Chains for the fits presented in this thesis span both hierarchies in a single fit. This is achieved by choosing equal priors on both the mass hierarchies ($P(\text{NH}) = P(\text{IH}) = 0.5$) and allowing the chain to jump from one hierarchy to the other at each step of the chain. This provides an interesting and natural way to compare the preference for the mass hierarchies and the two octants of θ_{23} by comparing their posterior probabilities. Table 10.2 provides these probabilities, which are simply the fraction of the steps of the chain in that region of the phase space.

	$\sin^2 \theta_{23} < 0.5$	$\sin^2 \theta_{23} > 0.5$	Sum
IH ($\Delta m_{32}^2 < 0$)	0.173	0.227	0.4
NH ($\Delta m_{32}^2 > 0$)	0.251	0.349	0.6
Sum	0.424	0.576	1

Table 10.2: Model comparison probabilities for normal and inverted hierarchies, as well as upper and lower octants, from the posterior of the Asimov fit to T2K data only.

With an input value of the oscillation parameters in the normal hierarchy and in the upper octant (see Table 10.1), a 60% posterior probability in normal hierarchy and 57% of the posterior

probability in the upper octant are obtained. Bayes factors provide a way to compare models in a Bayesian framework and can be calculated from these probabilities [187]. They are interpreted as the evidence from the data that one of the hypothesis is true. In our case of equal priors for both hypothesis the Bayes factor reduces to the ratio of the posterior odds. From Table 10.2, the Bayes factor for normal vs. inverted hierarchy hypotheses is $B(\text{NH}/\text{IH}) = 1.5$, while that for upper vs. lower octant hypothesis is $B(\sin^2 \theta_{23} > 0.5 / \sin^2 \theta_{23} < 0.5) = 1.36$. This indicates that little sensitivity to selecting either hypothesis is to be expected¹, assuming the oscillation parameters in nature are those used for this input Asimov study.

10.1.2 T2K + Reactor Constraint Fit

Figures 10.4 and 10.5 show the posterior probability densities, best-fit points and credible intervals for the disappearance and appearance parameters, respectively, for an Asimov fit with the reactor constraint on $\sin^2 \theta_{13}$. Closed contours for the 68% and 90% credible intervals are obtained, exemplifying the power of using the reactor information, and indicating that there is sensitivity to exclude some values of δ_{CP} at 90% probability. In addition, in can be seen in Figure 10.6 that the 90% credible interval of δ_{CP} in 1D excludes both 0 and π , which was not the case in previous T2K analyses [53].

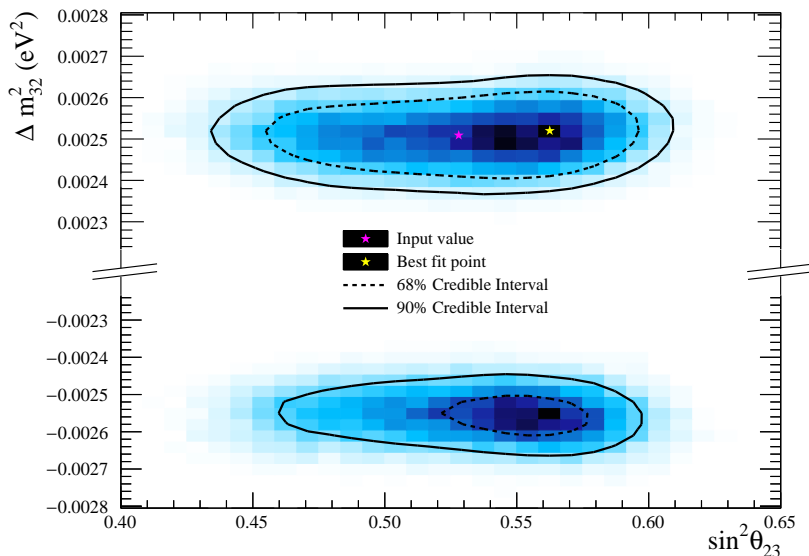


Figure 10.4: Posterior probability density for the disappearance parameters from a T2K + Reactor constraint Asimov fit. The 68% and 90% credible intervals are shown as the dashed and solid lines, respectively. Notice the break in the vertical axis to allow for a better visualization of the posteriors for each mass hierarchy hypothesis.

Similarly to the T2K-Only case, Table 10.3 shows the posterior probabilities for the hierarchy

¹According to Jeffreys Scale [187], these values of the Bayes factor correspond to “weak” model preferences. A Bayes factor between 10-100 corresponds to “strong” model preference, while values higher than 100 suggest a “decisive” model preference.

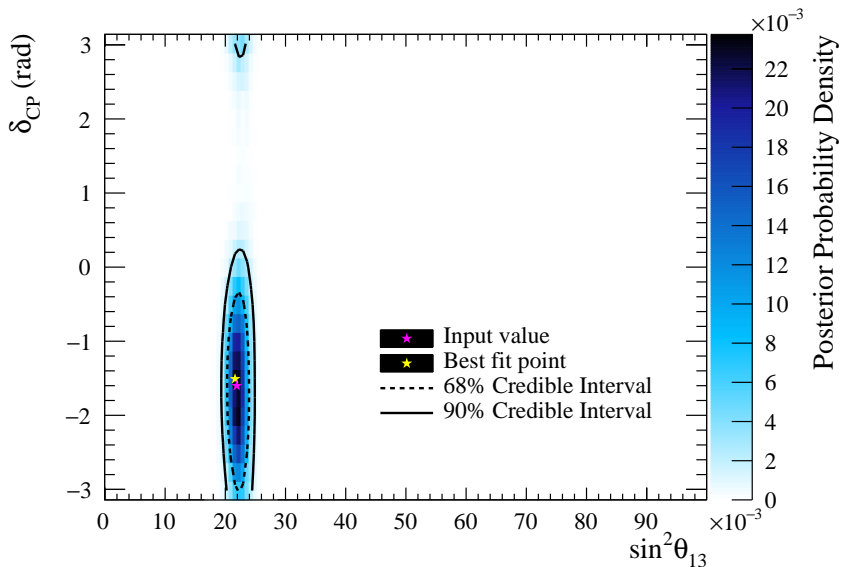


Figure 10.5: Posterior probability density for the appearance parameters from a T2K + Reactor constraint Asimov fit. The 68% and 90% credible intervals are shown as the dashed and solid lines, respectively. The horizontal scale is the same as Figure 10.1.

and octant hypothesis. The Bayes factor for the mass hierarchy and octant hypotheses are 3.12 and 3.22, respectively. While these point to slightly stronger preferences, it is far from enough to expect strong sensitivities from the data, assuming the input oscillation parameters used for this Asimov study.

	$\sin^2 \theta_{23} < 0.5$	$\sin^2 \theta_{23} > 0.5$	Sum
IH ($\Delta m_{32}^2 < 0$)	0.051	0.212	0.263
NH ($\Delta m_{32}^2 > 0$)	0.186	0.551	0.737
Sum	0.237	0.763	1

Table 10.3: Model comparison probabilities for normal and inverted hierarchies, as well as upper and lower octants, from the posterior of the Asimov fit to T2K + Reactor constraint.

Further validations of the fitting framework have been completed [166], but are not described here to due to space constraints. These include Asimov fits with input oscillation parameters for non-maximal mixing ($\sin^2 \theta_{23} = 0.45$) and no CP violation ($\delta_{CP} = 0$). Likelihood scans for the oscillation parameters similar to those shown in Section 9.3.2.3 for the FSI parameters were also performed. These scans confirm the non-biased nature of the fitting framework, as they are not affected by marginalization issues. Finally, the results of Asimov fits are routinely compared to those obtained by other groups using different frameworks and fitting techniques [188, 189].

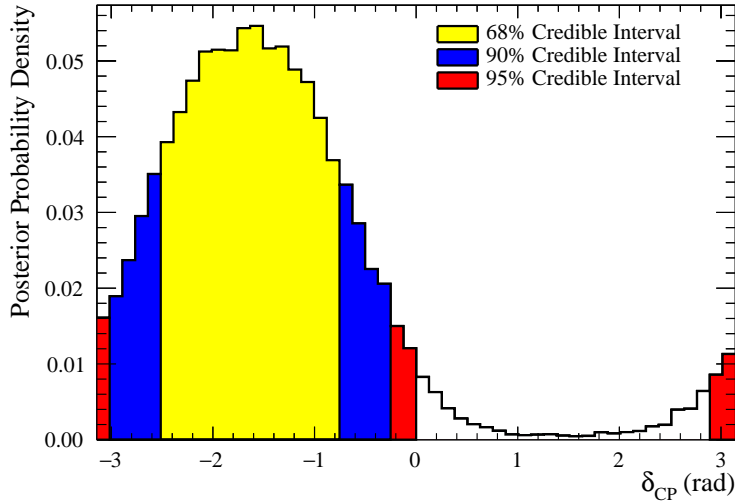


Figure 10.6: Posterior probability density for δ_{CP} from a T2K + Reactor constraint Asimov fit.

10.2 Data Fits

The results from fitting the T2K Run 1-8 data set corresponding to 14.735×10^{20} POT in FHC mode and 7.557×10^{20} POT in RHC mode are presented in this section. Similarly to the Asimov fits in the previous section, two fits were performed: with and without the reactor constraint. In both cases, Markov Chains with an excess of 2.5×10^7 steps were used to produce the posterior probability densities.

10.2.1 Nuisance Parameters

The goal of this analysis is to estimate the values of the oscillation parameters, however, it is important to examine the behaviour of the nuisance parameters in the fit since they affect the posterior of interest via marginalization effects. Figure 10.7 shows a comparison of the central value and 1σ ranges for the flux, cross section, and detector modelling parameters described in Section 9.2. The mean and 1σ values are obtained from the mean and RMS of Gaussian fits to the posteriors. This is not an accurate representation of the posterior of some parameters that have non-Gaussian shapes, however, it remains an informative study as it allows to check for systematic effects.

In general, good agreement is observed in the posterior of the nuisance parameters obtained from T2K-Only and T2K + Reactor constraint Data fits. Most parameters stay within their prior uncertainties. The flux and cross section parameters are strongly correlated in the post-fit and are constrained by the ND280 data, showcasing the importance of the near detector. The ND280 detector parameters, which contribute the largest number of nuisance parameters to the fit, are

also constrained by the fit and stay within their priors. The FSI parameters are constrained by migrations between the near detector samples. The effect of this reduction to the prediction of the SK spectra is discussed in Section 10.2.3. Finally, the SK detector systematics parameters are relatively unchanged by the data fit, likely due to the reduced sample statistics relative to the ND280 samples.

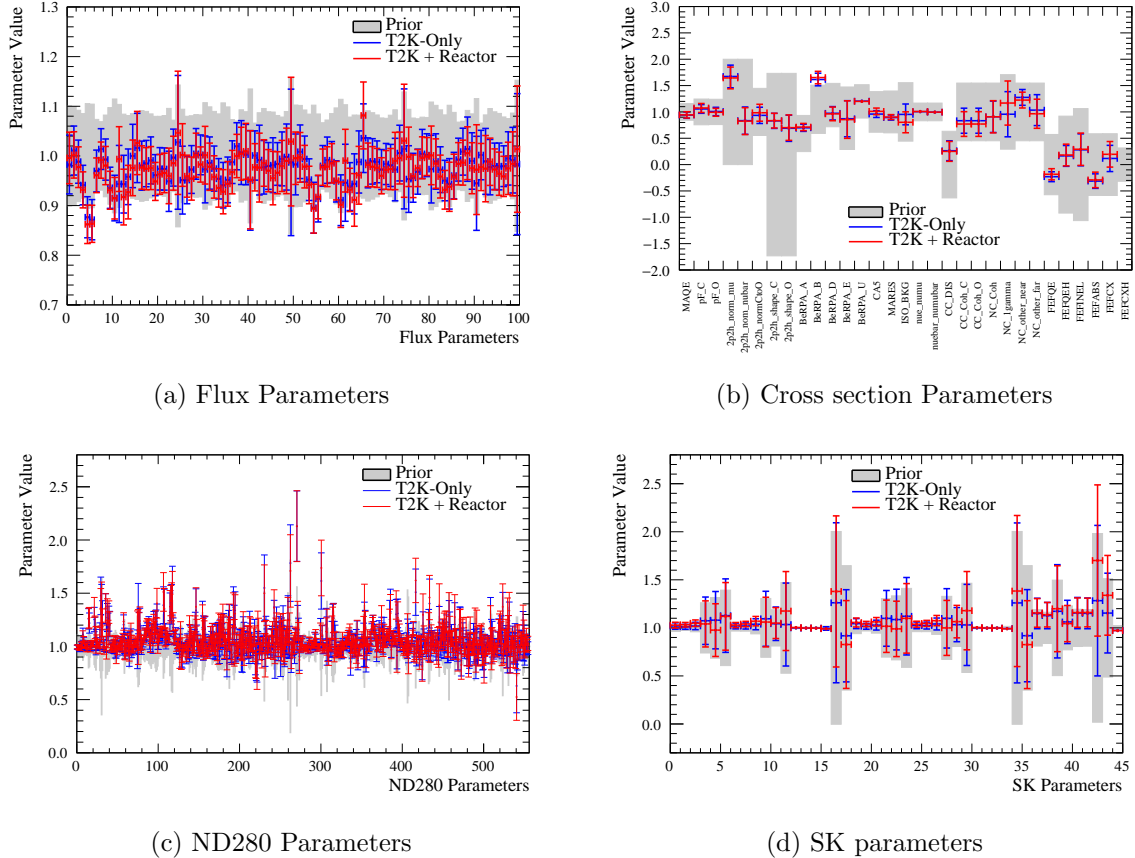


Figure 10.7: Central and $\pm 1\sigma$ values of the nuisance parameters described in Section 9.2 for T2K-Only (blue) and T2K + Reactor constraint (red) Data fits. The prior uncertainty for each parameter is plotted as the grey filled band.

10.2.2 Posterior Predictive Spectra

The “best-fit” spectra at ND280 and SK assuming the posterior probability densities for the oscillation and nuisance parameters can be estimated using a *posterior predictive* method. This method marginalizes over all the parameters to find the posterior probability distribution as a function of the reconstructed variables.

The method starts by selecting at random 5000 steps from the Markov Chain. Because there are more steps in the region of higher posterior density, these steps are more likely to have values for the oscillation and nuisance parameters close to their respective regions of large posterior

probability density. We then consider a single bin in the reconstructed variable spectrum. For each step, we calculate the predicted event rate in that bin, assuming the parameter values defined by that step. The combination of all 5000 points creates a distribution of event rates in that given bin. The mean and RMS of a Gaussian fit to that distribution are taken to be the predicted event rate and 1σ uncertainty for that bin.

Figure 10.8 shows the 1σ pre-fit and post-fit band for the FGD1 and FGD2 FHC mode samples at ND280, along with the data. The pre-fit band is obtained by varying the underlying nuisance parameters according to their prior uncertainties (described in Section 9.2). The post-fit band is obtained by applying the posterior predictive method described above to the Markov Chain obtained for the T2K + Reactor constraint Data fit to be described in Section 10.2.5. The ND280 RHC mode samples show similar levels of agreement in the post-fit spectra. The reduction in the uncertainty of the flux, cross section, and ND280 detector nuisance parameters shown in Figure 10.7 translates to the reduced post-fit 1σ bands in Figure 10.8.

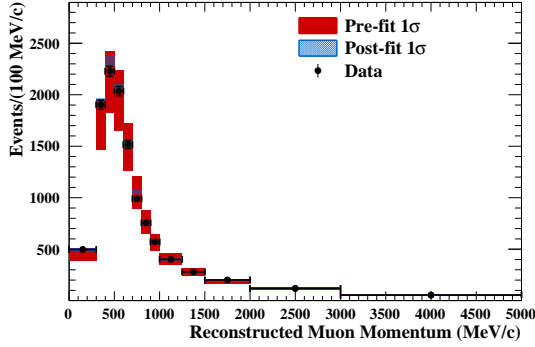
Figure 10.9 shows the 1σ pre-fit and post-fit band for the five SK samples considered in this analysis, along with the data. The same posterior predictive procedures used to obtain the ND280 1σ bands are used to obtain these bands. The post-fit errors are reduced relative to the pre-fit as a result of the ND280 constraint to the flux and cross section uncertainties, which are common (or highly correlated) to both ND280 and SK samples as was described in Section 9.2.

Figure 10.10 shows the ratio of the SK data, the pre-fit, and the post-fit 1σ bands to the unoscillated spectra. The uncertainty bands are drawn for illustrative purposes, the correct interpretations of the coverage of the data should be obtained from Figure 10.9. The characteristic “oscillation dip” in the region of the first oscillation maximum ($\sim 0.6\text{GeV}$) provides clear evidence of the ν_μ and $\bar{\nu}_\mu$ disappearance phenomenon in Figures 10.10a and 10.10c. Similarly, there are significant excess in the measured data for $1R_e$ samples over the unoscillated prediction, consistent with the ν_e appearance oscillation phenomenon.

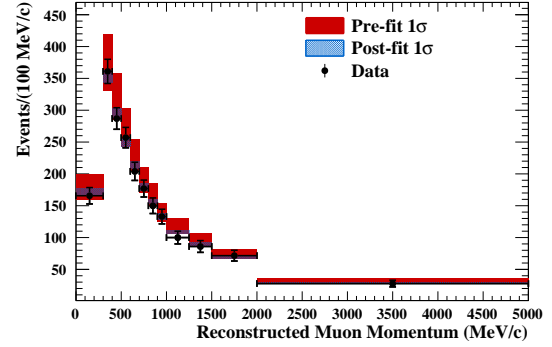
10.2.3 Effect of Propagating ND280 Constraints on FSI Uncertainties

As was discussed in Section 9.3.3, one of the main new features of the oscillation analysis presented in this thesis is that for the first time the constraints to the FSI parameters obtained from the ND280 data are propagated to the SK prediction. The relative size of the constraint can be seen on the right hand side of Figure 10.7b. The reduction of the 1σ bands shown in Figure 10.9 already factored in this constraint.

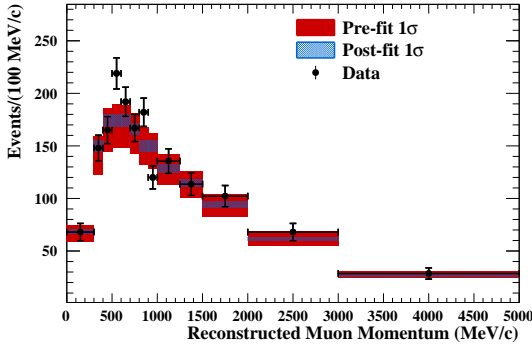
As was shown in Figure 9.4, the FHC $1R_e$ 1 d.e sample contains a large fraction of $CC1\pi$ interactions². One additional way to visualize the effect of the reduced post-fit uncertainties for the FSI parameters is to draw the pre-fit and post-fit 1σ band for the true charged pion spectrum from the FHC $1R_e$ 1 d.e sample. Similarly to Section 10.2.2, the pre-fit band is drawn from estimating the effect of variations of the spectra for random correlated throws of the FSI parameters from their priors, while the post-fit band is drawn using the posterior predictive method. Figure 10.11 shows the resulting uncertainty bands for the true momentum (before



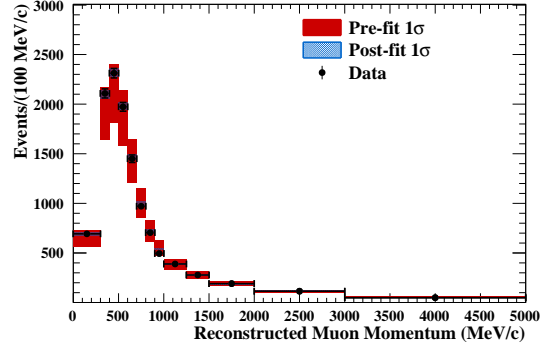
(a) FGD1 FHC CC0 π



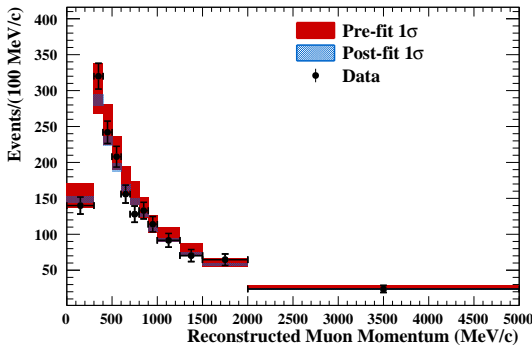
(b) FGD1 FHC CC1 π



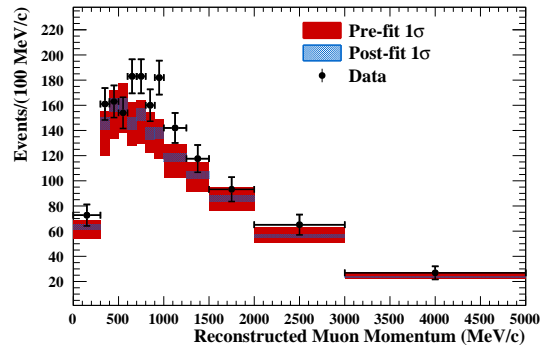
(c) FGD1 FHC CC-Other



(d) FGD2 FHC CC0 π

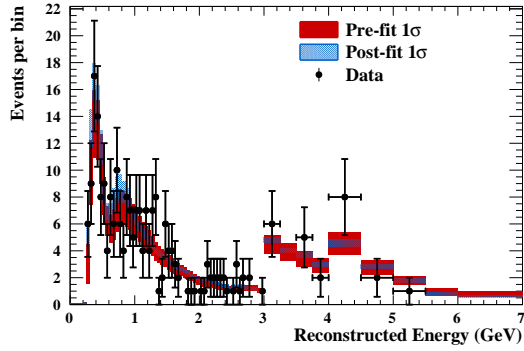


(e) FGD2 FHC CC1 π

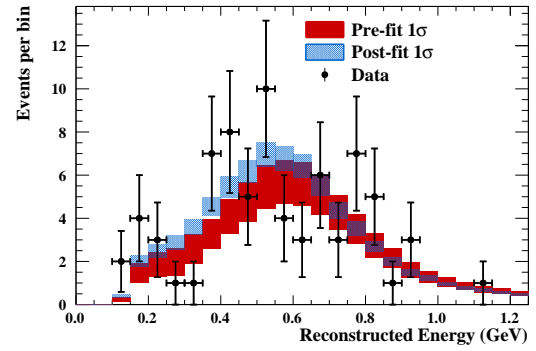


(f) FGD2 FHC CC-Other

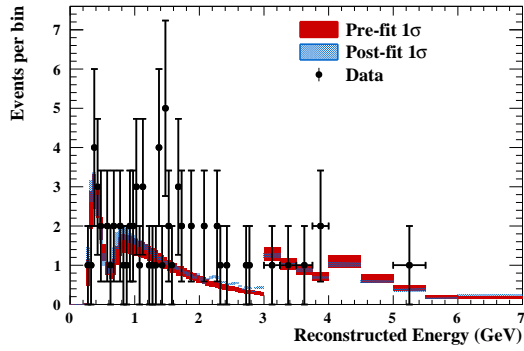
Figure 10.8: ND280 pre-fit (red) and post-fit (blue) 1σ bands for the FGD1 and FGD2 FHC mode samples, along with the data (black points). The pre-fit band is obtained by calculating the variations to the spectra for values of the nuisance parameters obtained from throws of the prior covariance matrices. The post-fit band is obtained using a posterior predictive method applied to the Markov Chain from the T2K + Reactor Constraint Data fit.



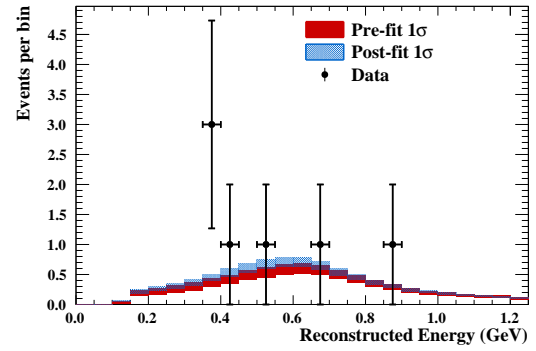
(a) FHC $1R_\mu$



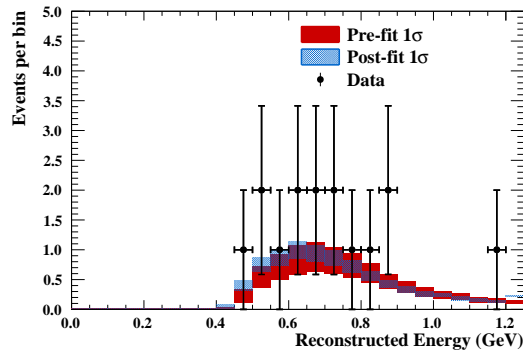
(b) FHC $1R_e$



(c) RHC $1R_\mu$

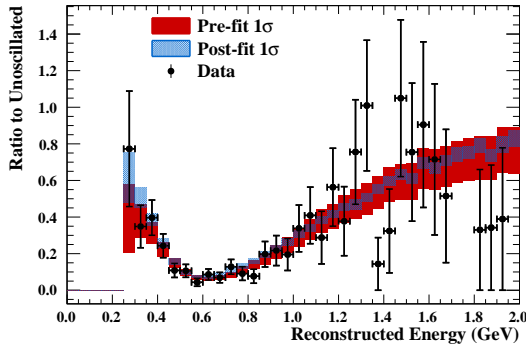


(d) RHC $1R_e$

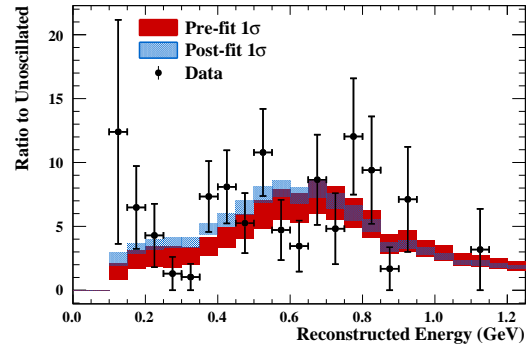


(e) FHC $1R_e$ 1 d.e.

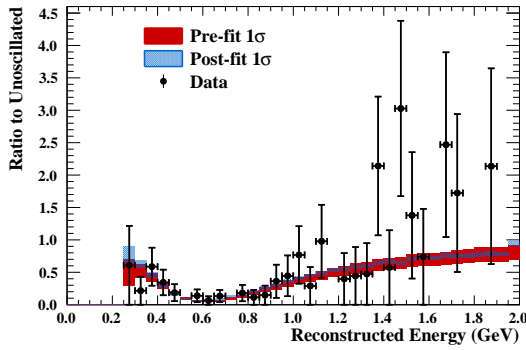
Figure 10.9: SK pre-fit (red) and post-fit (blue) 1σ bands for the five SK samples used in this analysis, along with the data (black points). The pre-fit band is obtained by calculating the variations to the spectra for values of the nuisance parameters obtained from throws of the prior covariance matrices. The post-fit band is obtained using a posterior predictive method applied to the Markov Chain from the T2K + Reactor Constraint Data fit.



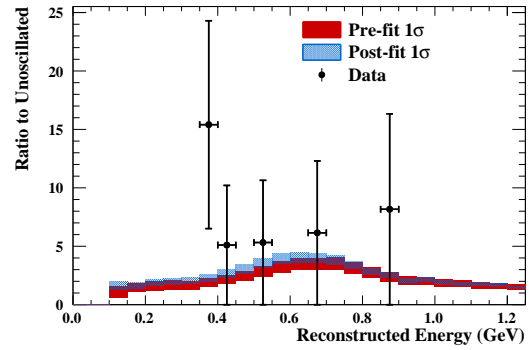
(a) FHC $1R_\mu$



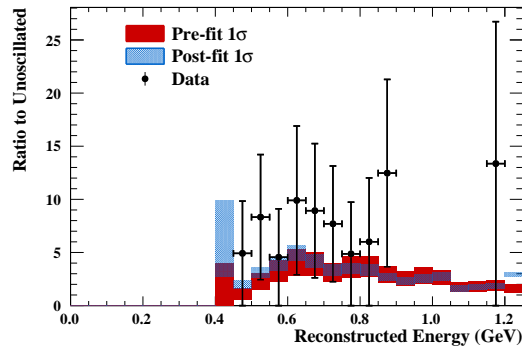
(b) FHC $1R_e$



(c) RHC $1R_\mu$



(d) RHC $1R_e$



(e) FHC $1R_e$ 1 d.e.

Figure 10.10: Ratio of the SK data (black points), pre-fit (red), and post-fit (blue) 1σ bands to the predicted unoscillated spectra. The effect of the oscillation phenomenon to the FHC $1R_\mu$, RHC $1R_\mu$, and FHC $1R_e$ is clearly visible.

FSI interactions) spectrum of pions. The overall normalization of the spectrum is increased, but remains within the prior band, as was expected from Figure 10.7b.

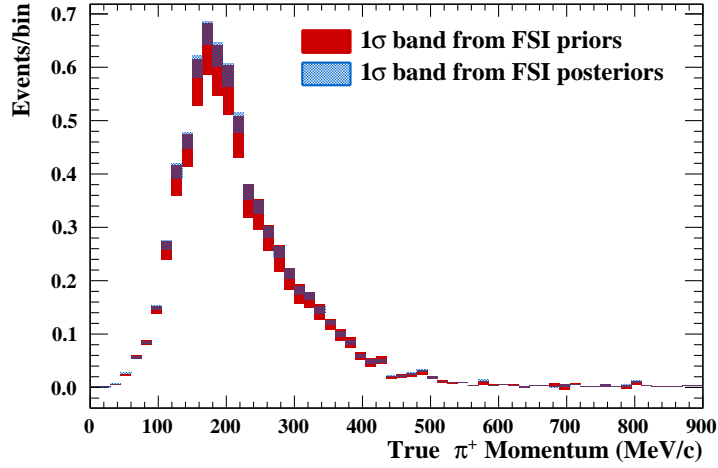


Figure 10.11: Pre-fit (red) and post-fit (blue) 1σ bands for the true momentum spectrum of charged pions in the FHC $1R_e$ 1 d.e. sample. The bands only contain errors from FSI uncertainties.

Finally, Table 10.4 shows the impact of the FSI uncertainties on the SK samples as an uncertainty on the total number of events in each sample. In addition to the reduction of the FSI uncertainties from the tuning of the NEUT cascade model presented in Chapter 7, by propagating the constraints by the ND280 data, the FSI uncertainties are further reduced by $\sim 45\%$ for all the SK samples.

	FHC $1R_\mu$	RHC $1R_\mu$	FHC $1R_e$	RHC $1R_e$	FHC $1R_e$ 1d.e
FSI (from prior)	2.0	1.7	1.6	0.9	7.5
FSI (from posterior)	1.1	0.9	1.0	0.5	4.0

Table 10.4: Effect of 1σ variation of the FSI parameters uncertainties on the predicted event rates of the SK samples used in this analysis. The pre-fit uncertainties are calculated from random correlated throws from the prior of the FSI parameters, while the post-fit errors are calculated using the posterior predictive method.

10.2.4 T2K-Only Fit

Figure 10.12 shows the 1D posterior distribution and credible intervals for the appearance and disappearance parameters obtained from a fit without the reactor constraint. The 2D credible intervals are shown in Figure 10.13. Table 10.5 shows the best-fit value and 68% and 90% 1D

²In fact the FHC $1R_e$ 1 d.e sample is referred to as the FHC $1R_e$ CC $1\pi^+$ sample in [53]. The name was changed to avoid confusion once ongoing work to improve the SK reconstruction such that events where the pion Cerenkov ring are reconstructed. These samples are scheduled to be used in future iterations of the oscillation analysis.

credible interval ranges for each parameter. The best-fit values are extracted from the mode of the 2D marginal posteriors for the $\sin^2 \theta_{23}$ vs. Δm_{32}^2 and $\sin^2 \theta_{13}$ vs. δ_{CP} parameter spaces. The CP-conserving values ($-\pi$, 0 , and π) are only excluded at the 68% level.

	$\sin^2 \theta_{23}$	$\Delta m_{32}^2 (\times 10^{-3} \text{eV}^2)$	$\sin^2 \theta_{13}$	δ_{CP} (rad.)
2D best fit	0.513	2.46	0.0263	-1.97
68% C.I. (1σ) range	(0.48, 0.54)	(-2.54, -2.48) & (2.39, 2.54)	(0.023, 0.035)	(-2.89, -0.82)
90% C.I. range	(0.46, 0.56)	(-2.58, -2.43) & (2.36, 2.57)	(0.021, 0.039)	$(-\pi, -0.01)$ & $(2.76, +\pi)$
95.45% C.I. (2σ) range	(0.45, 0.57)	(-2.61, -2.41) & (2.34, 2.58)	(0.019, 0.042)	$(-\pi, 0.31)$ & $(2.32, +\pi)$

Table 10.5: Best-fit values and 68%, 90% and 95.45% 1D credible interval ranges for oscillation parameters for the data fit without reactor constraint. The 2D best-fit values are taken from the mode of the 2D marginal posterior distributions in $\sin^2 \theta_{23}$ – Δm_{32}^2 and $\sin^2 \theta_{13}$ – δ_{CP} , and the 1D 68% (95%) credible intervals correspond to the 1 (2) σ range for each parameter.

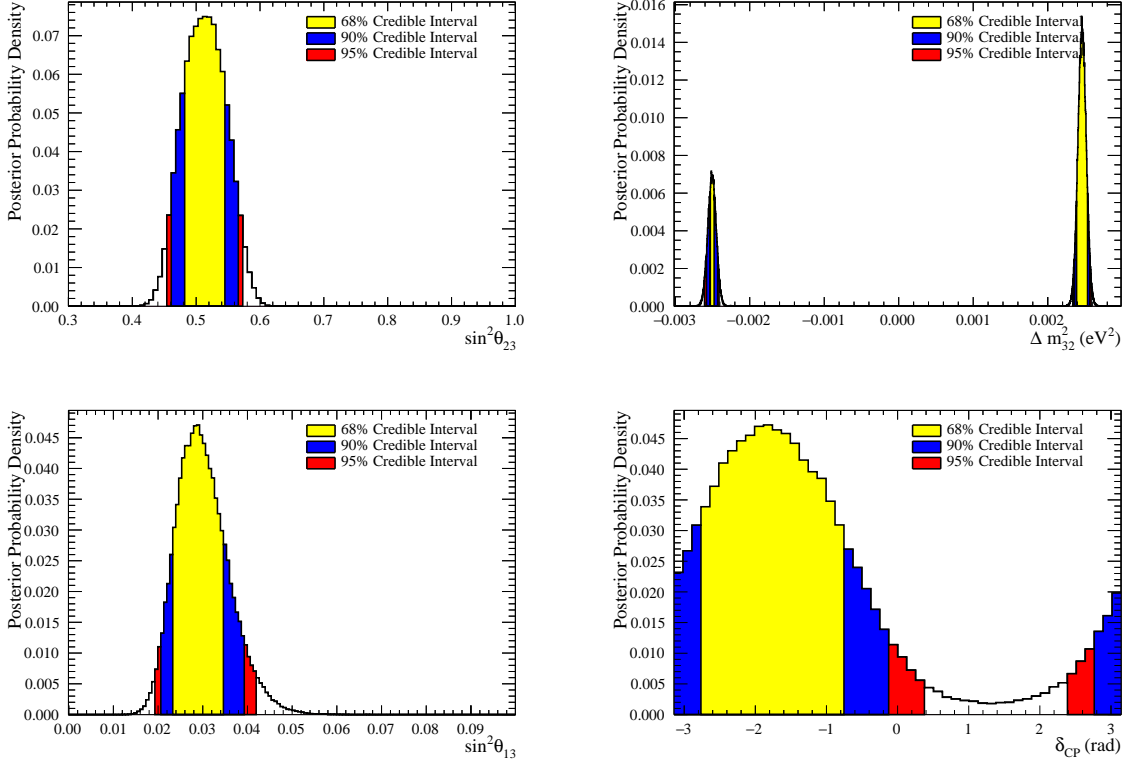


Figure 10.12: Posterior probability density for the appearance and disappearance parameters from a T2K-Only Data fit.

The T2K-Only Data fit results in stronger constraints of the oscillation parameters relative to the T2K-Only Asimov fit. Unlike the Asimov fit, the 90% credible interval for the appearance parameters is contiguous for the T2K-Only Data fit. The goodness of fit was calculated using the best-fit spectra obtained using the posterior predictive method. The p-values obtained are above the threshold of 0.05 chosen beforehand. This suggests that the model is able to fit these

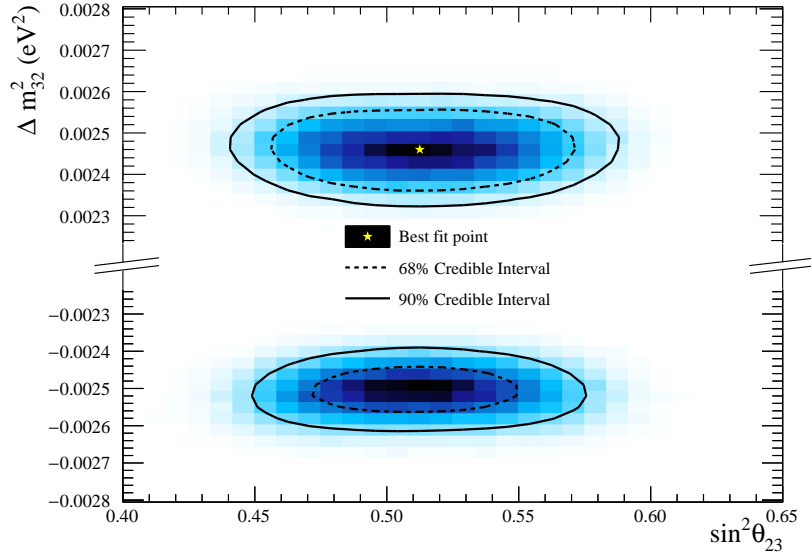


Figure 10.13: Posterior probability density for the disappearance parameters from a T2K-Only Data fit. The 68% and 90% credible intervals are shown as the dashed and solid lines, respectively. Notice the break in the vertical axis to allow for a better visualization of the posteriors for each mass hierarchy hypothesis.

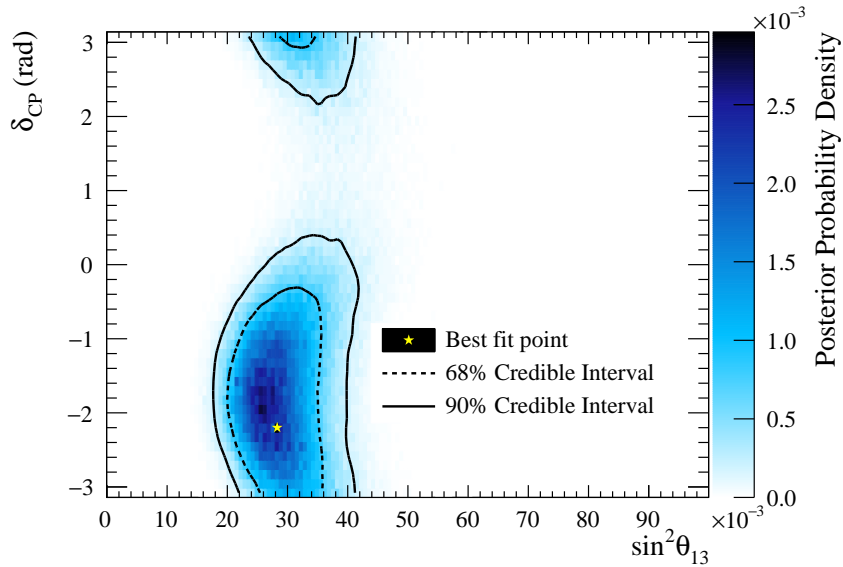


Figure 10.14: Posterior probability density for the appearance parameters from a T2K-Only Data fit. The 68% and 90% credible intervals are shown as the dashed and solid lines, respectively.

upwards fluctuations, and that this stronger constraint does not provide evidence for oscillations beyond the PMNS model.

Similarly to what was shown in Section 10.1 for the Asimov fits, Table 10.6 shows the probabilities for the octant and mass hierarchy hypothesis. The Bayes factor for the mass hierarchy and octant hypotheses are 2.12 and 1.76, respectively.

	$\sin^2 \theta_{23} < 0.5$	$\sin^2 \theta_{23} > 0.5$	Sum
IH ($\Delta m_{32}^2 < 0$)	0.120	0.200	0.320
NH ($\Delta m_{32}^2 > 0$)	0.241	0.438	0.679
Sum	0.361	0.638	1

Table 10.6: Model comparison probabilities for normal and inverted hierarchies, as well as upper and lower octants, from the posterior of a T2K-Only Data fit.

10.2.5 T2K + Reactor Constraint Fit

Figure 10.15 shows the 1D posterior distribution and credible intervals for the appearance and disappearance parameters obtained from a fit with the reactor constraint. The 2D credible intervals are shown in Figures 10.16 and 10.17. Table 10.7 shows the best-fit value and 68% and 90% 1D credible interval ranges for each parameter. The best-fit values are extracted from the mode of the 2D marginal posteriors for the $\sin^2 \theta_{23}$ vs. Δm_{23}^2 and $\sin^2 \theta_{13}$ vs. δ_{CP} parameter spaces. The CP-conserving values ($-\pi$, 0 , and π) are now excluded at the 68%, 90%, and 95.4% levels. This is in agreement with the hints of δ_{CP} from the latest results from T2K presented this summer [186] and being finalized for publication.

	$\sin^2 \theta_{23}$	Δm_{32}^2 ($\times 10^{-3} \text{eV}^2$)	$\sin^2 \theta_{13}$	$\delta_{CP}(\text{rad.})$
2D best fit	0.521	2.46	0.0222	-1.79
68% (1σ) C.I. range	0.50 – 0.55	2.40 – 2.54	0.0213 – 0.0238	-2.39 – -1.07
90% C.I. range	0.47 – 0.57	-2.56 – -2.47 & 2.35 – 2.59	0.0205 – 0.0245	-2.77 – -0.63
95.45% (2σ) C.I. range	0.46 – 0.58	-2.59 – -2.45 & 2.34 – 2.60	0.0200 – 0.0248	-3.02 – -0.44

Table 10.7: Best-fit values and 68%, 90% and 95.45% 1D credible interval ranges for oscillation parameters for the T2K + Reactor constraint Data fit. The 2D best-fit values are taken from the mode of the 2D marginal posterior distributions in $\sin^2 \theta_{23}$ – Δm_{32}^2 and $\sin^2 \theta_{13}$ – δ_{CP} , and the 1D 68% (95%) credible intervals correspond to the 1 (2) σ range for each parameter.

Table 10.8 shows the probabilities for the octant and mass hierarchy hypothesis. The Bayes factor for the mass hierarchy and octant hypotheses are 5.61 and 3.38, respectively. While these provide the strongest preferences for the fits presented in this thesis, these numbers still do not approach the level of statistical significance where conclusions can be drawn to exclude either hypothesis. It is important to note that the significance of this result has been steadily increasing as T2K has collected more data, so if nothing else this is an interesting hint to keep an eye on.

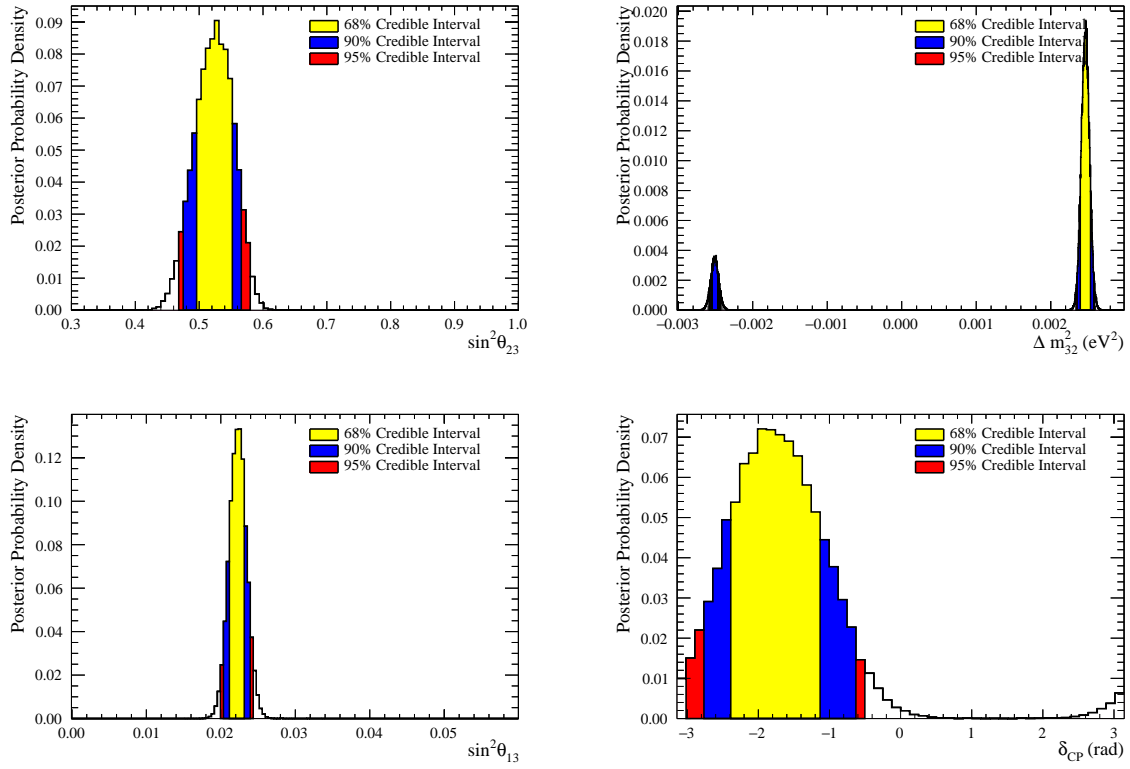


Figure 10.15: Posterior probability density for the appearance and disappearance parameters from a T2K + Reactor constraint Data fit.

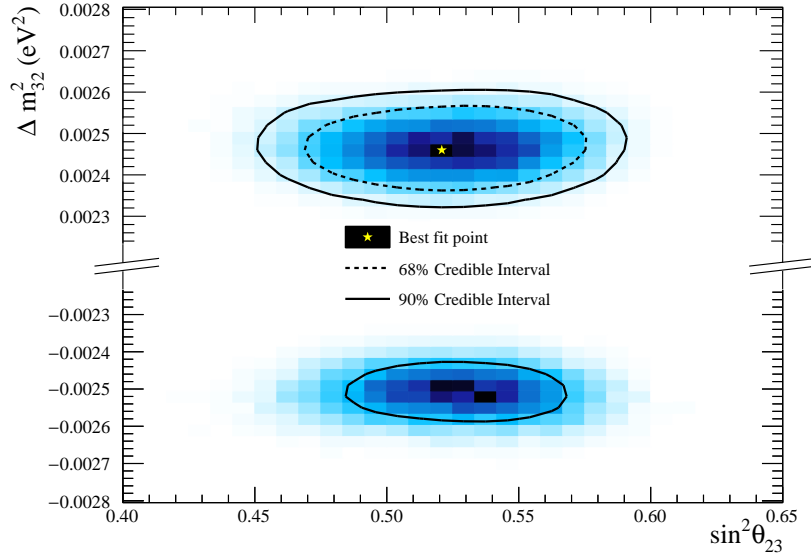


Figure 10.16: Posterior probability density for the disappearance parameters from a T2K + Reactor constraint Data fit. The 68% and 90% credible intervals are shown as the dashed and solid lines, respectively. Notice the break in the vertical axis to allow for a better visualization of the posteriors for each mass hierarchy hypothesis.

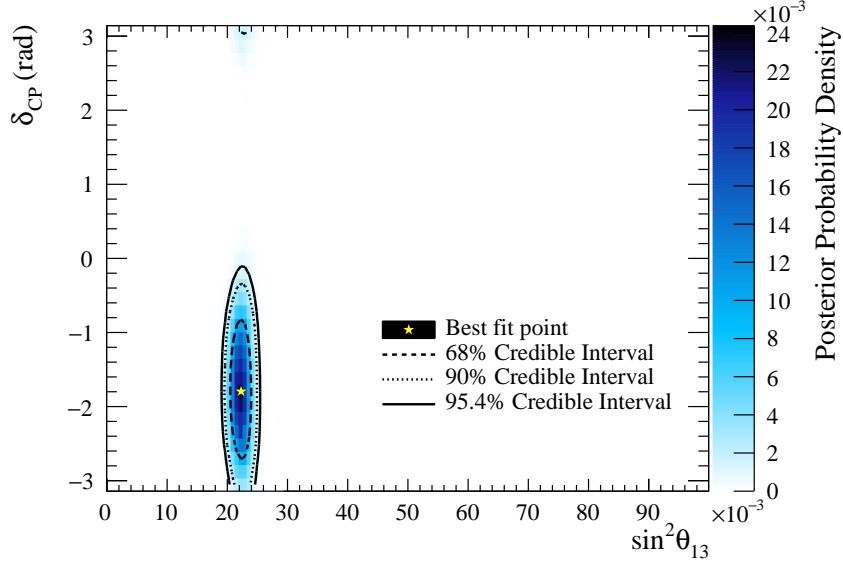


Figure 10.17: Posterior probability density for the appearance parameters from a T2K + Reactor Data fit. The 68%, 90%, and 95.4% credible intervals are shown as the dashed and solid lines, respectively. The horizontal scale is the same as Figure 10.14.

	$\sin^2 \theta_{23} < 0.5$	$\sin^2 \theta_{23} > 0.5$	Sum
IH ($\Delta m_{32}^2 < 0$)	0.030	0.121	0.151
NH ($\Delta m_{32}^2 > 0$)	0.198	0.650	0.848
Sum	0.228	0.771	1

Table 10.8: Model comparison probabilities for normal and inverted hierarchies, as well as upper and lower octants, from the posterior of a T2K + Reactor constraint Data fit.

10.2.6 Comparison to T2K Results and Other Experiments

The results in this thesis have been presented as Bayesian credible intervals. Most other experiments employ frequentist analysis frameworks in which results are presented as confidence intervals. The interpretation of a 90% confidence interval is that, if the experiment were to be repeated a large number of times, 90% of those times the measured best-fit point would lie within the 90% confidence interval. On the other hand, a 90% credible interval simply means that – given this experiment – there is a 90% probability that the true parameter value lies in the 90% credible interval.

To produce constant- $\Delta\chi^2$ confidence intervals from the Markov Chain, the bin contents of a marginal posterior can be used if interpreted as a likelihood, \mathcal{L}_{bin} ³. The bin in which the posterior is largest is found, and the posterior density in that bin is defined as the maximum likelihood, \mathcal{L}_{max} . For each bin in the histogram, $\Delta\chi^2$ is calculated,

$$\Delta\chi^2 = -2 \ln \left(\frac{\mathcal{L}_{bin}}{\mathcal{L}_{max}} \right) \quad (10.1)$$

Once the $\Delta\chi^2$ distribution is built, the confidence intervals are produced by drawing contours at the critical $\Delta\chi^2$ values: $\Delta\chi^2 = 2.30$ for 68% and $\Delta\chi^2 = 4.61$ for 90% confidence intervals in 2D. The confidence and credible intervals agree perfectly in the limit of a perfectly Gaussian posterior.

Figure 10.18 shows the confidence intervals in the $\sin^2\theta_{23}$ - Δm_{23}^2 space from the T2K + Reactor constraint Data fit compared with other published results. The T2K Run 1-7 results from 2017 were included [53]. Results from NOvA [52], MINOS [51], Ice Cube Deepcore [190], and Super-K IV [191] are included. Only the 90% confidence intervals for normal hierarchy (preferred by this analysis) are shown for an easier reading. Super-K agrees with all experiments, given their lower sensitivity. T2K continues to favour maximal mixing, and the recently improved results from Ice Cube support this preference. On the other hand, this means that the significance for the discrepancy with NOvA’s non-maximal preference increases. As both experiments continue to take data, the evolution of these constraints will remain a hot topic in the next years.

Figure 10.19 shows the 68% and 90% confidence intervals in the $\sin^2\theta_{23}$ - δ_{CP} parameter space in which NOvA has reported their constraints. The next iteration of the NOvA analysis is expected to have a much improved sensitivity for δ_{CP} as antineutrino data currently being collected is considered for the analysis.

10.3 Considerations for the Future

The oscillation analysis presented in this thesis was developed as an improvement to the soon to be published T2K Run 1-8 analysis [186]. “Fake data” studies, in which Asimov fits similar

³This is not strictly valid, but it is true that the content of each bin can be interpreted as proportional to a likelihood, and the constant of proportionality cancels out in Equation 10.1

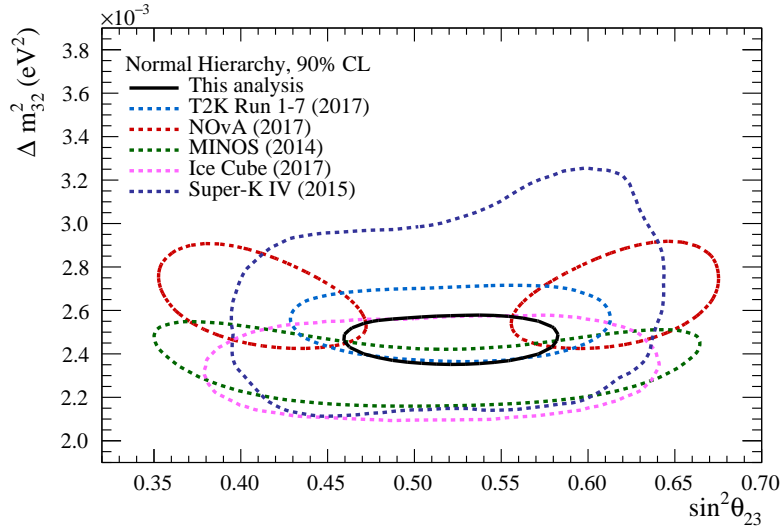


Figure 10.18: 90% CL for the disappearance parameters assuming normal hierarchy from this analysis (black line) compared to the most recent T2K results [53] (blue dashed line) and other experiments [52, 51, 190, 191] (dashed lines). The constant $\Delta\chi^2$ interval was obtained from the Markov Chain for the T2K + Reactor constraint Data fit from Section 10.2.5.

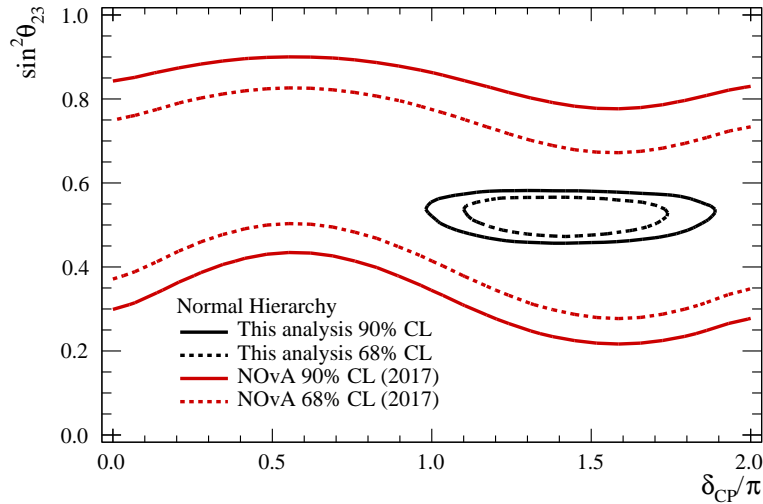


Figure 10.19: 68% and 90% CL in the $\sin^2 \theta_{23} - \delta_{CP}$ parameter space for normal hierarchy from this analysis (black) compared to the NOvA experiment [52] (red). The constant $\Delta\chi^2$ interval was obtained from the Markov Chain for the T2K + Reactor constraint Data fit from Section 10.2.5.

to those presented in Section 10.1 are carried out in the final stages. The robustness of the cross section model presented in Section 4.2 is tested in these studies, and the potential biases to the oscillation parameter measurements introduced by incorrect extrapolations from the ND280 data to the SK spectra predictions are investigated. The general strategy is to generate “fake data” sets at ND280 and SK assuming interaction models different than the nominal, fit these data sets using the full fitting framework with the nominal model, and compare to the nominal Asimov results [192].

Appendix G shows the fake data studies that I carried out. The biases found for those particular fake data studies were negligible. However, other fake data studies have suggested biases in the $\sin^2 \theta_{23}$ - Δm_{23}^2 parameter space. On-going studies are aiming to determine if this type of variations represent a physical effect that should be included as a systematic uncertainty. In that sense, the results in this thesis are presented with the caveat that the T2K systematic error model may be updated in the near future, and that the sensitivity to the oscillation parameters could decrease accordingly.

Currently the events samples at ND280 are categorized topologically by the number of reconstructed pion tracks but are binned only in terms of the reconstructed kinematics of the muon candidate track. The constraints to the FSI parameters are obtained from the migration of events across the CC0 π , CC1 π , and CC-Other samples. There are plans to also use the kinematic information of reconstructed pion tracks. This will lead to more powerful constraints on the FSI uncertainties, as the FSI parameters can modify the shape of the pion spectra. This will further increase the value of the work to propagate FSI uncertainties to SK that was presented in this thesis.

10.4 Summary

In summary, the results of a joint fit of ND280 and SK neutrino and antineutrino data corresponding to 14.735×10^{20} POT in FHC mode and 7.557×10^{20} POT in RHC mode were presented in this thesis. The best-fit values and confidence intervals for the T2K-Only and T2K + Reactor constraint fits from Tables 10.5 and 10.7 are summarized in Table 10.9. The mixing angle $\sin^2 \theta_{23}$ is found to be consistent with maximal mixing, and the normal hierarchy is preferred for Δm_{23}^2 .

	$\sin^2 \theta_{23}$	Δm_{32}^2 ($\times 10^{-3} \text{eV}^2$)	$\sin^2 \theta_{13}$	δ_{CP} (rad.)
T2K - Only	$0.513^{+0.027}_{-0.033}$	$2.46^{+0.08}_{-0.07}$ and (-2.54, -2.48)	$0.02632^{+0.0087}_{-0.033}$	$-1.97^{+1.15}_{-0.92}$
T2K + Reactor	$0.521^{+0.029}_{-0.021}$	$2.46^{+0.08}_{-0.06}$	$0.0222^{+0.0016}_{-0.0009}$	$-1.79^{+0.72}_{-0.60}$

Table 10.9: Best-fit values and 68% credible interval ranges for oscillation parameters for the T2K-Only and T2K + Reactor constraint Data fits presented in Section 10.2.

The best-fit value for $\sin^2 \theta_{13}$ from the T2K-Only Data fit is found to be higher than that measured by reactor experiments, but consistent at the 68% level. The T2K data is able to

produce closed 68% and 90% credible intervals for δ_{CP} , and to exclude the CP-conserving values at the 68% level. Incorporating the PDG value for $\sin^2 \theta_{13}$ from reactor experiment measurements to the prior for $\sin^2 \theta_{13}$ leads to tighter constraints on δ_{CP} , as these parameters are degenerate. The CP-conserving values are excluded at the 95.4% level for the T2K + Reactor constraint Data fit. This constitutes the world-leading constraint for CP-violation in the leptonic sector.

Appendix A

Glossary

- σ_{ABS} : The pion-nucleus absorption cross section.
- σ_{ABS} : The pion-nucleus single charge exchange cross section.
- $\theta_{12}, \theta_{13}, \theta_{23}$: The mixing angles in the PMNS neutrino oscillation framework.
- δ_{CP} : The phase in the PMNS neutrino oscillation framework that encapsulates the matter-antimatter asymmetry in the neutrino sector.
- $\Delta m_{12}^2, \Delta m_{32}^2, \Delta m_{31}^2$: The mass squared splittings in the PMNS neutrino oscillation framework.
- $1R_{\mu}$: Sample of Super-Kamiokande detector events in which a single muon-like ring of Cherenkov light is required.
- $1R_e$: Sample of Super-Kamiokande detector events in which a single electron-like ring of Cherenkov light is required.
- $1R_e$ 1 d.e: Sample of Super-Kamiokande detector events in which a single electron-like ring of Cherenkov light and an additional decay electron are required.
- 1p-1h: One-particle one-hole. A neutrino interaction in which the scatter occurs off a single nucleon.
- 2p-2h: Two-particle two-hole. A neutrino interaction in which the scatter occurs off a multi-nucleon state rather than a single nucleon.
- Asimov fit: An oscillation fit in which the full MC prediction, without any statistical fluctuation, is used as the data.
- CCQE: Charged current quasi-elastic.
- $CC1\pi$: Charged current single pion production.

- CEMBALOS: The downstream detector of DUET.
- Credible interval: Bayesian method for defining the range of values within which an unobserved parameter value falls with a particular subjective probability. A 90% credible interval is defined such that it contains 90% of the posterior probability density.
- Cross section: The interaction probability for a given scattering process.
- DUET: Dual Use Experiment at TRIUMF.
- E_{rec} : Reconstructed neutrino energy.
- FGD: Fine Grained Detector, a sub-detector of the ND280 suite and the primary target. ND280 contains two FGDs: FGD1 has a hydrocarbon target, FGD2 has hydrocarbon and water target.
- FHC mode: Forward horn current mode representing the beam configuration which produces a ν_μ beam.
- Flux: A measure of the number of particles per unit of area per unit of time.
- FSI: Final State Interactions. Pion interactions that occur inside the nucleus in which the neutrino interaction took place.
- FSIFitter: The fitting framework developed by this author to tune the NEUT pion cascade model to external pion scattering data.
- f_{FSI} : The FSI parameters of the NEUT pion cascade model. These are used when tuning to external scattering data, as well as when propagating the FSI uncertainties in the T2K oscillation analysis.
- GEANT4: A platform for the simulation of the passage of particles through matter, using Monte Carlo methods. Used in T2K for the description of the ND280 detector.
- GNU-Octave interpolation: A cubic spline interpolation routine.
- Inverted Hierarchy (IH): The hypothesis of $m_3^2 < m_2^2$ for the neutrino masses.
- J-PARC: Japan Proton Accelerator Research Complex.
- MC: The prediction obtained from a Monte Carlo model simulation.
- MCMC: Markov Chain Monte Carlo. The Bayesian statistical technique used for the oscillation analysis.
- N_{dof} : Number of degrees of freedom.
- Michel electron: The electron produced by the decay of a muon.

- ND280: The Near Detector located 280 m from the target.
- NEUT: The neutrino interaction simulation program used in T2K.
- Nuisance Parameters: A model parameter that affects the posterior probability distribution, but that should be marginalized over to estimate the parameters of interest.
- Normal Hierarchy (NH): The hypothesis of $m_3^2 > m_2^2$ for the neutrino masses.
- OTR: Optical Transition Radiation.
- PIA ν O: The upstream detector and primary target of DUET.
- PID: Particle identification.
- PMT: Photo-Multiplier Tube which is used to detect Cherenkov light at SK.
- PMNS matrix: The Pontecorvo-Maki-Nakawaga-Sakata neutrino mixing matrix.
- Posterior distribution $P(D|\vec{\theta})$: Probability distribution for some model parameters $\vec{\theta}$ given the observed data D .
- POT: Protons-on-target which represent the amount of data collected by the T2K Experiment.
- Prior probability distribution $\pi(\vec{\theta})$: Probability distribution for the model parameters $\vec{\theta}$ containing the prior knowledge about the model.
- RHC mode: Reverse horn current mode representing the beam configuration which produces a $\bar{\nu}_\mu$ beam.
- SI: Secondary Interactions. Pion interactions that occur outside the nucleus in which the neutrino interaction took place, i.e., elsewhere in the detectors.
- Super-Kamiokande: Alternatively Super-K or SK. The far detector located 295 km from the target.
- T2K: Tokai-to-Kamioka.
- TMultiDimFit interpolation: A polynomial interpolation routine.
- TPC: Time projection chamber detector, a sub-detector of the ND280 suite.
- TRIUMF: Tri-University Meson Facility. Canada's national particle accelerator centre.

Appendix B

OTR Post-Earthquake Alignment Studies

J-PARC experienced a high seismic activity during the Great East Japan Earthquake of March 2011. An alignment and surveying campaign was carried out as part of the efforts to return to beam operation. A measurement of the relative alignment of the baffle was achieved by performing low intensity horizontal and vertical beam scans at wide angles, such that the beam would hit the edge of the baffle. The strategy is to find the shadow of the baffle. This can be done by taking the first derivatives in the x and y directions for the horizontal and vertical directions, respectively, and fitting an ellipse to find its centre, semi-minor, and semi-major axes.

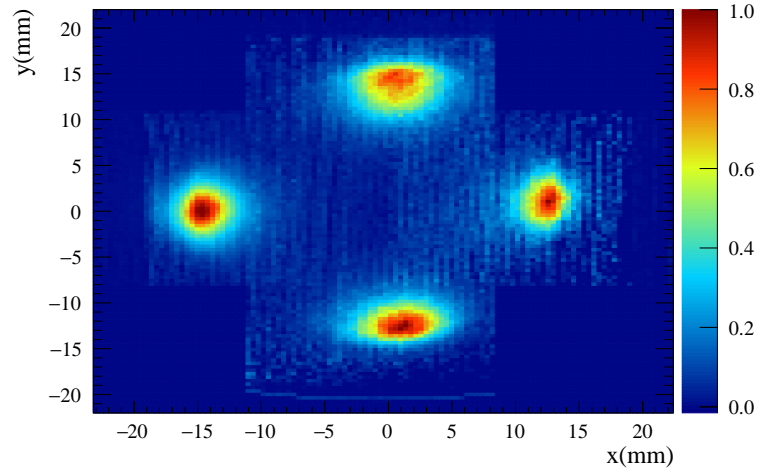
Figure B.1a shows the normalized OTR beam profiles from these scans combined into a single image. Figure B.1b shows the first derivative of the combined profiles, where only bins with a large (positive) derivative are drawn. The χ^2 described in Equation B.1 was minimized using MINUIT [157]:

$$\chi^2 = \sum_{i,j} \left[w_{ij} \left(1 - \left(\frac{x_j - x_0}{a} \right)^2 + \left(\frac{y_i - y_0}{b} \right)^2 \right) \right]^2 \quad (\text{B.1})$$

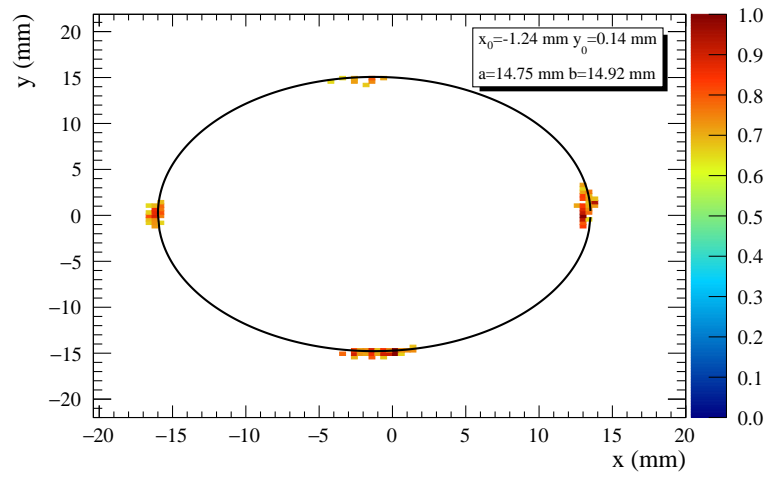
where (x_0, y_0) are the coordinates of the centre of the ellipse, a and b are the semi-minor and semi-major axes, respectively, i and j run over the number of horizontal and vertical pixels, and w_{ij} is the derivative in pixel in the (i, j) position. Table B.1 shows the measured baffle centre and width before and after the earthquake. The measured centres agree within the uncertainties in the OTR profile measurements and the baffle shadow method.

	x Centre (mm)	y Centre (mm)	x Width (mm)	y Width (mm)
Pre-earthquake	-0.55	0.17	15.0	14.8
Post-earthquake	-1.24	0.14	14.8	14.9

Table B.1: Baffle centre and width measurements before and after the earthquake.



(a)



(b)

Figure B.1: OTR profiles and analysis for the baffle alignment studies. (a) Combined OTR beam profiles from horizontal and vertical beam scans. (b) Bins with large derivative of the combined profiles and fitted ellipse to find the baffle edge.

Appendix C

FSIFitter Validation Studies

In order to check the robustness of the fit and its minimization algorithm to the initial position in the 5D parameter space, the fit was started at random positions within the finite grid defined in Table 7.2. Figure C.1 shows the distribution of the 100 starting positions used for this study.

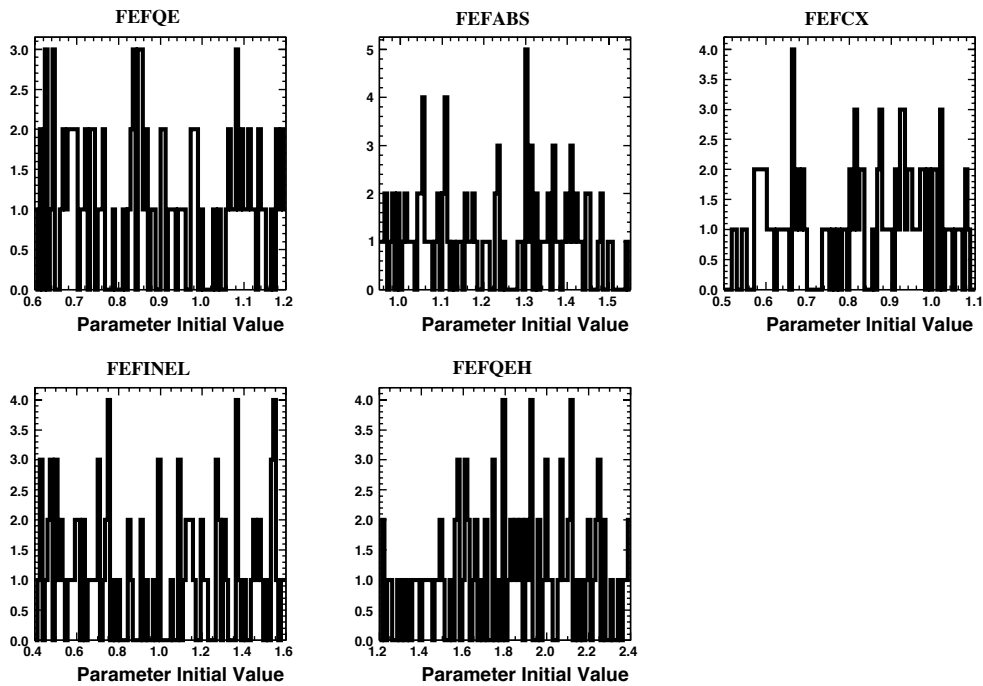


Figure C.1: Distribution of starting values for the 5 FSI parameters thrown randomly inside the finite grid defined in Table 7.2.

Figure C.2 shows the distribution of post-fit values for these 100 random starting positions. The distribution of post-fit parameters obtained are consistent within their uncertainties. This indicates the robustness of the interpolation and minimization algorithms, and ensures that a global minimum is being found.

The effect of manually adding correlations across the data points has been discussed in detail

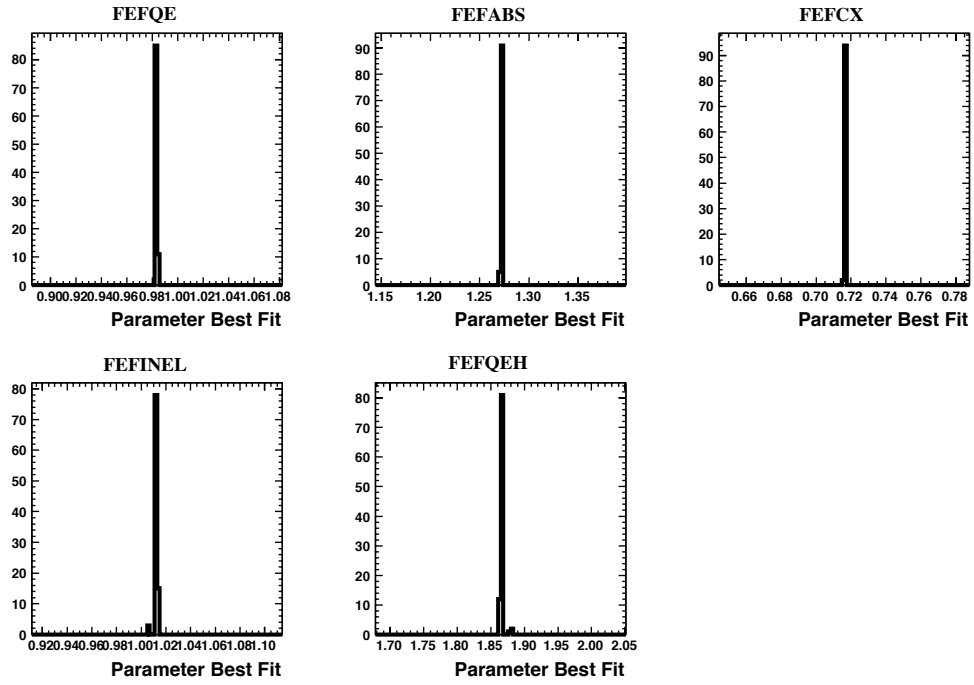


Figure C.2: Distribution of best fit values for the 5 FSI parameters thrown randomly inside the finite grid defined in Table 7.2.

in [152].

Appendix D

Ratio of Data and NEUT Best-fit Comparisons

Figures D.1 to D.12 show the comparisons between the external pion scattering data used for tuning of the NEUT cascade model in Chapter 7 and the obtained NEUT best fit as a ratio between these two. The 1σ error band is also plotted as a ratio to the best-fit value. These plots are meant to aid in the interpretation of the coverage of the external data achieved by the error inflation procedure described in Section 7.3.4.

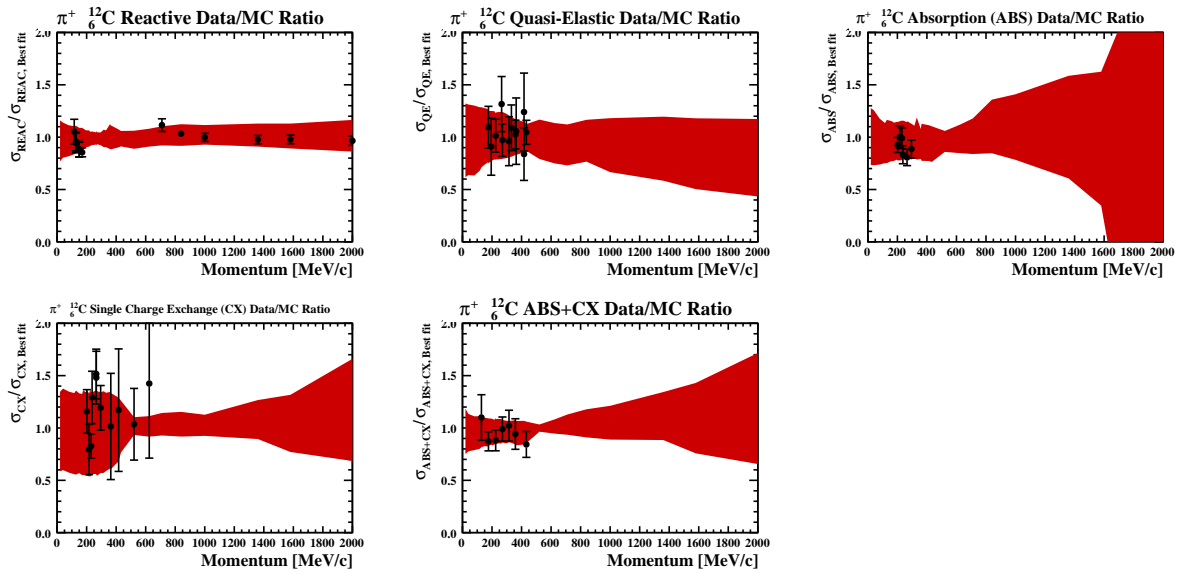


Figure D.1: Ratio of Data and NEUT best fit for π^+ -C cross sections. The red band represents the 1σ error band.

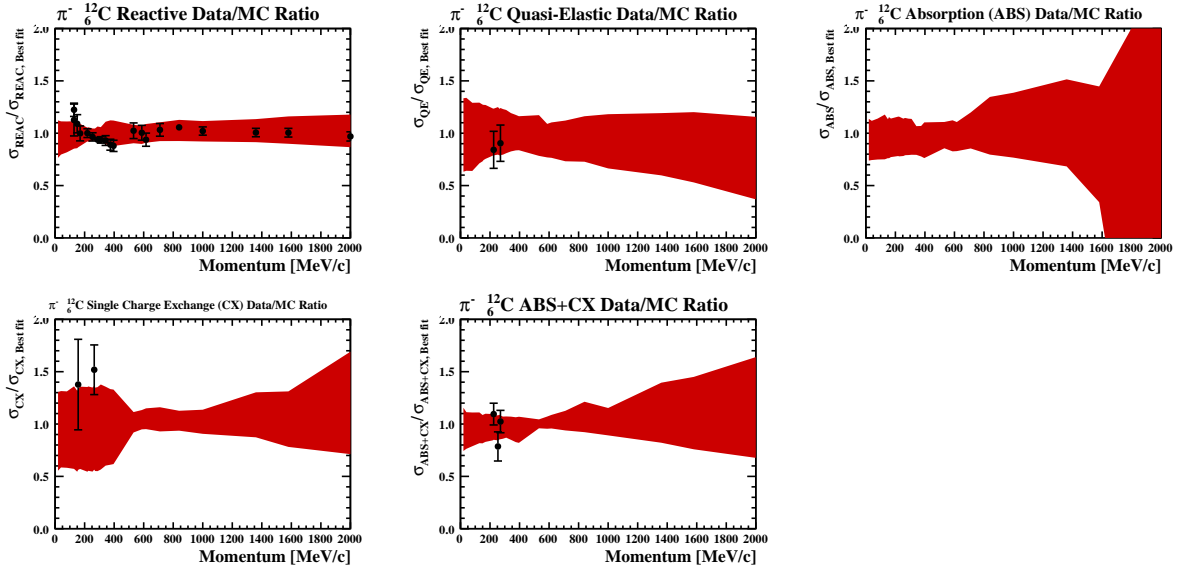


Figure D.2: Ratio of Data and NEUT best fit for π^- -C cross sections. The red band represents the 1σ error band.

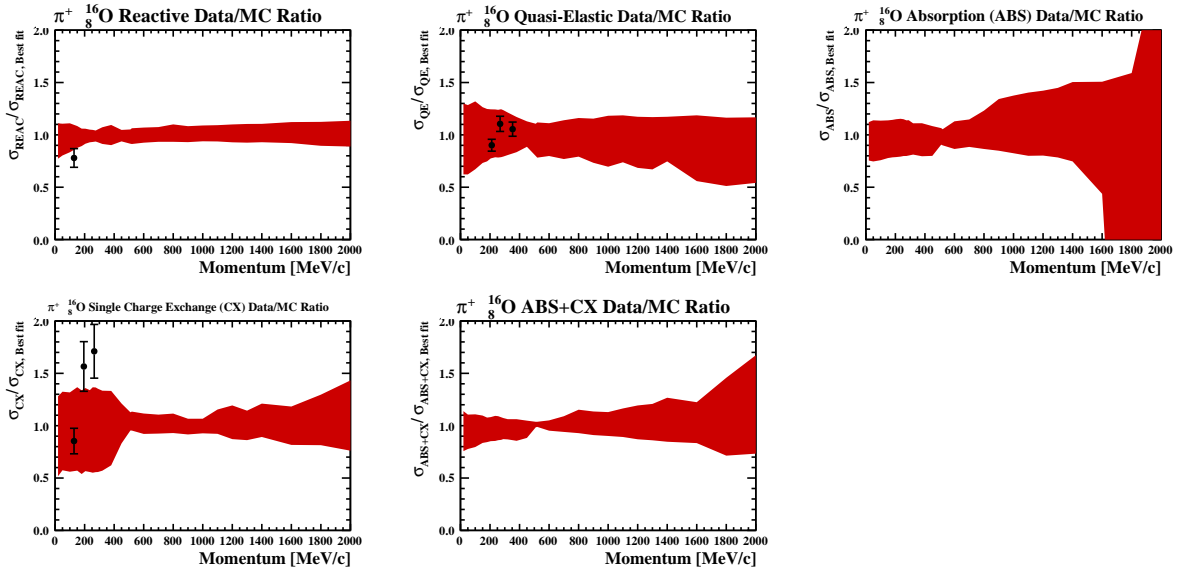


Figure D.3: Ratio of Data and NEUT best fit for π^+ -O cross sections. The red band represents the 1σ error band.

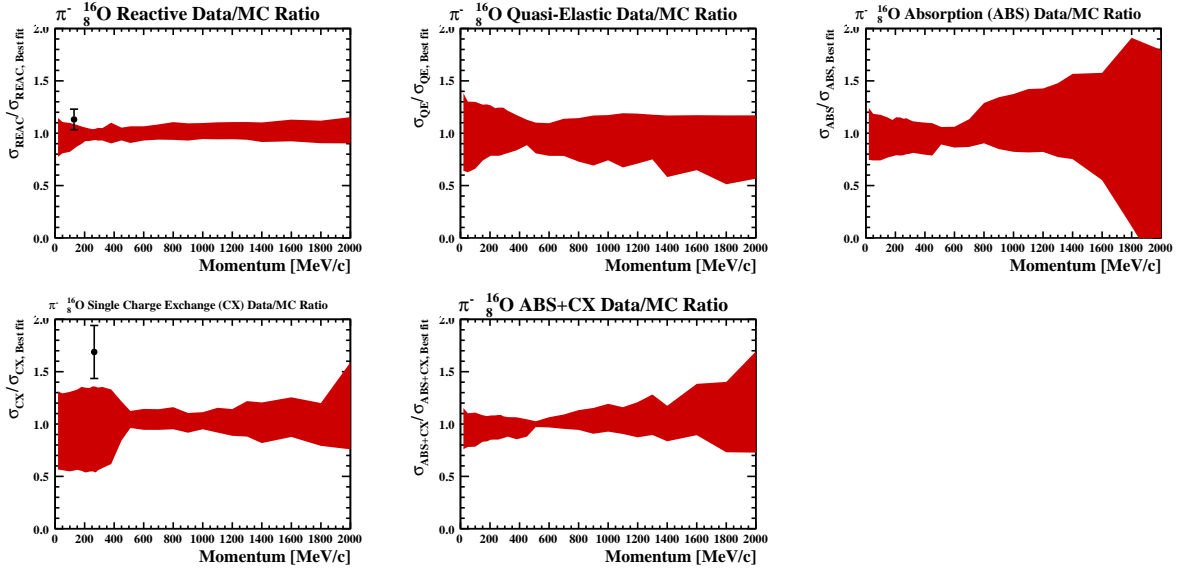


Figure D.4: Ratio of Data and NEUT best fit for π^- -O cross sections. The red band represents the 1σ error band.

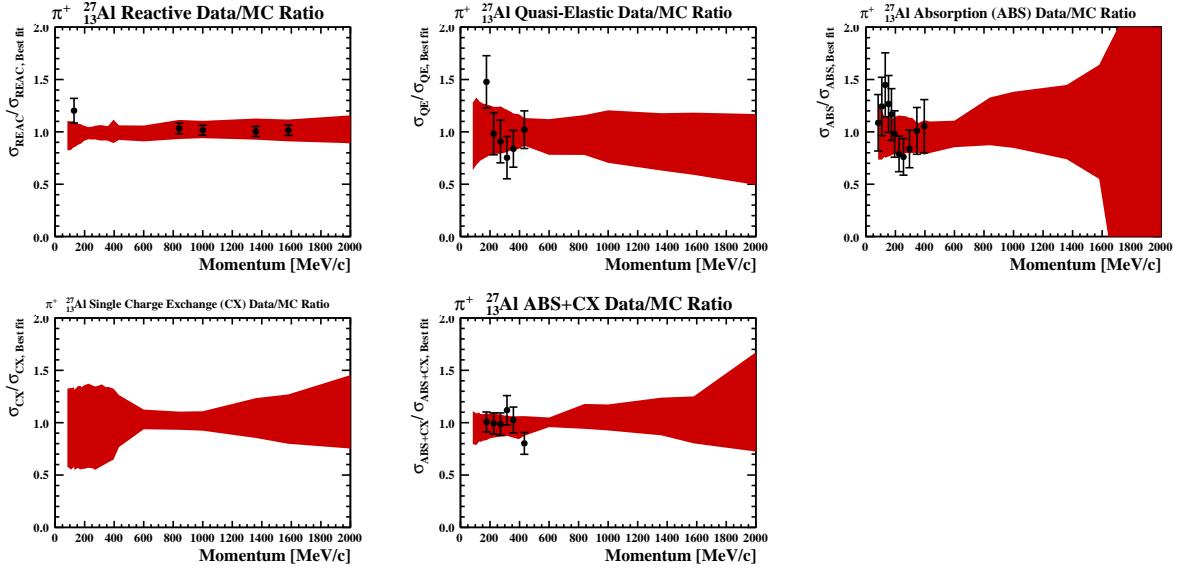


Figure D.5: Ratio of Data and NEUT best fit for π^+ -Al cross sections. The red band represents the 1σ error band.

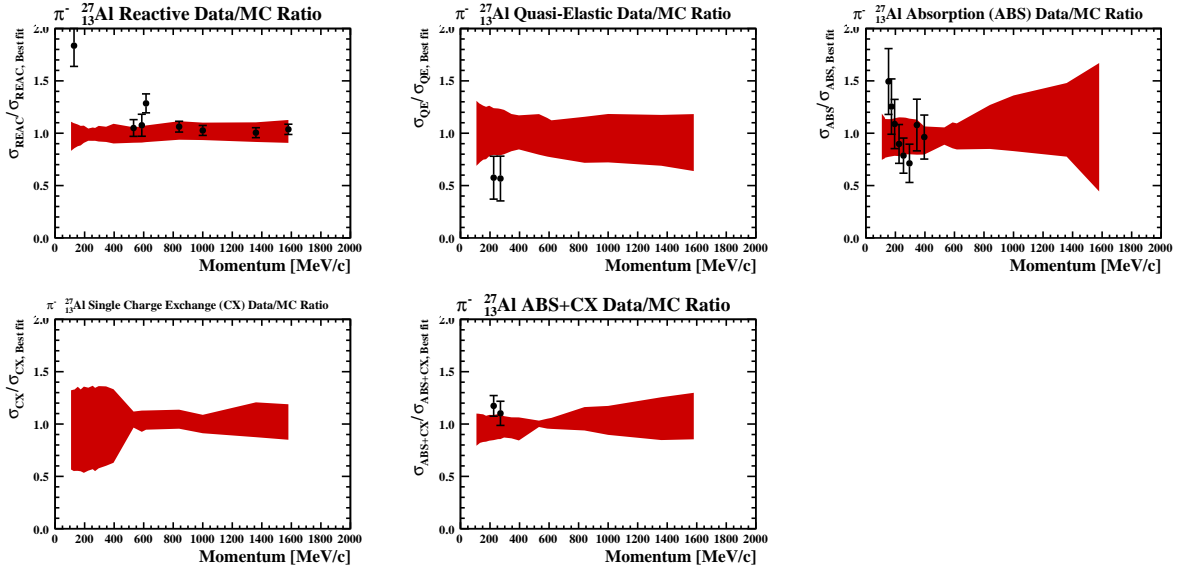


Figure D.6: Ratio of Data and NEUT best fit for π^- -Al cross sections. The red band represents the 1σ error band.

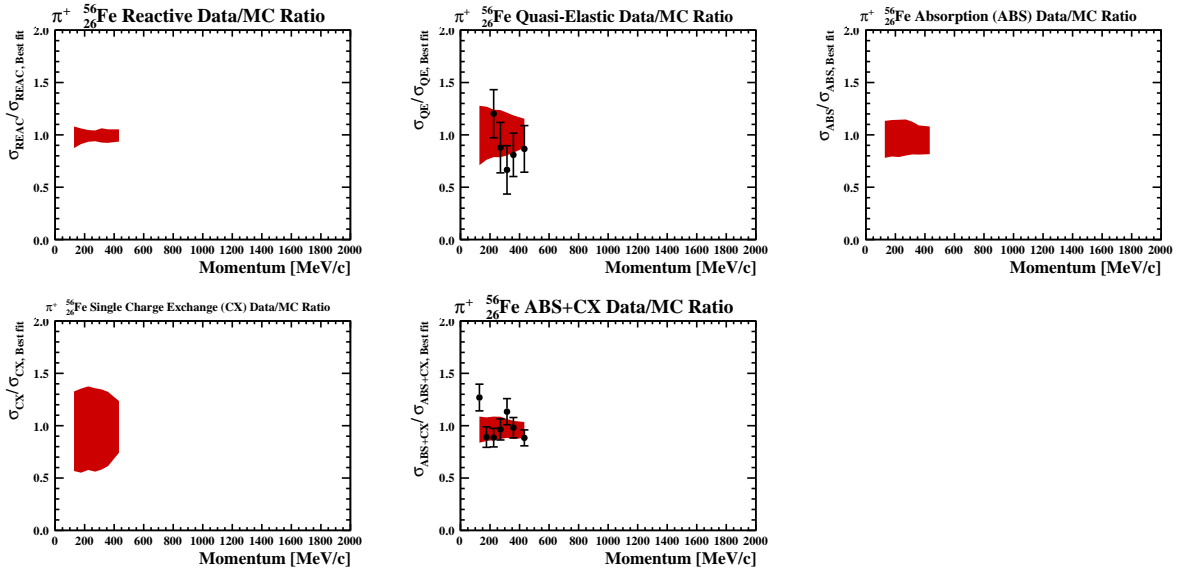


Figure D.7: Ratio of Data and NEUT best fit for π^+ -Fe cross sections. The red band represents the 1σ error band.

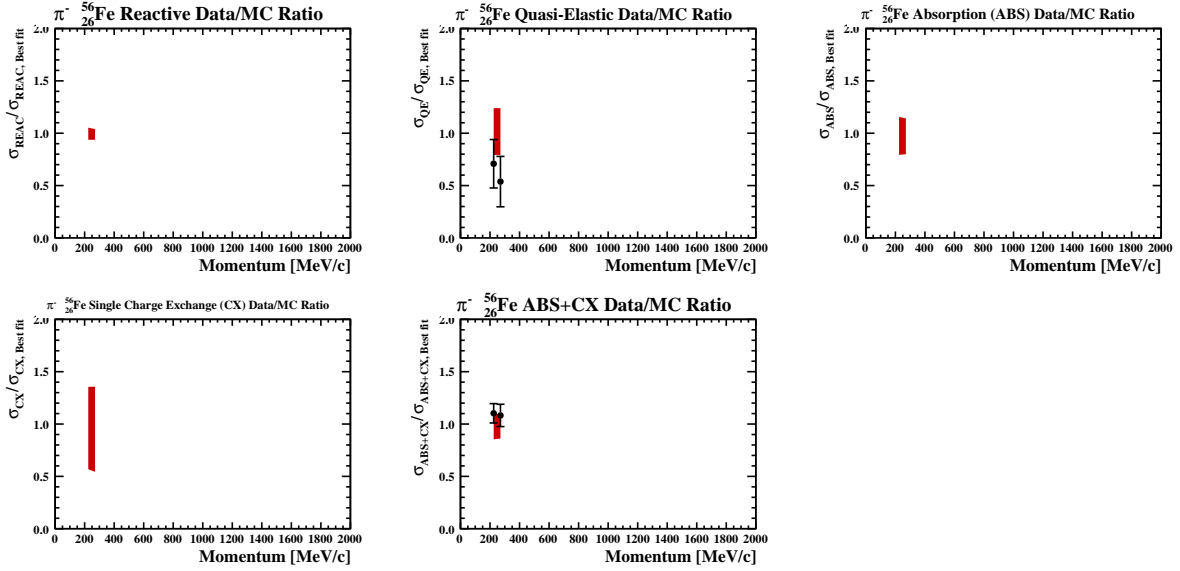


Figure D.8: Ratio of Data and NEUT best fit for π^- -Fe cross sections. The red band represents the 1σ error band.

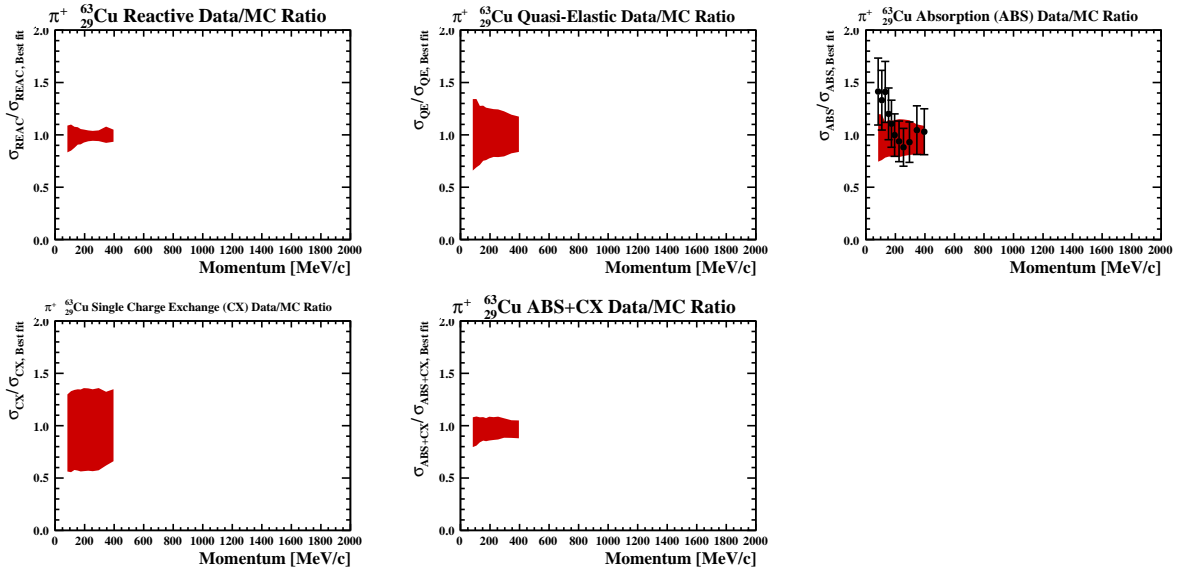


Figure D.9: Ratio of Data and NEUT best fit for π^+ -Cu cross sections. The red band represents the 1σ error band.

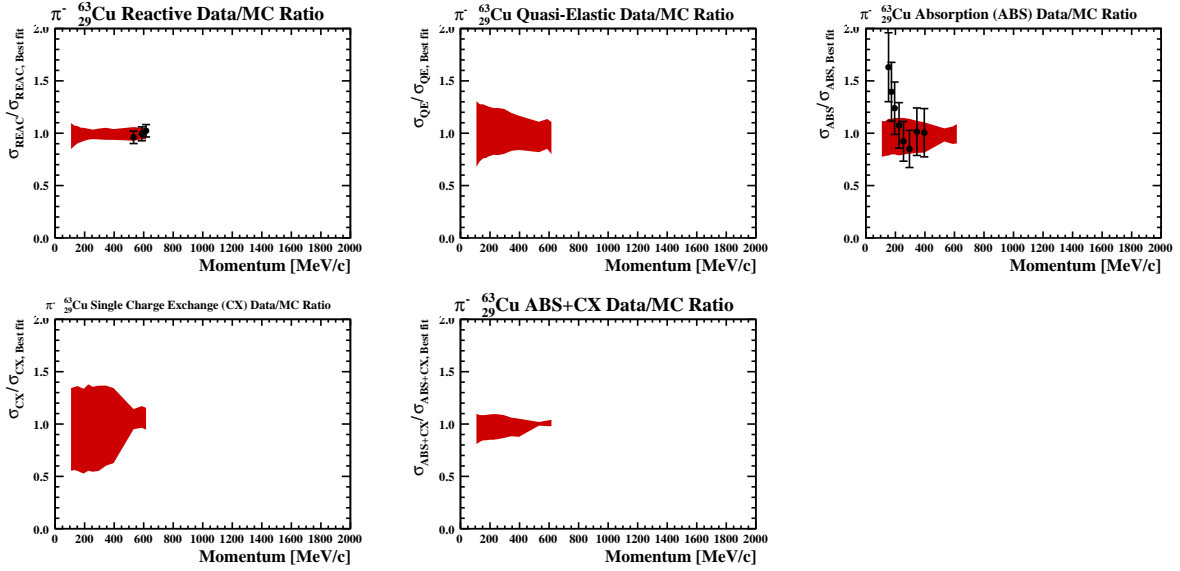


Figure D.10: Ratio of Data and NEUT best fit for π^- -Cu cross sections. The red band represents the 1σ error band.

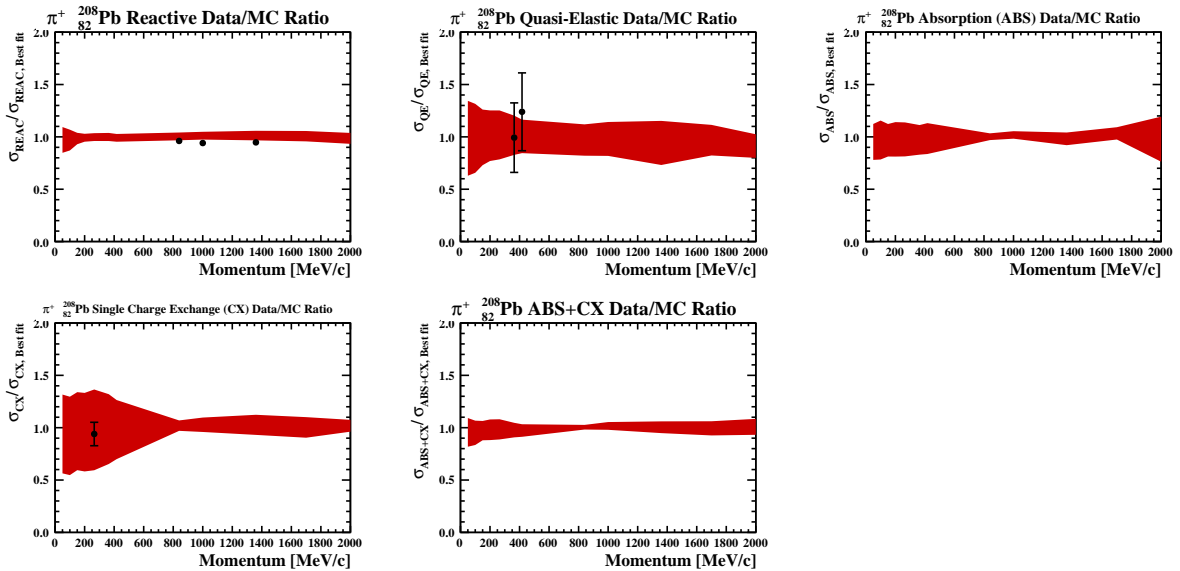


Figure D.11: Ratio of Data and NEUT best fit for π^+ -Pb cross sections. The red band represents the 1σ error band.

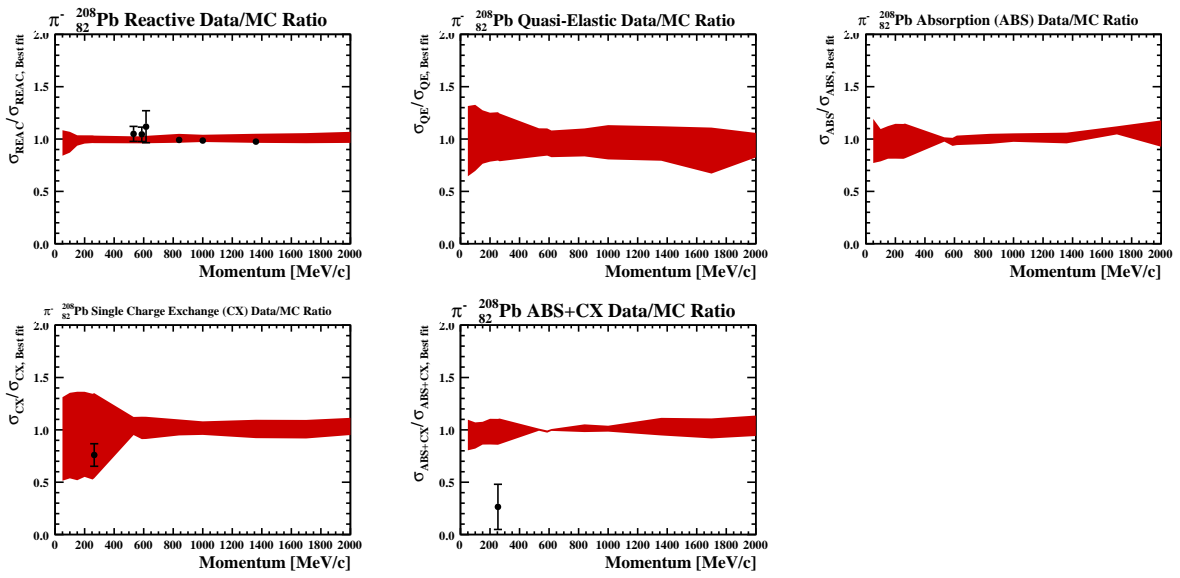


Figure D.12: Ratio of Data and NEUT best fit for π^- -Pb cross sections. The red band represents the 1σ error band.

Appendix E

Comparison of π^\pm -A Scattering Models

The modelling of pion-nucleus interactions is fundamental for a complete description of neutrino-nucleus interactions. Hence, every neutrino event generator on the market includes a model for these final state interactions. A brief description of the various approaches used by generators is presented in Section E.1.

In this section the tuned NEUT cascade model and the selection of external data described in Section 7.1.3 are contrasted with various models. These comparisons are meant to be purely informative, and no quantitative conclusions are drawn at this time.

This work was developed under the FSI/SI Task Force of T2K. The GENIE and NUWRO predictions were produced by Dr. Arturo Fiorentini (York U.), while the FLUKA predictions were produced by Mitchell Yu (York U.).

E.1 Brief Description of Models

The models used to describe pion-nucleus can be divided into the following three categories:

(1) **Effective Models**

- GENIE hA is a simple, data-driven, effective model [126]. It uses an interpolation of external data of cross-section for each possible interaction channel as a function of energy (up to 1.2 GeV) to determine the final state. It was developed for MINOS, so only π -Fe external data was used. Cross sections for targets other than iron are obtained by scaling by $A^{2/3}$. It uses identical cross sections for π^+ and π^- . This is the default model in GENIE and has been used by most MINERvA and NOvA analyses published to date.
- The GENIE hA 2014 is meant to be a developmental version of this model and is also included in these comparisons for completeness.

(2) Cascade models

While the following cascade models follow the same general principles as the NEUT cascade model described in Section 4.3, the numerical implementations and input data and theory models are often different, and are a reflection of different motivations and priorities in the development of the models.

- GENIE hN is an alternative model for FSI in GENIE [126]. Only data on free nucleons is used as input. The development version of this model, GENIE hN2015 is used for this comparisons. Work is ongoing to incorporate the Oset *et al.* model [115] used in NEUT.
- The PEANUT (Pre-Equilibrium Approach to NUClear Thermalization) model is an intra-nuclear cascade model implemented in FLUKA [84, 85]. Similarly to NEUT, it uses the Oset *et al.* model [115] to describe the absorptive width of the optical potential for pion momenta below 300 MeV/ c . Cross-sections of pions on free nucleons are combined to describe elastic, quasi-elastic, and charge exchange interactions.
- The Bertini cascade model of GEANT4 v4.9.4 [120] is part of the QGSP_BERT physics list used in detector simulations of ND280. It's valid from 0.0 to 9.9 GeV/ c pion momentum. It also handles all other long-live hadrons. A detailed treatment of pre-equilibrium and evaporation physics is included, relevant at energies below 200 MeV where the cascade model approach begins to fail as the de Broglie wavelength of the probe is roughly the same as the distance between nucleons in the target nucleus. The CERN-HERA compilation of hadron-nucleus elementary cross-section data is used as input [193].
- The NUWRO event generator also includes a cascade model [125] based on the Oset *et al.* model [115]. It introduces a phenomenological treatment of the formation zone (or time) effect, which can interplay with the pion absorption probability in a non-trivial momentum dependent way.

(3) Transport models

- The Giessen Boltzmann-Uehling-Uhlenbeck (GiBUU) model is an implementation of transport model for nuclear reactions [118]. It describes the dynamical evolution of the interacting nuclear system through a coupled set of semi-classical kinetic equations, while taking into account the hadronic potentials and the equation of state of nuclear matter within the Boltzmann-Uehling-Uhlenbeck (BUU) theory.

E.2 Comparison to NEUT

The following model predictions were generated by running thin target particle gun simulations. The exception being GiBUU, where the predictions for REAC and ABS of π^\pm -C and

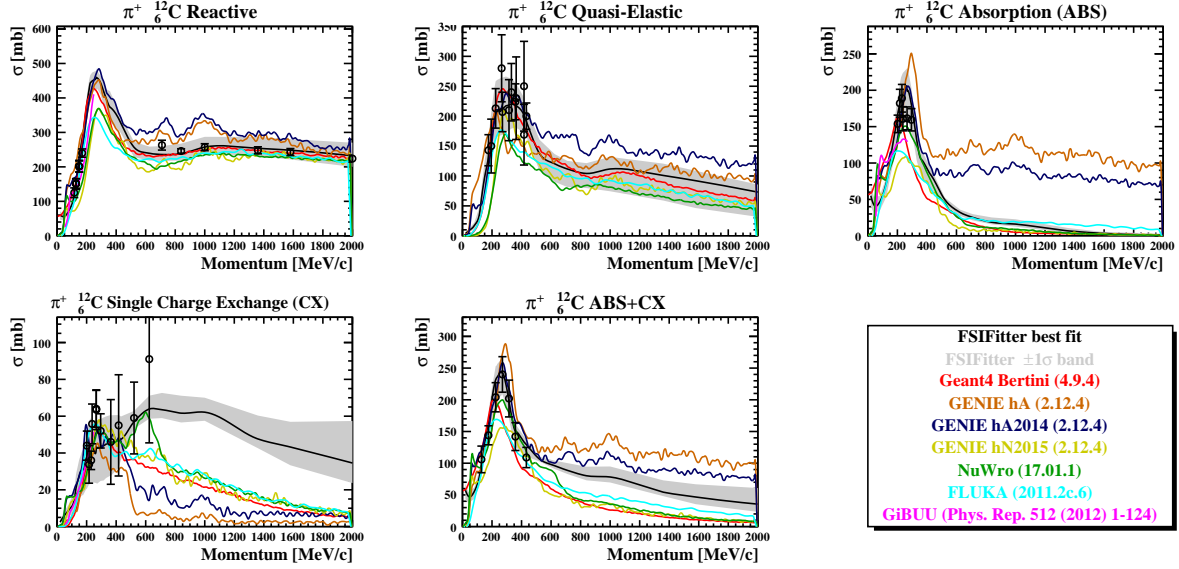


Figure E.1: Comparison of the available π^+ -C cross section external data with the FSIFitter best fit and its 1σ band, and other models.

π^\pm -Cu were digitized from [118]. To allow for a consistent comparison, the interactions channels were defined using only the final state particles as described in Section 7.1.2.

Figures E.1 to E.12 show the comparison for π^\pm cross sections on carbon, Oxygen, Aluminum, Iron, and Lead. In general, all models produce consistent predictions in the Δ region. At higher momentum, the NEUT model predicts a much larger cross-section for the single charge exchange channel. However, given that the agreement is recovered in the reactive channel, this is likely to be caused by differences in the tagging of hadron production events (π^\pm -A \rightarrow $\pi^+\pi^-X$ where the π^+ is absorbed).

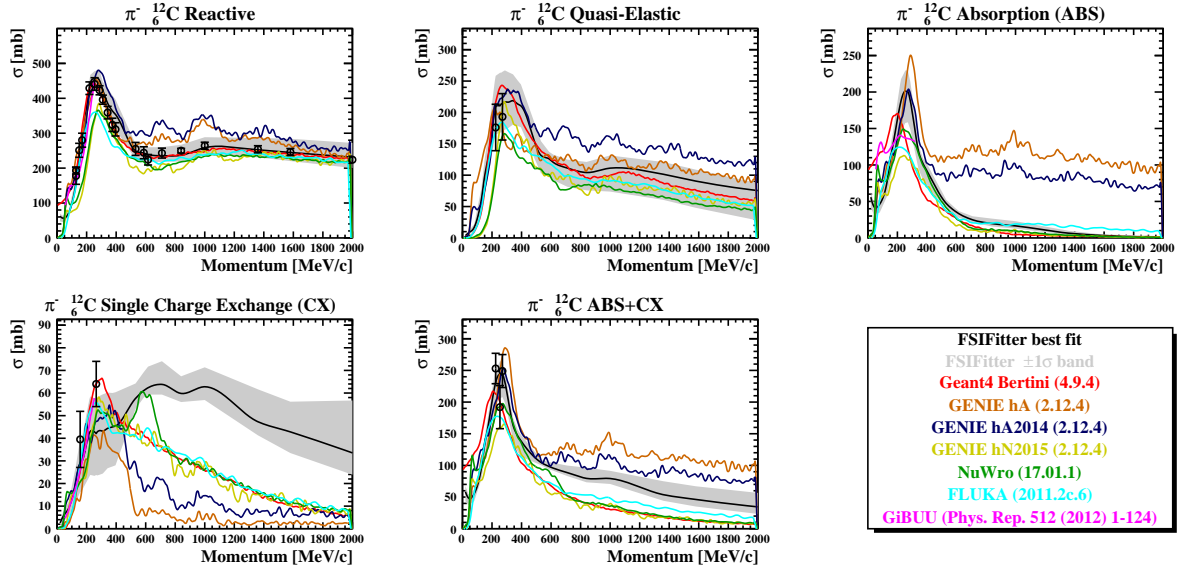


Figure E.2: Comparison of the available π^- -C cross section external data with the FSIFitter best fit and its 1σ band, and other models.

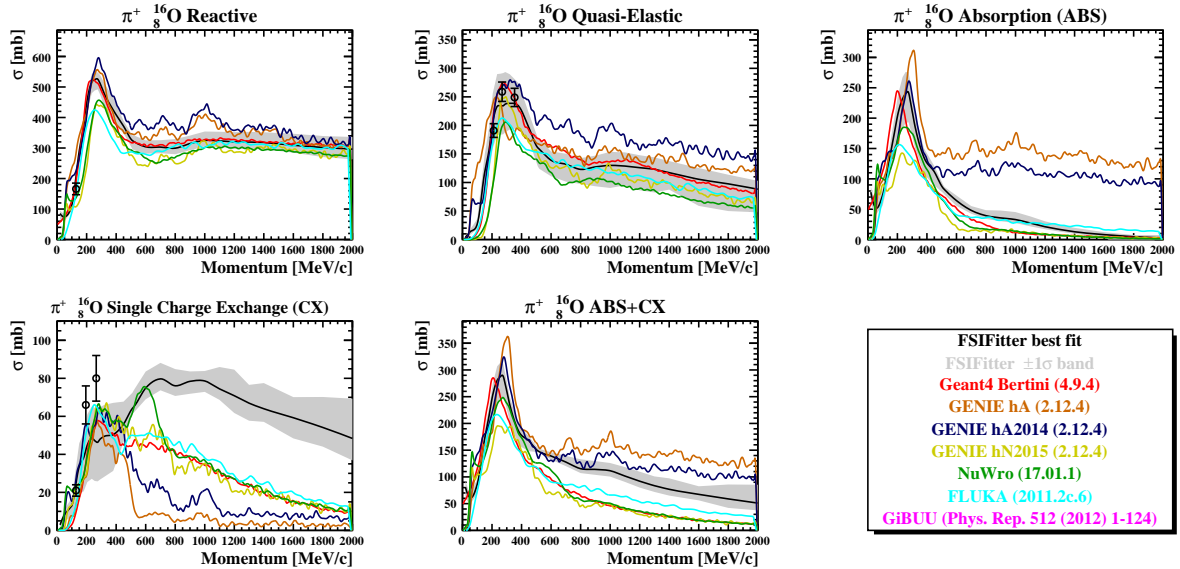


Figure E.3: Comparison of the available π^+ -O cross section external data with the FSIFitter best fit and its 1σ band, and other models.

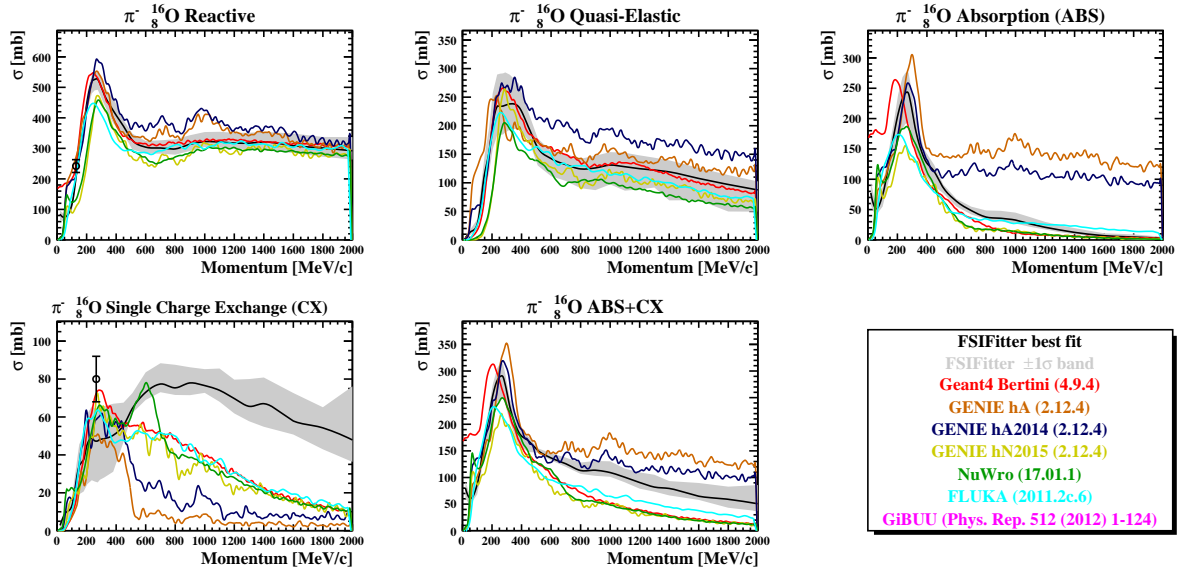


Figure E.4: Comparison of the available π^- -O cross section external data with the FSIFitter best fit and its 1σ band, and other models.

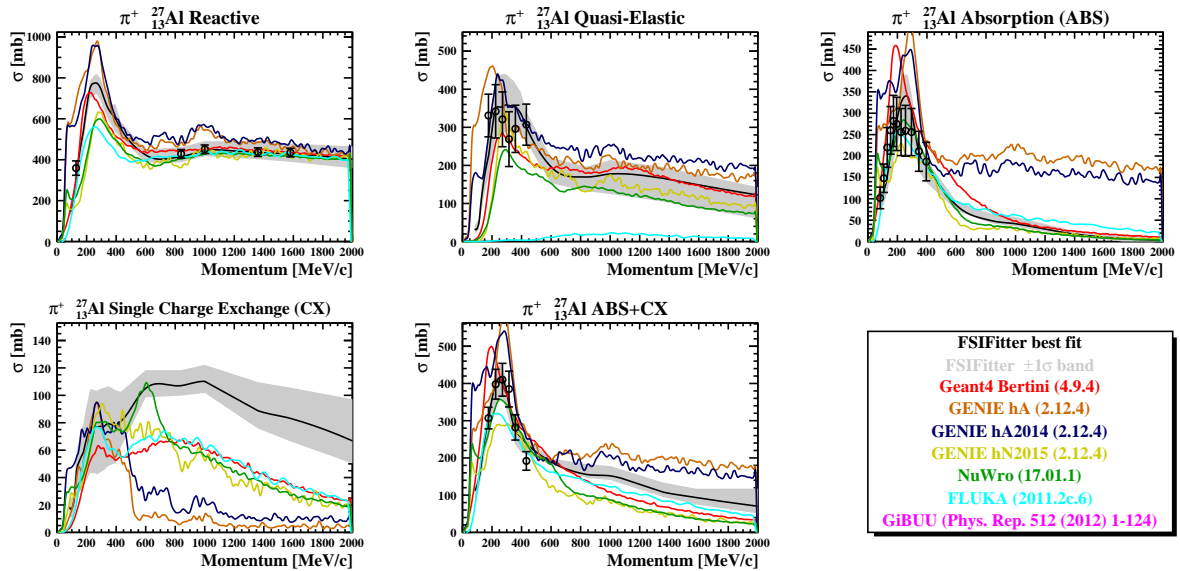


Figure E.5: Comparison of the available π^+ -Al cross section external data with the FSIFitter best fit and its 1σ band, and other models.

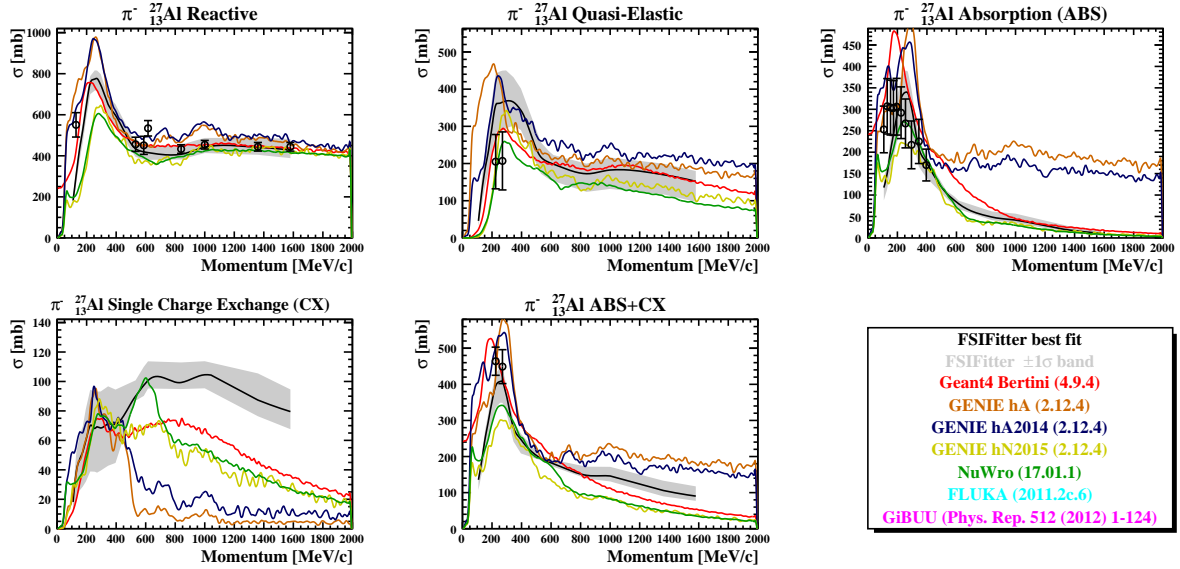


Figure E.6: Comparison of the available π^- -Al cross section external data with the FSIFitter best fit and its 1σ band, and other models.

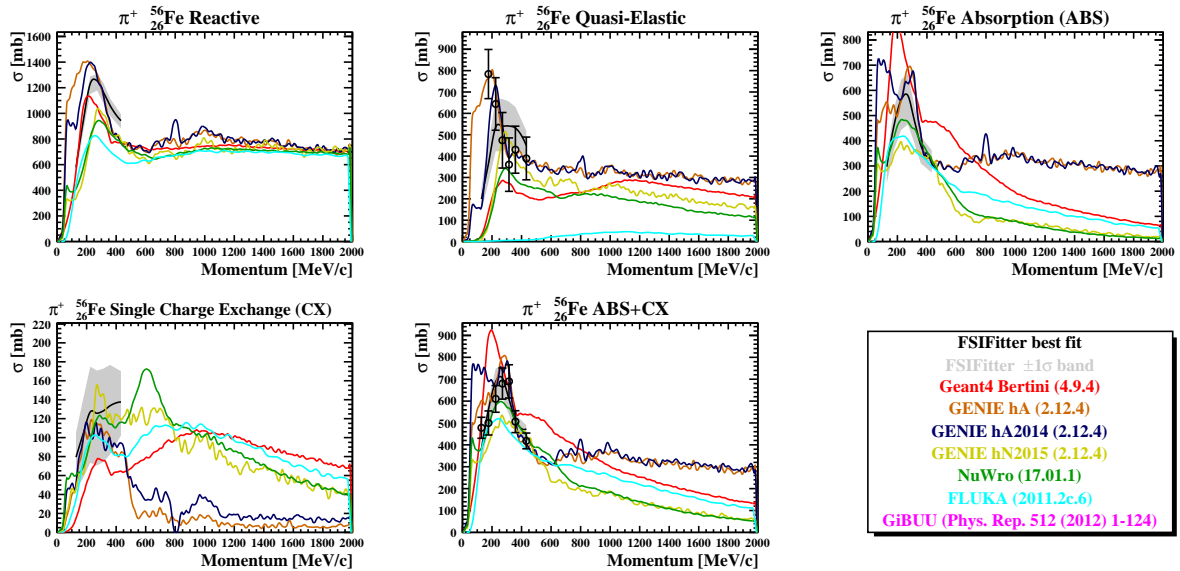


Figure E.7: Comparison of the available π^+ -Fe cross section external data with the FSIFitter best fit and its 1σ band, and other models.

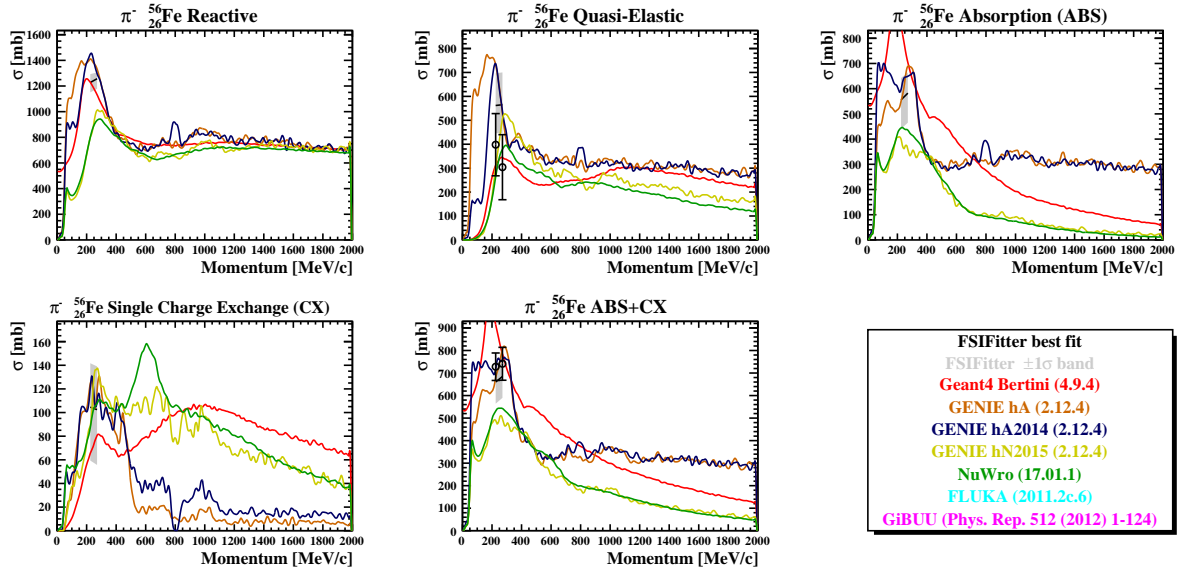


Figure E.8: Comparison of the available π^- -Fe cross section external data with the FSIFitter best fit and its 1σ band, and other models.

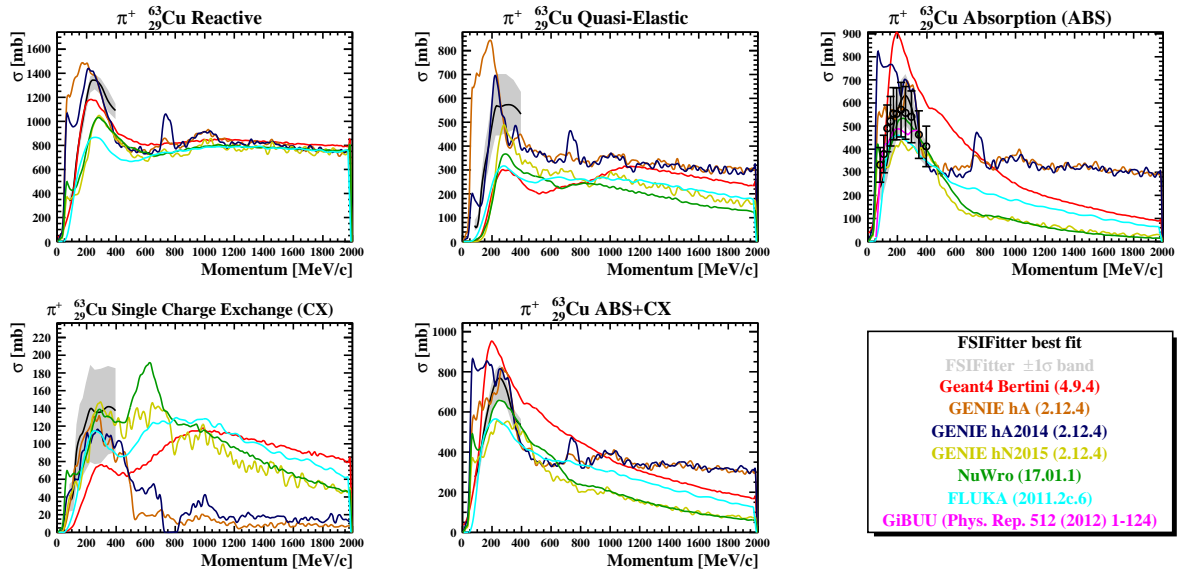


Figure E.9: Comparison of the available π^+ -Cu cross section external data with the FSIFitter best fit and its 1σ band, and other models.

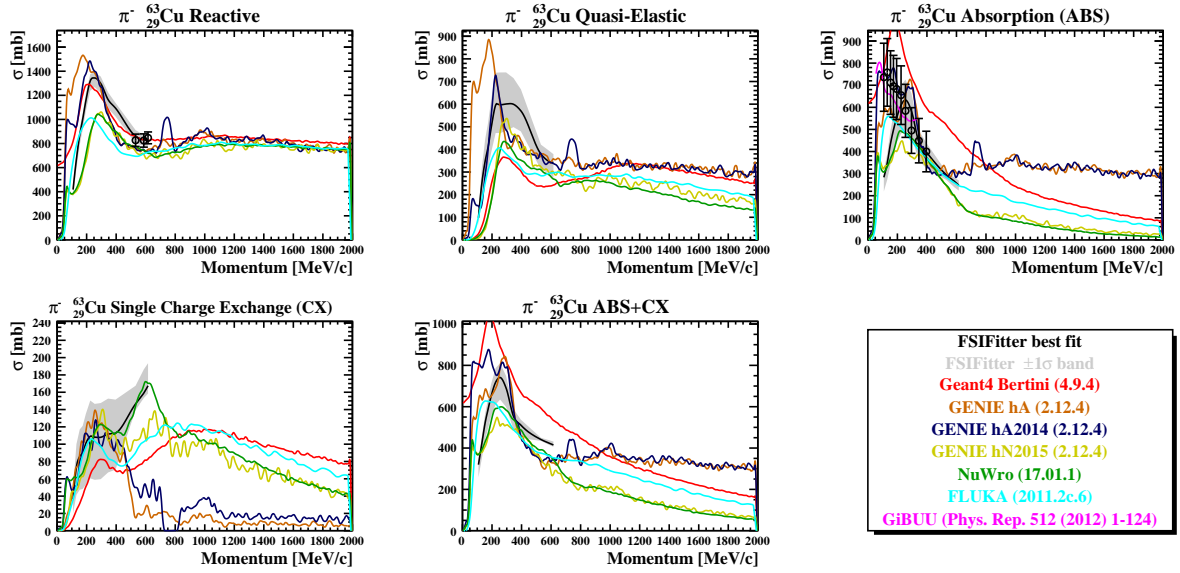


Figure E.10: Comparison of the available π^- -Cu cross section external data with the FSIFitter best fit and its 1σ band, and other models.

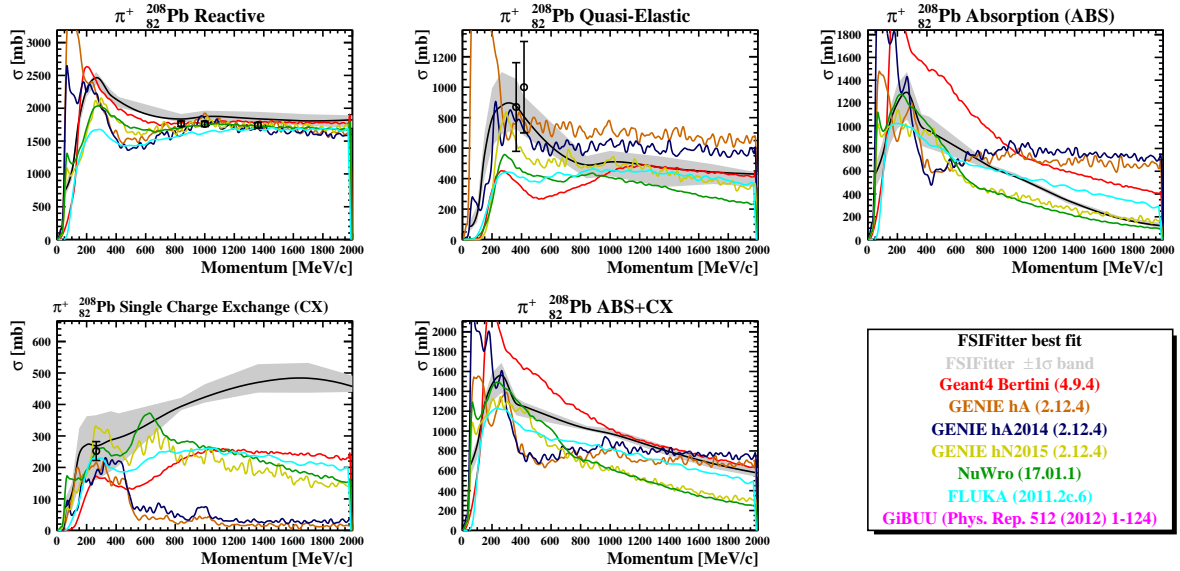


Figure E.11: Comparison of the available π^+ -Pb cross section external data with the FSIFitter best fit and its 1σ band, and other models.

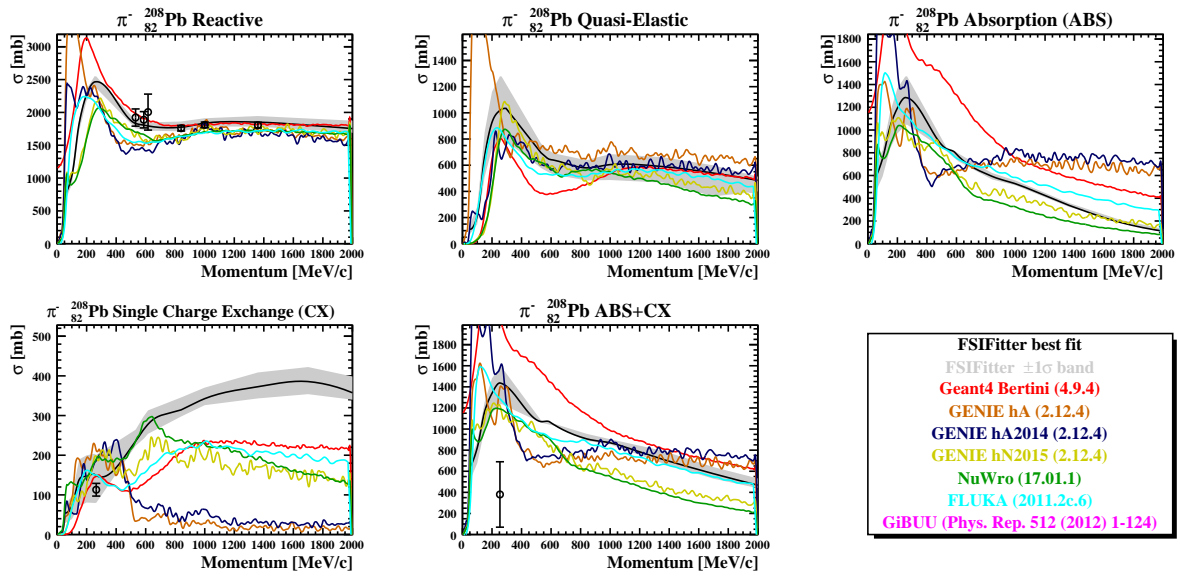


Figure E.12: Comparison of the available π^- -Pb cross section external data with the FSIFitter best fit and its 1σ band, and other models.

Appendix F

Comparison to the Official MaCh3 Run 1-8 Oscillation Analysis

This Appendix presents a comparison between the Asimov fit results described in Section 10.1 and the Asimov fits for the official T2K Run 1-8 oscillation analysis [166]. As was described in Section 9.3, the analysis presented in this thesis features an improved treatment of Final State Interaction and Secondary Interactions, relative to the official analysis. The ND280 and SK data sets and POT are the same between the two analyses. The implementation and prior uncertainties for the flux, cross section, and SK detector models are also the same between the two analyses.

F.1 Nuisance Parameters

Figures F.1, F.2, and F.3 show comparisons of the mean and RMS of the posterior probabilities for the flux, cross-section and SK detector model parameters for Asimov T2K-Only fits from each analysis. The results from the official T2K analysis are labelled “Nominal”, while the results from this thesis are labelled “Correlated FSI”.

The only differences observed for the nuisance parameters between the two analyses are those expected from the changes to the FSI and SI framework improvements. The two fits used different priors for the FSI parameters (last 6 parameters in Figure F.1) and for the analysis presented in this thesis, the FSI parameters applied to both ND280 and SK samples.

Similarly, the large differences in the posterior of some of the SK detector parameters arises from the improved treatment of FSI uncertainties. As was discussed in Sections 3.3 and 9.3, the SK detector normalization parameters for the analysis presented in this thesis no longer contain the uncertainties for FSI. In addition, the SI uncertainties were reduced relative to the T2K Run 1-8 official analysis by taking advantage of the improved constraints from the fit to π -A scattering data presented in Chapter 7. This resulted in reduced prior uncertainties for the SK detector parameters previously dominated by FSI effects, which translated to the reduced post-fit uncertainties seen in Figure F.3.

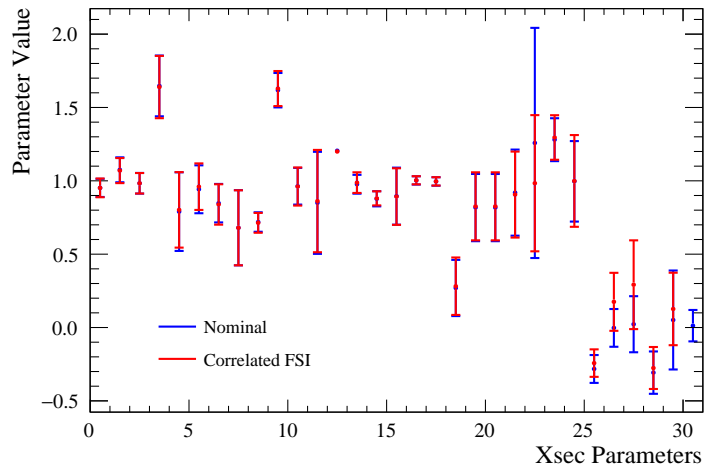


Figure F.1: Comparison of the Mean and RMS of the posteriors for all cross-section parameters for the official T2K Run 1-8 oscillation analysis (blue) and the analysis presented in this thesis (red).

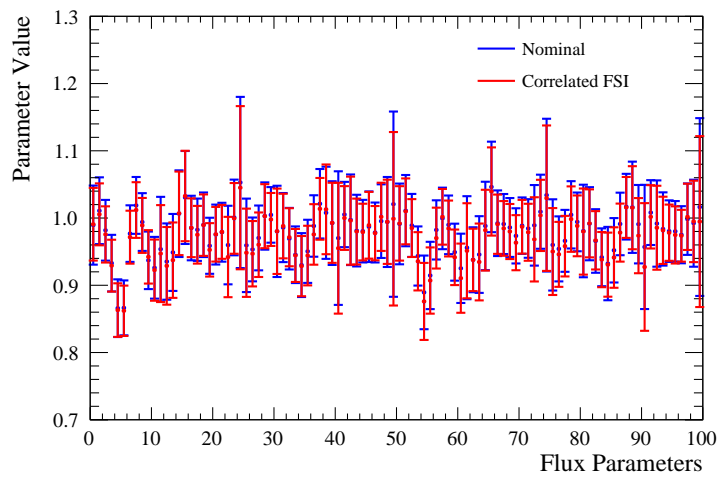


Figure F.2: Comparison of the Mean and RMS of the posteriors for all flux parameters for the official T2K Run 1-8 oscillation analysis (blue) and the analysis presented in this thesis (red).

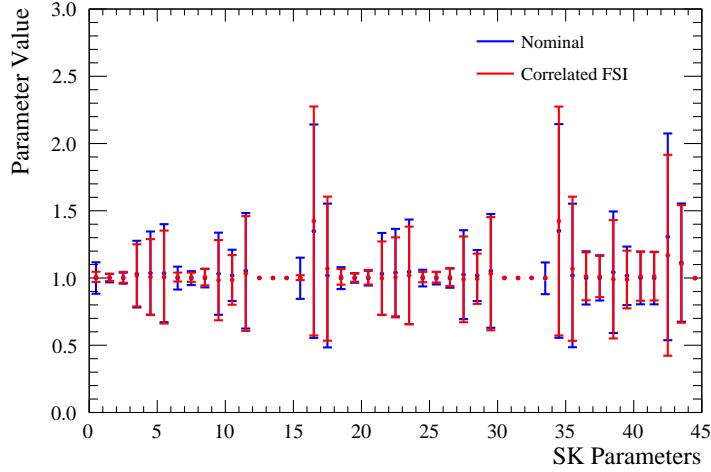


Figure F.3: Comparison of the Mean and RMS of the posteriors for all SK detector parameters for the official T2K Run 1-8 oscillation analysis (blue) and the analysis presented in this thesis (red).

F.2 Oscillation Parameters

Figures F.4 and F.5 shows a comparison of 1D posteriors for the oscillation parameters of interest obtained from T2K-Only Asimov and T2K + Reactor constraint fits. The results from the official T2K analysis are labelled “Nominal”, while the results from this thesis are labelled “Correlated FSI”.

Similar to what was seen for the nuisance parameters, the differences observed between the posteriors from the two analyses are those expected from the improvements to the FSI treatment. As was discussed in Section 9.3.2.1, the finer binning used to parameterize the FSI uncertainties at SK becomes most significant for the $1R_\mu$ samples, as can be seen from Figure 9.13. The effect of variations of the FSI parameters, particularly FEFABS, can modify the shape and normalization of the spectrum in the area where the oscillation dip occurs. The location and height of this dip are directly correlated to the values of $\sin^2 \theta_{23}$ and Δm_{23}^2 . For this reason, it is natural to expect differences in the posteriors for these parameters.

The similar posterior probability densities between the two analyses for $\sin^2 \theta_{13}$ can be interpreted from the fact that this parameter is not highly correlated with the shape information of the $1R_e$ samples, rather with its normalization. Finally, the effect of the FSI parameters is similar for FHC mode and RHC mode samples, so the similar posteriors for δ_{CP} were expected.

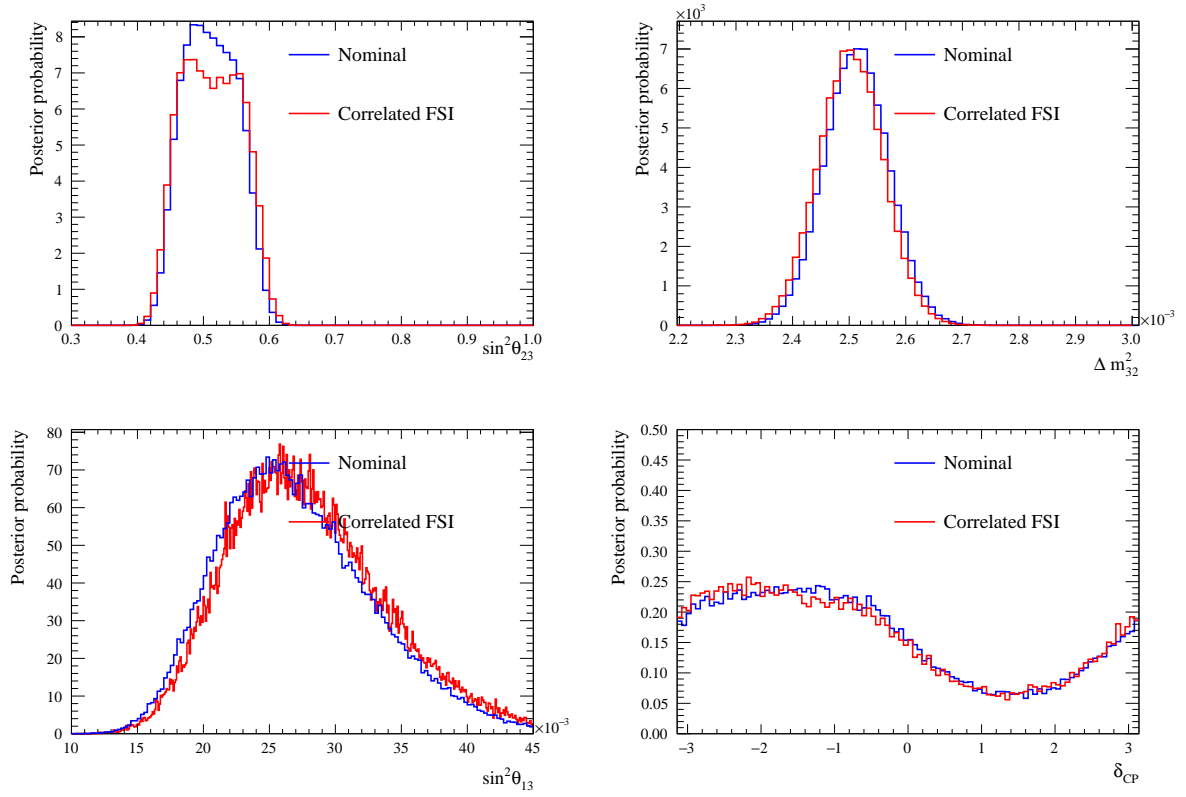


Figure F.4: Posterior probability densities for the appearance and disappearance parameters from T2K-Only Asimov fits for the official T2K Run 1-8 oscillation analysis (blue) and the analysis presented in this thesis (red).

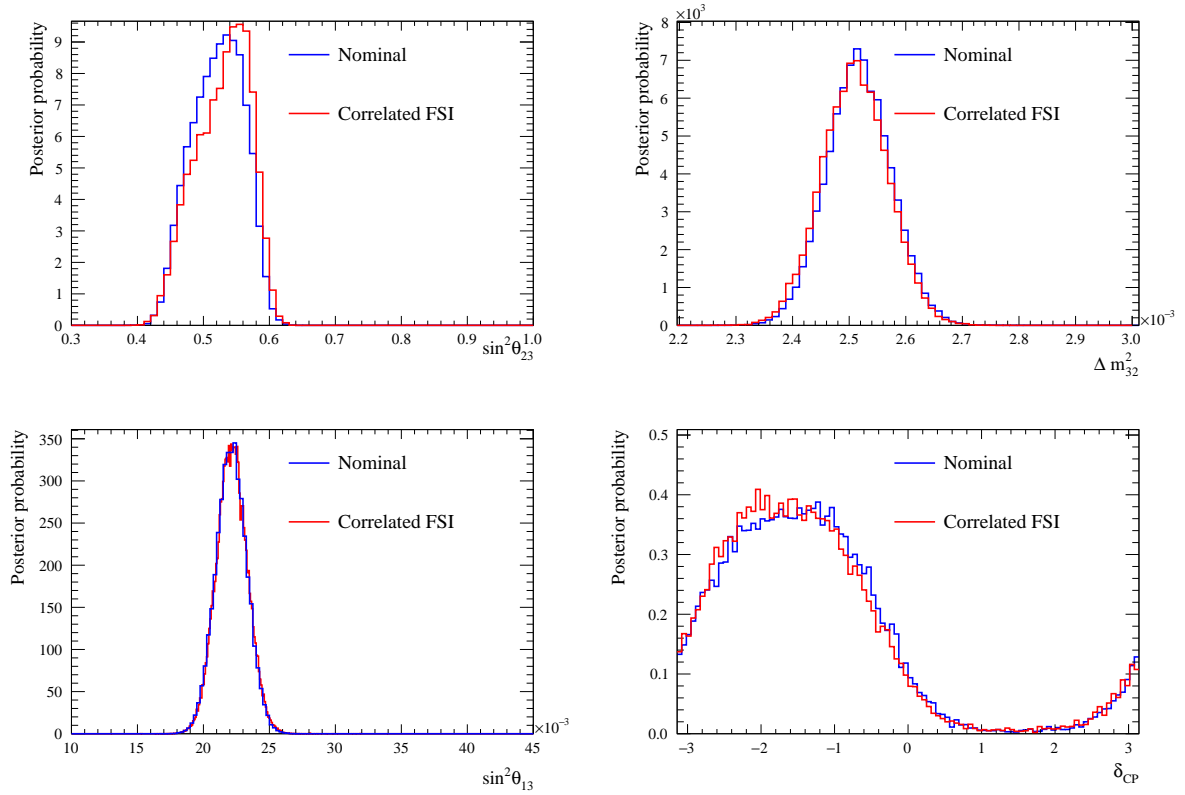


Figure F.5: Posterior probability densities for the appearance and disappearance parameters from T2K + Reactor Asimov fits for the official T2K Run 1-8 oscillation analysis (blue) and the analysis presented in this thesis (red).

Appendix G

Fake Data Study for the Oscillation Analysis

The field of neutrino interactions has been evolving rapidly in the last decade as some areas of the long-baseline neutrino experimental program reach the precision era. Some of these changes may affect current and future T2K results. It is important to evaluate the robustness of the oscillation analysis results against potential neutrino interaction modelling effects not yet included in NEUT neutrino interaction models described in Section 4.2.

The strategy is as follows: a desired interaction model improvement is identified. “Fake data” at ND280 and SK are generated with this model using reweighting techniques to overcome the need of a computationally expensive regeneration of the Monte Carlo simulations. These fake data are fitted using the full oscillation analysis framework, which only includes the “nominal” model described in Section 4.2. Finally, the resulting constraints of the oscillation parameters from these analysis are compared to those of an Asimov fit to identify possible biases.

In this Appendix, one such fake data studies is presented. The interaction model being tested is described in Section G.1. The resulting contours are compared to Asimov contours in Section G.2. A complete summary of the results of the fake data studies can be found in [192].

G.1 Alternative Form Factor Model

The dipole form factor ansatz is used in the baseline model for CCQE interactions:

$$F_A(Q^2) = \frac{g_A}{(1 + Q^2/M_A^{QE2})} \quad (\text{G.1})$$

where the normalization $g_A = F_A(0) = 1.2670 \pm 0.0035$ is well known from neutron β decay, and the axial mass term M_A^{QE} is constrained by neutrino-deuterium scattering at low momentum transfer Q^2 from bubble chamber experiments to be 1.026 ± 0.021 GeV [194]. A *3-component* form factor model has been developed by the NIWG group to increase the freedom of the model at high Q^2 [100]. The form factor then takes the following form:

$$F_A^{3\text{-Comp}}(Q^2) = \left[(1 + \gamma Q^2)^{-2} \times \left(1 - \alpha + \alpha \frac{m_a^2}{m_a^2 + Q^2} \right) \right] + \left[\theta' C Q^2 e^{-\beta Q^2} \right], \quad (\text{G.2})$$

where

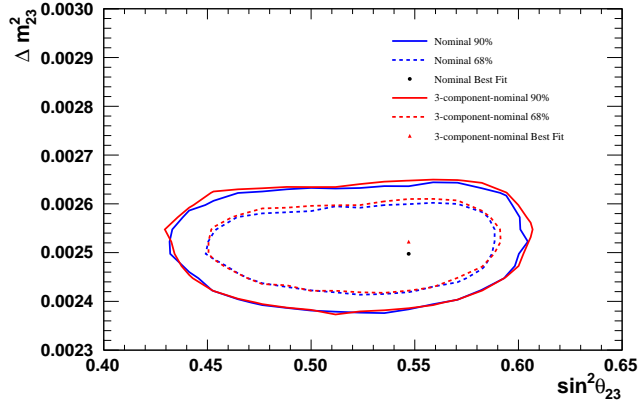
$$\theta' = \text{sgn}(\theta) \sqrt{|\theta| \beta}. \quad (\text{G.3})$$

and the parameters α , γ , β , and θ are allowed to vary in a fit to neutrino bubble chamber data. The nominal prediction and $\pm 1\sigma$ band of this alternative model has been used to build three alternative fake datasets to test the effect on the oscillation analysis of a possible mis-modelling of the high Q^2 shape of the form factor.

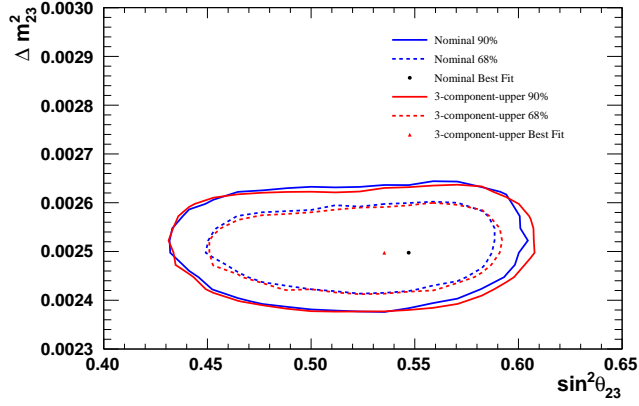
G.2 Fake Data Fit Results

The “Nominal” contours in the following plots were obtained from an Asimov fit to SK data only. The constraints from the ND280 data were introduced separately by using the post-fit values obtained by the BANFF fit to ND280-only. Figure G.1, G.2, and G.3 show the result for “Nominal” and “Fake data” T2K + Reactor constraint fits. The results for the three fake data sets (nominal and $\pm 1\sigma$) are shown.

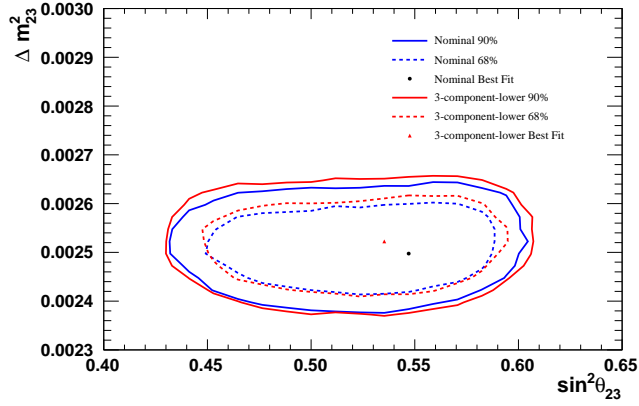
In general, the effect to the contours is smaller than other fake data studies described in [192]. The largest effect arises in the disappearance contours for the -1σ 3-component fake data, as can be seen in G.1. The conclusion of this fake data study is that no significant bias to the neutrino oscillation parameter measurement is introduced by this alternative description of neutrino interactions, and consequently no further action is required.



(a) Nominal

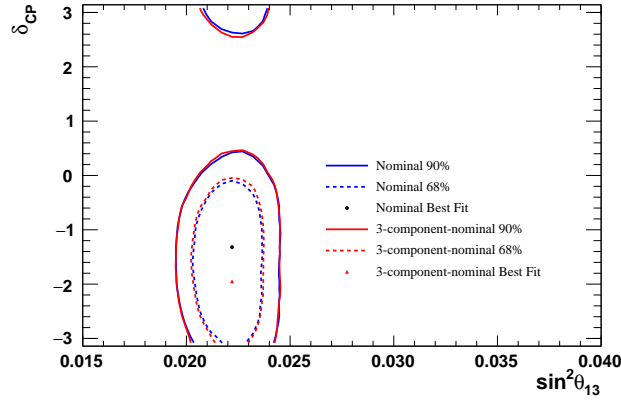


(b) $+1\sigma$

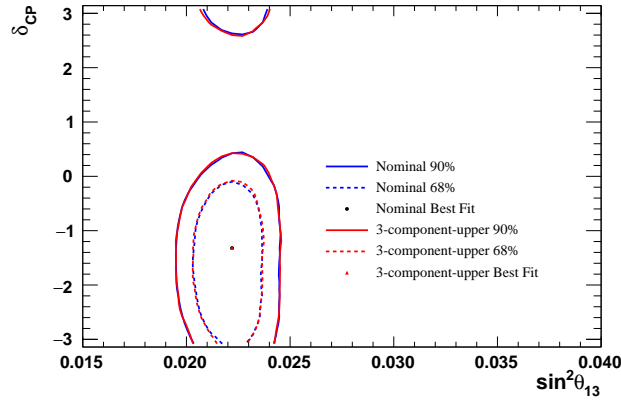


(c) -1σ

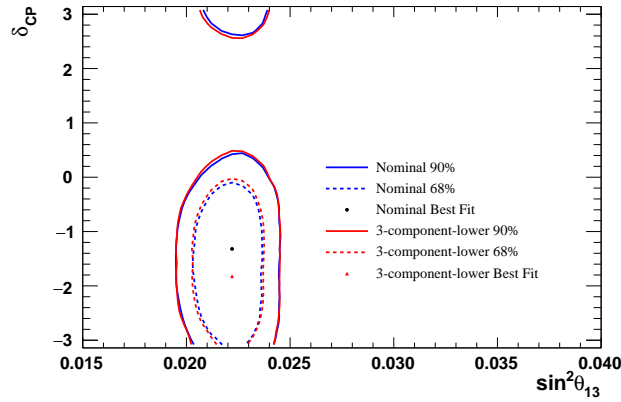
Figure G.1: 2-D 68% and 90% contours in $\sin^2 \theta_{23}$ – Δm_{23}^2 for the “Nominal” (blue) and fake data (red) Asimov fits with the reactor constraint on $\sin^2 \theta_{13}$, assuming normal hierarchy. The three fake data sets (corresponding to the nominal and $\pm 1\sigma$ alternate form factor fake data) are shown.



(a) Nominal

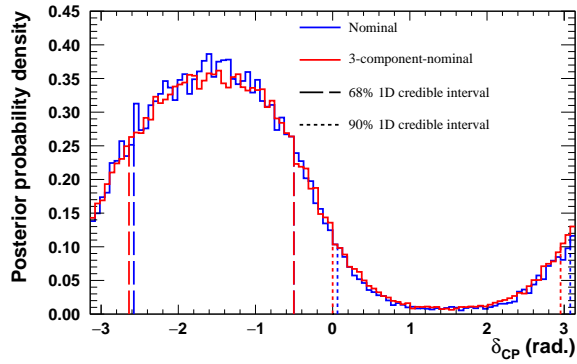


(b) $+1 \sigma$

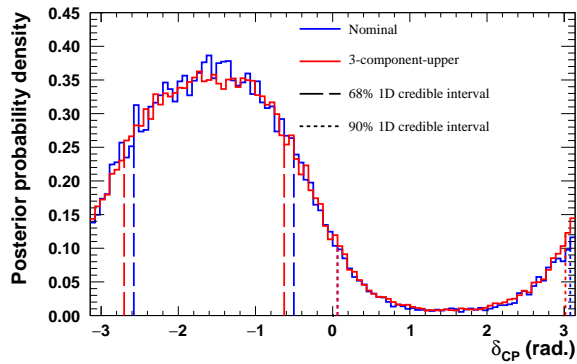


(c) -1σ

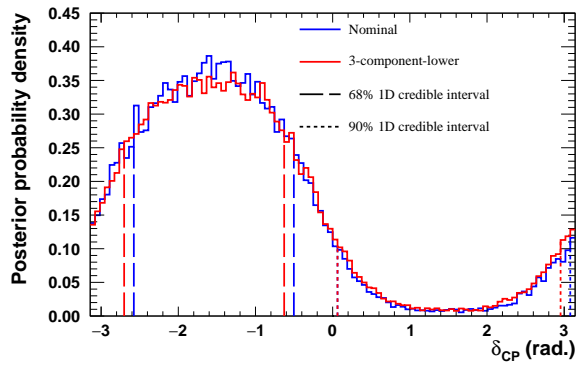
Figure G.2: 2-D 68% and 90% contours in $\sin^2 \theta_{13} - \delta_{CP}$ for fits with the reactor constraint on $\sin^2 \theta_{13}$ for the “Nominal” (blue) and fake data (red) Asimov fits with the reactor constraint on $\sin^2 \theta_{13}$, assuming normal hierarchy. The three fake data sets (corresponding to the nominal and $\pm 1\sigma$ alternate form factor fake data) are shown.



(a) Nominal



(b) $+1 \sigma$



(c) -1σ

Figure G.3: 1-D posterior probability density plots for δ_{CP} from fits with the reactor constraint on $\sin^2 \theta_{13}$ for the “Nominal” (blue) and fake data (red) Asimov fits with the reactor constraint on $\sin^2 \theta_{13}$, assuming normal hierarchy. The three fake data sets (corresponding to the nominal and $\pm 1\sigma$ alternate form factor fake data) are shown.

Bibliography

- [1] K. Ieki, E. S. Pinzon Guerra, *et al.* (DUET Collaboration), *Phys. Rev. C* **92**, 035205 (2015).
- [2] E. S. Pinzon Guerra, S. Bhadra, *et al.* (DUET Collaboration), *Phys. Rev. C* **95**, 045203 (2017).
- [3] J. J. Thomson, *The London, Edinburgh, and Dublin Philosophical Magazine and Journal of Science* **44**, 293 (1897).
- [4] G. Aad *et al.* (ATLAS Collaboration), *Physics Letters B* **716**, 1 (2012).
- [5] S. Chatrchyan *et al.* (CMS Collaboration), *Physics Letters B* **716**, 30 (2012).
- [6] MissMJ, *Standard model of elementary particles* (Wikimedia Commons) https://commons.wikimedia.org/wiki/File:Standard_Model_of_Elementary_Particles.svg (visited: 2017-11-09).
- [7] T. Kajita, *Rev. Mod. Phys.* **88**, 030501 (2016).
- [8] A. B. McDonald, *Rev. Mod. Phys.* **88**, 030502 (2016).
- [9] J. H. Christenson, J. W. Cronin, V. L. Fitch, and R. Turlay, *Phys. Rev. Lett.* **13**, 138 (1964).
- [10] A. Alavi-Harati *et al.* (KTeV Collaboration), *Phys. Rev. Lett.* **83**, 22 (1999).
- [11] B. Aubert *et al.* (BABAR Collaboration), *Phys. Rev. Lett.* **86**, 2515 (2001).
- [12] K. Abe *et al.* (Belle Collaboration), *Phys. Rev. Lett.* **87**, 091802 (2001).
- [13] R. Aaij *et al.* (LHCb Collaboration), *Phys. Rev. Lett.* **110**, 221601 (2013).
- [14] H. Becquerel, *Compt. Rend. Hebd. Seances Acad. Sci.* **122**, 420 (1896).
- [15] E. Rutherford, *The London, Edinburgh, and Dublin Philosophical Magazine and Journal of Science* **47**, 109 (1899).
- [16] J. Chadwick, *Verhandl. Dtsc. Phys. Ges.* **16**, 383 (1914).

- [17] W. Pauli, *Phys. Today* **31**, 27 (1978), Re-print translation into English of telegram from Dec. 4th 1930.
- [18] E. Fermi, *Zeitschrift für Physik* **88**, 161 (1934).
- [19] C. L. Cowan, F. Reines, F. B. Harrison, H. W. Kruse, and A. D. McGuire, *Science* **124**, 103 (1956).
- [20] G. Danby, J.-M. Gaillard, K. Goulianos, L. M. Lederman, N. Mistry, M. Schwartz, and J. Steinberger, *Phys. Rev. Lett.* **9**, 36 (1962).
- [21] K. Kodama *et al.* (DONUT Collaboration), *Physics Letters B* **504**, 218 (2001).
- [22] The ALEPH Collaboration, The DELPHI Collaboration, The L3 Collaboration, The OPAL Collaboration, The SLD Collaboration, The LEP Electroweak Working Group, The SLD Electroweak and Heavy Flavour Groups, *Physics Reports* **427**, 257 (2006).
- [23] Ade, P. A. R. *et al.* (Planck Collaboration), *A&A* **594**, A13 (2016).
- [24] M. Goldhaber, L. Grodzins, and A. W. Sunyar, *Phys. Rev.* **109**, 1015 (1958).
- [25] R. N. Mohapatra and G. Senjanović, *Phys. Rev. Lett.* **44**, 912 (1980).
- [26] J. N. Bahcall, A. M. Serenelli, and S. Basu, *The Astrophysical Journal Letters* **621**, L85 (2005).
- [27] R. Davis, D. S. Harmer, and K. C. Hoffman, *Phys. Rev. Lett.* **20**, 1205 (1968).
- [28] K. S. Hirata, T. Kajita, *et al.* (Kamiokande Collaboration), *Phys. Rev. Lett.* **63**, 16 (1989).
- [29] W. Hampel *et al.* (GALLEX Collaboration), *Physics Letters B* **447**, 127 (1999).
- [30] J. N. Abdurashitov *et al.* (SAGE Collaboration), *Journal of Experimental and Theoretical Physics* **95**, 181 (2002).
- [31] B. Pontecorvo, *Sov. Phys. JETP* **26**, 984 (1968).
- [32] Z. Maki, M. Nakagawa, and S. Sakata, *Progress of Theoretical Physics* **28**, 870 (1962).
- [33] Q. R. Ahmad *et al.* (SNO Collaboration), *Phys. Rev. Lett.* **87**, 071301 (2001).
- [34] K. Zuber, *Neutrino Physics*, 2nd ed. (CRC Press, 2011).
- [35] Y. Fukuda *et al.* (Super-Kamiokande Collaboration), *Phys. Rev. Lett.* **81**, 1562 (1998).
- [36] T. Araki *et al.* (KamLAND Collaboration), *Phys. Rev. Lett.* **94**, 081801 (2005).
- [37] S. Mondal, (2015), [arXiv:1511.06752 \[hep-ex\]](https://arxiv.org/abs/1511.06752) .

- [38] B. Kayser, in *Neutrinos in particle physics, astrophysics and cosmology. Proceedings, 61st Scottish Universities Summer School in Physics, SUSSP61, St. Andrews, UK, August 8-23, 2006* (2008) pp. 51–64, arXiv:0804.1121 [hep-ph] .
- [39] M. Kobayashi and T. Maskawa, *Prog. Theor. Phys.* **49**, 652 (1973).
- [40] S. Bilenky, J. Hošek, and S. Petcov, *Physics Letters B* **94**, 495 (1980).
- [41] S. M. Bilenky and S. T. Petcov, *Rev. Mod. Phys.* **59**, 671 (1987).
- [42] C. Giganti, S. Lavignac, and M. Zito, *Progress in Particle and Nuclear Physics* **98**, 1 (2018).
- [43] L. Wolfenstein, *Phys. Rev. D* **17**, 2369 (1978).
- [44] S. Mikheev and A. Y. Smirnov, *Sov. J. Nucl. Phys.* **42** (1985).
- [45] V. Barger, K. Whisnant, S. Pakvasa, and R. J. N. Phillips, *Phys. Rev. D* **22**, 2718 (1980).
- [46] R. Wendell, *Prob3++ software for computing three flavor neutrino oscillation probabilities* (2012) <http://www.phy.duke.edu/~raw22/public/Prob3++>.
- [47] I. Esteban, M. C. Gonzalez-Garcia, M. Maltoni, I. Martinez-Soler, and T. Schwetz, *Journal of High Energy Physics* **2017**, 87 (2017).
- [48] C. Patrignani *et al.* (Particle Data Group), *Chinese Physics C* **40**, 100001 (2016 and 2017 update).
- [49] A. Gando *et al.* (KamLAND Collaboration), *Phys. Rev. D* **88**, 033001 (2013).
- [50] M. G. Aartsen *et al.* (IceCube Collaboration), *Phys. Rev. D* **91**, 072004 (2015).
- [51] P. Adamson *et al.* (MINOS Collaboration), *Phys. Rev. Lett.* **112**, 191801 (2014).
- [52] P. Adamson *et al.* (NOvA Collaboration), *Phys. Rev. Lett.* **118**, 151802 (2017).
- [53] K. Abe *et al.* (T2K Collaboration), *Phys. Rev. D* **96**, 092006 (2017).
- [54] F. P. An *et al.* (Daya Bay Collaboration), *Phys. Rev. Lett.* **108**, 171803 (2012).
- [55] Y. Abe *et al.* (Double Chooz Collaboration), *Physics Letters B* **735**, 51 (2014).
- [56] J. K. Ahn *et al.* (RENO Collaboration), *Phys. Rev. Lett.* **108**, 191802 (2012).
- [57] K. Abe *et al.* (T2K Collaboration), (2016), arXiv:1609.04111 [hep-ex] .
- [58] R. Acciarri *et al.* (DUNE Collaboration), (2016), arXiv:1601.05471 [physics.ins-det] .
- [59] K. Abe *et al.* (Hyper-Kamiokande Collaboration), *Progress of Theoretical and Experimental Physics* **2015**, 053C02 (2015).

- [60] K. Abe *et al.* (T2K Collaboration), Nuclear Instruments and Methods in Physics Research Section A: Accelerators, Spectrometers, Detectors and Associated Equipment **659**, 106 (2011).
- [61] K. Abe *et al.* (T2K Collaboration), Phys. Rev. D **87**, 012001 (2013).
- [62] A. Ichikawa, Nuclear Instruments and Methods in Physics Research Section A: Accelerators, Spectrometers, Detectors and Associated Equipment **690**, 27 (2012).
- [63] K. Matsuoka *et al.*, Nuclear Instruments and Methods in Physics Research Section A: Accelerators, Spectrometers, Detectors and Associated Equipment **624**, 591 (2010).
- [64] S. Bhadra *et al.*, Nuclear Instruments and Methods in Physics Research Section A: Accelerators, Spectrometers, Detectors and Associated Equipment **703**, 45 (2013).
- [65] V. L. Ginzburg and I. M. Frank, J. Phys.(USSR) **9**, 353 (1945), [Zh. Eksp. Teor. Fiz.16,15(1946)].
- [66] J. D. Jackson, *Classical Electrodynamics*, Third ed. (John Wiley and Sons, 1999).
- [67] L. Wartski, S. Roland, J. Lasalle, M. Bolore, and G. Filippi, Journal of Applied Physics **46**, 3644 (1975), <http://dx.doi.org/10.1063/1.322092> .
- [68] V. Galymov, *Neutrino flux predictions for the T2K long baseline neutrino oscillation experiment*, Ph.D. thesis, York University (2012).
- [69] S. Ritt, P. Amaudruz, and K. Olchanski, “MIDAS (Maximum Integration Data Acquisition System,” (2001).
- [70] D. Beavis, A. Carroll, and I. Chiang, *Physics Design Report Brookhaven National Lab., Upton, NY.*, Tech. Rep. (1995).
- [71] K. Abe *et al.* (T2K Collaboration), Phys. Rev. D **88**, 032002 (2013).
- [72] K. Abe *et al.* (T2K Collaboration), Nuclear Instruments and Methods in Physics Research Section A: Accelerators, Spectrometers, Detectors and Associated Equipment **694**, 211 (2012).
- [73] S. Assylbekov *et al.*, Nuclear Instruments and Methods in Physics Research Section A: Accelerators, Spectrometers, Detectors and Associated Equipment **686**, 48 (2012).
- [74] D. Allan *et al.*, Journal of Instrumentation **8**, P10019 (2013).
- [75] P.-A. Amaudruz *et al.*, Nuclear Instruments and Methods in Physics Research Section A: Accelerators, Spectrometers, Detectors and Associated Equipment **696**, 1 (2012).
- [76] D. B. CLINE, Annals of the New York Academy of Sciences **490**, 120 (1987).

- [77] N. Abgrall *et al.* (T2K ND280 TPC), *Nucl. Instrum. Meth.* **A637**, 25 (2011), [arXiv:1012.0865 \[physics.ins-det\]](#) .
- [78] S. Fukuda *et al.* (The Super-Kamiokande Collaboration), *Nuclear Instruments and Methods in Physics Research Section A: Accelerators, Spectrometers, Detectors and Associated Equipment* **501**, 418 (2003).
- [79] K. Abe *et al.* (Super-Kamiokande), *Phys. Rev.* **D96**, 012003 (2017), [arXiv:1705.07221 \[hep-ex\]](#) .
- [80] K. Choi *et al.* (Super-Kamiokande), *Phys. Rev. Lett.* **114**, 141301 (2015), [arXiv:1503.04858 \[hep-ex\]](#) .
- [81] K. Bays *et al.* (Super-Kamiokande Collaboration), *Phys. Rev. D* **85**, 052007 (2012).
- [82] K. Ueno *et al.*, *Astroparticle Physics* **36**, 131 (2012).
- [83] T. Barszczak, (Accessed 09-27-2017), http://www.ps.uci.edu/tomba/~sk/tscan/compare_mu_e/.
- [84] T. T. Böhlen *et al.*, *Nuclear Data Sheets* **120**, 211 (2014).
- [85] A. Ferrari, P. R. Sala, A. Fassò, and J. Ranft, *FLUKA: A multi-particle transport code* (CERN, Geneva, 2005).
- [86] R. Brun, F. Bruyant, M. Maire, A. McPherson, and P. Zancarini, *GEANT3*, Tech. Rep. CERN-DD-EE-84-1 (1987).
- [87] C. Zeitnitz and T. A. Gabriel, in *3rd International Conference on Calorimetry in High-energy Physics (Note: dates changed from Oct 6-9) Corpus Christi, Texas, September 29-October 2, 1992* (1992) pp. 394–404.
- [88] N. Abgrall *et al.*, *The European Physical Journal C* **76**, 84 (2016).
- [89] A. Fiorentini *et al.*, *Flux Prediction and Uncertainty Updates with NA61 2009 Thin 2 Target Data and Negative Focussing Mode Predictions*, Tech. Rep. T2K-TN-217 (2017).
- [90] Y. Hayato, *Nuclear Physics B - Proceedings Supplements* **112**, 171 (2002).
- [91] G. Garvey, D. Harris, H. Tanaka, R. Tayloe, and G. Zeller, *Physics Reports* **580**, 1 (2015).
- [92] L. Alvarez-Ruso, Y. Hayato, and J. Nieves, *New Journal of Physics* **16**, 075015 (2014).
- [93] O. Benhar, P. Huber, C. Mariani, and D. Meloni, *Physics Reports* **700**, 1 (2017).
- [94] L. Alvarez-Ruso *et al.* (Neutrino Scattering Theory Experiment Collaboration), (2017), [arXiv:1706.03621v2 \[physics.hep-ph\]](#) .
- [95] S. X. Nakamura *et al.*, *Reports on Progress in Physics* **80**, 056301 (2017).

- [96] R. A. Smith and E. J. Moniz, *Nucl. Phys.* **B43**, 605 (1972), [Erratum: *Nucl. Phys.*B101,547(1975)].
- [97] E. J. Moniz, I. Sick, R. R. Whitney, J. R. Ficenec, R. D. Kephart, and W. P. Trower, *Phys. Rev. Lett.* **26**, 445 (1971).
- [98] O. Benhar and A. Fabrocini, *Phys. Rev. C* **62**, 034304 (2000).
- [99] C. Wilkinson *et al.*, *Phys. Rev. D* **93**, 072010 (2016).
- [100] S. Bolognesi *et al.*, *Updated recommendation of the 2017 NIWG parameters*, Tech. Rep. T2K-TN-315 (2017).
- [101] C. Wilkinson, P. Rodrigues, S. Cartwright, L. Thompson, and K. McFarland, *Phys. Rev. D* **90**, 112017 (2014).
- [102] D. Casper, *Nuclear Physics B - Proceedings Supplements* **112**, 161 (2002).
- [103] J. A. Formaggio and G. P. Zeller, *Rev. Mod. Phys.* **84**, 1307 (2012).
- [104] C. L. Smith, *Physics Reports* **3**, 261 (1972).
- [105] A. Bodek, S. Avvakumov, R. Bradford, and H. Budd, *The European Physical Journal C* **53**, 349 (2008).
- [106] T. Katori, *A Measurement of the muon neutrino charged current quasielastic interaction and a test of Lorentz violation with the MiniBooNE experiment*, Ph.D. thesis, Indiana University (2008).
- [107] H. Gallagher, G. Garvey, and G. Zeller, *Annual Review of Nuclear and Particle Science* **61**, 355 (2011), <https://doi.org/10.1146/annurev-nucl-102010-130255> .
- [108] J. Nieves, I. R. Simo, and M. J. V. Vacas, *Phys. Rev. C* **83**, 045501 (2011).
- [109] M. Martini, M. Ericson, G. Chanfray, and J. Marteau, *Phys. Rev. C* **80**, 065501 (2009).
- [110] J. Nieves, J. E. Amaro, and M. Valverde, *Phys. Rev. C* **70**, 055503 (2004).
- [111] D. Rein and L. M. Sehgal, *Annals of Physics* **133**, 79 (1981).
- [112] P. de Perio, *Joint Three-Flavour Oscillation Analysis of ν_μ Disappearance and ν_e Appearance in the T2K Neutrino Beam*, Ph.D. thesis, University of Toronto (2014).
- [113] Jager *et al.*, *Atomic Data and Nuclear Data Tables* **14**, 479 (1974).
- [114] P. de Perio *et al.*, *NEUT Nuclear Effects (FSI)*, Tech. Rep. T2K-TN-033 (2010).
- [115] L. Salcedo, E. Oset, M. Vicente-Vacas, and C. Garcia-Recio, *Nuclear Physics A* **484**, 557 (1988).

- [116] K. Nakamura *et al.* (Particle Data Group), *Journal of Physics G: Nuclear and Particle Physics* **37**, 075021 (2010).
- [117] R. Workman *et al.* (SAID Partial Wave Analysis Program), (Accessed 2009), <http://gwdac.phys.gwu.edu>.
- [118] O. Buss *et al.*, *Physics Reports* **512**, 1 (2012).
- [119] S. Agostinelli *et al.*, *Nucl. Instrum. Meth. A* **506**, 250 (2003).
- [120] A. Heikkinen *et al.*, *Bertini intra-nuclear cascade implementation in Geant4*, <http://arxiv.org/abs/nucl-th/0306008> (2003).
- [121] E. S. Pinzon Guerra, *neutPiA Package*, Presentation at the ND280 Software Meeting (2015).
- [122] E. S. Pinzon Guerra, *NeutG4CascadeInterface Status*, Presentation at the ND280 Software Meeting (2017).
- [123] K. Abe *et al.*, *Nuclear Instruments and Methods in Physics Research Section A: Accelerators, Spectrometers, Detectors and Associated Equipment* **737**, 253 (2014).
- [124] A. D. Missert (T2K), *Proceedings, 27th International Conference on Neutrino Physics and Astrophysics (Neutrino 2016): London, United Kingdom, July 4-9, 2016*, *J. Phys. Conf. Ser.* **888**, 012066 (2017).
- [125] T. Golan, C. Juszczak, and J. T. Sobczyk, *Phys. Rev. C* **86**, 015505 (2012).
- [126] C. Andreopoulos *et al.* (GENIE Collaboration), (2015), [arXiv:1510.05494 \[hep-ex\]](https://arxiv.org/abs/1510.05494) .
- [127] D. Ashery and J. P. Schiffer, *Annual Review of Nuclear and Particle Science* **36**, 207 (1986).
- [128] T.-S. H. Lee and R. P. Redwine, *Annual Review of Nuclear and Particle Science* **52**, 23 (2002).
- [129] B. W. Allardyce *et al.*, *Nucl. Phys.* **A209**, 1 (1973).
- [130] F. Binon *et al.*, *Nuclear Physics B* **17**, 168 (1970).
- [131] C. J. Gelderloos *et al.*, *Phys. Rev. C* **62**, 024612 (2000).
- [132] O. Meirav, E. Friedman, R. R. Johnson, R. Olszewski, and P. Weber, *Phys. Rev. C* **40**, 843 (1989).
- [133] M. A. Moinester *et al.*, *Phys. Rev. C* **18**, 2678 (1978).
- [134] S. M. Levenson *et al.*, *Phys. Rev. C* **28**, 326 (1983).
- [135] D. Ashery *et al.*, *Phys. Rev. C* **23**, 2173 (1981).

- [136] A. Saunders *et al.*, *Phys. Rev. C* **53**, 1745 (1996).
- [137] M. K. Jones *et al.*, *Phys. Rev. C* **48**, 2800 (1993).
- [138] D. Ashery *et al.*, *Phys. Rev. C* **30**, 946 (1984).
- [139] H. Hilscher *et al.*, *Nuclear Physics A* **158**, 602 (1970).
- [140] T. J. Bowles *et al.*, *Phys. Rev. C* **23**, 439 (1981).
- [141] E. Bellotti, D. Cavalli, and C. Matteuzzi, *Il Nuovo Cimento A (1965-1970)* **18**, 75 (1973).
- [142] E. Bellotti, S. Bonetti, D. Cavalli, and C. Matteuzzi, *Il Nuovo Cimento A (1965-1970)* **14**, 567 (1973).
- [143] R. D. Ransome *et al.*, *Phys. Rev. C* **46**, 273 (1992).
- [144] R. A. Giannelli *et al.*, *Phys. Rev. C* **61**, 054615 (2000).
- [145] R. H. Miller, *Nuovo Cimento* **6**, 882 (1957).
- [146] I. Navon *et al.*, *Phys. Rev. Lett.* **42**, 1465 (1979).
- [147] I. Navon *et al.*, *Phys. Rev. C* **28**, 2548 (1983).
- [148] J. Pumplin, D. R. Stump, and W. K. Tung, *Phys. Rev. D* **65**, 014011 (2001).
- [149] D. Stump *et al.*, *Phys. Rev. D* **65**, 014012 (2001).
- [150] M. Hasegawa, *Measurement of Neutrino Oscillation Parameters with Neutrino Nucleus Interaction Studies in the K2K Experiment*, Ph.D. thesis, Kyoto University (2005).
- [151] D. Rowntree *et al.* (LADS Collaboration), *Phys. Rev. C* **60**, 054610 (1999).
- [152] T. Feusels, A. Fiorentini, E. S. Pinzon Guerra, C. Wilkinson, and M. Yu, *Tuning the NEUT Cascade Model using π^\pm -A Scattering External Data to Improve Final State Interaction and Secondary Interaction Systematic Uncertainties*, Tech. Rep. T2K-TN-325 (2017).
- [153] C. H. Q. Ingram *et al.*, *Phys. Rev. C* **27**, 1578 (1983).
- [154] K. Nakai *et al.*, *Phys. Rev. Lett.* **44**, 1446 (1980).
- [155] T. Takahashi *et al.*, *Phys. Rev. C* **51**, 2542 (1995).
- [156] A. S. Carroll *et al.*, *Physical Review C* **14**, 635 (1976).
- [157] F. James and M. Roos, *Computer Physics Communications* **10**, 343 (1975).
- [158] FSIFitter package (2017), <https://repo.nd280.org/viewvc/T2K/NIWG/FSIFitter/>.

- [159] TMultiDimFit - ROOT (2017), <https://root.cern.ch/doc/master/classTMultiDimFit.html>.
- [160] GNU-Octave n-dim interpolation <https://www.gnu.org/software/octave/doc/>.
- [161] N. J. Higham, *Accuracy and Stability of Numerical Algorithms* (Society for Industrial and Applied Mathematics, Philadelphia, PA, USA, 1996).
- [162] P. de Perio *et al.*, *NEUT Systematic Studies for 2010a Analysis*, Tech. Rep. T2K-TN-032 (2010).
- [163] R. G. Calland, *A 3 flavour Joint Near and Far Detector Neutrino Oscillation Analysis at T2K*, Ph.D. thesis, University of Liverpool (2014).
- [164] K. E. Duffy, *Measurement of the neutrino oscillation parameters $\sin^2 \theta_{23}$, Δm_{32}^2 , $\sin^2 \theta_{13}$, and δ_{CP} in neutrino and antineutrino oscillation at T2K*, Ph.D. thesis, University of Oxford (2016).
- [165] L. Haegel, *Measurement of neutrino oscillation parameters using neutrino and antineutrino data of the T2K Experiment*, Ph.D. thesis, University of Geneva (2017).
- [166] K. Duffy, P. Dunne, L. Haegel, A. Kaboth, E. Pinzon, and C. Wret, *A Joint ND280-SK 1R μ SK 1Re fit of neutrino and antineutrino mode data using MCMC*, Tech. Rep. T2K-TN-320 (2017).
- [167] G. Cowan, *Statistical Data Analysis*, Oxford science publications (Clarendon Press, 1998).
- [168] D. Barber, A. Taylan Cemgil, and S. Chiappa, *Bayesian time series models* (Cambridge University Press, 2011).
- [169] OpenMP Architecture Review Board, *OpenMP application program interface version 3.0* (2008) <http://www.openmp.org/mp-documents/spec30.pdf>.
- [170] NVIDIA Corporation, *NVIDIA CUDA C Programming Guide* (2013).
- [171] N. Metropolis, A. W. Rosenbluth, M. N. Rosenbluth, A. H. Teller, and E. Teller, *The Journal of Chemical Physics* **21**, 1087 (1953), <http://dx.doi.org/10.1063/1.1699114> .
- [172] W. K. Hastings, *Biometrika* **57**, 97 (1970).
- [173] R. G. Calland, A. C. Kaboth, and D. Payne, *Journal of Instrumentation* **9**, P04016 (2014).
- [174] R. Brun and F. Rademakers, *Nucl. Inst. & Meth. in Phys. Res. A* **389** (1997), [10.1016/S0168-9002\(97\)00048-X](https://doi.org/10.1016/S0168-9002(97)00048-X).
- [175] S. Bienstock, A. Kaboth, M. Scott, and C. Wret, *Constraining the Flux and Cross Section Models with Data from the ND280 Detector using FGD1 and FGD2 for the 2017 Joint Oscillation Analysis*, Tech. Rep. T2K-TN-324 (2017).

- [176] A. Missert, *Fit to Super-K Atmospheric Neutrino Data for Optimization of the $fiTQun$ Fiducial Volume Cuts and Estimation of Detector Uncertainties*, Tech. Rep. T2K-TN-318 (2017).
- [177] X. Li and M. Wilking, *$FiTQun$ Event Selection Optimization*, Tech. Rep. T2K-TN-319 (2017).
- [178] R. Akutsu *et al.*, *Super-Kamiokande events and data quality studies for T2K Run 8. Part I – $fiTQun$ Samples*, Tech. Rep. T2K-TN-317 (2017).
- [179] K. Abe *et al.* (T2K Collaboration), *Phys. Rev. D* **91**, 072010 (2015).
- [180] S. Dulat, T.-J. Hou, J. Gao, M. Guzzi, J. Huston, P. Nadolsky, J. Pumplin, C. Schmidt, D. Stump, and C.-P. Yuan, *Phys. Rev. D* **93**, 033006 (2016).
- [181] A. A. Aguilar-Arevalo *et al.* (MiniBooNE Collaboration), *Phys. Rev. D* **83**, 052007 (2011).
- [182] M. Day and K. S. McFarland, *Phys. Rev. D* **86**, 053003 (2012).
- [183] P. Bartet *et al.*, *ν_μ CC event selections in the ND280 tracker using Run 2+3+4 data*, Tech. Rep. T2K-TN-212 (2015).
- [184] J. Imber, A. Missert, T. Mueller, C. Vilela, S. Mine, and R. Wendell, *T2K-SK Systematic Error Summary for the 2017 Oscillation Analysis*, Tech. Rep. T2K-TN-326 (T2K, 2017).
- [185] J. Hignight, *Observation of ν_e appearance from an off-axis μ beam utilizing the neutrino energy spectrum*, Ph.D. thesis, Stony Brook University (2014).
- [186] M. Hartz, in *The 50th KEK colloquium: T2K neutrino oscillation results with data up to 2017 Summer* (2017).
- [187] H. Jeffreys, *Theory of Probability*, Third ed. (Oxford University, 1998).
- [188] W. Ma *et al.*, *Five Sample Joint Oscillation Analysis with T2K Run 1-8 Data*, Tech. Rep. T2K-TN-321 (2017).
- [189] C. Andreopoulos *et al.*, *T2K Neutrino and Anti-neutrino 3-Flavour Joint Analysis of Run 1-8 data sets*, Tech. Rep. T2K-TN-327 (2017).
- [190] M. G. Aartsen *et al.* (IceCube Collaboration), (2017), [arXiv:1707.07081 \[hep-ex\]](https://arxiv.org/abs/1707.07081) .
- [191] R. W. for the Super-Kamiokande Collaboration, *AIP Conference Proceedings* **1666**, 100001 (2015).
- [192] S. Bienstock *et al.*, *Assessing the effect of cross-section model uncertainties on the T2K oscillation analyses with fake data studies using the BANFF, MaCh3, P-Theta and VALOR fit frameworks*, Tech. Rep. T2K-TN-331 (T2K, 2017).

- [193] V. Flaminio, W. Moorhead, D. Morrison, and N. Rivoire, *CERN-HERA* **83**, 01 (1983).
- [194] V. Bernard, L. Elouadrhiri, and U.-G. Meissner, *J. Phys.* **G28**, R1 (2002).